QUANTUM CONTROL METHODS FOR NEUTRAL ATOMS

Inaugural-Dissertation

zur

Erlangung des Doktorgrades
der Mathematisch-Naturwissenschaftlichen Fakultät
der Universität zu Köln
vorgelegt von

Juhi Singh

geboren in Durgapur, India

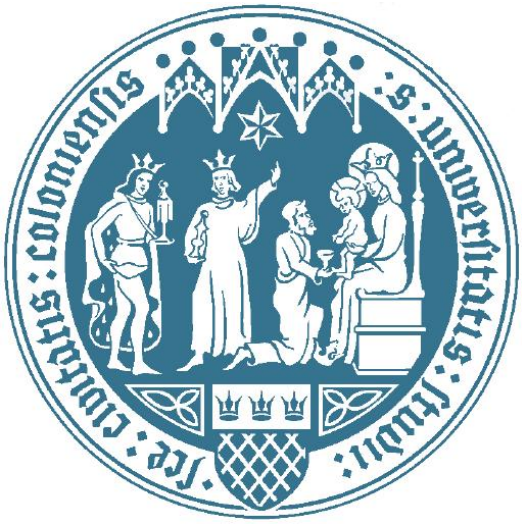

June 2025

Supervisors:

Prof. Dr. Tommaso Calarco

Prof. Dr. Felix Motzoi

Dr. Robert Zeier

Examination committee:

Prof. Dr. Tommaso Calarco

Prof. Dr. Christian Gross

Prof. Dr. Joachim Hemberger

Prof. Dr. Felix Motzoi

To Bhaiya and Didi...
for walking through storms so I could chase the sun...

Abstract

Neutral atoms, trapped in optical tweezers and lattices, have gained significant attention owing to advances in laser technologies, control hardware, and innovative experimental techniques. These systems offer unique advantages such as long coherence times, natural homogeneity, and scalability, while also presenting challenges related to gate speed limitations, atom loss, slow measurements, and other imperfections. Quantum control theory has emerged as a crucial tool for advancing these technologies by enabling precise manipulation of atoms.

In this thesis, we review the foundational concepts in quantum control theory, outlining both analytical approaches and numerical optimization techniques, including methods to account for experimental imperfections. A concise overview of neutral atom platforms follows, covering two distinct operational regimes: Rydberg atoms in optical tweezers and fermionic atoms in optical superlattices.

The core of the thesis is dedicated to our work addressing practical control problems in neutral atom systems. First, we develop a platform-independent method for estimating and compensating nonlinear pulse distortions in experimental setups and demonstrate its use numerically for Rydberg atom excitations. Next, we tackle the challenge of implementing fast and robust gates in fermionic atom systems trapped in superlattices by optimizing lattice depths. Finally, we explore the application of Rydberg-based analog quantum simulators for variational quantum eigensolvers, using Lie-algebraic tools to analyze symmetry restrictions.

This work highlights the essential role of quantum control methods in enhancing the fidelity, robustness, and applicability of neutral atom quantum technologies. It also demonstrates how combining theoretical tools, numerical optimization, and experimental considerations leads to practical solutions for scalable and high-performance quantum systems. The methods and insights developed here also offer transferable strategies for other quantum hardware architectures.

Contents

1 Introduction

Quantum technologies are rapidly evolving from the pure theoretical principles proposed in the early 1900s to the experimental implementation of these ideas [1, 2]. Built upon powerful concepts such as superposition and entanglement [3], these technologies promise capabilities that go far beyond classical computation [4]. The promises of quantum computing extend widely across modern science, from secure communication and drug discovery to complex simulations of natural systems. To realize these possibilities, scientists have been developing various quantum devices in parallel, including quantum processors, simulators, sensors, and communication systems. Since the early 21st century, these technologies have made remarkable strides towards what is often called the "second quantum revolution" [1]. However, the actual, large-scale use cases and practical applications of these technologies remain an open and evolving question [5, 6]. Though still in development and facing significant technical challenges, the field is emerging rapidly and holds the potential to redefine the future of modern science and technology.

Quantum technologies are being pursued from many different directions, both experimentally and theoretically. Experimentalists are using various platforms, each with their own advantages and challenges, to build these devices. Some of the leading platforms are superconducting qubits, trapped ions, neutral atoms, and photonic systems [7–9]. These systems differ significantly in their construction but aim to follow the same quantum mechanical ideas to perform similar tasks. For example, most of them work on the idea of storing quantum information in two different energy levels of the system, known as a qubit. In superconducting systems, qubits are formed artificially using electrical circuits at cryogenic temperatures [10, 11], while in trapped ions [12, 13], charged atoms trapped in electromagnetic traps are used to store qubit information.

Similar to trapped ions, neutral atoms are also natural atom-based technologies, where the atoms are uncharged and stored in optical tweezers or optical lattices [14–

17]. The initial proposal for using neutral atoms in quantum technologies was made in the early 2000s, and in recent years, these systems have gained significant attention once again. This renewed interest has mainly come from technical advancements in lasers and control hardware, along with experimental progress in developing innovative methods for trapping and interacting with these atoms. The basic principle of this platform comes from light-matter interaction, where atoms are stored in optical traps created by laser fields interacting with the atoms and forming a dipole potential. Qubit states are mostly stored in the hyperfine energy levels of these atoms and are driven by another set of laser fields. The specific type of quantum operation depends on the interactions used within the platform, such as dipole-dipole, long-range Rydberg, or collisional interactions [18–21]. Overall, neutral atom systems offer several advantages over other platforms, including long coherence times, comparatively easier scalability, and naturally occurring, more homogeneous interactions between qubits [22]. However, they also face notable challenges when compared to similarly advanced platforms — such as slower gate speeds, which limit the circuit depths achievable for quantum algorithms; restrictions in performing digital quantum processing tasks with parallel gates; measurement speed; and atom loss, which results in the loss of the stored quantum information. Some of these challenges are being addressed experimentally by improving the lasers, making the traps more confined etc. Despite these challenges, this platform remain one of the leading technology due to its reconfigurable geometries, well-defined interactions suited for quantum simulation of many-body physics.

The experimental advancements in recent years have brought neutral atom platforms into close competition with other leading quantum technologies. Now, a crucial goal is to achieve high-fidelity quantum operations necessary for efficient quantum information tasks. This objective remains particularly challenging, as several factors, including the finite lifetime of atomic states, laser noise, bandwidth limitations, and technical imperfections, limit the achievable fidelity of quantum operations. To fine-tune qubit states and design efficient, reliable gates in the presence of these hurdles, quantum control techniques have become a dominant tool [23, 24]. Additionally, these techniques have been employed to optimize quantum processes so that the desired operations are performed in the minimal possible time. This is crucial for quantum computation tasks with long circuits, where every gate duration impacts the overall system performance and coherence.

Both analytical and numerical quantum control methods have been used for optimizing quantum operations; however, numerical methods have seen greater success for neutral atom devices [25–27], as they are more adaptable to the complex lattice potentials and many-body interactions present in atomic systems. In particular, numerical techniques such as GRAPE (Gradient Ascent Pulse Engineering) [28] and CRAB

(Chopped Random Basis) [29] have been successfully applied to achieve complex state preparation and gate design tasks. These control techniques are becoming increasingly sophisticated, incorporating not only the ideal quantum Hamiltonian into the modeling but also various technical imperfections present in real experiments. Characterizing and modeling these imperfections, such as pulse distortion, phase noise, and intensity inhomogeneity has become an active and important field of research. Only by systematically combining these effects and carefully engineering control pulses we can achieve the operational efficiencies required for scalable, fault-tolerant quantum computing with neutral atom systems.

While the efforts for making fault-tolerent quantum computers continues, researchers and even industries are also trying to make use of the currently available noisy devices known as the devices of Noisy Intermediate-Scale Quantum (NISQ) era [2]. In the NISQ era, neutral atom quantum simulators combined with variational quantum algorithms hold the potential to solve classically difficult problems. For example, the Quantum Approximate Optimization Algorithm (QAOA) and Variational Quantum Eigensolver (VQE) are hybrid quantum-classical algorithms that, when implemented on quantum simulators, have been used to solve problems such as max-cut, the Traveling Salesperson problem, and finding ground states of quantum systems [30, 31]. However, these algorithms come with their own limitations, including scalability issues, barren plateaus in the optimization landscape, and challenges with convergence. While many of these obstacles arise from the scalability of both the system and the problem size, some challenges are inherent to the quantum simulator itself. Particularly in analog quantum simulators driven by global laser fields, the system tends to be more constrained with limited control over individual components, reducing the flexibility to tune the system's dynamics. In such cases, the potential of the quantum simulator becomes restricted, yielding reliable results only for certain tasks that align with the system's symmetries. Therefore, through careful analysis of these systems possibily using control theory tools, existing algorithms can be matched with suitable tasks, and new, more efficient algorithms tailored to the specific symmetries and constraints of these platforms can potentially be developed.

In this thesis, we cover a broad range of control theory methods, including both analytical and numerical approaches, to aid neutral atom devices from both the engineering and application perspectives. While some of the developments in control techniques are general in nature, they are specifically applied to various experimental setups based on neutral atom platforms. This demonstrates the versatility and effectiveness of these control methods in enhancing the performance of practical quantum technologies.

The organization of the thesis is as follows: The thesis begins with an overview

of quantum control methods in Chapter 2, where we start by briefly discussing the fundamental concepts relevant to quantum technologies. We then describe the general structure of different types of quantum systems and illustrate some examples using two-level systems. Following this, we introduce the general quantum control problem and various algorithms developed to solve it, with a particular focus on numerical methods, while also mentioning other approaches. Finally, we discuss the practical extensions of these control methods and how they are adapted to bring theoretical techniques closer to experimental implementation.

Since all the work presented in this thesis is heavily centered around neutral atoms, a focused review of this platform is presented in Chapter 3. While a comprehensive explanation of all the experimental details and advancements in this field is beyond the scope of this work and not crucial for our purposes, we still outline the essential physics of neutral atoms and their interaction with light. This chapter is divided into two parts. In the first part, we discuss the widely studied Rydberg atom platform, where quantum operations are based on long-range interactions between highly excited Rydberg states. In the second part, we describe a relatively lesser-known neutral atom platform, where quantum operations rely on controlled collisions between atoms.

Using the concepts from Chapter 2 and Chapter 3, we then present our original research work in Chapter 4, Chapter 5, and Chapter 6. In Chapter 4, we build upon the control methods introduced in Chapter 2 and provide a mathematical framework for estimating possible non-linear distortions that occur in experiments. While the methods presented here are general and can be applied to any quantum platform, the development of this approach is originally motivated by the distortions observed in acousto-optic modulators (AOMs) used during the Rydberg atom excitation process. We demonstrate that including these distortions within the optimization process can effectively suppress pulse distortion effects, and as a practical example, we show how this leads to an improvement in Rydberg excitation fidelity.

Next, using similar control techniques as in Chapter 4, we address a new and challenging control problem in Chapter 5, focusing on the optimization of quantum gates in a fermionic atom-based system. In this work, the modeling and optimization methods are adapted to a relatively new and complex experimental setup, where the atoms are trapped in a superlattice potential. Through numerical optimization, we efficiently suppress leakage to higher energy levels and design fast, high-fidelity, and robust quantum gates suitable for this platform.

In our final work, presented in Chapter 6, we shift towards the application side of neutral atom devices, focusing in particular on Rydberg atom-based analog simulators used to perform variational algorithms. We explore one specific algorithm, the variational quantum eigensolver, for finding the ground states of given target Hamil-

tonians. To better understand the performance and limitations of this approach, we employ Lie algebra-based control theory tools to analyze the symmetries of the system and comment on the reachability of the target ground states. Through this study, we demonstrate how such analysis can reveal both the potential and inherent constraints of variational algorithms on analog quantum simulators, providing valuable guidance for future applications and algorithm design. Finally, we discuss and conclude in Chapter 7.

Summary of key results and impact

This thesis presents several important advances in quantum control theory for neutral atom platforms and the key results are highlighted below.

- Formulation of a mathematical framework to model and compensate non-linear distortions originating from the control hardware, leading to improved Rydberg excitation fidelities.
- Design of quantum control methods for two-qubit gates for fermionic atoms in optical superlattice potentials, improving the gate performance and achieving fast gates.
- Development and application of Lie algebra-based control theory tools to analyze the controllability and reachable state spaces of Rydberg-based analog quantum simulators executing variational algorithms, identifying the symmetry restrictions and possible remedies for ground state preparation.

Impact: These contributions bridge theoretical control methods and practical quantum hardware, show the possibilities of improvement in the performance of neutral atom-based quantum operations, and offer valuable tools for the analysis of quantum algorithms. While demonstrated on neutral atom systems, the generality of most of the methods developed ensures their relevance and applicability across multiple quantum hardware platforms.

2 Quantum control

Recent developments in quantum technologies arise from a mixture of fundamental physics, engineering, mathematics, and computer science, with the advancement in the understanding of quantum physics at the core of these technologies. One such subfield, developed at the intersection of these different fields, is quantum control [23, 24, 27, 32–34]. Quantum control helps in efficiently control and manipulate the dynamics of quantum systems to perform different quantum operations.

Originally developed for manipulating chemical reactions in molecules, in the last few decades quantum control has expanded its scope from NMR to solid-state systems [35, 36]. This advancement has been a result of both new theoretical concepts and experimental improvements, such as the refinement of laser technology. In recent years, with the growing interests in different aspects of quantum technologies, especially quantum computation and simulation, the need for precise control has increased, opening a new set of goals and challenges for quantum control [25, 37–45].

While the basic principles of quantum control resemble the classical control theory, it engages with the quantum mechanical properties of a system, making the problem far from straightforward. At the heart of these quantum properties lie fundamental quantum physics concepts such as superposition, entanglement, and tunneling, which distinguish them from classical systems, where the most foundational component is the qubit, or quantum bit [3, 46, 47].

In the first half of this chapter, we provide a brief overview of these fundamental quantum properties. We begin by describing the basic elements of quantum physics, such as qubits, superposition, entanglement, and related concepts. Following this, we explain the fundamental principles of quantum control, where we give more emphasis to the numerical techniques that will be used later in this thesis.

2.1 Fundamentals

2.1.1 Qubits

The basic computational unit in a quantum computer is the qubit (quantum bit). Unlike classical bits, which can only be in the states $|0\rangle$ or $|1\rangle$, qubits can exist in a linear combination of these states, a phenomenon known as superposition. For example, a qubit state can be represented as

$$|\psi\rangle = c_1 |0\rangle + c_2 |1\rangle = \begin{pmatrix} c_1 \\ c_2 \end{pmatrix}, \tag{2.1}$$

where c_1 and c_2 are complex numbers representing the probability amplitudes for the qubit to be in the state $|0\rangle$ or $|1\rangle$, respectively. These amplitudes must satisfy the condition $|c_1|^2 + |c_2|^2 = 1$ to ensure the total probability equals one [3]. A physical measurement, e.g., a projective measurement, causes the qubit state $|\psi\rangle$ to collapse into either $|0\rangle$ or $|1\rangle$ with probabilities $|c_1|^2$ and $|c_2|^2$, respectively.

For an intuitive picture of a qubit, we can represent it using a three-dimensional unit sphere, known as the Bloch sphere, as shown in Fig. 2.1. On the sphere, each qubit state corresponds to a point, and its amplitudes can be expressed in terms of angles θ and ϕ (shown in Fig. 2.1) as [3]

$$c_1 = \cos\frac{\theta}{2}, \; c_2 = e^{i\varphi} \sin\frac{\theta}{2}. \tag{2.2}$$

In principle, infinitely many distinct qubit states $|\psi\rangle$ exist, parameterized by the angles θ and φ. However, upon measurement, the state collapses to either $|0\rangle$ or $|1\rangle$ based on the probabilities $|c_1|^2$ and $|c_2|^2$. This implies that an infinite number of measurements would be needed to precisely reconstruct the values of c_1 and c_2, and thereby the state $|\psi\rangle$.

The concept of superposition can be extended to multiple qubits. For example, a two-qubit system has four computational basis states, typically written as $|00\rangle$, $|01\rangle$, $|10\rangle$, and $|11\rangle$. The system can exist in a superposition of these four states. Similar to the one-qubit case in Eq. (2.1), the quantum state of two qubits is represented as a linear combination of these basis states, associated with complex coefficients

$$|\Psi\rangle = c_1 |00\rangle + c_2 |01\rangle + c_3 |10\rangle + c_4 |11\rangle . \tag{2.3}$$

Upon measuring both qubits, the state $|\Psi\rangle$ collapses into one of these computational basis states with probabilities $|c_1|^2$, $|c_2|^2$, $|c_3|^2$, or $|c_4|^2$.

If we measure only one qubit — say the first one — and obtain the result $|0\rangle$, the

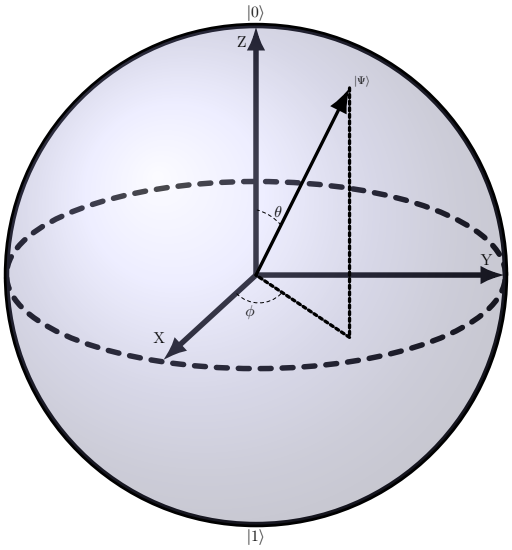

Figure 2.1: Bloch-sphere representation of a qubit. Each qubit state $|\psi\rangle$ corresponds to a point on the unit sphere. The angle θ is between the z-axis and the vector representing $|\psi\rangle$. The angle φ is the azimuthal angle in the x-y plane. The two orthogonal states $|0\rangle$ and $|1\rangle$ are located at the opposite poles.

post-measurement state becomes

$$|\Psi\rangle_M = \frac{c_1 |00\rangle + c_2 |01\rangle}{\sqrt{|c_1|^2 + |c_2|^2}}. \tag{2.4}$$

This is still a superposition of $|0\rangle$ and $|1\rangle$ for the second qubit, with renormalized probabilities.

Depending on whether the qubits are independent or correlated, the overall state may be a product (separable) state or an entangled state [46]. If the states of different qubits are correlated, we call it an entangled state. For example, the Bell state $\frac{1}{\sqrt{2}}(|00\rangle + |11\rangle)$ is an entangled state. Measuring one qubit immediately determines the state of the other, even if they are spatially separated. For instance, if the first qubit of this Bell state is measured and found to be $|0\rangle$, we instantly know that the second qubit is also in state $|0\rangle$. This phenomenon persists even when the two qubits are far apart. The study of such fundamental quantum properties has led to intriguing topics such as the EPR paradox, the no-communication theorem, and quantum nonlocality, which are beyond the scope of this thesis.

Quantum states can be classified into pure and mixed states. A pure state represents complete knowledge of the system, while a mixed state provides only statistical knowledge. Qubit states can also be represented using density operators, which are particularly useful when dealing with mixed states. A density operator is a matrix formed from the orthonormal basis states (e.g., $|0\rangle$ and $|1\rangle$ for a single qubit). A pure

state $|\Psi\rangle$ is represented by the density matrix

$$\rho = |\Psi\rangle \langle\Psi| . \tag{2.5}$$

A mixed state, on the other hand, has the density matrix form

$$\rho = \sum_i f_i |\Psi_i\rangle \langle\Psi_i| , \tag{2.6}$$

where each $|\Psi_i\rangle$ is a pure state and f_i are the corresponding probabilities. The purity of a density operator is given by $\mathrm{Tr}(\rho^2)$, where Tr represents the trace operation. The density matrix of pure states satisfy $\mathrm{Tr}(\rho^2) = 1$, while mixed states have $\mathrm{Tr}(\rho^2) < 1$. For a more comprehensive treatment of mixed states and related topics, readers are referred to [3]. With these basic ideas in mind, we briefly explain quantum gates, which are the building block of quantum computation and simulation tasks.

2.1.2 Quantum gates

Similar to how qubits have classical counterparts in bits, quantum gates serve as the quantum analog of classical Boolean operations or logic gates. A quantum gate is an operation performed on qubits to manipulate their states. Quantum gates possess several properties that arise directly from the principles of quantum mechanics, distinguishing them from their classical counterparts. Since qubit states can exist in superposition or be entangled with one another, the outcomes of quantum gate operations are often non-trivial and extend beyond what classical gates can achieve. Every quantum gate can be represented by a unitray matrix U whose dimension corresponds to that of the system's Hilbert space. A matrix U is unitary if $U^{-1} = U^\dagger$, which ensures the conservation of the total probability in a closed quantum system and makes quantum gates reversible. Additionally, Quantum gates are linear transformations such that

$$U(|\Psi_1\rangle + |\Psi_2\rangle) = U|\Psi_1\rangle + U|\Psi_2\rangle . \tag{2.7}$$

While some gates are both unitary and Hermitian satisfying $U = U^{-1} = U^\dagger$ (such as the Pauli-X, Pauli-Y, and Pauli-Z gates), this is not a general property shared by all quantum gates. A set of quantum gates that allows us to approximate any quantum gate with a desired precision is called a universal gate set [3]. By using a universal gate set, any multi-qubit gate can be implemented, as universal gate set contains all single-qubit gates and two-qubit gates like CNOT or $\sqrt{\mathrm{SWAP}}$. Next, we will introduce some fundamental single- and two-qubit gates.

Single-qubit gates are 2×2 unitary matrices, which preserve the qubit's normaliza-

tion, $|c_1|^2 + |c_2|^2 = 1$, where c_1 and c_2 are the complex coefficients shown in Eq. (2.1). Key examples include the Pauli gates (X, Y, Z), which correspond to rotations around the x, y, and z axes of the Bloch sphere by π radians, as shown in Fig. 2.1. We can also define an identity gate (I), which leaves the qubit's state unchanged. These Pauli gates are expressed in matrix form as

$$X = \begin{pmatrix} 0 & 1 \\ 1 & 0 \end{pmatrix}, \quad Y = \begin{pmatrix} 0 & -i \\ i & 0 \end{pmatrix}, \quad Z = \begin{pmatrix} 1 & 0 \\ 0 & -1 \end{pmatrix}, \quad I = \begin{pmatrix} 1 & 0 \\ 0 & 1 \end{pmatrix}. \tag{2.8}$$

One of the widely used single-qubit gates is the Hadamard gate, H. The Hadamard gate is defined by the matrix

$$H = \frac{1}{\sqrt{2}} \begin{pmatrix} 1 & 1 \\ 1 & -1 \end{pmatrix}. \tag{2.9}$$

It maps computational basis states into superposition states and vice versa, as follows

$$H|0\rangle = \frac{1}{\sqrt{2}}(|0\rangle + |1\rangle), \tag{2.10}$$

$$H|1\rangle = \frac{1}{\sqrt{2}}(|0\rangle - |1\rangle). \tag{2.11}$$

The Hadamard gate plays a crucial role in quantum computing. Despite its simple appearance, it possesses a powerful property: when applied to n qubits initially set to $|0\rangle$, it generates an equal superposition of all integers from 0 to $2^n - 1$, enabling the exponential power of a quantum circuit. We can also construct arbitrary rotation gates that rotate a qubit's state around any axis on the Bloch sphere. Depending on the axis of rotation, we have $R_x(\theta)$, $R_y(\theta)$, and $R_z(\theta)$ gates, defined as

$$R_x(\theta) = \exp(-i\theta X/2) = \begin{pmatrix} \cos\frac{\theta}{2} & -i\sin\frac{\theta}{2} \\ -i\sin\frac{\theta}{2} & \cos\frac{\theta}{2} \end{pmatrix}, \tag{2.12}$$

$$R_y(\theta) = \exp(-i\theta Y/2) = \begin{pmatrix} \cos\frac{\theta}{2} & -\sin\frac{\theta}{2} \\ \sin\frac{\theta}{2} & \cos\frac{\theta}{2} \end{pmatrix}, \tag{2.13}$$

$$R_z(\theta) = \exp(-i\theta Z/2) = \begin{pmatrix} e^{-i\theta/2} & 0 \\ 0 & e^{i\theta/2} \end{pmatrix}. \tag{2.14}$$

In general, we can use different decomposition techniques such as Euler decompositions to split any arbitrary qubit rotation into multiple rotations about different axes on the Bloch sphere. This approach is particularly useful for implementing gates on various quantum hardware platforms, with restricted set of possible operations.

We construct multi-qubit gates, which can generate entanglement between qubits,

by enabling interactions between them. An n qubit state is represented by 2^n probability amplitudes, and the n qubit gate matrix operating on them has the dimension of $2^n \times 2^n$. Single and two-qubit gates are, so far, the most widely used gates in quantum technologies. Different platforms have different realizations of two-qubit gates, but they all have some basic computational gate set. One of the most common and useful gates is the controlled gate, where a control qubit determines the operation on the target qubit(s). One example of these types of gates is the Controlled-NOT (CNOT) gate, which applies a NOT gate to the target qubit if the control qubit is $|1\rangle$. A second example is the Controlled-Z (CZ) gate, which applies a Z gate to the target qubit if the control qubit is $|1\rangle$. The CNOT gate is not symmetric between the two qubits; therefore, it depends on the choice of control and target qubits. In contrast, the CZ gate is independent of the choice of control qubit and is diagonal in the computational basis, making it suitable for implementing in some experimental platform such as ultracold atoms as discussed in Chapter 3. The matrix representations of these gates are

$$CNOT = \begin{pmatrix} 1 & 0 & 0 & 0 \\ 0 & 1 & 0 & 0 \\ 0 & 0 & 0 & 1 \\ 0 & 0 & 1 & 0 \end{pmatrix}, \quad CZ = \begin{pmatrix} 1 & 0 & 0 & 0 \\ 0 & 1 & 0 & 0 \\ 0 & 0 & 1 & 0 \\ 0 & 0 & 0 & -1 \end{pmatrix}. \tag{2.15}$$

For Rydberg atoms, one can also construct a C-PHASE gate as discussed in Sec. 3.1.3, which, up to local phase corrections, is equivalent to the conventional CZ gate. Combining the C-PHASE gate with Hadamard operations allows the construction of a CNOT gate, and together with arbitrary single-qubit rotations, forms a universal gate set for quantum computing with neutral atoms [3].

For some experimental setup, e.g., fermionic atoms described in Chapter 3 and 5, other two-qubit gates may be more feasible such the SWAP gate, which exchanges the states of the qubits, without generating entanglement. For generating entanglement in this setting, $\sqrt{\text{SWAP}}$ gate is widely used. The $\sqrt{\text{SWAP}}$ gate occurs naturally in many physical systems and entangles the two qubits as follows,

$$\sqrt{\text{SWAP}} = \begin{pmatrix} 1 & 0 & 0 & 0 \\ 0 & \frac{1}{2}(1+i) & \frac{1}{2}(1-i) & 0 \\ 0 & \frac{1}{2}(1-i) & \frac{1}{2}(1+i) & 0 \\ 0 & 0 & 0 & -1 \end{pmatrix}. \tag{2.16}$$

Gates beyond two-qubit gates enable more complex algorithms and circuits, but they are very difficult to construct experimentally. One important example is the Toffoli gate (also known as the CCNOT gate), a three-qubit gate that performs a

NOT operation on the target qubit when both control qubits are in the state $|1\rangle$. Another example is the Fredkin gate, or controlled-SWAP gate, which swaps the states of two qubits based on the state of a control qubit. These multi-qubit gates are often decomposed into a series of single- and two-qubit gates, making their implementation easier at the cost of increasing the circuit depth.

The implementation of quantum gates corresponds to a specific unitary time evolution generated by a Hamiltonian acting over a defined duration. In the next section, we will explain how these gates are implemented through the time evolution of a quantum system, where we first introduce two types of quantum systems: closed and open systems.

2.2 Quantum dynamics

In its most basic form, the time evolution expresses the relationship between the change in the state and the forces applied to it. It is one of the main concepts for understanding the properties of any physical system. In the classical world, different differential equations like the Euler-Lagrange equations, Hamilton's equations, and Liouville's equation are used to describe the time evolution. For several years, researchers have attempted to develop methods similar to these classical approaches to describe the evolution of quantum systems. These methods depend on the nature of the quantum system, for example, if they interact with the enviornment or not. In this section, we will discuss two important methods namely, Schrödinger equation for closed systems and master equation for open systems [48–51].

2.2.1 Closed system

A closed or isolated system does not exchange any energy or mass with another system, often referred to as the environment [3, 52]. For a state $|\Psi(t)\rangle \in \mathcal{H}$, where $\mathcal{H}$ is the Hilbert space of the system, we can write the Schrödinger time evolution equation as

$$\frac{d}{dt}|\Psi(t)\rangle = -\frac{i}{\hbar}H(t)|\Psi(t)\rangle\,, \tag{2.17}$$

where $H(t)$ is the Hamiltonian of the system. We can also write the time-independent Schrödinger equation for a stationary state $|\Psi\rangle$ as

$$H|\Psi\rangle = E|\Psi\rangle\,.$$

Any linear combination $c_1|\Psi_1\rangle + c_2|\Psi_2\rangle$ of two solutions $|\Psi_1\rangle$ and $|\Psi_2\rangle$ is also a solution to the corresponding Schrödinger equation, demonstrating its linearity. The time

evolution operator from time $t = 0$ to $t = T$ is given by the time-ordered exponential,

$$U(T, 0) = \mathcal{T} \exp\left[-\frac{i}{\hbar}\int_0^T H(\tau)\, d\tau\right],$$

where $\mathcal{T}$ represents the time-ordering operation. The final quantum state can then be written as $|\Psi(T)\rangle = U(T, 0)\,|\Psi(0)\rangle$. The operator $U(T, 0)$ is unitary and generates all quantum gates described in Sec. 2.1.2. It has the following properties:

$$U(t_0, t_0) = \mathbb{I}, \quad U(t', t)^{-1} = U(t', t)^\dagger, \quad \text{and} \quad U(t_2, t_1)U(t_1, t_0) = U(t_2, t_0),$$

where $\mathbb{I}$ is the identity operator [53, 54]. For a time-independent Hamiltonian H, the solution to Eq. (2.17) is

$$|\Psi(t)\rangle = e^{-iHt/\hbar}\,|\Psi(0)\rangle\,. \tag{2.18}$$

The evolution of the system along the interval $[0, T]$ can also be evaluated at intermediate times t, giving the state $|\Psi(t)\rangle$. To achieve this, we can decompose the time-ordered evolution operator as

$$U(T, 0) = U(t_N, t_{N-1}) \cdots U(t_2, t_1)U(t_1, t_0), \tag{2.19}$$

where $t_N = T$, and we can compute $|\Psi(t_j)\rangle$ at different discrete times t_j. Now, for a constant time interval dt, we can write

$$U(t + dt, t) = \mathcal{T} \exp\left[-\frac{i}{\hbar}\int_t^{t+dt} H(\tau)\, d\tau\right].$$

If the Hamiltonian $H(t)$ is approximately constant over the time duration $[t, t + dt]$, the evolution operator reduces to an approximate time-independent form:

$$U(t + dt, t) = \exp\left[-\frac{i}{\hbar}H(t)\, dt\right]. \tag{2.20}$$

In the general case where $H(t)$ is time-dependent between t and $t+dt$, the Hamiltonian may not commute with itself at different times, and hence a simple closed-form solution for $U(t', t)$ may not exist.

So far, we have discussed everything in terms of state vectors. However, in general, quantum operations e.g., application of a gate, are described by the evolution of the density matrix [3]. From Eq. (2.6), the density operator for a discrete set of pure states

$|\Psi_i\rangle$ with weights f_i is written as

$$\begin{aligned}\rho(t) &= \sum_i f_i \,|\Psi_i(t)\rangle \,\langle\Psi_i(t)| \\ &= U(t,t_0)\left(\sum_i f_i \,|\Psi_i(0)\rangle \,\langle\Psi_i(0)|\right) U^\dagger(t,t_0) \\ &= U(t,t_0)\,\rho(0)\,U^\dagger(t,t_0). \end{aligned} \tag{2.21}$$

Differentiating this, we obtain the von Neumann equation for the evolution of density matrices as,

$$i\hbar\frac{\partial\rho}{\partial t} = [H,\rho]. \tag{2.22}$$

This is analogous to the classical Liouville equation and is used whenever we are dealing with mixed states. Apart from the Schrödinger time evolution method, we can also work in the Heisenberg picture, where operators evolve in time instead of the states. Next, we explain the time evolution method for open system dynamics.

2.2.2 Open system

Closed quantum systems are idealized constructs, and in most cases, we can control their dynamics and perform certain quantum processes. However, in practice, these systems interact with other systems or with their environment, and these interactions make the system's dynamics non-unitary (the combined system and environment are still unitary) [55–57]. In principle, to simulate the dynamics of such a system, we need to time-evolve the total system, i.e., the closed system plus its environment. However, since we are mainly interested in the closed system's subspace, for practical purposes, we solve a reduced equation of motion where we effectively eliminate the environment by making several approximations. The interaction with the environment can be of either Markovian or non-Markovian nature [58, 59]. Markovian dynamics means that any quantum state at time $t+1$ depends only on the state and the interactions happening at time t, without any effect from previous states or interactions — in other words, the environment has no memory.

Suppose we have a system Hamiltonian H_S and an environment Hamiltonian H_E. The full system dynamics are then governed by the Hamiltonian

$$H_{S-E} = H_S + H_E + H_{\text{int}},$$

where H_{int} represents the interaction between the system and the environment. If we

know the unitary $U(t, t_0)$ of Eq. (2.21) for the composite system described by H_{S-E}, we can obtain the reduced state of the system S by tracing over the environment as,

$$\rho_S(t) = \mathrm{Tr}_E[\rho(t)].$$

However, in most cases, it is unfeasible to determine the full system unitary $U(t, t_0)$, and to address this, we take the partial trace of Eq. (2.22). This forms the basis for master equations, where we effectively ignore the environment's explicit dynamics. The computations are made scalable by disregarding the environment's information, which is typically uncontrollable in most practical cases. This requires the assumptions that the system is weakly coupled to the environment and that the environment is Markovian. A particularly important example of the master equation approach is the Gorini-Kossakowski-Sudarshan-Lindblad (GKSL) master equation or Lindblad equation [60, 61], given by

$$\dot{\rho}(t) = -\frac{i}{\hbar}[H, \rho(t)] + \sum_k \gamma_k \left(L_k \rho(t) L_k^\dagger - \frac{1}{2}\{L_k^\dagger L_k, \rho(t)\} \right), \tag{2.23}$$

where we omit the subscript S from the system density operator ρ and the Hamiltonian H. The Lindblad operators L_k represent non-unitary Markovian processes such as decoherence, occurring at rates γ_k. The Lindblad operators generally differ from the system's Hamiltonian; for example, L_k need not be Hermitian and they generate incoherent dynamics. Instead of working directly with Eq. (2.23), it is often convenient to express the master equation in vector notation:

$$\dot{\vec{\rho}} = \mathcal{L}\vec{\rho}, \tag{2.24}$$

or, for a time-dependent Hamiltonian and/or decoherence rates,

$$\dot{\vec{\rho}} = \mathcal{L}(t)\vec{\rho}, \tag{2.25}$$

which is known as the superoperator or Liouville form [62]. Here, $\vec{\rho}$ is the vectorized form of the density matrix ρ, and $\mathcal{L}$ is the superoperator associated with $\dot{\vec{\rho}}$. The general solution of Eq. (2.25) is given by

$$\vec{\rho}(t) = \mathcal{T}\left\{ \exp\left[\int_0^t d\tau\, \mathcal{L}(\tau) \right] \right\} \vec{\rho}(0), \tag{2.26}$$

where $\mathcal{T}$ is the time-ordering operator. For numerical purposes, this equation can be approximated similarly to Eq. (2.19) by assuming that the Hamiltonian is piecewise constant, and applying Eq. (2.26) to each time step.

In realistic settings, these unitary operations corresponding to quantum gates, are implemented through carefully engineered control fields, such as laser pulses, microwave drives, or magnetic fields, that modulate the system's Hamiltonian. The design and optimization of these control fields to achieve desired unitary operations form the foundation of quantum control. In the following section, we discuss the principles of quantum control, its role in quantum technologies, and how it is used to manipulate the dynamics of both closed and open quantum systems.

2.3 Quantum control theory

The field of quantum control is developing rapidly, as it plays a critical role in the advancement of modern quantum technologies. Quantum control has its roots in classical control theory, where controllable parameters are optimized to achieve a desired task in a dynamical process. In quantum control theory, we manipulate quantum systems to realize a target quantum process while respecting the constraints of the system. Over the years, various quantum platforms such as ultracold atoms, superconducting qubits, nitrogen-vacancy centers, and spin qubits have been developed and have reached a level of maturity where they can serve as testbeds for quantum control techniques. The more well-modeled and well-characterized a system is, the easier it becomes for quantum control methods to identify optimized controls for a given task. However, in recent years, techniques such as closed-loop control and feedback control have been developed to enable quantum control in systems that are not perfectly modeled or fully characterized. In this section, we will discuss the fundamentals of quantum control problems and provide a brief review of various control methodologies.

2.3.1 Control problem

Similar to its classical counterpart, any quantum control problem is constructed upon key ingredients: the model, the objective, the method, and the constraints. The model of a quantum control problem is derived from the microscopic knowledge of the system, which can be constructed from either theoretical analysis or experimental results. When well-characterized, the theoretical model, such as the Hamiltonian of the system, provides the most leverage for any control problem, as it encapsulates nearly all the knowledge of the system. By using this knowledge of the Hamiltonian, one can perform open-loop optimal control, as discussed in Sec. 2.3.4. In contrast, experimental results-based modeling is often used in closed-loop optimization. In this section, we describe the framework for constructing a control problem with theoretical knowledge of the system.

For a bilinear system, we can decompose the Hamiltonian $H(t)$ into two terms as [63–65]

$$H(t) = H_d + \sum_{j=1}^{m} u_j(t) H_j, \tag{2.27}$$

where H_d represents the uncontrollable drift Hamiltonian, and the interaction with an external field is expressed as a collection of control Hamiltonians H_j. Each control Hamiltonian is modulated by a time-dependent function $u_j(t)$. The dynamics of the system for a state $|\psi(t)\rangle$ are governed by Eq. (2.17) and Eq. (2.22) (when working with density operators). We first detail the control problem for a closed system using the example of the two-level system and later incorporate decoherence mechanisms into the equations.

Two-level system example

We consider a two-level quantum system with basis states $|0\rangle$ (ground state) and $|1\rangle$ (excited state). The system is driven by a classical control field applied along the x-axis, resulting in a time-dependent Hamiltonian:

$$H(t) = \frac{\omega_0}{2}\sigma_z + E(t)\sigma_x,$$

where ω_0 is the energy splitting between the two levels, $E(t)$ is the time-dependent control amplitude (Rabi frequency), and $\sigma_z = |1\rangle\langle 1| - |0\rangle\langle 0|$, $\sigma_x = |0\rangle\langle 1| + |1\rangle\langle 0|$. Compared to Eq. (2.27), ω_0 is the coefficient of the drift term $H_d = \sigma_z$, and $E(t)$ is the control $u_j(t)$ associated with the control Hamiltonian $H_j = \sigma_x$. From Eq. (2.1), the quantum state can be written as a sum of the basis states with time-dependent coefficients $c_1(t)$ and $c_2(t)$

$$|\psi(t)\rangle = \begin{pmatrix} c_1(t) \\ c_2(t) \end{pmatrix}. \tag{2.28}$$

The time evolution of these coefficients is governed by the Schrödinger equation,

$$\frac{d}{dt}\begin{pmatrix} c_1(t) \\ c_2(t) \end{pmatrix} = -i \begin{pmatrix} \frac{\omega_0}{2} & E(t) \\ E(t) & -\frac{\omega_0}{2} \end{pmatrix} \begin{pmatrix} c_1(t) \\ c_2(t) \end{pmatrix}. \tag{2.29}$$

Assuming the form $E(t) = \Omega(t)\cos(\omega t)$, representing an oscillating magnetic field, we can apply frame transformations and the rotating wave approximation (RWA) to remove the high-frequency oscillations [66]. First, we perform a frame transformation using the unitary operator

$$\mathcal{U}(t) = \begin{pmatrix} e^{-i\omega t} & 0 \\ 0 & e^{i\omega t} \end{pmatrix}. \tag{2.30}$$

The transformed Hamiltonian is

$$H'(t) = \mathcal{U}(t)^\dagger H(t)\mathcal{U}(t) - i\mathcal{U}(t)^\dagger \frac{d\mathcal{U}(t)}{dt}. \tag{2.31}$$

The first term becomes

$$\mathcal{U}(t)^\dagger H(t)\mathcal{U}(t) = \begin{pmatrix} \frac{\omega_0}{2} & \frac{\Omega(t)}{2} \\ \frac{\Omega(t)}{2} & -\frac{\omega_0}{2} \end{pmatrix} + \begin{pmatrix} 0 & \frac{\Omega(t)}{2}e^{2i\omega t} \\ \frac{\Omega(t)}{2}e^{-2i\omega t} & 0 \end{pmatrix}.$$

Using the RWA, we discard the second term with frequency 2ω as it averages to zero. The second term of the frame transformation gives

$$-i\mathcal{U}(t)^\dagger \frac{d\mathcal{U}(t)}{dt} = \begin{pmatrix} -\frac{\omega}{2} & 0 \\ 0 & \frac{\omega}{2} \end{pmatrix}.$$

Therefore, the total Hamiltonian in the RWA becomes

$$H'(t) = \begin{pmatrix} \frac{\Delta}{2} & \frac{\Omega(t)}{2} \\ \frac{\Omega(t)}{2} & -\frac{\Delta}{2} \end{pmatrix}, \tag{2.32}$$

where $\Delta = \omega_0 - \omega$. The frame-transformed state is:

$$\Psi'(t) = e^{i\omega t}c_1(t)\,|0\rangle + e^{-i\omega t}c_2(t)\,|1\rangle = \alpha_1(t)\,|0\rangle + \alpha_2(t)\,|1\rangle\,. \tag{2.33}$$

We can now rewrite the Schrödinger equation with the transformed state and Hamiltonian

$$\frac{d}{dt}\,|\Psi'(t)\rangle = -\frac{i}{\hbar}H'(t)\,|\Psi'(t)\rangle\,, \tag{2.34}$$

where $|c_1(t)|^2 + |c_2(t)|^2 = |\alpha_1(t)|^2 + |\alpha_2(t)|^2 = 1$ conserves the normalization. If $\Omega(t)$ is a constant control, the system undergoes Rabi oscillations between $|0\rangle$ and $|1\rangle$ [67] at the frequency

$$\Omega_R = \sqrt{\Delta^2 + \Omega^2}. \tag{2.35}$$

Note that, system will not reach state $|1\rangle$ starting from $|0\rangle$ with probablity one, if $\Delta \neq 0$. In Fig. 2.2(a), we show an example of coherent oscillations between the ground and excited states in the presence of a negligible detuning Δ and an external time-independent drive $\Omega_{max} > \Omega \gg \Delta$, where Ω_{max} is the maximum acheivable amplitude. However, faster Rabi oscillations can be achieved by making the drive Ω time-dependent and/or increasing the magnitude. Using quantum optimal control techniques, in Sec. 2.3.4, we will show how to optimize $\Omega(t)$ to engineer controls beyond simple sinusoidal driving.

In addition to coherent control, the two-level system undergoes spontaneous emis-

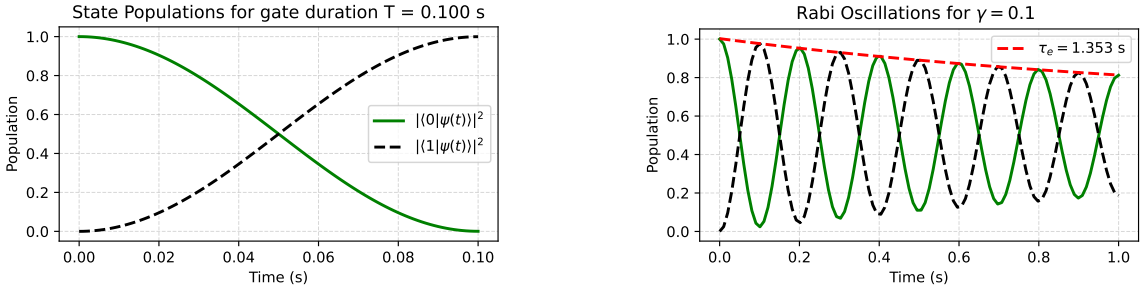

Figure 2.2: Comparison of Rabi oscillations in a two-level quantum system. On the left (a), the system undergoes Rabi oscillations in a closed system with constant $\Omega = 5.0$ and detuning $\Delta = 0.1$. On the right (b), dissipation with $\gamma = 0.1$ is included, and the system exhibits damped Rabi oscillations, where the population in the excited state $|1\rangle$ decays back to the ground state $|0\rangle$ due to the interaction with the environment.

sion from the excited state $|1\rangle$ to the ground state $|0\rangle$ making it an open quantum system discussed in Sec. 2.2.2. This dissipative process is modeled via the Lindblad master equation of Eq. (2.23) as

$$\frac{d\rho(t)}{dt} = -i\left[H'(t), \rho(t)\right] + \gamma\left(\sigma_-\rho(t)\sigma_+ - \frac{1}{2}\left\{\sigma_+\sigma_-, \rho(t)\right\}\right), \tag{2.36}$$

where $\sigma_- = |0\rangle\langle 1|$ and $\sigma_+ = |1\rangle\langle 0|$ are the lowering and raising operators, respectively, and γ is the spontaneous emission rate. This captures the unified dynamics of coherent Rabi oscillations driven by the control field $\Omega(t)$, and irreversible population decay to the ground state via spontaneous emission at rate γ. This interplay between control and dissipation forms the basis for open quantum systems. In Fig. 2.2(b), we show one example of incoherent oscillations between the ground and excited state in presence of spontaneous emission from the excited state $|1\rangle$ to the ground state $|0\rangle$ with $\gamma = 0.1$. We observe that the coherence of the system decreases over time due to dephasing. By fitting an exponentially decaying curve to the coherence signal, we extract the coherence time (or T_1 time) as $\tau_e = 1.353$ s. This dephasing poses a major challenge in quantum systems, as it limits the ability to reliably perform circuits involving many quantum gates.

After indentifyig the system along with its control and drift terms, we proceed in the following section to outline the key objectives that can be pursued using quantum control techniques.

2.3.2 Objective

Through quantum control, we want to perform any given quantum operation with efficiency and in some cases minimum time. This operations forming the objective

for a quantum control task, are in most cases crucial for quantum computation and information tasks. Some interesting and important objectives in optimal control of quantum systems involve the synthesis of quantum gates or the transfer of quantum states [68]. For open quantum systems, the quantum control objective involves not only steering the dynamics through unitary evolution but also optimizing in presence of non-unitary effects such as relaxation and dephasing. Mathematically, these objectives are often described with a cost function or infidelity function that quantifies the difference between the achieved and desired process. Optimal control techniques are then employed to minimize this cost function, subject to the available control fields. We explain below some of the quantum control tasks that we work in this thesis on.

State preparation– One fundamental operation in quantum control is the transfer of a given quantum system to a target quantum state i.e. preparing a particular state. This is essential for almost every sub-field of quantum technolgies e.g. quantum computation, information, simulation, chemistry, etc. The cost function for the state preparation task is defined by an infidelity function, which quantifies the distance between the target state $|\Psi_{tar}\rangle$ and the final state $|\Psi(T)\rangle$ achieved after the control process [69, 70]. Specifically, the infidelity is defined as

$$C_{\text{state}} = 1 - |\langle\Psi(T)|\Psi_{tar}\rangle|^2, \tag{2.37}$$

where a value of zero indicates perfect overlap between the states.

Unitary gate optimization– From a quantum computation point of view, having gates with low errors and smaller gate duration is crucial. The gate errors and time directly affect the quantum circuit, especially for high depth circuits. Therefore, realization of unitary gate operations with high fidelity is a central objective in quantum control. The objective of unitary gate optimization is to drive the system dynamics in such a way that the resulting unitary $U(T)$ at the final time T, closely matches with the target unitary gate U_{tar}. A common optimization cost function for this task is defined as

$$C_{\text{gate}} = 1 - \frac{1}{d^2}\left|\text{Tr}\left(U_{\text{tar}}^{\dagger}U(T)\right)\right|^2,$$

where d is the dimension of the system's Hilbert space [71]. For cases, where we need to fix the global phase, the real part of the trace operation can be considered. Gate optimization becomes challenging in open quantum systems, since there is a trade-off between incoherent effects which requires the gate times to be smaller and experimental constraints which require the gate times to be longer.

Partial gate optimization- In some quantum applications, for example in quantum chemistry simulations, optimizing unitary gate fidelity over the full Hilbert space may not be important. Often, we want to efficiently time evolve only a subset of quantum states relevant to the given problem. In such scenarios, optimizing the entire unitary gate is unnecessary and computationally expensive. To address this, the cost function for the unitary gate optimization can be relaxed to focus only on a selected set of initial states. Instead of requiring the implemented evolution $U(T)$ to match the full target unitary U_{target}, we compare the output of a set of chosen input states $|\Psi_j(0)\rangle$ under the controlled evolution to their ideal target states $|\Psi_{\text{tar},j}\rangle$. The cost function is then defined as the average infidelity over these N_0 states:

$$C_{\text{gate}} = 1 - \frac{1}{N_0^2} \sum_{j=1}^{N_0} |\langle \Psi_{\text{tar},j} | \Psi_j(T) \rangle|^2 ,$$

where $|\Psi_j(T)\rangle$ denotes the evolved state under the actual control protocol. This formulation is especially useful when the interested subspace is small compared to the full Hilbert space, allowing for efficient optimization.

In the following sections, we explore different methods for achieving these control objectives within both closed and open quantum systems. First, we will introduce a numerical gradient-based optimization algorithm, which is implemented in Chapter 4 and 5. This approach utilizes the knowledge of the Hamiltonian for the system to iteratively refine control parameters toward an optimal solution. Subsequently, we will briefly review other widely adopted techniques, including analytical methods and gradient-free optimization strategies, which have gained considerable attention for their applicability to complex quantum systems. Together, these methods constitute a comprehensive toolkit for modern quantum control.

2.3.3 Types of quantum control methods

Analytical vs numerical – Analytical methods rely on mathematical frameworks to derive explicit control protocols, often using tools such as the Pontryagin maximum principle (PMP), Lie algebraic techniques, and parameterized pulse sequences. These methods are particularly suitable for smaller system sizes with well-defined degrees of freedom. In most cases, they solve the system dynamics to find control for a specific task. For instance, a series of works has demonstrated an analytical framework to find time-optimal controls for reaching certain target states or unitaries using PMP or the Euler-Lagrange equation. These methods work by solving a minimization or maximization problem based on coupled differential equations. Another example use case of analytical control is to suppress diabatic errors using shortcut-to-adiabaticity

(STA) approaches or to suppress leakage errors using Derivative Removal by Adiabatic Gate (DRAG) [44, 72–76]. Both of these methods work by adding a correction term to the effective Hamiltonian, derived from a time-dependent frame transformation. While the principles of DRAG bear resemblances to STA, DRAG specifically addresses the challenges posed by degenerate subspaces and inherently on-resonant dynamics typical in practical quantum systems [77].

Analytical solutions provide valuable physical insight and can be easily implemented when they exist, but their applicability is often restricted to systems with relatively simple or highly symmetric Hamiltonians. In this work, we do not explore analytical techniques; however, we use the Euler-Lagrange method to find the time-optimal pulse for the primitive control problem in Chapter 5. In most realistic quantum systems, finding exact control solutions is often not feasible and we use numerical methods. The main idea behind numerical quantum control is to find time-dependent control fields that steer the system's dynamics to minimize the given cost function. To achieve this, the system's evolution is simulated numerically using one of the time evolution Eqs. (2.17),(2.22), and optimization algorithms iteratively update the control parameters to improve performance. In these numerical methods, we can further include constraints on controls, technical noise, making it well-suited for experimental implementation.

Open-loop vs closed-loop – Open-loop control methods rely on a theoretical model of the quantum system's dynamics without any direct connection to the experiment [37, 68, 78–82]. Often referred to as offline optimization, these methods use the system Hamiltonian to precompute control pulses that drive the system toward a desired target state or operation. Open-loop control is advantageous for its speed and efficiency but can suffer from inaccuracies due to model imperfections and noise, limiting its robustness in practical applications. Alternatively, one can evaluate the cost function directly on the experiment and optimize the controls accordingly. This approach, known as closed-loop control [83–86], enables real-time adaptation to noise, imperfections, and other experimental constraints, making it particularly useful for calibrating pulses in noisy intermediate-scale quantum (NISQ) devices or hardware-aware gate optimization. However, it typically requires many experimental runs, which can be impractical, especially for systems like neutral atoms, where gates and measurements are relatively slow. In such cases, a carefully characterized open-loop optimization (see Sec. 2.4) is often preferred. Hybrid strategies also exist, such as closed-loop designed open-loop control, where feedback is gathered offline to optimize control sequences that are subsequently applied in an open-loop fashion, combining the advantages of both approaches.

Gradient-based vs gradient-free – One more parameter to categorize different quantum control algorithms is gradient calculation. Some algorithms are gradient-based, e.g., GRAPE, GOAT, and Krotov's method [37, 40, 68, 78–82, 87–89], while others are gradient-free algorithms [29, 90]. Gradient-based methods use the information of the Hamiltonian to derive the gradient of the cost function with respect to the control values u_j defined in Sec. 2.3.1. Different cost functions C can be defined depending on the objective of the quantum control task (some of them are described in Sec. 5.2.2). Based on the gradient values, the optimizer updates the control values u_j to minimize C. This significantly improves convergence and makes the optimization more scalable, especially for systems with many control parameters. In this work, we use gradient-based methods like GRAPE, which is discussed in Sec. 2.3.4.

While having access to gradient information accelerates optimization and improves convergence, it is not always feasible to calculate gradients. This can be due to the complexity of the model or the unavailability of gradient information from experiments in a closed-loop approach. In some cases, finite-difference methods can be used as a replacement for analytical gradients, but these are usually quite slow and inaccurate, necessitating the use of gradient-free methods. Though widely used in closed-loop approaches, some gradient-free methods are also implementable within open-loop schemes. One such widely used method is the Chopped Random Basis (CRAB) algorithm [29, 90]. CRAB parameterizes the control function using a finite number of basis functions, often Fourier or Chebyshev polynomials with randomized frequencies, thereby reducing the search space and allowing fast convergence without requiring gradient information. CRAB has been successfully employed on various platforms, along with its variant dressed CRAB (dCRAB), which uses super-iterations to avoid falling into local minima. For a detailed description of these algorithms, refer to [91]. The CRAB algorithms have also been implemented in several packages such as QuOCS [92] and QuTiP [93].

2.3.4 Gradient Ascent Pulse Engineering (GRAPE)

Among gardient-based algorithms, the Gradient Ascent Pulse Engineering (GRAPE) algorithm is one of the most widely used, offering high efficiency for closed and open quantum systems [37]. For example, we want to minimize the cost function of state-to-state transfer given by Eq. (2.37). To compute the gradient of the cost function with respect to the control amplitudes, we discretize time into N_T steps of equal length $\Delta t = T/N_T$. At each time step $t_k = k\Delta t$, the control amplitudes $u_j(t_k)$ are treated as piecewise constant. The total unitary evolution is decomposed into product of

short-time evolutions [see Eq. (2.19)] as

$$U(T) = U_{N_T} U_{N_T-1} \cdots U_1,$$

where each short-time propagator is given by

$$U_k = \exp\left(-iH_k \Delta t\right), \quad \text{with} \quad H_k = H_d + \sum_j u_j(t_k) H_j.$$

To compute the gradient of the fidelity with respect to the control $u_j(t_k)$, we define forward and backward propagators. The forward propagator up to time step k is

$$P_k = U_k U_{k-1} \cdots |\Psi_0\rangle,$$

and the backward propagator from step $k+1$ to final time is

$$\Lambda_k = U_{N_T}^\dagger \cdots U_{k+1}^\dagger |\Psi_{\text{tar}}\rangle.$$

The fidelity gradient can be written as

$$\frac{\partial C_{\text{state}}}{\partial u_j(t_k)} = \frac{\partial}{\partial u_j(t_k)} \left\{1 - |\langle \Psi_{\text{tar}}|U(T)\Psi_0\rangle|^2\right\}. \tag{2.38}$$

Using the chain rule and assuming small Δt, we approximate the derivative of the unitary evolution as

$$\frac{\partial U(T)}{\partial u_j(t_k)} \approx U_{N_T} \cdots U_{k+1} \left(-i\Delta t H_j U_k\right) U_{k-1} \cdots U_1.$$

This approximation calculates gradients faster, but can produce larger error, in which case, the finite-difference method can be used to calculate $\frac{\partial U_k}{\partial u_j(t_k)}$. Substituting this into the gradient expression, we obtain

$$\frac{\partial C_{\text{state}}}{\partial u_j(t_k)} = -2\Delta t \,\text{Re}\left\{\langle \Psi_{\text{tar}}|U(T)\Psi_0\rangle \langle \Lambda_k | iH_k P_k\rangle\right\}.$$

Therefore, the control update in GRAPE is carried out by computing this gradient for each control parameter and applying an ascent step,

$$u_j'(t_k) = u_j(t_k) + \epsilon \frac{\partial C_{\text{state}}}{\partial u_j(t_k)},$$

where ϵ is the step size. This process is repeated iteratively until convergence, resulting in optimized control fields that maximize the fidelity or minimize the infiedility. This

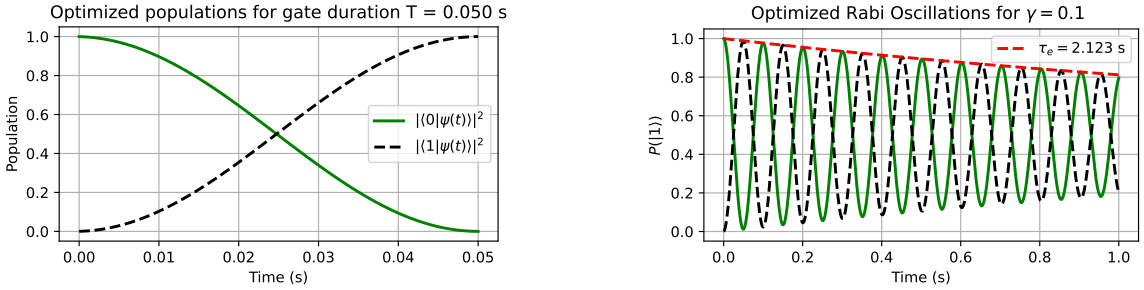

Figure 2.3: Application of the GRAPE algorithm to a two-level system for time-optimal population transfer from the initial state $|0\rangle$ to the target state $|1\rangle$ in the presence of a drift Hamiltonian with detuning $\Delta = 0.1$. The control $\Omega(t)$ is implemented as a piecewise constant pulse, with $N_T = 100$ equal time steps. (a) The optimized control pulse $\Omega(t)$ achieves the desired state transfer in $T = 0.05$ s, which is half the time required by the unoptimized control in Fig. 2.2(a). (b) Time evolution of the system including spontaneous emission shows that the coherence time τ_e increases twofold under the faster, optimized control compared to the unoptimized case in Fig. 2.2(b).

method is orignally described for density operators and can be easilty adapted for open-system control problems.

Two-level example – We apply the GRAPE algorithm on our two-level system example described in Sec. 2.3.1. In this case, we want to optimize the transfer of the state population from the initial state $\Psi(0) = |0\rangle$ to the target state $\Psi_{\text{tar}} = |1\rangle$ in a time-optimal way, in the presence of a drift Hamiltonian H_0 with detuning $\Delta = 0.1$. We choose our control $u_j(t) = \Omega(t)$ as a time-dependent, piecewise-constant pulse. We take the total time T into $N_T = 100$ equal time steps and optimize $\Omega(t_k)$ for each time step t_k. As shown in Fig. 2.3(a), the optimized $\Omega(t)$ performs the state-to-state transfer in $T = 0.05\,\text{s}$, which is half of the time taken by the unoptimized controls in Fig. 2.2(a). Note that, the optimized $\Omega(t)$ is again a constant pulse equal to only limited by the numerical upper bound Ω_{max} used in the optimizer. We will discuss more about these limitations in Sec. 2.4. The optimized $\Omega(t)$ and the total transfer time τ are related by the π-pulse relation of $T = \frac{\pi}{\Omega} s$. With these optimized $\Omega(t_k)$, we simulate the system in the presence of spontaneous emission as described in Sec. 2.3.1. As shown in Fig. 2.3(b), we see that the coherence time τ_e increases by a factor of two compared to the slower unoptimized time evolution in Fig. 2.2(b).

Another variant of gradient-based algorithms is Krotov's method [82], which also discretizes the control fields and updates them iteratively. However, unlike GRAPE, the gradient calculation and update conditions in Krotov's method are derived from a different variational principle, ensuring monotonic convergence toward the optimization objective [68]. Another method for gradient-based optimization is GOAT (Gra-

dient Optimization of Analytic Controls), which focuses on optimizing control fields expressed in an analytic functional form rather than a piecewise-constant discretization [94]. In GOAT, the gradients are computed efficiently by integrating a set of coupled differential equations. Most of these method also incorporates additional constraints (for a description of constraints, see Sec. 2.4.1).

All these control methods are useful, and choosing among them depends on the system and the problem at hand. In our work, we have predominantly used gradient-based numerical control methods, mainly GRAPE-like algorithms. Therefore, in the next section, we will describe how these algorithms can be made more practical so that the resulting controls are realistic and feasible for direct implementation in experiments.

2.4 Practical quantum optimal control

2.4.1 Constrained optimization

So far, we have assumed that the controls can be tuned to arbitrary values to reach the desired quantum process. However, in practice, the controls are subject to experimental restrictions, and the optimization must often be performed under those constraints. Constrained optimization techniques incorporate such requirements directly into the control algorithm, ensuring that the resulting pulse sequences are not only optimal in theory but also feasible in practice. These constraints can be hard (e.g., strict bounds on control amplitudes) or soft (e.g., penalizing certain behaviors in the cost function). Methods such as penalty functions, Lagrange multipliers, or projection techniques can be used to enforce constraints. Constrained optimization [95, 96] is essential for bridging the gap between theoretical control designs and their experimental implementation, particularly in systems with limited coherence times and precise hardware requirements.

More generally, constraints can be mathematically included as follows. Let $\mathcal{C}$ denote the set of admissible controls, incorporating both equality and inequality constraints. The constrained optimization problem can be formulated as:

$$\min_{\{u_j(t)\}\in\mathcal{C}} C[\{u_j(t)\}] \tag{2.39}$$

subject to:

$$g_i[\{u_j(t)\}] = 0, \quad i = 1, \ldots, m, \tag{2.40}$$

$$h_k[\{u_j(t)\}] \leq 0, \quad k = 1, \ldots, n, \tag{2.41}$$

where g_i are equality constraints and h_k are inequality constraints. To solve such problems, one common approach is to augment the cost function using penalty or barrier methods. For instance, a penalty-augmented cost function becomes

$$C_{\text{aug}} = C[\{u_j(t)\}] + \sum_i \lambda_i g_i[\{u_j(t)\}] + \sum_k \mu_k \max(0, h_k[\{u_j(t)\}])^2, \tag{2.42}$$

where λ_i and μ_k are penalty parameters. Alternatively, projection methods or constrained optimization frameworks such as Sequential Quadratic Programming (SQP) or Riemannian optimization may be used to ensure that the control updates always satisfy the constraints. In SciPy, the SLSQP solver implements an SQP-style algorithm with a limited-memory BFGS Hessian update, supporting both equality and inequality constraints via a convenient interface. Next, we describe common experimental constraints that any quantum control task need to take into account. All of these constraints are included in some form in our work presented in Chapter 4 and 5.

Maximum amplitude constraints – In practical quantum systems, one of the most common hard constraints is a bound on the maximum control amplitude [68, 97]. This arises due to the finite power output of experimental hardware, such as microwave sources or laser systems. Mathematically, this constraint is typically expressed as

$$|u_j(t)| \leq u_{\max} \tag{2.43}$$

for each control parameter $u_j(t)$. In Chapter 4 and 5, we ensure that the optimized pulse sequences remain within the hardware's feasible operating range, preventing signal clipping, distortion, or damage to the electronics. In optimization algorithms, maximum amplitude constraints can be incorporated using projection methods—where control updates exceeding $u_{\max}$ are clipped or rescaled—or via penalty terms added to the cost function to discourage solutions approaching or surpassing this bound.

Rise time constraints – Another important constraint in quantum control is the limitation on the rise time of control pulses, referring to the minimum time required for a control signal to transition between different amplitude levels. This constraint arises from the finite bandwidth of hardware, such as arbitrary waveform generators and amplifiers [78]. It becomes particularly significant for piecewise-constant controls, where optimization algorithms tend to produce results with sharp changes between time steps. Rapid changes in control amplitudes can lead to distortions, overshoot, and ringing effects that degrade the fidelity of quantum operations. To account for this, rise time constraints are often imposed by limiting the derivative of the control

functions as

$$\left|\frac{du_j(t)}{dt}\right| \leq r_{\max}, \tag{2.44}$$

where $r_{\max}$ denotes the maximum allowable rate of change. In optimization algorithms, these constraints can be enforced either through explicit inequality constraints or by adding penalty terms to the cost function that penalize large derivatives. In the optimization performed in Chapter 4, we implement rise time constraints as linear constraints using Eq. (2.44). One can also include it as bandwidth information in the Fourier domain [78]. Alternatively, one can work with analytic, smooth pulse shapes, which are inherently realistic and naturally comply with rise time limitations.

Pulse distortion – In addition to simple bound constraints such as maximum amplitude and linear constraints like rise time, control pulses also suffer various distortions as they propagate through the control hardware before reaching the quantum system. These distortions can arise from the finite bandwidth of transmission lines, filters, amplifiers, and other electronic components, which alter both the amplitude and phase of the optimized control signals [98]. As a result, the control pulse experienced by the quantum system may differ significantly from the designed waveform, leading to control errors and reduced fidelities. These distortions are often modeled as a convolution between the input control pulse and the impulse response function $h(t)$ of the hardware as

$$\tilde{u}_j(t) = \int_0^t h(t-\tau)u_j(\tau)\,d\tau, \tag{2.45}$$

where $\tilde{u}_j(t)$ represents the distorted pulse experienced by the system. In the frequency domain, this corresponds to a filtering effect governed by the system's transfer function gievn by

$$\tilde{U}_j(\omega) = H(\omega)U_j(\omega), \tag{2.46}$$

where $U_j(\omega)$ and $\tilde{U}_j(\omega)$ are the Fourier transforms of the intended and distorted pulses, respectively, and $H(\omega)$ is the transfer function characterizing the hardware's frequency response. To address these distortions, control algorithms may incorporate compensation techniques such as predistortion, where the input pulse is intentionally modified to counteract the distortions, bringing the output pulse closer to the desired shape. Alternatively, a hardware model can be included directly within the optimization loop, allowing the algorithm to account for distortion effects. This eliminates the need for predistortion, which is often inconvenient to perform and can introduce additional errors. For either of these remedies, it is first necessary to experimentally measure the distortion effects in the form of either the impulse response or the transfer function. These distortions are often more complex than the simple linear models in Eq. (2.45)

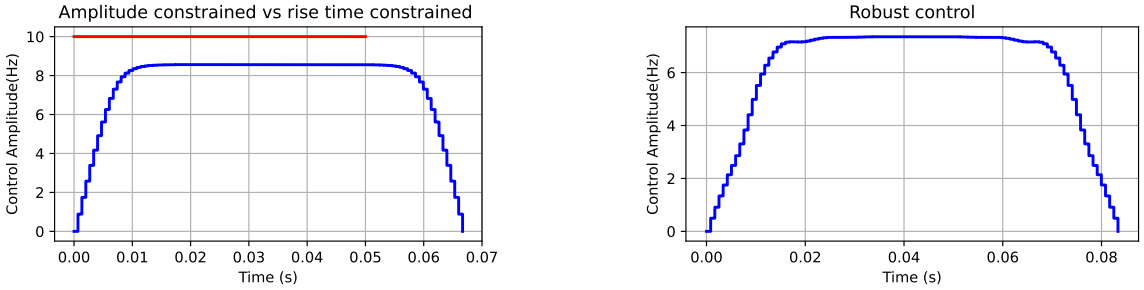

Figure 2.4: Comparison of optimized control pulses with practical constraints. (a) The red curve shows the amplitude-constrained optimal pulse which takes the value $\Omega_{\max}$. The blue curve shows the optimized pulse with additional boundary conditions and rise-time constraints. The rise-time constrained pulse is more feasible for experimental implementation, but the total gate duration is larger compared to the amplitude-constrained one. (b) Optimized controls with robustness constraints against drifts in the Rabi frequency Ω and detuning Δ. The pulse is obtained by averaging the fidelity cost over a grid of fluctuating parameters $(1+\epsilon_1)\Omega$ and $\Delta+\epsilon_2$, and then performing gradient-based optimization. The resulting pulse is smoother and shaped to maintain high fidelity across a range of parameter uncertainties.

and Eq. (2.46), and can exhibit nonlinear behavior. We present for the first time, an efficient mathematical model to estimate these nonlinear distortions in Chapter 4.

Two-level system example – In the optimization performed for the two-level system in Sec. 2.3.4, we already impose a maximum amplitude constraint $\Omega_{\max} = 10\,\text{Hz}$ on the control $\Omega(t)$. Specifically, we require that each control value satisfies

$$0 \leq \Omega(t_k) \leq \Omega_{\max}$$

for all time steps t_k. As shown in Fig. 2.4, the resulting amplitude-constrained optimized pulse is a constant pulse at the maximum value $\Omega_{\max}$. However, generating such a pulse in a real experiment is unrealistic, since it starts at a high amplitude instantaneously. To make the pulse more realistic, we add a condition that the pulse should start and end at zero, i.e.,

$$\Omega(t_0) = \Omega(t_{N_T}) = 0.$$

Next, we also limit how fast the pulse can change by including a rise-time constraint. This is done by requiring

$$\left| \frac{\Omega(t_{k+1}) - \Omega(t_k)}{dt} \right| \leq r_{\max}$$

for each time step t_k, where $r_{\max}$ is the maximum allowed rate of change.

This can be implemented as a linear constraint problem of the form

$$\frac{1}{dt} A\mathbf{\Omega} \leq \mathbf{b},$$

where $\mathbf{\Omega}$ is a vector containing all control values $\Omega(t_k)$, $\mathbf{b}$ is a vector with entries equal to $r_{\max}$, and A is a matrix storing the coefficients that generate the inequalities.

With these additional boundary conditions and rise-time constraints, the resulting optimized pulse is significantly smoother and more realistic, as shown in Fig. 2.4(a). As a consequence of these practical limitations, the optimized pulse is also longer than the one obtained with only the amplitude constraint.

2.4.2 Robust optimization

There has been a significant improvement in the characterization of quantum devices, but there are often uncertainties in the system parameters. Moreover, these parameters can sometimes fluctuate, which may occur even during the execution of a quantum circuit. In addition to the uncertain system parameters, the control fields also exhibit fluctuations, which can be either static or dynamic — for example, noise in the amplitude and phase of the driving field $\Omega(t)$ [99, 100].

One method to address these errors is to find a robust set of controls by optimizing an ensemble cost function that averages performance over a set of plausible system variations. Concretely, if $\{H_i\}_{i=1}^{N_{\text{rob}}}$ are Hamiltonians sampled from an uncertainty set (e.g., variations in drift frequency, coupling strengths, or decoherence rates), one defines the robust cost as

$$C_{\text{robust}} = \frac{1}{N_{\text{rob}}} \sum_{i=1}^{N_{\text{rob}}} C\big(H_i\big)\,, \tag{2.47}$$

where $C(H_i)$ is the fidelity-based cost for the ith model. Minimizing C_{robust} ensures that the optimized control field $u(t)$ delivers high fidelity on average across all sampled variations.

Two-level system example – To demonstrate the idea of robust optimization, we return to the two-level system. The Hamiltonian of the system has two terms, the control amplitude Ω and the detuning Δ [see Eq. (2.32)], both of which can potentially suffer from fluctuations in a real experiment. To account for this, we numerically include a grid of perturbed values $(1+\epsilon_1)\Omega$ and $\Delta+\epsilon_2$, and calculate the cost function of Eq. (2.37) for each combination. We then average all the fidelities using Eq. (2.47), which defines the robust cost function as the mean performance over the error grid.

The optimization generates control amplitudes shown in Fig. 2.4(b), which not only maximize the fidelity but also maintain high fidelity in the presence of small fluctuations in both Ω and Δ.

Although in this thesis we do not perform any robust optimization, in Chapter 5, we show that the optimized controls are inherently robust against some of the experimental noise in the controls. In our work, we use these control techniques to optimize the performance of certain gates or to perform efficient state-to-state transfer for ultracold atoms. Therefore, in the next chapter, we will briefly discuss the fundamentals of different ultracold platforms.

3 Neutral atoms technologies

For decades, many quantum systems have evolved as a potential platform for performing quantum computation and simulations tasks. With a significant development in the experiemental methods for precise control of the systems, physicists are able to manipulate individual particles and their interactions. It is not obvious which of these quantum platforms will succeed with each of them possibly having specific use cases depending on their resources and constraints. Among these different platforms, neutral atoms has gained a lot of attention because of its unique properties [14–17]. These are naturally occurring quantum systems, and with advanced control techniques, atoms can be loaded and moved around in an optical lattice or tweezers, which can accommodate more than a thousand qubits at a time.

In this work, we explore two types of neutral atoms experiments. In this work, we explore two types of neutral atoms experiments. The first type is the typical Rydberg atom system where excitation to Rydberg states facilitates strong and controllable interactions [101–105]. The second system is the fermionic atom system where collisions between ground-state atoms provide the necessary interactions for many-body dynamics [106, 107].

3.1 Rydberg atoms

Rydberg atoms are atoms in highly excited states, where one or more of their electrons occupy energy levels with very large principal quantum numbers n. As the value of n increases, the average distance of the electron from the nucleus grows significantly. Mostly alkali and alkaline-earth atoms are used as Rydberg atom systems. In chapter 4, we focus on alkali atoms with particular parameters related to rubidium ^{87}Rb atoms. Alkali atoms are similar to hydrogen atoms, where hydrogen atoms contain a single valence electron and alkali atoms possess one valance electron with the rest of the electrons forming a closed inner shell. When the valence electron of an alkali atom is

highly excited, its orbital wavefunction significantly reduces its overlap with the ionic core. That means the effect of the nuclear charge onto the valence electron is sheilded, hence effectively behaving like a hydrogen atom. This similarity to the hydrogen atom's single-electron environment allows high-angular-momentum Rydberg states in alkali atoms to be effectively described using a hydrogenic model. The historical study of these atoms dates back to the 1880s, when Johann Balmer described the energy spectrum of hydrogen atoms [108, 109]. Later, Johannes Rydberg extended this to more general alkali atoms and introduced the Rydberg formula [110] given by

$$\frac{1}{\lambda} = R_H \left(\frac{1}{n^2} - \frac{1}{m^2} \right), \tag{3.1}$$

where λ is the wavelength, $R_H = 1.097 \times 10^7\,\mathrm{m}^{-1}$ is the Rydberg constant for the hydrogen atom, and n, m are the principal quantum numbers. Based on the Rydberg formula, in 1913, Niels Bohr proposed that energy levels within an atom are quantized, successfully predicting hydrogen's energy levels as

$$E_n \propto -\frac{R_H hc}{n^2}, \tag{3.2}$$

where n is the principal quantum number, h is Planck's constant and c is the speed of light. Subsequent advancements in quantum mechanics revealed limitations in Bohr's model for explaining the finer details of atomic spectra. As experimental accuracy increased, the discovery of additional energy level splittings necessitated the inclusion of electron spin and its interactions with the nucleus and orbital angular momentum to accurately describe the observed states. Nevertheless, for describing the fundamental properties of Rydberg atoms, the simple hydrogen atom model remains highly valuable. With slight modifications, it can be extended to describe any one-electron system, including alkali atoms such as sodium, rubidium, and others.

3.1.1 Properties of Rydberg Atoms

To understand the properties of Rydberg atoms, which scale drastically with the principal quantum number n, we use the hydrogen atom model of Eq. (3.2). To account for the core electrons of Rydberg atoms, a correction term is added to Eq. (3.2) as

$$E_n \propto -\frac{R_H hc}{(n - \delta_\ell)^2}, \tag{3.3}$$

where δ_ℓ is known as the quantum defect. δ_ℓ depends only on the angular momentum quantum number ℓ and becomes very small for large ℓ e.g, for $\ell \geq 5$. Using this knowledge, we can state some universal properties of any Rydberg atom in Table 3.1.1.

Properties	Symbol	Scaling
Energy levels	E_n	n^{-2}
Level spacing	ΔE_n	n^{-3}
Radius	$\langle r \rangle$	n^2
Radiative lifetime	τ	n^3
Resonant dipole-dipole interaction coefficient	C_3	n^4
Polarisability	α	n^7
van der Waals interaction coefficient	C_6	n^{11}

Table 3.1: Scaling of the most important properties of Rydberg states with n.

For example, the average radius of a Rydberg atom scales as $\propto n^2$, the transition dipole moment between neighboring states scales as $\mu \propto n^2$, and the polarizability scales as $\alpha \propto n^7$ [104, 111]. Among these properties, one of the most important is Rydberg state's long lifetime and strong interaction as described below.

Lifetime – Similar to any excited state, a Rydberg state with high n also decays back to the ground state, emitting a photon but with long lifetime. The decay primarily occurs via two mechanisms: spontaneous decay and stimulated emission induced by blackbody radiation. The total lifetime of a Rydberg atom, i.e., the lifetime of the Rydberg state, is given by

$$\frac{1}{\tau} = \frac{1}{\tau_0} + \frac{1}{\tau_{\text{bb}}}, \tag{3.4}$$

where τ_{bb} and τ_0 are the inverse rates of blackbody radiation-induced decay and spontaneous emission, respectively [112]. The dependence of the lifetime τ on n varies from atom to atom and also for different ℓ values. Typically, $\tau \propto n^3$ for decays to the ground state and $\propto n^5$ for decays to neighboring Rydberg states. Interestingly, for Rydberg atoms with high n and high ℓ, such as circular states, the lifetime scales as $\tau \propto n^5$ even for decays to the ground state. This makes them attractive candidates for performing quantum information tasks [113, 114]. However, the preparation of such circular Rydberg states is experimentally challenging [115] and is not discussed in this work. This decay resulting from interactions with the environment, makes the Rydberg system an open quantum system as described in Sec. 2.2.2.

Rydberg-Rydberg interaction – When excited to Rydberg states, atoms behave as dipoles composed of their excited electron e and the ionic core. When two pair states are nearly degenerate, i.e., the energy defect $\Delta E \approx 0$, the dipole-dipole interaction couples them resonantly. The effective Hamiltonian in the two-state basis can be written as:

$$H = \begin{pmatrix} 0 & V_{dd} \\ V_{dd} & \Delta E \end{pmatrix} \tag{3.5}$$

with

$$V_{dd} \sim \frac{C_3}{R^3} \tag{3.6}$$

where C_3 is the dipole-dipole coupling coefficient. Diagonalizing H leads to energy splitting proportional to $1/R^3$. When the pair states are far off-resonant, $|\Delta E| \gg |V_{dd}|$, the dipole-dipole interaction acts as a perturbation in second order, yielding the van der Waals interaction. This results in an effective potential:

$$V_{vdW} \sim \frac{C_6}{R^6} \tag{3.7}$$

where, the van der Waals coefficient C_6 scales approximately as n^{11} for Rydberg atoms.

Rydberg blockade – Due to the van der Waals interactions between atoms with same Rydberg states, a phenomenon known as the Rydberg blockade occurs [104, 111]. In this mechanism, if one atom within an ensemble is excited to a Rydberg state by an external driving field, nearby atoms within a certain distance are prevented from being excited to Rydberg states. This happens because the excitation of the first atom induces an energy shift in the Rydberg levels of neighboring atoms via dipolar interactions, effectively detuning their transition frequencies from the driving laser. As a result, the laser becomes off-resonant to those atoms, suppressing further Rydberg excitations within the affected region. The characteristic distance within which this suppression takes place is referred to as the Rydberg blockade radius, denoted by R_b. Beyond this distance, the interaction strength falls off rapidly, and the blockade effect diminishes accordingly as the interatomic separation increases.

By leveraging these properties, we aim to use Rydberg atoms for a variety of quantum technologies, including quantum simulation, quantum computation, and quantum sensing. Although this thesis does not focus on Rydberg gates, we briefly describe single- and two-qubit gates to provide context and motivation for the work presented in Chapter 4.

3.1.2 Single-qubit Rydberg gates

An atom with two isolated, distinct energy levels is an ideal example of a qubit. By arranging many such atoms in dipole traps (see Sec. 3.1.5), one can build a quantum device capable of performing quantum computation and simulation tasks. Neutral atoms offer ample flexibility in choosing these two levels from their rich energy spectrum to serve as qubit states. The choice of levels depends on the type of atom, the coherence time, the accessibility to couple those levels, and other experimental considerations. In general, for quantum computation tasks, long coherence times are

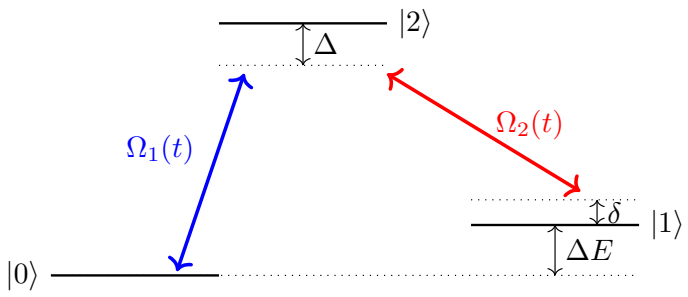

Figure 3.1: Energy level diagram illustrating a Raman transition scheme involving the states $|0\rangle$, $|1\rangle$, and $|2\rangle$. Two laser fields $\Omega_0(t)$ and $\Omega_1(t)$ couple the ground state $|0\rangle$ and target state $|1\rangle$ via a virtual excitation to the intermediate state $|2\rangle$. The detuning from the excited state $\Delta \gg \Omega_0(t), \Omega_1(t)$ determine the coherent population transfer between $|0\rangle$ and $|1\rangle$.

essential. Therefore, qubit states are typically stored in two low-lying hyperfine energy levels of the atom, for example, $|0\rangle = |F = 1, m_F = 0\rangle$ and $|1\rangle = |F = 2, m_F = 0\rangle$ of $5S_{1/2}$ for ^{87}Rb with few kHz of energy spacing [116–119]. On the other hand, for certain quantum simulation tasks, such as the variational quantum eigensolver (VQE) discussed in chapter 6, one can also use either one ground state and one Rydberg state or two different Rydberg states as the qubit [120]. For the qubit states stored in two hyperfine energy levels, we can use microwave fields [116–118] to perform the single-qubit gates discussed in Sec. 2.1.2. In strontium ^{88}Sr atom, the $^3P_0$ state, coupled to the electronic ground-state $^1S_0$ at a wavelength of 698 nm is used as an optical qubit [121, 122], whereas recent explorations are being done for hyperfine levels as well [123]. However, in most of these cases, single-site addressability is difficult, as the atoms are closely spaced in the lattice and the external fields are typically applied globally to the entire system. In certain situations, R_z gates can be implemented with single-site addressability through lightshift. As discussed in Sec. 2.3.1, a single qubit can be modeled as a two-level system in the presence of an external driving field, with the Hamiltonian

$$H(t)/\hbar = \Omega(t)\left(e^{i\phi(t)}\,|0\rangle\langle 1| + e^{-i\phi(t)}\,|1\rangle\langle 0|\right) - \frac{\Delta}{2}\left(|1\rangle\langle 1| - |0\rangle\langle 0|\right), \tag{3.8}$$

where $\Omega(t)$ is the Rabi frequency, controlled by the external field amplitude E_0, $\phi(t)$ is the phase of the laser and Δ is the detuning.

These microwaves field drive are used for high-fidelity control, however the gate times are slower with Rabi frequency in kHz [117, 124]. For faster gates on the megahertz-scale, Raman transition using lasers can be used, which can also offer the opportunity for local addressing of individual qubits separated by micrometer length scales [125, 126]. Raman transitions are two-photon processes involving the interaction

of two optical fields to induce a transition in the system [127, 128]. Both hyperfine qubit states are coupled with a mutual excited state $|2\rangle$ with Rabi frequency $\Omega_0(t)$ and $\Omega_1(t)$ respectively, and large detuning Δ as shown in Fig. 3.1. In the rotating wave approximation, the following Hamiltonian describes the system,

$$H(t)/\hbar = \frac{\Omega_0(t)}{2} e^{-i\phi_0(t)} |2\rangle\langle 0| + \frac{\Omega_1(t)}{2} e^{-i\phi_1(t)} |2\rangle\langle 1| - \delta |1\rangle\langle 1| - \Delta |2\rangle\langle 2| + h.c. \quad (3.9)$$

Since, $\Delta \gg \Omega_0(t), \Omega_1(t)$, we can adiabatically eliminate the excited state $|2\rangle$ [129, 130] giving an effective two-level Hamiltonian as

$$\hat{H}_{\text{eff}}(t) = \frac{\hbar}{2} \begin{pmatrix} \frac{\Omega_0(t)^2}{2\Delta} & \frac{\Omega_0(t)\Omega_1(t)}{2\Delta} \\ \frac{\Omega_0(t)\Omega_1(t)}{2\Delta} & \frac{\Omega_1(t)^2}{2\Delta} - 2\delta \end{pmatrix}. \quad (3.10)$$

The ground state energy levels are shifted by an amount $\delta_i = \Omega_i^2/4\Delta$ (for $i = 0, 1$). The Rabi frequency for the two-level transition is given by $\Omega_{TLS}(t) = \frac{\Omega_0(t)\Omega_1(t)}{2\Delta}$, with a detuning of δ plus the differential light shift of $\Delta\delta = \delta_0 - \delta_1$. The phase of the effective field that is driving the Rabi oscillations is defined by the difference of the local phase of the two optical fields, $\Delta\phi = \phi_0 - \phi_1$. This transition through a virtual process where one photon from the first field is absorbed and another photon from the second field is emitted via a short-lived, intermediate state. The term virtual signifies that the system doesn't actually reach a stable, real excited state, or in other words, the state remains mostly unpopulated, with transient population being quickly eliminated by destructive interference processes. This is because the laser frequencies are significantly detuned from the resonance frequency of the real transition, minimizing the likelihood of actual absorption and spontaneous emission.

3.1.3 Two-qubit Rydberg gate

Hyperfine levels of neutral atoms are excellent candidates for storing qubit states, owing to their long coherence times. However, the direct interactions between these states are typically very weak, making the entanglement generation challenging. To overcome this limitation and enable feasible two-qubit gates, Rydberg states are coupled with ground states, offering strong and controllable interactions. A key technique employed is the Rydberg blockade mechanism (see Sec. 3.1.1), which can be used to implement a controlled-phase (C-PHASE) gate between two qubits. The foundational idea of the Rydberg blockade two-qubit gate relies on single-site addressability [131], where, the ground state $|0\rangle$ is resonantly coupled to a highly excited Rydberg state $|r\rangle$. The protocol consists of a three-pulse sequence: first, a π pulse is applied to the control atom; second, a 2π pulse is applied to the target atom; and finally, another

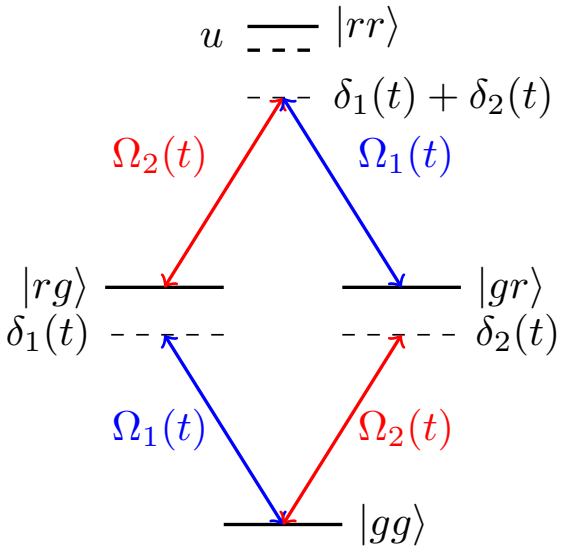

Figure 3.2: Level scheme for the demonstration of C-PHASE gate with Rydberg blockade. The ground state $|gg\rangle$ is coupled to the intermediate singly excited states $|rg\rangle$ and $|gr\rangle$ with time-dependent Rabi frequencies $\Omega_1(t)$ (blue) and $\Omega_2(t)$ (red), respectively. The doubly excited Rydberg state $|rr\rangle$ is shifted by an interaction energy u, preventing simultaneous excitation.

π pulse is applied to the control atom. In this arrangement, the two-atom state $|11\rangle$ remains unaffected, since the state $|1\rangle$ is not coupled to the Rydberg state $|r\rangle$. States $|01\rangle$ and $|10\rangle$ acquire a phase change. For the $|00\rangle$ state, assuming the blockade shift B (induced by the Rydberg-Rydberg interaction) is much larger than the Rabi frequency Ω, excitation of the target atom is suppressed [as shown in Fig. 3.2], and the state picks up a π phase. Further refinements have introduced implementations using global laser pulses, removing the need for single-site addressability and operating effectively at finite blockade strengths [19, 132]. Rydberg blockade gate scheme with global pulses has been experimentally realized in several setups [15, 133, 134]. All these variations ultimately realize a C-PHASE gate, which, up to local phase corrections, is equivalent to the conventional CZ gate discussed in Sec. 2.1.2. Combining the C-PHASE gate with Hadamard operations allows the construction of a C-NOT gate, and together with arbitrary single-qubit rotations, forms a universal gate set for quantum computing with neutral atoms.

Another scheme for implementing two-qubit gates, with the qubit states being the low-lying ground levels, is based on the dipole-dipole interaction between Rydberg states. In this approach, two different Rydberg states of the atoms are coupled via a microwave field, and the interaction between them is controlled to realize a C-PHASE gate [135].

All of these schemes require the excitation of the ground state to a Rydberg state. Therefore, in Chapter 4, we study the problem of Rydberg state excitation using

quantum optimal control, and optimize the process in the presence of several physical and technical imperfections. To this end, in the next section we briefly explain the Rydberg excitation process.

3.1.4 Rydberg excitation process

Excitation from a ground state to a Rydberg state is a key ingredient for quantum computation and simulation tasks using Rydberg atoms. The simplest way to perform this excitation is via a single-photon transition [121, 131, 136]. However, these transitions have wavelengths in the ultraviolet region, which is experimentally challenging to prepare. To avoid these issues, a two-photon excitation scheme is commonly used, e.g., for ^{87}Rb, coupling the ground $5S_{1/2}$ state to a Rydberg nS state via an intermediate state [137, 138]. Two possible choices for the intermediate state are $5P_{3/2}$ and $6P_{3/2}$. In most experiments, the $6P_{3/2}$ state is preferred as it provides higher optical power for the transition from the intermediate to the Rydberg state [137]. In this scheme, a first laser field $\Omega_b(t)$ at a wavelength of 420 nm transfers the atom from the ground state $|g\rangle$ to an intermediate state $|i\rangle$. Subsequently, a second laser field $\Omega_r(t)$ at a wavelength of 1013 nm drives the transition from $|i\rangle$ to the Rydberg state $|r\rangle$.

One well-known two-photon scheme is the Stimulated Raman Adiabatic Passage (STIRAP) [139–141], which achieves population transfer from the ground state to the Rydberg state while minimizing population in the intermediate state as shown in Fig. 3.3(a). In STIRAP, the unpopulated states $|i\rangle$ and $|r\rangle$ are first coupled using a drive field $\Omega_r(t)$. Subsequently, the intermediate state $|i\rangle$ is coupled to the ground state $|g\rangle$ via a second drive field $\Omega_b(t)$. The Hamiltonian is given by,

$$H(t) = \hbar \begin{pmatrix} 0 & \frac{1}{2}\Omega_b(t) & 0 \\ \frac{1}{2}\Omega_b(t) & \delta & \frac{1}{2}\Omega_r(t) \\ 0 & \frac{1}{2}\Omega_r(t) & \Delta \end{pmatrix}. \tag{3.11}$$

This counterintuitive pulse sequence enables efficient population transfer from $|g\rangle$ to $|r\rangle$ by exploiting a so-called "dark state". This dark state is formed, when the two-photon resonance $\Delta = 0$, and one of the eigenvalues of the Hamiltonian of vanishes, $\lambda_0 = 0$. The corresponding eigenstate known as the dark state of the Hamiltonian is given by [139]

$$|d\rangle = \cos\theta\,|g\rangle - \sin\theta\,|r\rangle\,. \tag{3.12}$$

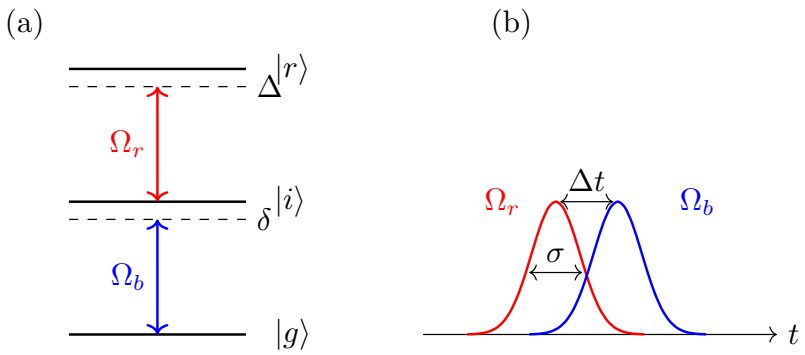

Figure 3.3: STIRAP pulse sequence and energy level scheme. (a) Three-level ladder system with states $|g\rangle$, $|i\rangle$, and $|r\rangle$. The lower transition $|g\rangle \leftrightarrow |i\rangle$ is driven by a field with Rabi frequency Ω_b (blue), and the upper transition $|i\rangle \leftrightarrow |r\rangle$ is driven by a field with Rabi frequency Ω_r (red). The one and two-photon detunings are δ and Δ respectively. (b) Temporal pulse sequence for counterintuitive STIRAP: the Ω_r (red) pulse precedes the Ω_b (blue) pulse with a time delay Δt and pulse width σ, enabling coherent population transfer via an adiabatic passage without populating the intermediate state $|i\rangle$.

The other two eigenstates of the Hamiltonian are

$$\begin{aligned} |a\rangle &= \sin\theta(t)\sin\phi(t)\,|g\rangle + \cos\phi(t)\,|i\rangle + \cos\theta(t)\sin\phi(t)\,|r\rangle\,, \\ |b\rangle &= \sin\theta(t)\cos\phi(t)\,|g\rangle - \sin\phi(t)\,|i\rangle + \cos\theta(t)\cos\phi(t)\,|r\rangle\,. \end{aligned} \tag{3.13}$$

The mixing angles are defined as

$$\begin{aligned} \tan\theta &= \frac{\Omega_b(t)}{\Omega_r(t)}, \\ \tan 2\phi &= \frac{\sqrt{\Omega_b^2(t)+\Omega_r^2(t)}}{\Delta}. \end{aligned} \tag{3.14}$$

In the absence of dissipation, perfect population transfer from the ground state to the Rydberg state can be achieved by satisfying the adiabaticity condition:

$$\dot{\theta} \ll \sqrt{\Omega_b^2(t)+\Omega_r^2(t)}. \tag{3.15}$$

This condition can be realized using Gaussian-shaped pulses, for example,

$$\begin{aligned} \Omega_b(t) &= \Omega_0 \exp\left(-\frac{(t-\Delta t/2)^2}{2\sigma^2}\right), \\ \Omega_r(t) &= \Omega_0 \exp\left(-\frac{(t+\Delta t/2)^2}{2\sigma^2}\right), \end{aligned} \tag{3.16}$$

where σ is the Gaussian pulse width, Ω_0 is the maximum Rabi coupling, and Δt is the

temporal delay between the two laser pulses as shown in Fig. 3.3(b).

In Chapter 4, we optimize the two-photon Rydberg excitation process using quantum optimal control, taking into account various physical and technical imperfections. Our numerically optimized pulses follow the characteristic STIRAP counterintuitive sequence, demonstrating the effectiveness and robustness of this scheme for high-fidelity Rydberg excitation.

3.1.5 Trapping Rydberg atoms

Optical tweezers – Neutral atoms can be trapped using tightly focused far off-resonant laser beams, forming optical tweezers [121, 142–144]. These create conservative dipole potentials where the induced atomic dipole moment interacts with the light's oscillating electric field. Consider a laser field with frequency ω, polarization $\hat{\mathbf{e}}$, and amplitude E, given by $\mathbf{E}(t) = \hat{\mathbf{e}}Ee^{-i\omega t} + c.c.$. This model uses the dipole approximation, which assumes that the size of the atom is much smaller than the wavelength of the incident light. With this approximation, the electron only sees the field at the nuclear position, and no spatial dependence of the field-atom interaction is required. We can treat the atom in a classical approach, where it is considered as a damped harmonic oscillator with oscillation frequency ω_0 of the electron. The incident light induces an electric dipole with dipole moment $\mathbf{d} = \alpha(\omega)\mathbf{E}$, where $\alpha(\omega)$ is the frequency dependant polarizability. The interaction of the dipole moment with the incident light constructs a dipole potential

$$U_{\text{dip}} = -\frac{\mathbf{d}.\mathbf{E}}{2}. \tag{3.17}$$

When approximating the atom with two-level system in a semi-classical approach, we want to minimize the heating of the atom. We ensure this by making the field far resonant compared to the spontaneous emission rate γ of the atomic transition (also means the damping rate in the classical picture of the atom), i.e., $\Delta = \omega - \omega_0 \gg \gamma$. Additionally, in order to perform the roatating wave approximation, we assume that the light is close enough to resonace such that $\Delta \ll \omega$ [145].

When the laser frequency is relatively close to resonance, i.e. $\Delta = \omega - \omega_0$ is small compared to ω_0, the interaction potential can be written using the rotating wave approximation as

$$U_{\text{dip}}(\mathbf{r}) = \frac{3\pi c^2}{2\omega_0^3}\frac{\gamma}{\Delta}\mathbf{I}(\mathbf{r}), \tag{3.18}$$

where c is the speed of light and $I(\mathbf{r})$ is the intensity of the light field. The potential is attractive for red-detuned light ($\Delta < 0$) and repulsive for blue-detuned light ($\Delta > 0$).

In experiments, arrays of tweezers are formed using acousto-optic deflectors (AODs) or spatial light modulators (SLMs), allowing individual control over each trap's posi-

tion and intensity [146]. In certain cases, a magic wavelength is employed to ensure identical light shifts for different hyperfine states, improving coherence and stability [147]. However, achieving such conditions for Rydberg states is challenging, as red-detuned tweezers induces heating of these highly excited states [148, 149], which limits the coherence time. To address this, traps are often turned off during Rydberg excitation, which limits interaction time and can induce further heating [149].

Optical lattices – The dipole trapping concept is extended to periodic potentials formed by the interference of multiple laser beams [150, 151]. Two superimposed counter propagating plane laser waves will result in a standing wave pattern as,

$$\mathbf{E}(x,t) = \hat{\mathbf{e}}E(\exp[i(kx-\omega t)] + \exp[i(-kx-\omega t)]) + c.c. \tag{3.19}$$

$$= 4\hat{\mathbf{e}}E\cos(kx)\cos(\omega t), \tag{3.20}$$

where k is the wavevector. The corresponding potential is given by

$$U_{\text{dip}}(x) = A\cos^2(kx), \tag{3.21}$$

where A is called the lattice depth, typically expressed in units of recoil energy $E_r = \hbar^2 k_L^2/2m$. By combining multiple laser beams, one-, two-, and three-dimensional lattice geometries can be created, providing a versatile platform for simulating quantum many-body systems. Compared to reconfigurable tweezer arrays, optical lattices offer larger and significantly more homogeneous systems, at the cost of limited connectivity through nearest-neighbor tunneling only [152].

3.1.6 Error sources in Rydberg-atom setup

Rydberg lifetime – Although Rydberg states have a very long coherence time, spontaneous decay limits the gate fidelities [153]. Spontaneous decay is a phenomenon where the Rydberg state $|r\rangle$ decays to one of the ground states $|g\rangle$ with decay rate Γ. The ground state $|g\rangle$ can be computational basis states or some other ground state. This causes a loss of coherence in the system and decreases the gate fidelity. To avoid decoherence, fast excitation can be performed, minimizing spontaneous emission. In chapter 4, optimize the Rydberg exciation process, by including these spontaneous decay mechanisms for ^{87}Rb atom.

Finite blockade – In practice, the blockade interaction is finite, limiting the two-qubit gate's performance [154, 155]. One of the major consequences of the finite blockade is the population of the state $|rr\rangle$ during the C_Z gate. The probability of

this is $\pi\Omega^2/2V_{rr}^2$ where V_{rr} is the interaction strength. This can be reduced by using lower Rabi frequency Ω but at the risk of increased spontaneous emission. In recent work, two-qubit gates have been optimized in presence of finite blockade with the help of quantum optimal control.

Technical limitations – In addition to the important atomic limitations mentioned above, various physical and technical imperfections in the experiment affect the fidelity of quantum operations performed with Rydberg atoms [156–158]. In Chapter 4, we include technical errors of the control lasers, such as amplitude constraints and bandwidth limitations, which are discussed in detail in Sec. 2.4.1. When working with an ensemble of atoms, the lasers used for Rabi transitions between $|0\rangle$ and $|1\rangle$, or $|0\rangle$ and $|r\rangle$, are typically global, meaning a single laser field is applied over the entire lattice. However, the laser intensity is spatially inhomogeneous, resulting in atoms at the edges of the lattice experiencing different Rabi frequencies compared to those at the center. This leads to variations and inefficiencies in single-qubit gate operations across the array. A second important source of error is the phase instability of the clock laser. This becomes particularly relevant when optimizing the phase of the laser while keeping its intensity constant. These effects are examined in more detail in Sec. 3.2.5 and are incorporated into the robustness analysis presented in Chapter 5. Beyond these issues, additional imperfections such as atom heating, trap laser fluctuations, and intensity noise also contribute to operational infidelity. While identifying, characterizing, and mitigating all sources of technical error is essential for achieving reliable and scalable quantum operations, this remains a challenging and active area of research from both theoretical and experimental perspectives.

One can also implement two-qubit gates using collisional interactions between atoms [20, 21, 26]. In Chapter 5, we optimize one such system using the Fermi-Hubbard model to realize efficient SWAP and $\sqrt{\text{SWAP}}$ gates. While key concepts — including superlattices, Wannier functions, and the Fermi-Hubbard model — are explained in detail also in Chapter 5, we present an brief overview of these topics, along with a discussion of the associated physical and technical challenges of this platform, in the following section.

3.2 Fermionic atoms

Short-range collisional interactions between atoms in their hyperfine levels provide an alternative mechanism for implementing two-qubit gates, distinct from the Rydberg interaction-based schemes discussed previously. In this approach, ultracold atoms—either bosonic or fermionic—are trapped in an optical potential and interact

via on-site collisions, with the nature of these interactions determined by the quantum statistics of the atoms. These interactions are induced by dynamically tuning the trapping potentials, rather than applying external laser fields [159–164]. The optical lattices used to confine the atoms are created by standing wave patterns formed from interfering laser beams, as introduced in Sec. 3.1.5, producing a potential capable of trapping atoms at periodic points in space [150, 151]. The dynamics of ultracold atoms in these periodic potentials closely resemble the behavior of electrons in solid-state systems. In Chapter 5, we focus on a specific type of optical lattice—a periodic structure of double wells known as a superlattice. These superlattices offer enhanced control over tunneling rates and interaction strengths by modulating the depth and phase of individual wells within the lattice [26, 157, 165]. In the following, we explain the working principle of optical superlattices and describe how the behavior of atoms confined in such potentials can be effectively modeled using the Hubbard model framework.

3.2.1 Superlattices

In the work described in chapter 5, a three-dimensional optical lattice is created where, in the x-direction, two standing waves with different periodicity are superimposed to create a superlattice [157]. One of the lattice (short lattice) has approximately twice the frequency of the other (long lattice) i.e., $\omega_s \approx 2\omega_\ell$, where ω_s and ω_ℓ are the frequencies of the short and long lattice, with corresponding wavelengths $\lambda_s = 532$ nm and $\lambda_\ell = 1064$ nm. The resulting three-dimensional potential is given by,

$$V_{lat}(r) = -V_\ell \cos^2(k_\ell x) + V_s \cos^2(2k_\ell x + \phi) + V_y \cos^2(k_y y) + V_z \cos^2(k_z z).$$

Here ϕ is the relative phase between the two standing waves. The quantities V_ℓ, V_s, $V_y, V_z > 0$ are called the lattice depths of the corresponding lattices. The sign in front of each term takes into account that the long lattice is red-detuned from the atomic transition, while all other lattices are blue-detuned. The Hamiltonian for a single atom trapped in the periodic superlattice potential is given by,

$$H = \frac{\hbar^2}{2m}\Delta + V_{lat}(r) \tag{3.22}$$

where Δ is the three-dimensional kinetic energy operator and $V_{lat}(r)$ is the three-dimensional potential energy term. The Hamiltonian is separable in three axes, allowing us to solve and work with only the x-direction superlattice Hamiltonian. The eigenfunctions of a periodic potential can be written as [166],

$$\Psi_q^n(x) = e^{iqx/\hbar} u_q^n(x) \tag{3.23}$$

where $u_q^n(x)$ is a periodic function and q is the quasi-momentum ranging from $-\hbar k_\ell$ to $\hbar k_\ell$, i.e., the first Brillouin zone. The periodicty is given by $d = \lambda_\ell/2$ and the bands are represented by the band index n. With the quasi-momentum q, the Hamiltonian is given as,

$$H_q(x) = \frac{1}{2m}(-i\hbar\frac{\partial}{\partial x} + q)^2 + V_{lat}(x). \tag{3.24}$$

The corresponding system evolution equation is

$$H_q(x)u_q^n(x) = E_q^n(x)u_q^n(x), \tag{3.25}$$

where $E_q^n(x)$ is the eigenenergies corresponding to different bands n. Now, $u_q^n(x)$ and the superlattice potential $V_{lat}(x)$ are periodic with $d = \lambda_\ell/2$, they can be written as [167],

$$u_q^n(x) = \sum_{r\in\mathbb{Z}} c_{q,r}^n e^{i2k_\ell rx}$$
$$V_{lat}(x) = \sum_{r\in\mathbb{Z}} d_r e^{i2k_\ell rx}$$

Substituting these values in Schrodinger's equation above gives

$$\frac{1}{2m}(-i\hbar\frac{\partial}{\partial x} + q)^2 \sum_{r\in\mathbb{Z}} c_{q,r}^n e^{i2k_\ell rx} + \sum_{r\in\mathbb{Z}} d_r e^{i2k_\ell rx} \sum_{r\in\mathbb{Z}} c_{q,r}^n e^{i2k_\ell rx} = E_q^n \sum_{r\in\mathbb{Z}} c_{q,r}^n e^{i2k_\ell rx}$$

$$\implies \frac{1}{2m}(2\hbar k_\ell r + q)^2 c_{q,r}^n + \sum_{r'} d_{r'} c_{q,r-r'}^n = E_q^n c_{q,r}^n.$$

For determining d_r we can write the superlattice potential as

$$\begin{aligned} V_{lat}(x) &= -V_\ell \cos^2(k_\ell x) + V_s \cos^2(2k_\ell x + \phi) \\ &= -\frac{V_\ell}{2}(\cos(2k_\ell x) + 1) + \frac{V_s}{2}(\cos(4k_\ell x + 2\phi) + 1) \\ &= -\frac{V_\ell}{2}(\frac{e^{i2k_\ell x} + e^{-i2k_\ell x}}{2} + 1) + \frac{V_s}{2}(\frac{e^{i4k_\ell x + i2\phi} + e^{-i4k_\ell x - i2\phi}}{2} + 1) \\ &= \frac{V_s}{4}e^{-2i\phi}e^{-4ik_\ell x} - \frac{V_\ell}{4}e^{-2ik_\ell x} + \frac{V_s - V_\ell}{2} - \frac{V_\ell}{4}e^{2ik_\ell x} + \frac{V_s}{4}e^{2i\phi}e^{4ik_\ell x}. \end{aligned} \tag{3.26}$$

Hence, coefficients other than $d_0, d_{\pm1}$ and $d_{\pm2}$ are zero and the Evolution equation can be written as,

$$\sum_{r'} H_{rr'} c_{q,r'}^n = \epsilon_q^n c_{q,r}^n \tag{3.27}$$

where ϵ_q^n are in units of recoil energy and $H_{r,r'}$ is

$$\begin{aligned} H_{rr'} &= (2r + \frac{q}{\hbar k_\ell})^2 + \frac{V_s - V_\ell}{4} && \text{for } r = r' \\ &= -\frac{V_\ell}{4} && \text{for } r - r' = \pm 1 \\ &= \frac{V_s}{4} e^{\pm i\phi} && \text{for } r - r' = \pm 2 \\ &= 0 && \text{else .} \end{aligned} \tag{3.28}$$

We can calculate the eigenvalues ϵ_q^n and eigenfunctions $u_q^n(x)$ by diagonalizing the matrix $H_{r,r'}$. In principle, the matrix is infinite-dimensional but can be truncated to a smaller matrix since c_q^n becomes negligible for long r and small n [167, 168].

The eigen- or band energies ϵ_q^n are periodic in the quasi-momentum and symmetric around $q = 0$. They are a function of V_s, V_ℓ, and ϕ. In the superlattice, an increase in the short lattice amplitude V_s decreases the energy between the first and second as well as third and fourth bands. This brings the bands closer to each other and forms pairs of energy bands. Additionally, increasing V_ℓ for a fixed V_s flattens the energy bands and increases the energy gap in the pairs. Similar to the band energies, the Bloch waves are also periodic in quasi-momentum, and their construction depends on the transformation properties of the Hamiltonian. In short, when the Hamiltonian is invariant under inversion, i.e., $\phi = 0$, the Bloch waves are either symmetric or anti-symmetric [for details refer to [167]].

3.2.2 Wannier functions

Although Bloch waves describe atoms in periodic lattices with well-defined quasi-momentum, they are delocalized in real space, which makes them impractical for certain applications. To address this, Wannier functions are introduced as localized eigenfunctions constructed from superpositions of all quasi-momentum states [169–171]. Mathematically, the Wannier function $w_l^n(x)$ at the lattice site l in band n is defined as

$$w_l^n(x) = \frac{1}{\sqrt{N_L}} \sum_q e^{-iqld} \Psi_q^n(x), \tag{3.29}$$

where d is the lattice constant and N_L is the number of lattice sites. Wannier functions are orthonormal, satisfying $\langle l, n | l', n' \rangle = \delta_{nn'} \delta_{ll'}$, and their symmetry properties mirror those of the underlying Bloch waves — they can be chosen to be real and either symmetric or antisymmetric about their respective lattice sites. However, Wannier functions are not unique, as they depend on the arbitrary phases of the Bloch states. To

obtain maximally localized Wannier functions from the set of orthonormal possibilities, they can be defined as the eigenstates of the band-projected position operator. We detail the procedure for calculating these functions following [168] in Chapter 5, and thus omit it here to avoid redundancy.

We would like to emphasize that the Wannier functions are only an approximate eigenstates and to get a maximally localized Wannier function, we must choose the right size of the manifold of bands [167]. However, using large number of bands is numerically exhausting and unnecessary for the superlattice case in Chapter 5. In the superlattice, only pairs of bands, such as first and second, third and fourth can be taken into different manifolds. This is because the energy gaps between the bands outside the pairs are large enough such that the admixture between them is negligible. Since our three-dimensional potential is separable, we can perform the similar Wannier function calculation in all x, y, and z directions. Note that the Wannier function in y and z direction will be constructed for a lattice with periodic single wells, unlike the double well structure of the superlattice. The three-dimensional Wannier function can thus be written as the product of the three one-dimensional Wannier functions. For non-separable potentials like honeycomb lattices, it becomes tricky since the projection operators of all directions may not commute with each other [168, 172].

3.2.3 Fermi-Hubbard model

Fermi-Hubbard model simply describes the electron's motion and the electron-electron interaction in a solid. This idea can also be extended to atoms trapped in array-like lattices where the bosonic atoms are described by the Bose-Hubbard model [173, 174] and the fermionic atoms are described by the Fermi-Hubbard model [175, 176]. In this work, we only discuss the Fermi-Hubbard model as we work with fermionic Lithium ^{6}Li atoms trapped in a superlattice [157]. In ^{6}Li atoms, the spin-up and spin-down states are stored in two hyperfine levels $F = 1/2$ and $F = 3/2$ of $2S_{1/2}$.

The Fermi-Hubbard model is generally implemented with an assumption that atoms are always in the lowest energy band of the lattice, which is widely true for tightly bound atoms distant from each other [166]. Now, for a superlattice, the gap between the two lowest energy bands is very low. This causes the admixture of the bands and their eigenfunctions. Therefore, we have to extend the ground-band Hubbard model to a two-band model given by [167]

$$H = -J \sum_{\sigma} (c^{\dagger}_{L\sigma} c_{R\sigma} + h.c.) + U \sum_{j \in L,R} n_{j\uparrow} n_{j\downarrow}. \tag{3.30}$$

The operator $c^{\dagger}_{lL\sigma}$ and $c^{\dagger}_{lR\sigma}$ create a fermion on the left or right side of the double

well at site l in the spin state σ (refer to Appendix 3.4.2 for details for creation and annihilation operators). This is the simplest form of the Fermi-Hubbard model used to explain the superlattice dynamics in Chapter 5. We explain thoroughly the two-band model starting from the typical single-band Fermi-Hubbard model in Chapter 5, and therefore do not repeat it here. Later in Chapter 5, we also show, how this model fails to explain the dynamics under fast gates, and extention to include higher bands and optimization with the higher-band model is required to find fast and efficient SWAP and $\sqrt{\text{SWAP}}$ gates. To understand the idea of these fermionic gates, we will explain the two-qubit SWAP and $\sqrt{\text{SWAP}}$ gates in the next section.

3.2.4 Gates with fermionic atoms in a superlattice

A double well can accommodate up to four fermionic atoms with two atoms in the spin-up state and two atoms in the spin-down state. While, one-atom states can serve as single-qubit states, states with three and four atoms are error states for two-qubit gates. We can have two possible basis sets for two-qubit gates in a superlattice. First is a spin conserving basis set $|D0\rangle$, $|\uparrow\downarrow\rangle$, $|\downarrow\uparrow\rangle$, and $|0D\rangle$, where one spin-up and one spin-down atom is in a double well [152]. $|D0\rangle$ means both atoms on the left side of the double well, $|\uparrow\downarrow\rangle$ means spin up on the left side and spin down on the right side of the double well and so on. This set is also the basis set for time evolution of the ground-band hubbard model when one spin-up and one spin-down atom is in a double well. The SWAP and $\sqrt{\text{SWAP}}$ gates are represented in this basis as

$$\text{SWAP} = \begin{bmatrix} 0&0&0&1\\0&0&1&0\\0&1&0&0\\1&0&0&0 \end{bmatrix}, \quad \sqrt{\text{SWAP}} = \begin{bmatrix} (1+i)/2 & 0 & 0 & (-1+i)/2 \\ 0 & (1+i)/2 & (-1+i)/2 & 0 \\ 0 & (-1+i)/2 & (1+i)/2 & 0 \\ (-1+i)/2 & 0 & 0 & (1+i)/2 \end{bmatrix}.$$

Note that this different from the conventional SWAP and $\sqrt{\text{SWAP}}$ gates used in quantum infromation. Second basis set is the spin non-conserving basis states $|\uparrow\uparrow\rangle$, $|\uparrow\downarrow\rangle$, $|\downarrow\uparrow\rangle$, and $|\downarrow\downarrow\rangle$ [106, 177]. In this basis, the total spin of the system is not conserved. This is a more conventional basis set for quantum computation and simulation purpose since the SWAP and $\sqrt{\text{SWAP}}$ gates are represented in this basis gives the conventional form

$$\text{SWAP} = \begin{bmatrix} 1&0&0&0\\0&0&1&0\\0&1&0&0\\0&0&0&1 \end{bmatrix}, \quad \sqrt{\text{SWAP}} = \begin{bmatrix} 1 & 0 & 0 & 0 \\ 0 & (1+i)/2 & (-1+i)/2 & 0 \\ 0 & (-1+i)/2 & (1+i)/2 & 0 \\ 0 & 0 & 0 & 1 \end{bmatrix}.$$

In Chapter 5, we work with the second set of basis states, which provides the advantage of formulating the problem as a state-to-state transfer optimization. This approach allows us to first optimize the transfer between selected basis states and subsequently evaluate the fidelity for the complete gate operation. The details of the different control objectives are discussed in Sec. 2.3.2. We include different error

sources in our robustness analysis performed in Chapter 5, which mainly comes from the technical limitations of the lasers constructing the superlattice. In the next section, we discuss some of the significant error sources.

3.2.5 Error sources in fermionic atoms

In the implementation of quantum gates using fermionic atoms in optical lattices, several error mechanisms can limit the achievable gate fidelity. Understanding and quantifying these sources is crucial for designing robust and scalable quantum systems. In this work, we identify and discuss three primary sources of error [157, 178].

The first source of error is associated with tunneling to neighboring lattice sites. While we optimize the tunneling of the atoms inside the double well, the boundaries of the target double well with the neighboring well is finite, and is modulated with tuning the lattice depths. This happens since the optical lattices are made from global lasers, and therefore atoms possess a nonzero probability to tunnel into adjacent double wells with tunneling strength J' [152, 178]. Such tunneling events not only reduce the gate efficiency by removing atoms from the target qubit space but can also lead to crosstalk in nearby sites. Typically, the tunneling strength J' is small comapred to the optimized strength J but is sensitive to the lattice depth. In Chapter 5, we show that our optimized pulses produces negligible tunneling to the neighboring wells.

The second significant error source arises from phase instability of the lasers producing the superlattice potential [179]. In our numerical simulations, we assume a perfectly symmetric double well configuration, corresponding to a relative phase of $\phi = 0$ mrad between the interfering laser beams. However, in experimental realizations, technical noise can induce phase drifts over time, leading to variations in the relative phase of the lasers. These fluctuations cause dephasing between the atomic states and reduce the coherence time of the system [157, 178]. Additionally, shot-to-shot phase fluctuations can produce random energy offset in the system, increasing the gate error. Phase instabilities are particularly determental in gate schemes that rely on tuning of relative phase instead of the lattice depths, which produces tilted double wells.

Lastly, we consider the influence of inhomogeneities in the laser intensities that form the optical lattice [180, 181]. In practice, the spatial profile of laser beams results in position-dependent lattice depths and coupling strengths across the atomic array. These inhomogeneities lead to variations in tunneling rates, on-site interaction energies, and hence, in gate operation times and fidelities from site to site [157, 178]. While, active feedback control systems are typically employed in experiments to mitigate the phase and intensity fluctuations, we can also include these variations in an

ensemble optimization to find robust controls as discussed in Sec. 2.4.2.

In addition to these primary sources, other experimental imperfections such as atom loss and magnetic field fluctuations [182, 183] can also contribute to the overall error budget, though they are not the primary focus of this study. A detailed understanding of these error mechanisms is essential for guiding future improvements in lattice design and gate protocols for fermionic quantum simulators and processors.

3.3 Quantum simulation with neutral atoms

In the early 1980s, scientists started proposing novel ways of simulating computationally demanding quantum mechanical systems [4]. The primary challenge of simulating these systems arises from the exponential growth of the quantum state's parameters with system size. Quantum simulation tackles these challenges by using quantum devices to simulate quantum systems [184, 185]. By a *quantum simulator*, we understand a controllable quantum system used to simulate or emulate other quantum systems (see, e.g., [4, 186]). Quantum simulators, ranging from specialized experiments to universal quantum computers, offer promising solutions to complex scientific and engineering problems. These devices leverage quantum phenomena like entanglement and many-particle behavior to explore and solve challenges in various fields. Neutral atom-based simulators exploit the controllable interactions and coherent manipulation of neutral atoms trapped in optical tweezers or lattices to emulate complex quantum systems [22, 187]. The atoms serve as qubits encoded in their internal states, often involving ground and Rydberg excited states as described in earlier sections. Their interactions can be tuned precisely to realize desired Hamiltonians. Consider a general quantum simulation problem: determining the state of a quantum system described by the wavefunction $|\phi\rangle$ at time t and calculating a desired physical quantity. For a time-independent Hamiltonians H, based on the method used to generate the unitary $U = \exp\left(-\frac{i}{\hbar}Ht\right)$, we can divide quantum simulation into two broad categories: *digital* and *analog* quantum simulation [22]. Neutral atom quantum simulators have the potential to perform both digital and analog quantum simulations, as described next.

3.3.1 Digital quantum simulation

In the digital or circuit model of quantum computation, to simulate the evolution of a state $|\phi(0)\rangle$ for time t, the unitary transformation $U = \exp\left(-\frac{i}{\hbar}Ht\right)$ is applied through a sequence of quantum gates [refer to Chapter 2 for introduction of quantum gates] [188, 189]. In the absence of high-fidelity gates beyond two-qubit operations, recent neutral atom quantum simulation algorithms rely on single- and two-qubit gates

discussed in Secs. 3.1.2, 3.1.3, and 3.2.4. Digital quantum simulation is theoretically universal; that is, it is capable of initializing, measuring, and performing universal quantum gates on well-defined qubits [190]. However, state-of-the-art devices are not yet fault-tolerant, and as a result, not all unitary operations can be efficiently simulated due to resource constraints and decoherence in the system [191].

3.3.2 Analog quantum simulation

Analog quantum simulation is another method of simulating quantum systems, using a paramterized Hamiltonian. This is more common form of quantum simulation for state of the art neutral atom devices, since it applies a globally acting unitary in layers with each layer having different parameter values [192, 193]. For Rydberg atom system, these controlable paramters are the laser amplitudes genrating the coupling frequencies e.g., $\Omega(t)$, the detuninigs $\Delta(t)$ [137, 194]. Analog simulation has a disadvanatage compared to digital simulation since it is not universal, i.e., given a quantum simultor with certain Hamiltonian represenation only a certain set of quantum systems can be simulated which match the symmetry and capabilities of the simulator [195]. An extensive studies have been performed to understand these criterias and make a set of tools to check these [196, 197]. Nonetheless, analog simulation has an adavantage that the error accumulation is lower as it do not need high circuit depths comapred to the digital counterpart [191].

3.3.3 Variational algorithms

Fault-tolerant quantum computing demands a large increase in qubit count alongside maintaining excellent qubit quality and operational accuracy. Quantum algorithms that come with performance guarantees typically need millions of physical qubits to support quantum error correction and ensure fault tolerance. Developing such scalable, fault-tolerant quantum machines is expected to take many years. Meanwhile, noisy intermediate-scale quantum (NISQ) devices, which currently have limited number of qubits, operate without error correction and are imperfect. The goal during the NISQ era is to harness the computational potential of these devices as much as possible while progressing toward fully fault-tolerant quantum computing. Algorithms designed for these limited devices often combine quantum and classical computing, performing some tasks on quantum hardware and others on conventional computers. Among these hybrid methods are variational quantum algorithms, which make use of existing quantum hardware by integrating classical optimization techniques [30, 198, 199]. These algorithms employ parameterized quantum circuits to prepare trial quantum states, which are iteratively refined through a feedback loop with a classical optimizer that

minimizes a cost function measuring the quality of the state. Variational Quantum Eigensolvers (VQE) focus on approximating the ground state of a given Hamiltonian by using the energy expectation as the cost function [200–203]. VQE adjusts the parameters of a quantum circuit composed of sequences of quantum gates, primarily on digital quantum simulators. Various ansätze have been proposed and studied for these variational tasks [204–207]. In contrast, analog quantum simulators use multiple unitary evolution blocks driven by parameterized controls that are variationally optimized [192]. These variational algorithms are especially promising for studying quantum phase transitions. Once the ground state is prepared, experiments can probe its properties, such as correlation functions, and explore how the system reacts to external perturbations.

These variational algorithms suffer from challenges such as barren plateaus, local minima, and limitations arising from the symmetries of the system [204, 205, 207]. In particular, for analog devices such as Rydberg atom-based systems, we do not have full controllability of the system and therefore cannot reach arbitrary states using variational algorithms like VQE. In this regard, in Chapter 6, we develop theoretical methods to understand these symmetry-induced restrictions. Our approach builds on the broad body of research on simulability and reachability conditions for quantum systems and provides necessary conditions for the success of VQE in such constrained settings.

3.4 Appendix

3.4.1 Many particle state

We can represent the two-atom state as $|\Psi\rangle = |\psi\rangle\,|\phi\rangle$ where $|\psi\rangle$ and $|\phi\rangle$ are the single-particle states [3, 47, 196]. The state $|\psi\rangle\,|\phi\rangle$ means that the first atom is in state $|\psi\rangle$ and the second atom is in state $|\phi\rangle$ and

$$P_{12}\,|\Psi\rangle = |\phi\rangle\,|\psi\rangle\,, \tag{3.31}$$

where P_{12} is the permutation operator with eigenvalues ± 1 and eigenstates $\frac{1}{\sqrt{2}}(|\psi\rangle\,|\phi\rangle \pm |\phi\rangle\,|\psi\rangle)$. A similar formula can be extended to many-body states where only the symmetric (for bosons) and antisymmetric (for fermions) states are realized. For two fermions with the same spin state, the antisymmetric total wavefunction vanishes if the spatial parts are identical, enforcing the Pauli exclusion principle. [47]. A fully

symmetric or anti-symmetric N-particle state is given by [208]

$$|\Psi\rangle_{\pm} = N_{\pm} \sum_{p} (\pm 1)^{p} \, |\chi_{p1}\rangle \, |\chi_{p2}\rangle \cdots |\chi_{pN}\rangle \tag{3.32}$$

where $|\chi_j\rangle$ are orthonormal (distinct or same) single-particle states. $N_{\pm}$ is a normalization factor, and the sum runs over all $N!$ permutations. The fermionic many-body state is also known as the Slater determinant [209, 210] and we can see that it can become complex and cumbersome. To simplify the representation, we introduce the second quantization of the states. We only indicate the number of times a single-particle state appears in the many-body wavefunction. For example, the state $|\phi_i\rangle$ appears n_i times giving the many-body state as,

$$|\Psi\rangle_{\pm} = |n_1, n_2, \cdots\rangle_{\pm} \tag{3.33}$$

For bosons and fermions, the occupation number n_i takes the values $n_i = 0, 1, 2, \cdots$ and $n_i = 0, 1$ respectively with $\sum_i n_i = N$. Any state of the many-body Hilbert space can be written as the linear combination of the orthonormal basis states $|n_1, n_2, \cdots\rangle$ as,

$$|\Psi\rangle = \sum_{n_1, n_2, \cdots} c(n_1, n_2, \cdots) \, |n_1, n_2, \cdots\rangle \, . \tag{3.34}$$

The Fock space is defined as the direct sum of the linear span of orthonormal basis states for the number of atoms ranging from 0 to ∞ as

$$F_{\pm} = \bigoplus_{N=0}^{\infty} H_{\pm}^{N}, \tag{3.35}$$

where $H_{\pm}^{N}$ denotes the symmetric (+) or antisymmetric (-) subspace of the N-particle Hilbert space. So, a general state $|\phi\rangle$ of $F_{\pm}$ is a linear combination of states with a variable number of atoms and $|0, 0, \cdots\rangle$ represents the vacuum state.

3.4.2 Creation and annihilation operator

In the formalism of second quantization, creation and annihilation operators play a central role in describing quantum many-body systems. These operators act on occupation number states, or Fock states, which specify the number of particles occupying each available single-particle state [208, 211]. While the bosonic operators have the same form as the harmonic oscillator operators, the fermionic creation and annihilation

operators are given as

$$c_i^\dagger \left|n_1, n_2, \cdots, n_i, \cdots\right\rangle = (1-n_i)(-1)^{\epsilon_i} \left|n_1, n_2, \cdots, n_i+1, \cdots\right\rangle,$$
$$c_i \left|n_1, n_2, \cdots, n_i, \cdots\right\rangle = n_i(-1)^{\epsilon_i} \left|n_1, n_2, \cdots, n_i-1, \cdots\right\rangle. \tag{3.36}$$

The factor $(1-n_i)$ ensures that the creation operator acts only if the site i is unoccupied (since $n_i = 0$ means empty). The factor n_i ensures that the annihilation operator acts only if the site i is occupied. The sign factor $(-1)^{\epsilon_i}$ arises from the fermionic anti-commutation relations and is given by

$$\epsilon_i = \sum_{j<i} n_j,$$

i.e., the total number of fermions in all sites with index less than i. This counts how many fermions the operator "passes through" to reach site i, yielding the correct fermionic sign. A quantum field operator is defined as

$$\Psi^\dagger(r)\left|0\right\rangle := \left|r\right\rangle \tag{3.37}$$

which creates a particle at position r. $\left|r\right\rangle$ can be written as a linear combination of the single-particle states $\left|\phi_i\right\rangle$,

$$\left|r\right\rangle = \sum_i \langle\phi_i|r\rangle \left|\phi_i\right\rangle = \sum_i \phi_i^*(r) c_i^\dagger \left|0\right\rangle. \tag{3.38}$$

which gives,

$$\Psi(r) := \sum_i \phi_i(r) c_i$$
$$\Psi^\dagger(r) := \sum_i \phi_i^*(r) c_i^\dagger \tag{3.39}$$

For the spin $\frac{1}{2}$ fermions the spin degree of freedom changes the operators to

$$c_i \to c_{i\sigma} \text{ and } n_i \to n_{i\sigma}.$$

If $n_{i\sigma} = 1$ then $c_{i\sigma}^\dagger \left|n_{1\sigma'}, n_{2\sigma'}, \cdots, n_{i\sigma}, \cdots\right\rangle = 0$. The operators satisfy the canonical fermionic anti-commutation relations, which reflect the underlying antisymmetry of fermionic wavefunctions as [212],

$$\{c_{i\sigma}, c_{j\sigma'}^\dagger\} = c_{i\sigma} c_{j\sigma'}^\dagger + c_{j\sigma'}^\dagger c_{i\sigma} = \delta_{ij}\delta_{\sigma\sigma'}, \tag{3.40}$$

where $\sigma = \uparrow, \downarrow$. The anti-commutation relations also state that when two fermions with different labels are exchanged, the wavefunction changes sign, i.e., $c^\dagger_{i\sigma} c^\dagger_{j\sigma'} = -c^\dagger_{j\sigma'} c^\dagger_{i\sigma}$. The fermionic field operators are defined as

$$\Psi_{i\sigma}(r) := \sum_i \phi_i(r) c_{i\sigma} \tag{3.41}$$

This formalism of creation and annihilation operators, along with their associated anti-commutation relations, forms the foundation for describing fermionic many-body systems in lattice models. In particular, the Fermi-Hubbard model, which we describe in Sec. 3.2.3, and employ in Chapter 5, is naturally expressed in terms of these operators. The model captures essential physics such as particle tunneling between lattice sites and on-site interactions, all of which are elegantly and compactly encoded through the algebra of the creation and annihilation operators introduced here.

4

Compensating non-linear distortions

Predictive design and optimization methods for controlled quantum systems depend on the accuracy of the system model. Any distortion of the input fields in an experimental platform alters the model accuracy and eventually disturbs the predicted dynamics. These distortions can be non-linear with a strong frequency dependence so that the field interacting with the microscopic quantum system has limited resemblance to the input signal. We present an effective method for estimating these distortions which is suitable for non-linear transfer functions of arbitrary lengths and magnitudes provided the available training data has enough spectral components. Using a quadratic estimation, we have successfully tested our approach for a numerical example of a single Rydberg atom system. The transfer function estimated from the presented method is incorporated into an open-loop control optimization algorithm allowing for high-fidelity operations in quantum experiments.

This chapter has been published, with minor changes, as Juhi Singh, Robert Zeier, Tommaso Calarco, and Felix Motzoi, *Compensating for Nonlinear Distortions in Controlled Quantum Systems*, Physical Review Applied 19, 064067 (2023). The thesis author conducted all the analysis, composed all the figures and wrote the manuscript with input from the advisors.

4.1 Introduction

Over the last few decades, various quantum systems, including superconducting circuits, neutral atoms, trapped ions, and spins [7–9], have shown exciting progress in controlling quantum effects for applications in quantum sensors [213], simulators [194], and computers [214]. In these setups, quantum operations are implemented using external fields or pulses which are generated and influenced by several electronic and optical devices. For high-fidelity and uptime applications, this requires high performance of, e.g., population transfers and quantum gates, while suppressing interactions with the environment as well as decoherence. By shaping temporal and spatial profiles of external fields and pulses, the time-dependent system Hamiltonian steers the quantum dynamics towards the targeted outcome.

Experimental distortions of the applied pulses may reduce the effectiveness and robustness of the desired quantum operation [78, 215]. Methods have been developed to characterize distortions based on the impulse response or transfer function of the experimental system [78, 215–222]. These approaches for estimating field distortions work well for distortions with a linear transfer function. This work, however, addresses the more general case with substantial non-linear distortions originating from the experimental hardware.

The description of the distortions can be challenging without knowing the exact characteristics of the experimental hardware. Also, approximating a significant non-linearity using a linear model will result in model coefficients and control pulses that are not robust against experimental distortions and suffer from a loss in fidelity. To account for this problem, we introduce a mathematical model and an estimation method which rely on limited experimental data and can characterize the system behavior up to a non-linearity of finite order. To streamline our presentation, we focus on quadratic non-linearities, but more general non-linearities can be treated similarly. We illustrate our estimation approach with numerical data for a single-Rydberg atom excitation experiment in the presence of significant non-linearities and we highlight how our approach can calibrate for and suppress large distortions. We describe an effective approach for estimating the coefficients of this non-linear model and correct the pulses accordingly. We emphasize that our approach is independent of a specific experimental setup and can therefore be applied to various (spatially or temporally) field-tunable phenomena on different quantum platforms.

Our estimation method for distortions is particularly effective in combination with methods from quantum optimal control [23, 24, 196, 223, 224] and it yields optimized pulses for highly efficient gates while accounting for estimated distortions. To this end, we provide an analytical expression for estimating the Jacobian of the transfer function

for quadratic distortions, which can be further generalized to higher orders. We also validate this combined approach with our Rydberg atom excitation example. In the context of quantum control, any inaccuracy in the system Hamiltonian can severely affect the performance of pulses produced by optimal control. Given a reasonably accurate model, control fields might also suffer from discretization effects, electronic distortions, and bandwidth limitations (mostly assumed to be linear). Accounting for these distortions by including the linear transfer function within the dynamics, as well as its combined gradient, has been incorporated in related optimization work [78, 222, 225–227]. Another strategy for minimizing non-linear pulse distortions is to avoid high frequencies altogether in control pulses [228, 229].

Starting from initial applications [35, 36], optimal control methods have been extensively used in quantum computing, quantum simulation, and quantum information processing [23, 24, 27, 32–34]. Analytic results applicable to smaller quantum systems shape our understanding for the limits to population transfers and quantum gates (see [23, 24, 73, 97, 230–244] and references therein). Increasing the efficiency of quantum operations by numerically optimizing and fine-tuning control parameters can rely on open-loop or model-based optimal control methods [37, 40, 68, 78–82, 87, 88]. Our work on the estimation of distortions can be seen in the context of model-based approaches, which might rely on an accurate gradient calculation of the analytical cost function and thus on the knowledge of the Hamiltonian of the system [23, 78]. This knowledge might be available in naturally occurring qubits (such as atomic, molecular, or optical systems), but may also be estimated in engineered (solid-state) technologies. Similarly, closed-loop (i.e. adaptive feed-forward) control methods [27, 29, 38, 90, 91, 245–247] are used in situ to reduce adverse experimental effects on the control pulses, while direct (real-time) feedback and reservoir engineering methods can also be used where appropriate to counteract control uncertainties [248, 249].

This chapter is organized as follows: Section 4.2 sketches the control setup for optimizing quantum experiments and describes the conventional method for estimating the transfer function and its inclusion in the optimization. In Sec. 4.3, we detail our non-linear estimation method using non-linear kernels. We also describe how to derive the transformation matrix and its gradient. The non-linear effects on quantum operations are shown with a numerical example of Rydberg atom excitations in Sec. 4.4. We apply the estimation methodology to our numerical Rydberg example in Sec. 4.5 and discuss requirements on the available measurement data. Finally, we consider different numerical optimization methods in combination with our estimation method in Sec. 4.6 (see also Appendix 4.8) and conclude in Sec. 4.7. The raw data files from the simulations performed for this work are provided in [250].

4.2 Time-dependent control problems

We aim to efficiently transferring the population from an initial quantum state to a final target state. The evolving state of a quantum system is described by its density operator $\rho(t)$ and the corresponding equation of motion is written for coherent dynamics as

$$\dot{\rho} = -i[H(t), \rho] + \mathcal{L}(\rho). \tag{4.1}$$

The form of the Lindblad term $\mathcal{L}(\rho)$ is discussed in Sec. 4.4 while the Hamiltonian can be expressed as

$$H(t) = H_d + \sum_i u_i(t)\, H_i. \tag{4.2}$$

The free-evolution or drift component is given by H_d, while H_i denotes the control Hamiltonians which are multiplied with time-dependent control pulses $u_i(t)$. More precisely, our goal is to transfer a quantum system from a given initial pure state with density operator ρ_i to a target pure-state density operator ρ_t in time T by varying the control pulses $u_i(t)$ while minimizing the cost function

$$C = 1 - |\langle \rho_t | \rho(T) \rangle|^2 = 1 - |\mathrm{Tr}[\rho_t^\dagger \rho(T)]|^2, \tag{4.3}$$

where $\mathrm{Tr}(M)$ denotes the trace of a matrix M. This cost function measures the difference between the target-state density operator ρ_t and the final-state density operator $\rho(T)$. In this work, we employ gradient-based optimization methods, which are described and discussed in Section 4.6 and Appendix 4.8.

The experimental realization of control pulses $u_i(t)$ relies on several devices, which might introduce systematic distortions and reduce the overall control efficiency. It is our objective to determine these systematic distortions in order to adapt the control pulses during the optimization and counteract any adverse effects. For a linear distortion, we can calculate its transfer function

$$T(\omega) = \frac{Y(\omega)}{X(\omega)} \tag{4.4}$$

in the Fourier domain as the ratio of the Fourier transform of the input and output pulses $x(t)$ and $y(t)$, i.e. before and after the distortion has taken place. Alternatively, we can calculate the impulse response $\mathcal{I}(t)$ of the system which relates the input and output pulse in the time domain using the convolution

$$y(t) = (x * \mathcal{I})(t) = \int_{-\infty}^{\infty} x(\tau)\, \mathcal{I}(t-\tau) d\tau. \tag{4.5}$$

Figure 4.1 highlights that a linear model might not be sufficient for estimating ex-

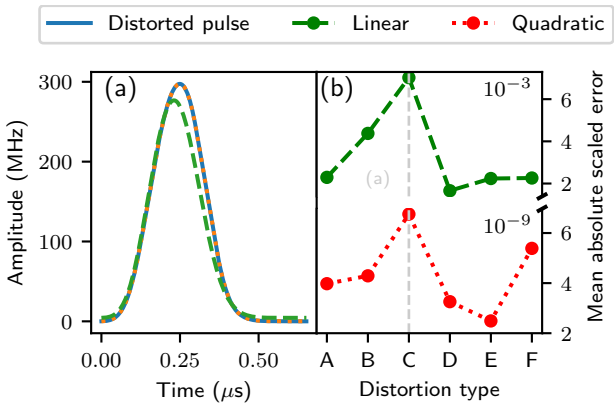

Figure 4.1: Quadratic estimation of distorted pulses [Eq. (4.7)] is preferable to linear estimation [Eq. (4.4)]: (a) A pulse is numerically distorted (solid line); later the distortion is estimated up to linear (dashed line) and quadratic terms (dotted line). The quadratic estimation better matches the actual distorted pulse when compared to the linear estimation. (b) Numerically computed errors for different types of distortions [including the distortion C plotted in (a)] generated by Eqs. (4.20)–(4.21) are plotted for both the linear and the quadratic estimation. The error is defined in Eq. (4.22) and describes the difference between the actual distorted and the estimated pulse.

perimental distortions as it cannot account for non-linear effects. Non-linear effects are demonstrated in Fig. 4.1(a) by passing one estimated example pulse through a numerically generated distortion [see Eqs. (4.20)–(4.21)]. When estimating the distortion coefficients using a linear model, the resulting distorted pulse does not match in Fig. 4.1(a) with the actual distorted pulse. However, the quadratic estimation with a non-linear model (as described in Sec. 4.3) precisely recovers the actual distorted pulse. Non-linear models are, e.g., preferable for Rydberg excitations which are detailed with realistic experimental parameters in Sec. 4.4.

4.3 Non-linear estimation method

We provide now a general approach for estimating non-linear distortions in a controlled quantum system and explain how this estimation approach can be incorporated into the synthesis of robust optimal control pulses.

4.3.1 Truncated Volterra series method

We characterize non-linear distortions using the truncated Volterra series method [251]. The Volterra series is a mathematical description of non-linear behaviors for a wide range of systems [252]. In analogy to Eq. (4.5), we can write the general form of the

Volterra series as

$$y(t) = h^{(0)} + \sum_{n=1}^{P} \int_a^b \dots \int_a^b h^{(n)}(\tau_1, \dots, \tau_n) \prod_{j=1}^{n} x(t-\tau_j) d\tau_j \tag{4.6}$$

where $x(t)$ is assumed to be zero for $t < 0$ as we consider general, non-periodic signals. The output function $y(t)$ can be expressed as a sum of the higher-order functionals of the input function $x(t)$ weighted by the corresponding Volterra kernels $h^{(n)}$. These kernels can be regarded as higher-order impulse responses of the system. The Volterra series in Eq. (4.6) is truncated to the order $P < \infty$ and it is called doubly finite if a and b are also finite. For a causal system, the output $y(t)$ can only depend on the input $x(t-\tau_j)$ for earlier times (i.e. $t \geq \tau_j$) which results in $a \geq 0$; recall that $x(t-\tau_j) = 0$ for $\tau_j > t$. The Volterra series can therefore also model memory effects (which are assumed to be of finite length) and it is not restricted to instantaneous effects.

The discretized form of the Volterra series truncated to second order (i.e. $P = 2$) is given by ([251, Eq. 2.25])

$$y_n = h^{(0)} + \sum_{j=0}^{R-1} h_j^{(1)}\, x_{n-j} + \sum_{k,\ell=0}^{R-1} h_{k\ell}^{(2)}\, x_{n-k}\, x_{n-\ell}, \tag{4.7}$$

The discrete output entries y_n have N time steps with $n \in \{0, \dots, N-1\}$ which are obtained from L discrete input entries x_q where $x_q = 0$ for $q < 0$. Note that $N = L + R - 1 \geq L$, where $R \geq 1$ denotes the assumed memory length of the distortion. The memory length R quantifies how the response at the current time step depends on the input of previous time steps, i.e., R bounds the number of previous time steps that can affect the current one. Volterra kernel coefficients of the zeroth, first, and second order are represented by $h^{(0)}$, $h_j^{(1)}$, and $h_{k\ell}^{(2)}$. The matrix given by $h_{k\ell}^{(2)}$ is symmetric. We are characterizing the transfer function by estimating the kernel coefficients in Eq. (4.7). The number M of the to-be-estimated coefficients scales quadratically with the memory length R (in general, the number of coefficients scales with R^P). Although the Volterra estimation can be extended to any higher order $P > 2$, we will focus in this work on the quadratic case.

For the estimation process, we assume that we are provided with a training data set consisting of input-output pulse pairs $(x(t), y(t))$ from an experimental device (or a sequence of devices) which causes the distortion. Next, we discuss how given the training data, we can estimate the kernel coefficients in Eq. (4.7) by minimizing some error measures (such as the mean square error) between the modeled output and the measured output.

4.3.2 Truncated Volterra series via least squares

We can choose from different methods to estimate the Volterra series. The most widely used ones are the crosscorrelation method of Lee and Schetzen [253] and the exact orthogonal method of Korenberg [254]. We choose the latter due to its simplicity and as it does not require an infinite-length input. We can write Eq. (4.7) as

$$y_n = \sum_{m=0}^{M-1} u_{nm}\, k_m \tag{4.8}$$

or equivalently as the matrix equation $Y = UK$ or

$$\begin{bmatrix} y_0 \\ y_1 \\ \vdots \\ y_{N-1} \end{bmatrix} = \begin{bmatrix} u_{00} & u_{01} & \cdots & u_{0,M-1} \\ u_{10} & u_{11} & \cdots & u_{1,M-1} \\ \vdots & \vdots & & \vdots \\ u_{N-1,0} & u_{N-1,1} & \cdots & u_{N-1,M-1} \end{bmatrix} \begin{bmatrix} k_0 \\ k_1 \\ \vdots \\ k_{M-1} \end{bmatrix}, \tag{4.9}$$

where K is defined in Eq. (4.11) below. We follow the convention that the entries of a given matrix (or vector) D are represented by d_{ij} (or d_i). Here, $n \in \{0, \ldots, N-1\}$ and $m \in \{0, \ldots, M-1\}$ where

$$M = 1+R+R(R+1)/2 \tag{4.10}$$

denotes the number of coefficients that need to be estimated to describe the quadratic Volterra series. In particular, u_{nm} are obtained from the input pulses via (recall again $x_q = 0$ for $q < 0$)

$$u_{nm} = \begin{cases} 1 & \text{for } \; m = 0, \\ x_{n-m+1} & \text{for } \; m \in \{1, \ldots, R\}, \\ x_{n-a}\, x_{n-b} & \text{for } \; m \in \{R+1, \ldots, M-1\}, \end{cases}$$

where (a, b) with $0 \le a \le b \le R-1$ is the $(m-R-1)$th element in the lexicographically ordered sequence from $(0, 0)$ to $(R-1, R-1)$. As the quadratic distortion coefficients $h^{(2)}_{k\ell}$ are symmetric, only the upper (or lower) triangular entries need to be considered. The column vector

$$K = [h^{(0)}, h^{(1)}_0, \ldots, h^{(1)}_{R-1}, h^{(2)}_{00}, \ldots, h^{(2)}_{R-1,R-1}]^T \tag{4.11}$$

consists of all the Volterra kernels, where $k_m = h^{(2)}_{ab}$ for $R+1 \le m \le M-1$ and (a, b) is chosen as above.

The example of $R = 2$, $L = 3$, $N = L + R - 1 = 4$, and $M = 6$ results in (with $x_q = 0$ for $q < 0$)

$$\begin{bmatrix} y_0 \\ y_1 \\ y_2 \\ y_3 \end{bmatrix} = \begin{bmatrix} 1 & x_0 & x_{-1} & x_0x_0 & x_0x_{-1} & x_{-1}x_{-1} \\ 1 & x_1 & x_0 & x_1x_1 & x_1x_0 & x_0x_0 \\ 1 & x_2 & x_1 & x_2x_2 & x_2x_1 & x_1x_1 \\ 1 & x_3 & x_2 & x_3x_3 & x_3x_2 & x_2x_2 \end{bmatrix} \begin{bmatrix} h^{(0)} \\ h_0^{(1)} \\ h_1^{(1)} \\ h_{00}^{(2)} \\ h_{01}^{(2)} \\ h_{11}^{(2)} \end{bmatrix}. \tag{4.12}$$

For the estimation of the distortions, we need to determine the values of K by solving the matrix equation (4.9) with the method of least squares. We assume now that the output data vector Y has been measured in an experimental setup. We can also concatenate multiple output pulses into a single vector to form Y, which allows us to perform the estimation using multiple short pulses with different characteristics as compared to a single long pulse. This provides the freedom of choosing the format for our training data while observing experimental constraints. In addition to taking a single long pulse or a set of short pulses, we can also repeatedly use the same set of pulses to reduce the measurement error.

As the matrix U contains higher-order terms of the input x_n, different columns of U are highly correlated with each other. This leads to the problem of solving a linear regression model with a correlated basis set, i.e., the input variables are dependent on each other. The precision of the estimation is adversely affected and less robust when naively applying the method of least squares to solve the matrix equation (4.9). We resolve this problem by first orthogonalizing the columns of the matrix U. The orthogonalization transforms the input variables (stacked in columns of U) such that they are independent of each other. After orthogonalizing U to V, Eq. (4.9) is transformed to

$$Y = VW. \tag{4.13}$$

Now we can solve the modified matrix equation (4.13) using the method of least squares to robustly obtain the values of the vector W. Finally, if the Gram-Schmidt method is used for orthogonalization, then one can convert W to K by recursive methods (as explained in [254]) to extract the Volterra kernels $h^{(0)}$, $h_j^{(1)}$, and $h_{k\ell}^{(2)}$. In this work, we use the QR factorization method which directly provides the values for K [255, 256].

4.3.3 Gradient of the input response function

Assuming that we have successfully estimated the transfer function, we want to include this information in our gradient-based optimization. This would allow us to also

go beyond the piecewise-constant control basis of GRAPE by including arbitrarily deformed controls, generalizing further along the lines of Ref. [78]. We provide now an analytic expression for the corresponding gradient (i.e. Jacobian) to build upon the earlier work discussed in Appendix 4.8.

We apply the commutativity of the convolution (i.e. $f*g = g*f$), e.g., by changing the integration variable from τ to $z = t - \tau$ in Eq. (4.5). Using a slight generalization, Eq. (4.7) can be rewritten as[1]

$$y_n = h^{(0)} + \sum_{j=0}^{L-1} h^{(1)}_{n-j}\, x_j + \sum_{k,\ell=0}^{L-1} h^{(2)}_{n-k,n-\ell}\, x_k\, x_\ell, \tag{4.14}$$

where the upper summation bound $L-1$ differs from $R-1$ in Eq. (4.7), i.e. integrating over the length of the input instead of the length of the kernel. From Eq. (4.14), we specify for each time step (indexed by n) a scalar $K^{(0)} = h^{(0)}$, a column vector $K^{(1)}_n$ with entries $[K^{(1)}_n]_j = h^{(1)}_{n-j}$, and a matrix $K^{(2)}_n$ with entries $[K^{(2)}_n]_{k\ell} = h^{(2)}_{n-k,n-\ell}$ for $j,k,\ell \in \{0,\ldots,L-1\}$. With this notation, we can write Eq. (4.14) as a matrix equation

$$y_n = K^{(0)} + X^T K^{(1)}_n + X^T K^{(2)}_n X, \tag{4.15}$$

where the column vector $X = (x_0,\ldots,x_{L-1})^T$ has length L. The corresponding partial derivatives are given by

$$\frac{\partial y_n}{\partial X} = K^{(1)}_n + X^T[K^{(2)}_n + (K^{(2)}_n)^T], \tag{4.16}$$

which simplifies for a symmetric quadratic kernel to

$$\frac{\partial y_n}{\partial X} = K^{(1)}_n + 2X^T K^{(2)}_n \tag{4.17}$$

We can calculate $\partial y_n/\partial X$ for all n and then determine the Jacobian. Eventually, the gradient of the cost function (4.3) is obtained using the chain rule as, e.g., in [78] and as discussed in Appendix 4.8.

4.4 Non-linear distortions during Rydberg excitations

We illustrate our scenario of non-linear distortions during controlled quantum dynamics with robust state-to-state transfers in a single Rydberg atom experiment. In recent years, Rydberg atoms have been proven to be a promising platform for quantum simulation [257] and quantum computation [104]. One of the most distinctive features of

[1] Note that using Eq. (4.14) for the estimation in Secs. 4.3.1-4.3.2 would require a number of coefficients given by $N \times M$ instead of only M and is therefore not recommended.

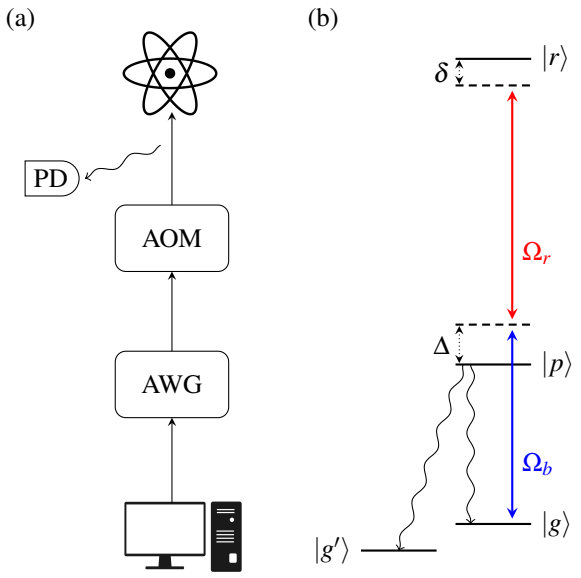

Figure 4.2: (a) Path of the input control pulse from the computer code via an arbitrary waveform generator (AWG) and an acousto-optic modulator (AOM) to the atom. Before the atom, the output control pulse can be measured using a photodiode (PD). (b) Energy diagram for the excitation of a single Rydberg atom (see text).

these atoms in quantum experiments is their strong and tunable dipole-dipole interactions [119, 258]. For larger Rydberg atom arrays as for quantum simulators, excitation protocols (and more general operations) from the ground state to the Rydberg state are crucial. We consider a gradient-based optimization of control pulses (without feedback) for tailored excitation pulses as outlined in Sec. 4.2, (see also Sec. 4.6 and Appendix 4.8).

The Lindblad master equation for the time evolution of the system is given by Eq. (4.1). Following [259], the model Hamiltonian for a single Rydberg atom is equal to

$$H(t) = \Omega_b(t)\frac{|g\rangle\langle p| + |p\rangle\langle g|}{2} + \Omega_r(t)\frac{|p\rangle\langle r| + |r\rangle\langle p|}{2} - \Delta\,|p\rangle\langle p| - \delta\,|r\rangle\langle r|\,. \tag{4.18}$$

The Rabi frequency $\Omega_b(t)$ of the blue laser excites the atom from the ground state $|g\rangle$ to the intermediate state $|p\rangle$ and the Rabi frequency $\Omega_r(t)$ excites the atom from $|p\rangle$ to the desired Rydberg state $|r\rangle$ (see Fig. 4.2(b)). In terms of Eq. (4.2), $\Omega_b(t)$ and $\Omega_r(t)$ constitute time-dependent control pulses (such as given by STIRAP [139]). Moreover, Δ and δ are the single-photon and the two-photon resonance detuning, which will be for simplicity assumed to be zero ($\Delta = 0$ MHz and $\delta = 0$ MHz). The Lindblad

operator [61] reads as [259]

$$\mathcal{L}(\rho) = \sum_{j\in\{d,g,g'\}} (V_j \rho V_j^\dagger) - \tfrac{1}{2}(V_j^\dagger V_j \rho + \rho V_j^\dagger V_j) \tag{4.19}$$

where $V_g = \sqrt{\Gamma_g}\,|g\rangle\langle p|$, $V_{g'} = \sqrt{\Gamma_{g'}}\,|g'\rangle\langle p|$, and $V_d = \sqrt{\Gamma_d}\,|r\rangle\langle r|$ are the Kraus operators. Here, $\Gamma_g = \Gamma/3$ and $\Gamma_{g'} = 2\Gamma/3$ denote the probability for spontaneous emission from $|p\rangle$ to the ground state $|g\rangle$ or to $|g'\rangle$ which represents all other ground-state sublevels. Realistic experimental parameters $\Gamma = 2\pi \times 1.41$ MHz and $\Gamma_d = 2\pi \times 0.043$ MHz have been provided by the Browaeys group, where Γ_d is the Doppler effect. In a real experiment, the gradients of the controls are restricted due to bandwidth limitations. In particular, the controls cannot have derivatives larger than a certain rise speed given by the experimental setup. In our simulations, we take realistic values for the rise times of $0.1\mu s$ and $0.15\mu s$ for the red and blue laser pulses respectively (which translate into rise speeds).

Let us now discuss how systematic distortions can be introduced in this experimental platform during the processing and forwarding of the control signals which finally act on the atom(s). The path of the control signals is sketched in Fig. 4.2(a). Starting from some computer program, the input pulse (modulated with a fixed carrier frequency) is passed through an arbitrary waveform generator (AWG) to produce the radio-frequency pulse. This pulse is then used as an input for an acousto-optic modulator (AOM) which modulates the intensity of a laser beam. The final laser pulse is then applied to the atom(s) to perform the excitation. The AOM can shape pulses using optical effects such as dispersion [260, 261]. In this experimental setup, one can measure the laser signal before it acts on the atom(s) using a photo diode. In summary, one can choose the input pulse and measure the output pulse; multiple measured input-output pulse pairs serve as training data, which is used to determine systematic distortions.

In our simulation, we excite the Rydberg atom using the system Hamiltonian from Eq. (4.18) by applying our optimized input control pulses. After that, we introduce quadratic distortions to the control pulses and repeat the simulation. The discrete linear and quadratic distortions are prepared from Gaussian distributions described by

$$h_1(t) = \frac{1}{\sigma\sqrt{2\pi}} \exp\left[-\tfrac{(t-\mu)^2}{2{\sigma_1}^2}\right], \tag{4.20}$$

$$h_2(t_1,t_2) = J \exp\left[-\frac{(t_1-\mu_1)^2 + (t_2-\mu_2)^2}{2{\sigma_2}^2}\right]. \tag{4.21}$$

The memory length of the discretized dimensionless distortion is R. For the distortions

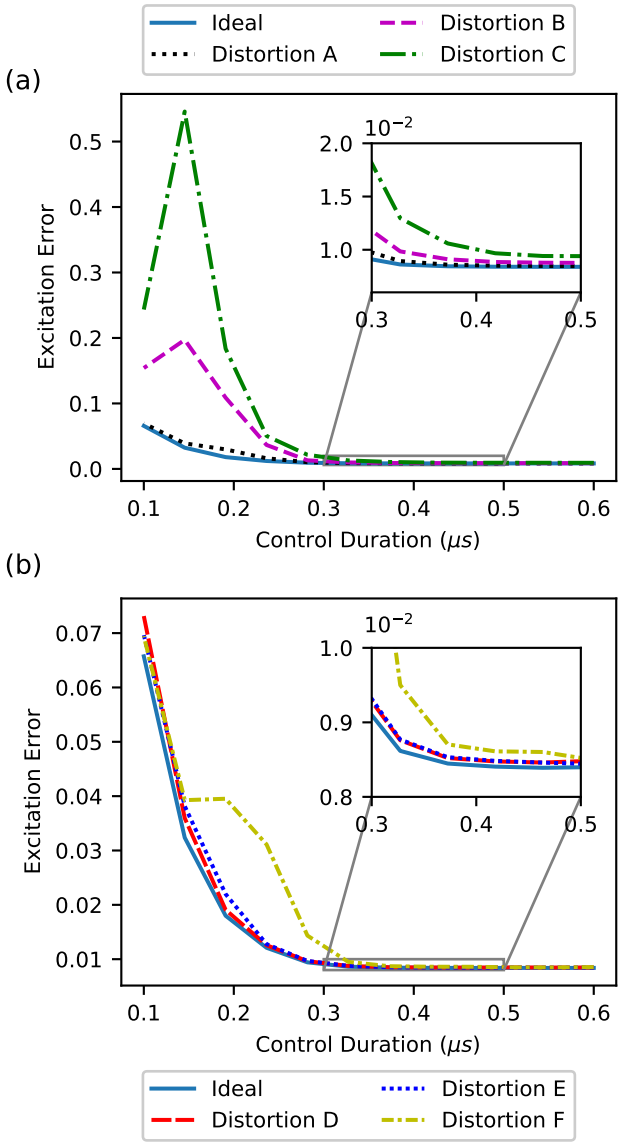

Figure 4.3: Reduced excitation efficiencies of optimized control pulses due to non-linear distortions in a simulated single Rydberg atom for distortions with (a) an increasing variance but constant memory length (A-C) and (b) a constant variance but increasing memory length (D-F); refer to Sec. 4.4.

A, B, and C, we have chosen $R = 50$, standard deviations σ_1 of 1, 6, and 11, and σ_2 of 4.25, 6.37, and 8.50. Similarly, for the distortions D, E, and F, we have varied R between 20, 40, and 60 while fixing $\sigma_1 = 1$ and $\sigma_2 = 4.25$. The amplitude term J has been kept constant at 5×10^{-6} in all cases. The example distortion C is shown in Figs. 4.4(a1) and 4.4(b1). Throughout this work, the zeroth order kernel is set to $h^0 = 0.1$.

We observe optimized controls with a simulated Rydberg excitation error in the range from 0.06 to 0.008 for different pulse lengths (see Fig. 4.3). As expected, longer total durations for the excitation lead to smaller simulated errors. But longer pulse durations might lead to further decoherence effects in the experimental implementation (particularly when combined with additional experimental steps). We, therefore, aim at reducing the length of the pulses (e.g. to a pulse duration around $0.3\mu s$) with reduced excitation errors. In Fig. 4.3(a), we notice a uniform increase in the error magnitude when we increase the standard deviation of the Gaussian kernels of Eqs. (4.20)-(4.21) for the distortions A to C. The distortions result in larger excitation errors for shorter control durations. The case of $0.1\mu s$ is however an exception, where the distorted pulse incidentally has a lower excitation error when compared with the duration of $0.15\mu s$. The standard deviation is kept constant in Fig. 4.3(b), but we increase the memory length for the distortions D to F which also results in a larger excitation error. Similar to Fig. 4.3(a), shorter pulses result in higher excitation errors in Fig. 4.3(b), where the excitation error for the distortion F for the durations $0.15\mu s$ and $0.2\mu s$ are coincidentally equal. The increased excitation errors suggest that optimized control pulses would be susceptible to distortions when applied in the Rydberg atom experiments (and particularly for short pulse lengths). In Sec. 4.5, we present estimation results building on Sec. 4.3 for the considered types of distortions.

4.5 Numerical estimation results

We report in this section on different simulated estimation results which describe the characteristics and precision of applying the Truncated Volterra series method while also comparing multiple types of input control pulses used in the estimation. We also perform the optimization for a single Rydberg excitation again by including the distortions in the algorithm. In each analysis, the estimated results are compared with the actual ones using the mean absolute scaled error (MASE) measure

$$\text{MASE} = \frac{1}{N}\sum_{i=1}^{N}\left|\frac{z_i^{\text{true}}}{\|z^{\text{true}}\|} - \frac{z_i^{\text{est}}}{\|z^{\text{est}}\|}\right| \tag{4.22}$$

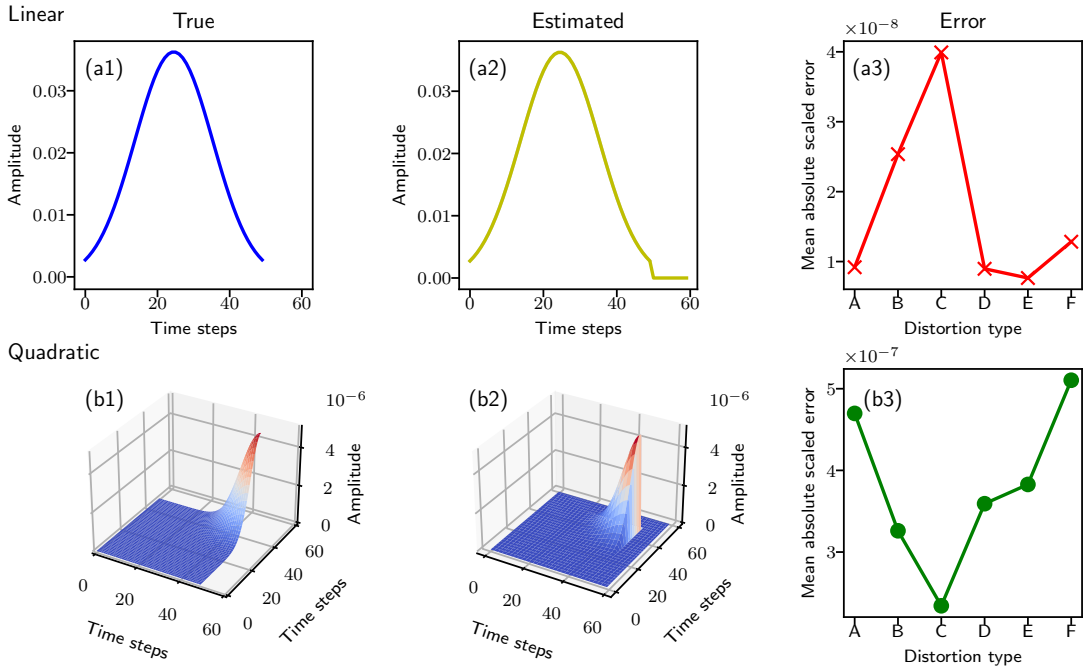

Figure 4.4: Estimation of both the linear and quadratic components for a non-linear distortion: (a) The linear component (a1) of the distortion C is compared with its estimated value (a2). The amplitude and time steps are dimensionless. (a3) The mean absolute scaled error [as defined in Eq. (4.22)] between the actual and the estimated values is calculated for various types of distortions A-F [see Eqs. (4.20)–(4.21)]. (b) Quadratic component similar as in (a).

where z^{true} is the actual value, z^{est} is the estimated value, and $\|z\|$ is the Frobenius norm of the observable z of length N. The MASE is numerically more stable compared to the mean relative error, which can be very large when the measured and the actual values are very small.

4.5.1 Estimation of distortions

We start with the results presented in Fig. 4.4 where numerical distortions are estimated by relying on a single randomly generated control pulse with 4000 time steps. We apply different distortions to the pulse and employ the resulting input-output pulse pairs in the estimation. In order to provide a more realistic analysis, we add an additional noise term to the output pulse

$$y_{\text{noise}} = y_{\text{output}} + \frac{1}{\sigma\sqrt{2\pi}} \exp\left[-\frac{(t-\mu)^2}{2\sigma^2}\right], \tag{4.23}$$

where the noise is drawn from a normal distribution with mean $\mu = 0$ and standard deviation $\sigma = 10^{-4}$. Figures 4.4(a1)-(b1) display the linear and quadratic contribution of the distortion C. The corresponding estimated contributions are shown in

Figs. 4.4(a2)-(b2) which match closely with values in Figs. 4.4(a1)-(b1). The results also emphasize that provided we can measure the output pulse accurately, we can calculate the memory length of the distortion (which is here $R = 50$) and redundant coefficients are automatically set to zero during the estimation for a sufficiently large R (here set to 60). The estimation process has been repeated for multiple distortions of type A to F and we observe in Figs. 4.4(a3)-(b3) low estimation errors of approximately 10^{-7} to 10^{-8}. Slight variations in the estimation error for different distortions could be attributed to the strength of the particular distortion or numerical noise.

We now also compare the estimation method of Sec. 4.3 with a linear estimation method in the time domain which relies on a linear impulse response [cf. Eq. (4.5)]. We omit here the very similar linear estimation in the frequency domain. We again use the distortion types A to F from Sec. 4.4 for this comparison and apply them again to a random-noise pulse of 4000 steps to obtain input-output pulse pairs for the estimation. Figure 4.1(a) shows the effect of the true and estimated distortion C when applied to an example pulse of $0.4\mu s$ duration. The example pulse is stretched under the distortion to a final duration of $0.65\mu s$. The linear estimation is considerably less precise when compared to the quadratic estimation. This effect is confirmed in Figure 4.1(b) which plots the estimation errors for the different distortion types A-F. Naturally, this also validates that the chosen distortion types contain some non-linearity which is not accounted for by a linear estimation.

4.5.2 Orthogonalization

One important step of the estimation method is orthogonalization and we have discussed its significance in Sec. 4.3. To further highlight the benefits of orthogonalizing the basis functionals, we test the estimation by directly solving the matrix equation

$$U^T Y = U^T U K, \tag{4.24}$$

where U is the matrix of the non-orthogonalized and correlated basis functionals, K is the to-be-estimated vector of linear or nonlinear kernel coefficients and Y is the measured output vector. We compare the results with coefficients we get from solving the matrix equation (4.13) with the orthogonalized basis set.

In this analysis, along with the benefit of orthogonalization, we also demonstrate how the estimation depends on the number M of the to-be-estimated coefficients for the distortion, the amount of training data, and the presence of noise in the output pulse. Figures 4.5(a)-(b) discuss the case without added noise. The nonlinear distortion with $\sigma_1 = 0.1, \sigma_2 = 0.42$ and $R = 5$ is estimated using spline input pulses as the training data. Each test and training pulse has 500 time steps and a unique frequency. For a

fixed number of spline pulses, we observe in Fig. 4.5(a) an increasing estimation error for an increasing number of coefficients M (or memory length R as $M \propto R^2$). For each M, we apply the estimation results on 50 different spline pulses which serve as test data. The corresponding mean error is plotted as a line and the 95% confidence interval is shown as a shaded region around the mean. In Fig. 4.5(b), we gradually increase the number of training pulses used in the estimation. For each fixed number of pulses, we perform the estimation on all the values of M as shown in Fig. 4.5(a). Hence each point in Fig. 4.5(b) is averaged over 500 results. In all cases, the estimation benefits from being performed with orthogonalization. Also, extending the amount of training data points by adding more spline pulses with different frequencies improves the estimation precision as seen in Fig. 4.5(b). For Figs. 4.5(c)-(d) in the presence of a noise term in the output pulse with a standard deviation of 10^{-9}, we observe higher estimation errors which need to be compensated with additional training data points. One can also reduce correlations present in the training data by considering a random input pulse as its autocorrelation is zero. However, even a completely random input pulse results in correlations in U from Eqs. (4.9) and (4.24) which contains various non-linear terms of the same input vector [251, p. 165]. In summary, Fig. 4.5 illustrates the positive effect of orthogonalization on the error rates in the estimation of the distortion.

4.5.3 Frequency requirements

We investigate different types of training data and their performance in the estimation following the setup of Fig. 4.6. We can order different training data types according to their increasing frequency content, with Gaussian pulses having the minimum frequency and random-noise pulses having the maximum. Here, the frequency content describes the spectral content of the training data while its value depends on the type of pulses used (see Fig. 4.5(b) and (d). There are different errors for spline and cosine pulses depending on the amount of data. For a fixed number of pulses, the estimation error grows with an increasing number of coefficients M [see Fig. 4.6(a)]. Gaussian input pulses are most strongly affected by this, while this effect is essentially negligible in the case of random-noise pulses. This illustrates the importance of spectrally rich input training pulses, which is further emphasized in Fig. 4.6(b) where the estimation error is plotted, relative to the frequency content. For different types of input pulses, the frequency content is increased differently: we add more pulses with different standard deviations for Gaussian pulses, we add more pulses with different frequencies for cosine pulses, we add more random knots to a single spline. Since a random-noise pulse has a very large bandwidth, we aim at increasing the frequency content by increasing

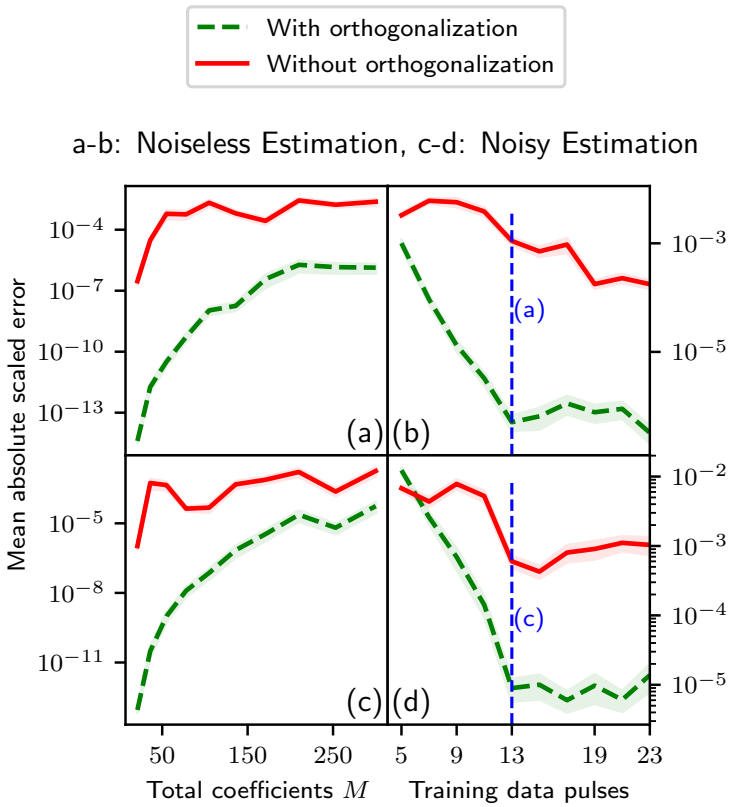

Figure 4.5: Comparison of the simulated estimation of non-linear distortions without and with orthogonalization solving respectively Eq. (4.24) and (4.13): (a) Using a fixed number of noiseless training data for spline input pulses, the relative error rises with an increasing number of coefficients M. The plotted line shows the mean error and the shaded area indicates the spread between the 95% confidence interval found from applying the estimation results to 50 different test pulses. Orthogonalization is advantageous for a larger number of coefficients. (b) Average estimation errors for different training data sets (see text) highlight the importance of increasing the frequency content of the available data. The averaging is performed over the full range of all number of coefficients M in (a). (c)-(d) As in (a)-(b), but the added noise in the output pulses of the data requires a higher frequency content for comparable error rates.

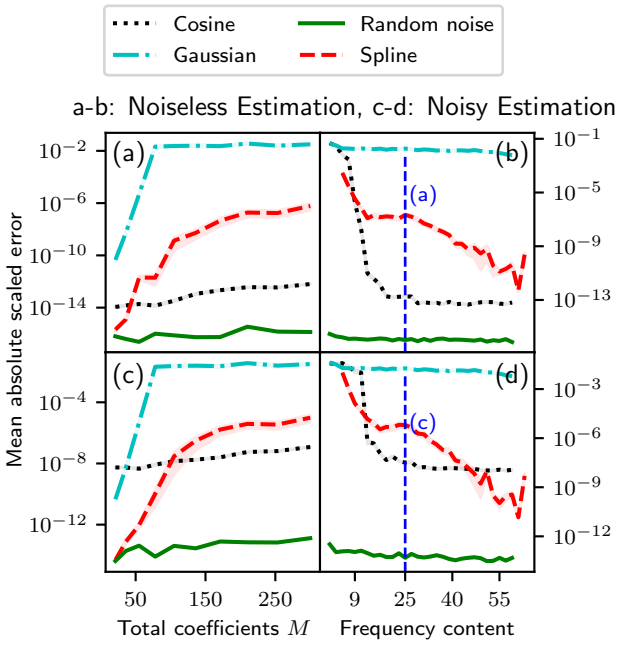

Figure 4.6: Simulated estimation errors of distortions with multiple types of data: (a) training data with more frequency content (such as random-noise pulses) perform better, even as the number of to-be-estimated coefficients M increases. (b) A lower error can be achieved by increasing the frequency content of the training data. For cosine and Gaussian pulses, the frequency content is increased by adding more pulses with different frequencies, whereas the number of knots is increased within a single pulse for splines. Spectrally rich random-noise pulses are highly effective while keeping the data requirements low. (c)-(d) Similar to (a) and (b), but noisy training data increases the overall error, while random-noise pulses are the most robust. The estimation setup is similar to Fig. 4.5.

the number of random-noise pulses which only slightly reduces the estimation error. Figure 4.6(b) highlights that the frequency content is crucial for the estimation and even a single random-noise pulse is highly effective due to its high-frequency content. Splines start to outperform the cosine pulses as soon as they attain higher frequency content than the latter. Similar conclusions hold under noise as shown in Fig. 4.6(c)-(d) while the overall estimation error increases for the different input pulse types when compared to the noiseless case. The data suggests that a high-frequency content in the training pulses might prevent overfitting noise, which is important when working with real experimental data. Also under noise, random-noise input pulses are most effective in the estimation due to their high frequency content.

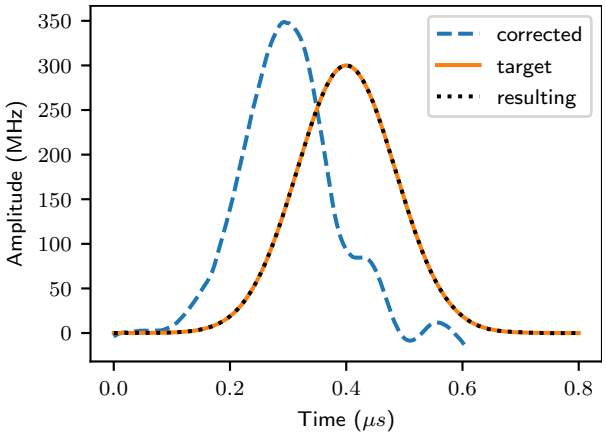

Figure 4.7: The estimated distortion can be inverted via Eq. (4.25) and applied to the ideal pulse to produce a pre-distorted pulse. The pre-distorted pulse produces the target Gaussian pulse shape after passing through distortion C.

4.5.4 Compensating for the distortion

With the help of the estimated linear or non-linear distortion coefficients, we compensate for the effect of the distortion on the pulses. One natural approach to find a pre-distorted input pulse shape is to apply the inverted distortion to the target pulse shape. In the case of a linear distortion $T(\omega)$, we would multiply $T^{-1}(\omega)$ with $X(\omega)$ [see Eq. (4.4)] and later transform it to the time domain. In the non-linear cases and for distortions expressed in time-domain kernels, we solve the following minimization problem to find the pre-distorted pulse

$$\text{argmin}_{x^{\text{input}}} \frac{1}{N} \sum_{i=1}^{N} \left| x_i^{\text{target}} - \mathcal{D}(x_i^{\text{input}}) \right|, \tag{4.25}$$

where $\mathcal{D}$ applies the distortion. As an example, we correct one analytical Gaussian pulse in order to compensate for the numerical distortion C (see Figure 4.7). The pre-distorted pulse constructed from the minimization problem produces the ideal Gaussian after passing through the distortion C. Next, we perform tests on more complex optimized pulses. As explained in Sec. 4.4 for the single Rydberg excitation, we have two pulses where the blue pulse $\Omega_b(t)$ excites the atom from the ground state $|g\rangle$ to the intermediate state $|p\rangle$ and the red pulse $\Omega_r(t)$ excites the atom from $|p\rangle$ to the desired Rydberg state $|r\rangle$ [see Fig. 4.2(b)]. Figure 4.8 shows pairs of these blue and red pulses as input pulses and the corresponding distorted output pairs. The input pulses in Figure 4.8(a) are the ideal optimized pulses and when we do not estimate and correct for the distortion, we receive the corresponding output pulses in the experiments.

Next, we estimate the distortion and construct the pre-distorted pulses using the

minimization scheme discussed in Eq. (4.25). The pre-distorted pulses and the corresponding outputs after passing through the distortion are shown in Figure 4.8(b). Unlike the analytical Gaussian pulse case (see Figure 4.7), we see that the input pre-distorted pulses do not completely reshape to the ideal optimized pulses after passing through the distortion. This suggests that for more complex pulse shapes, pre-distorting the pulse shape with this method is insufficient to reach a high excitation efficiency. However, we can include the estimated distortion in the optimization to produce pulse shapes that give minimum Rydberg excitation error in the presence of the distortion. The detailed discussion and results of this method are presented in Sec. 4.6. Figure 4.8(c) shows an example of input pulses produced from this method and the corresponding distorted output pulses. Note that the input-output pairs in Figure 4.8(a) and Figure 4.8(c) are quite similar. We expect this behavior since the excitation error from these example pulses of $0.4\mu s$ duration [see Fig. 4.9] is not much affected by the distortion. For shorter pulses, the optimization can however produce more complex pulses different from the ideal ones in order to compensate for the distortion. Therefore, we recommend to include the distortion in the optimization to compensate for the effect of the distortion as in Fig. 4.8(c) and Sec. 4.6, especially for complex pulse shapes.

4.6 Application in optimal control

Starting from early developments in the field, various theoretical and experimental aspects of quantum control have been discussed in the recent review [24]. The overall aim of quantum control is to shape a set of external field pulses that drive a quantum system and perform a given quantum process efficiently. While the analytical way of finding the control parameters works for special cases, one can use highly developed numerical tools in the context of optimal control theory. One solves the Schrödinger or master equation iteratively and produces pulse shapes that perform the desired time evolution. Quantum optimal control is broadly divided into at least the two categories of open-loop and closed-loop. Open-loop methods can be gradient-based or not. Open-loop control is based on the available information about the Hamiltonian of the system and hence it suffers when the system parameters are not completely known such as in the case of an engineered quantum system (such as solid state systems) or when the model cannot be solved precisely as in the case of many-body dynamics [262]. These limitations might be overcome by means of closed-loop optimal control where the control parameters are updated based on the earlier measurements results [29, 90]. Closed-loop quantum optimal control can be implemented via both gradient-based and gradient-free algorithms [263–265]. In some cases, hybrid approaches have also

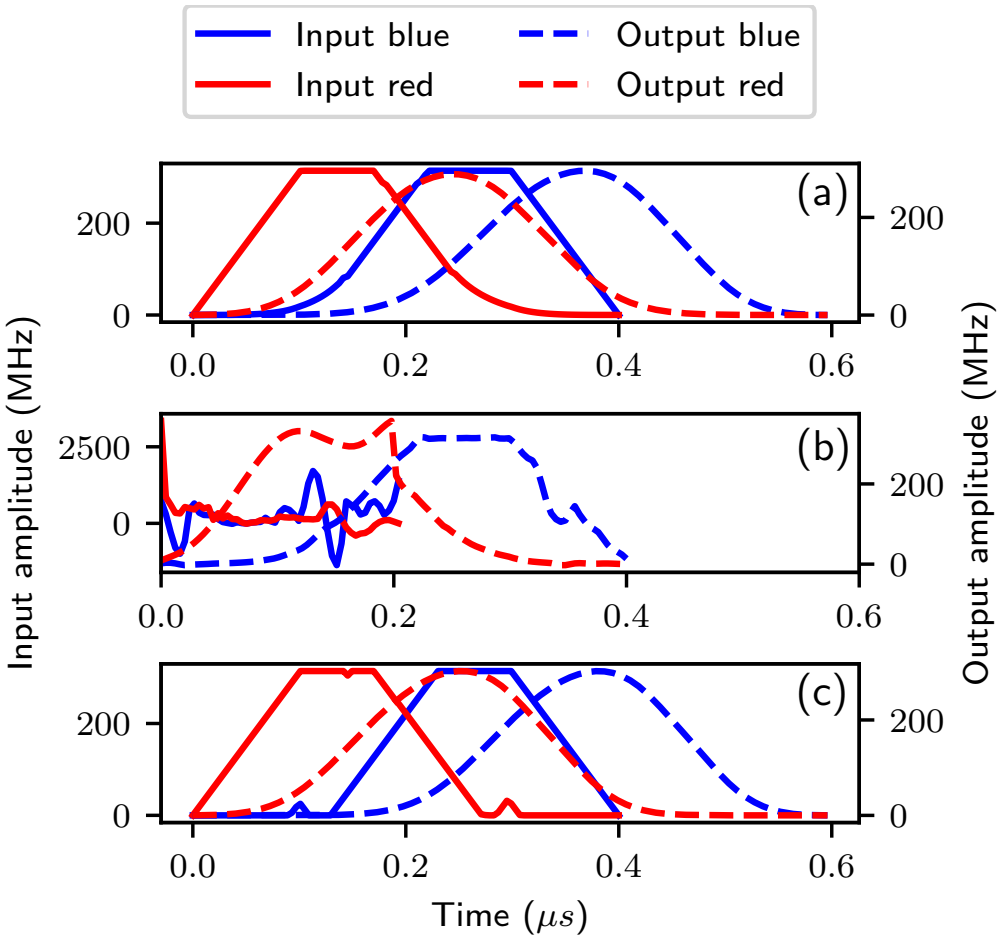

Figure 4.8: A set of pulses before and after passing through the numerical distortion C in the control chain for the single Rydberg atom excitation. The blue pulse $\Omega_b(t)$ excites the atom from the ground state $|g\rangle$ to the intermediate state $|p\rangle$ and the red pulse $\Omega_r(t)$ excites the atom from $|p\rangle$ to the desired Rydberg state $|r\rangle$ [see Fig. 4.2(b)] (a) Optimized input pulses and the corresponding outputs without correction for any distortion. (b) Pre-distorted pulses constructed from the distortion via Eq. (4.25) and the corresponding output pulses. The output pulses do not match the optimized input pulses from (a). (c) Instead of finding the pre-distorted pulses via Eq. (4.25), the distortion is included in the optimization to reach the minimum excitation error (see Sec. 4.6). Pulses from this optimization and the corresponding outputs are shown.

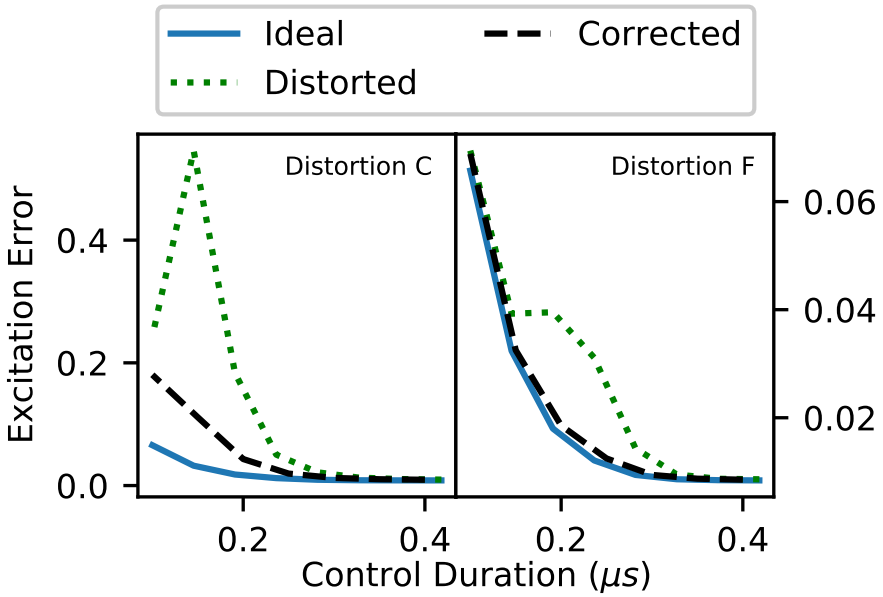

Figure 4.9: Reduced excitation errors after correcting for the distortion with a gradient-based optimization relying on the trust-region method. (a) distortion C: significant reduced errors, (d) distortion F: mostly recovers the ideal case.

been suggested [266]. But in the case where the system Hamiltonian is well known, open-loop control provides more freedom to precisely tune the controls depending on experimental constraints and generally explore a wider range of control solutions. Moreover, it also gives a better understanding of the system and works well with systems where fast measurements are not feasible or very noisy, in contrast to closed-loop methods which may require many measurements to converge.

To take full advantage of the open-loop control method and to provide more robust pulses, one can also characterize the experimental system completely or at least partially. Here, we highlight how the estimation method from Sec. 4.3 can be employed in an open-loop control setting to minimize the cost function C in Eq. (4.27) by relying on the corresponding gradients as computed via Eqs. (4.16) and (4.30). We refer to Appendix 4.8 for details. This compensates for distortions and decreases the error. Figure 4.9 shows test minimizations of the cost function using the trust-region constrained algorithm [267], which can perform constraint minimization with linear or non-linear constraints on the control pulses. Trust-region methods allow us to explicitly observe bandwidth limitations of the control hardware such as limited rise speeds as discussed in Sec. 4.4 by enforcing the corresponding pulse constraints. Since distortions C and F defined by Eqs. (4.20) and (4.21), have the strongest effects on the Rydberg excitation error (see Fig. 4.3), we correct the control pulses affected by them in the simulations. We limit our test to pulses with shorter durations ranging

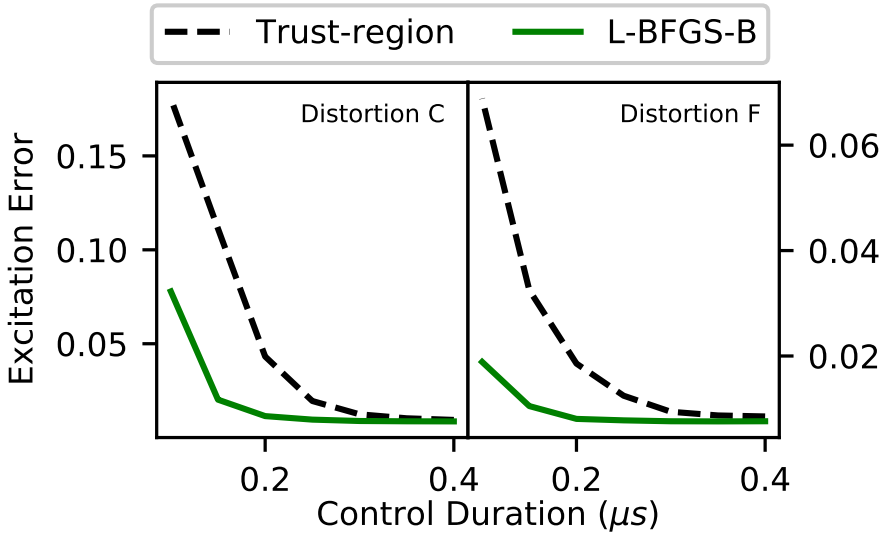

Figure 4.10: Reduced excitation error for L-BFGS-B when compared to the trust-region method, even though L-BFGS-B does not explicitly enforce constraints on the control pulses (such as limited rise speeds). But the correctly estimated transfer function will implicitly account for pulse constraints. Also, L-BFGS-B is more effective in the optimization.

from $0.1\mu s$ to $0.4\mu s$ as they are less susceptible to decoherence and hence might be more suitable for the excitation process. We compare the excitation error produced from the corrected pulse with the ideal and the distorted pulse excitation error. In particular, Figure 4.9 shows that the effect of the distortion C can be significantly reduced, but it cannot be completely corrected due to a large standard deviation and long memory length in the distortion. The distortion F has a small standard deviation combined with a long memory length which still produces strong effects on the control pulse but with a generally weaker distortion. In this case, the effect of the distortion can be almost completely corrected.

The estimation of transfer functions in order to correct for distortions has one additional benefit. The experimental hardware given by, e.g., AWGs and AOMs usually has bandwidth limitations which translate into limited rise speeds as discussed in Sec. 4.4. In the process of characterizing the experimental devices via their transfer function, we also estimate the effects of these bandwidth limitations. The estimated transfer function is then applied during the optimization, which mirrors the effects in the experimental platform and implicitly enforces limitations on the bandwidth or rise time. Assuming that the bandwidth-limiting effect of the estimated transfer function is pronounced enough, this allows us to use the limited memory Broyden–Fletcher–Goldfarb–Shanno (L-BFGS) algorithm to perform the minimization of the cost function [88]. L-BFGS usually offers a more efficient optimization but it can-

not explicitly account for general linear or non-linear constraints. In the corresponding optimizations, we only enforce simple box constraints to limit the amplitude of the controls while using the extended L-BFGS or L-BFGS-B algorithm [268]. The results are shown in Fig. 4.10 where L-BFGS-B improves the excitation efficiency more effectively than the trust-region method (which needs to also explicitly enforce the constraints on the rise speeds). In summary, combining the estimation of distortions with gradient-based optimizations can often effectively compensate for these non-linear distortions during an open-loop optimization.

4.7 Conclusion

We have proposed a method for estimating non-linear pulse distortions originating from experimental hardware. Hardware limitations affect the performance of optimal control pulses as highlighted using numerical data for single Rydberg atom excitations. In this case, the errors are increased for distorted control pulses beyond purely linear effects. We provide a general model for describing the complex characteristics of these non-linear effects. To incorporate estimated distortions into open-loop optimizations, we have detailed a formula to determine the Jacobian of the transfer function.

We tested and validated our proposed method by efficiently estimating different numerical quadratic distortions with varying strength and duration. We have also shown that linear estimation methods cannot effectively handle non-linear transfer functions. From our detailed analysis and tests, we deduce that the orthogonalization (as described in Sec. 4.5.2) is key for a robust estimation. A robust least-squares estimation is effective only after the orthogonalization is applied to the matrix containing the training data as its correlated columns would otherwise interfere with the estimation. Another critical requirement for effectively performing the estimation is training data with enough frequency content. Large frequency content such as in random-noise pulses better captures the non-linear features of transfer functions, particularly in the presence of measurement noise.

Since the estimation method is independent of any particular type of device characteristics, it can easily be adapted to a wide range of experimental platforms. Combining our estimation method with existing numerical optimization techniques can improve the quality and robustness of quantum operations. Our work thereby addresses a key challenge of enhancing the accuracy and robustness of experimental quantum technology platforms.

4.8 Appendix

We work with open-loop optimal control and detail how to incorporate the Jacobian of the transfer function which can be determined following Sec. 4.3.3. In the mathematical statement of an optimal control problem, the fidelity function C is minimized with regard to the control values u_i. We can apply the gradient-based optimization technique known as GRAPE [37] which can also utilize Newton or quasi-Newton (BFGS) methods [78, 88, 269]. We assume that the total control duration T is divided into L equal steps of duration $\Delta t = T/L$. During each time step, the control amplitudes u_i are constant. The time evolution of the quantum system during the jth time step is given by

$$U_j = \exp\left\{(-i\Delta t(H_0 + \sum_i u_i(j)H_i))\right\}. \tag{4.26}$$

The cost function can be written as

$$C = 1 - |\langle \rho_t | U_L \cdots U_1 \rho_i U_1^\dagger \cdots U_L^\dagger \rangle|^2. \tag{4.27}$$

From the inner product definition and invariance of the trace of a product under cyclic permutations of the factors, Eq. (4.27) can be rewritten as,

$$1 - |\underbrace{\langle U_{j+1}^\dagger \cdots U_L^\dagger \rho_t U_L \cdots U_{j+1}|}_{\lambda_j} \underbrace{U_j \cdots U_1 \rho_i U_1^\dagger \cdots U_j^\dagger \rangle}_{\rho_j}|^2. \tag{4.28}$$

Here, ρ_j denotes the density operator at the jth time step and ρ_t is the backward propagated target operator at the jth time step. If we perturb $u_i(j)$ to $u_i(j) + \delta u_i(j)$, the derivative of C is given in terms of the change in U_j to the first order in $\delta u_i(j)$ which is calculated by the Fréchet derivative method [270] using the Python package SciPy [271].

In order to minimize C, at every iteration of the algorithm, we update the controls by

$$u_i(j) \to u_i(j) - \epsilon \frac{\delta C}{\delta u_i(j)}, \tag{4.29}$$

where ϵ is a small unitless step matrix. Next, we follow the derivation in [78], where the product rule for gradient calculation is applied and one obtains

$$\frac{\delta C}{\delta u_i(j)} = \sum_{n=0}^{N-1} \frac{\delta s_k(n)}{\delta u_k(j)} \frac{\delta C}{\delta s_k(n)} \quad \text{where} \quad \frac{\delta s_k(n)}{\delta u_k(j)} = T_k(n, j). \tag{4.30}$$

Compared to (4.16), u_k corresponds to the input pulse x and s_n corresponds to the

output pulse y. Hence we can calculate each column of T_k from Eq. (4.16) as

$$T_k(n) = \frac{\delta y_n}{\delta X}, \tag{4.31}$$

and insert T_k into Eq. (4.30) to calculate the effective gradient.

5

Optimizing two-qubit fermionic gates

Ultracold atoms trapped in optical lattices have emerged as a scalable and promising platform for quantum simulation and computation. However, gate speeds remain a significant limitation for practical applications. In this work, we employ quantum optimal control to design fast, collision-based two-qubit gates within a superlattice based on a Fermi-Hubbard description, reaching errors in the range of 10^{-3} *for realistic parameters. Numerically optimizing the lattice depths and the scattering length, we effectively manipulate hopping and interaction strengths intrinsic to the Fermi-Hubbard model. Our results provide five times shorter gate durations by allowing for higher energy bands in the optimization, suggesting that standard modeling with a two-band Fermi-Hubbard model is insufficient for describing the dynamics of fast gates and we find that four to six bands are required. Additionally, we achieve non-adiabatic gates by employing time-dependent lattice depths rather than using only fixed depths. The optimized control pulses not only maintain high efficacy in the presence of laser intensity and phase noise but also result in negligible inter-well couplings.*

This chapter has been published as preprint, with minor changes, as Juhi Singh, Jan Reuter, Felix Motzoi, Tommaso Calarco, and Robert Zeier, *Optimizing two-qubit gates for ultracold atoms using Fermi-Hubbard models*, arXiv:2503.06768v2. The thesis author conducted most of the analysis, composed all the figures (with the exception of Fig. 5.3) and wrote the manuscript (with the exception of Sec. 5.2.1) with input from the advisors.

5.1 Introduction

After decades of research, many physical systems have been proven capable of serving as platform for quantum information processing, including superconducting circuits [7, 10, 11], trapped ions [8, 12, 13, 272], ultracold atoms [174, 273, 274], photons [275–278], defects in solids [279, 280], and quantum dots [281–283]. Among these promising systems, neutral atoms have emerged over the last decade as a leading platform for quantum simulation and computing [14–17]. These atoms are typically trapped in optical tweezers or lattices, allowing for the arrangement of hundreds of atoms in arbitrary geometries. Quantum information is generally encoded in the internal states of the atoms, with two-qubit gates utilizing atomic interactions [18, 19, 134, 284, 285]. These interactions can be short-ranged, such as van der Waals interactions [286], or have considerably longer ranges, such as dipole-dipole interactions [287]. One successful approach is excitation to Rydberg states, which facilitates strong and controllable interactions, enabling the study of many-body dynamics and the execution of quantum logic operations [288, 289].

An alternative approach to Rydberg atoms is to work with ground-state atoms trapped in optical lattices or superlattices [20, 21, 26, 159–164, 290, 291]. A superlattice is formed by superimposing at least two optical lattices with different wavelengths and has multiple double well structures [157, 178]. These systems naturally realize the Hubbard model [174, 292]. Neutral atoms in an optical lattice can be arranged in arbitrary configurations using efficient atom transport mechanisms [293–295]. The exchange of atoms and their entanglement is generated through controlled collisions between the atoms, enabling the implementation of essential quantum gates such as SWAP and $\sqrt{\text{SWAP}}$ [106, 161]. Combined with single-qubit rotations, these gates constitute a universal gate set for quantum simulation and computation [3, 177]. The collision interactions are tuned by adjusting the barrier height of the double well and its scattering length. To ensure that the system adheres to Hubbard-model dynamics, the exchange interactions must be controlled to prevent atom excitations [296, 297]. Most directly, this is achieved by adiabatically changing the barrier heights [177]. However, this approach results in slower gates which can reduce the coherence time and affect longer circuits in quantum simulation and computation.

Faster and more efficient gates can be achieved using optimal control methods, which have become an integral part of quantum computing, quantum simulation, and quantum information processing [23, 24, 27, 32, 33]. The efficiency of quantum operations is increased by shaping their driving fields using analytical and numerical techniques. Analytical methods are usually only applicable to smaller systems requiring a detailed understanding of their dynamics [28, 97, 230–235, 237, 240, 298],

while the results of [235, 236, 239, 241, 299] are relevant for the analytical aspects of our work. In contrast, numerical methods can often be implemented with partial (or no) knowledge of the system dynamics and they can depend on the system and rely on open-loop or closed-loop approaches (i.e. without or with feedback) [25, 29, 37–44, 68, 90, 91, 300, 301].

In this article, we use open-loop optimal control techniques to develop fast SWAP and $\sqrt{\text{SWAP}}$ gates for fermionic ^{6}Li atoms trapped in a superlattice. We describe our system with a Fermi-Hubbard model using realistic experimental parameters [157, 160, 178]. To this end, we optimize the lattice depths and s-wave scattering parameter to achieve high-fidelity state transfer from an initial state $\Psi_0 = |\uparrow\downarrow\rangle$ to target states $\Psi_{\text{SWAP}} = |\downarrow\uparrow\rangle$ and $\Psi_{\sqrt{\text{SWAP}}} := [(1+i)\,|\uparrow\downarrow\rangle - (1-i)\,|\downarrow\uparrow\rangle]/2$ and eventually find high-fidelity gates. Our study reveals that the two-band Fermi-Hubbard model is insufficient in explaining the dynamics of these fast gates (see Result 3).

The key idea of our fast gates is to extend the Fermi-Hubbard model to include the higher energy bands (see Sec. 5.4.1). We numerically demonstrate, using realistic experimental parameters that the control duration is as short as 0.08 ms for transferring the state Ψ_0 to Ψ_{SWAP} with fidelity 0.999, and 0.12 ms for transferring Ψ_0 to $\Psi_{\sqrt{\text{SWAP}}}$ with fidelity 0.995, which is five times shorter than typical experimental state transfer times [157, 178] (see Result 4). These fidelities can be further improved and we show that they are mainly limited by the available laser power. We also detail that these optimized controls are robust against intensity and phase noises and result in minimal inter-well tunneling (see Result 5), which enables improved coherence times of 460 Rabi oscillations compared to 33 Rabi oscillations in a recent experimental study [157]. Moreover, we analyze in Sec. 5.6 how our gates perform when they are applied to error states with three and four atoms in a double well, which provides a more complete understanding of the system dynamics under various experimentally possible scenarios. Lastly, in Sec. 5.8, we show that for fast gates, the initial states $|\uparrow\uparrow\rangle$ and $|\downarrow\downarrow\rangle$ can excite to higher levels, which can be minimized with a full gate optimization. The full gate optimization yields a SWAP gate with a fidelity of 0.997 in 0.10 ms and a $\sqrt{\text{SWAP}}$ gate with a fidelity of 0.993 for a gate duration of 0.16 ms (see Result 6).

Our results initially arise from analytical and numerical optimizations using a two-band Fermi-Hubbard model (see Results 1 and 2), where the gradients for the numerical optimization are computed based on a particularly effective spline-fit approach (see Sec. 5.3.2). For higher-band Fermi-Hubbard models, the spline-fit approach is not applicable in the presence of multiple hopping and interaction terms, and we instead develop an approach using an effective approximate analytical gradient in Appendix. 5.11.2. The performance of the different gradient approaches is compared in

Appendix 5.11.3. Thus our work combines faster, robust two-qubit gates for ultracold atoms under realistic experimental conditions with methodological advances.

The structure of the paper is as follows: In Sec. 5.2, we define the Hamiltonian for the superlattice potential, introduce the corresponding two-band Fermi-Hubbard model and explain the objective of the quantum control tasks. We then optimize the SWAP and $\sqrt{\text{SWAP}}$ gates using both analytical and numerical techniques in Sec. 5.3. In Sec. 5.4, we explore the impact of higher energy bands on the optimized fast gates and demonstrate the limitations of the two-band Fermi-Hubbard model. Next, in Sec. 5.5, we present the optimization of the SWAP and $\sqrt{\text{SWAP}}$ gates using the higher-band Fermi-Hubbard model. In Sec. 5.6, we investigate the dynamics of more than two atoms in a double well under the optimal control pulses, and analyze the robustness of the optimized control pulses in Sec. 5.7. We perform the full gate optimization to minimize the gate error for different basis states in Sec. 5.8. In Sec. 5.9, we discuss the effect of high interaction strength on $\sqrt{\text{SWAP}}$ transfer. Finally, we summarize our conclusions in Sec. 5.10. The raw data files from the simulations performed for this work are provided in Ref. [302].

5.2 Model and objective

5.2.1 Model

We consider a double well potential, barrier heights of which can be controlled dynamically [157, 178], as

$$\begin{aligned} V(\mathbf{r},t) =& V_s(t)\cos^2(k_s x+\varphi(t)) - V_\ell(t)\cos^2(k_\ell x) \\ & - V_y\cos^2(k_y y) - V_z\cos^2(k_z z) \end{aligned} \tag{5.1}$$

where $\mathbf{r} = (x, y, z)$. In the x direction, a superlattice or a double well potential [see Fig. 5.1] is created by standing waves from two tilted lasers with a short wavelength of λ_s=532 nm and two lasers with a long wavelength of λ_ℓ=1064 nm. The wave vectors of the lattice are then given by $k_b{=}2\pi/\lambda_b \sin(26.7°/2)$ with $b \in \{s, \ell\}$ where 26.7° is the angle between the tilted lasers constructing the lattice, chosen for the particular geometry of the experimental system [157]. Here, $V_s(t)$ and $V_\ell(t)$ respectively denote the tunable lattice depths for the short and long lattice, where the short lattice is blue detuned (repulsive) and the long lattice is red detuned (attractive). The tunable relative phase between the short and long lattice is given by $\varphi(t)$. We consider optical lattices with constant lattice depths $V_y = 45E_{ry}$ and $V_z = 45E_{rz}$ in the y and z direction, expressed in units of their respective recoil energies $E_{ry}{=}\hbar^2k_y^2/(2\mathfrak{m})$ and

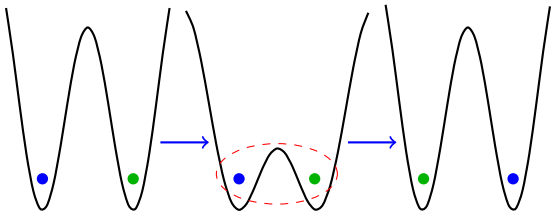

Figure 5.1: Collision gate in a double well. A double well is initialized with two ^{6}Li atoms, where the green one on the right is in the state $|\uparrow\rangle$ and the blue one on the left is in the state $|\downarrow\rangle$ which yields the state $|\uparrow\downarrow\rangle$. The barrier inside the double well is lowered in a controlled way to allow the two atoms to interact. This results in a SWAP or a $\sqrt{\text{SWAP}}$ gate between the two atoms. The SWAP gate exchanges the spins and prepares the state $|\downarrow\uparrow\rangle$, while the $\sqrt{\text{SWAP}}$ gate prepares the state $[(1+i)\,|\uparrow\downarrow\rangle - (1-i)\,|\downarrow\uparrow\rangle]/2$.

$E_{rz}=\hbar^2 k_z^2/(2\mathfrak{m})$. Following the experimental work of [157], we initialize the double well with two fermionic ^{6}Li atoms, where one atom is in the spin-up state and the other one in the spin-down state as shown in Fig. 5.1. We model the system of two atoms based on the Hamiltonian

$$H_1(\mathbf{r},t) = -\frac{\hbar^2}{2\mathfrak{m}}\nabla^2 + V(\mathbf{r},t), \tag{5.2}$$

$$H_2(\mathbf{r}_1,\mathbf{r}_2,t) = \sum_{j=1}^{2} H_1(\mathbf{r}_j,t) + U_{3\text{D}}(\mathbf{r}_1,\mathbf{r}_2), \tag{5.3}$$

where $\mathfrak{m}$ is the mass of the ^{6}Li atoms and H_1 is the single-atom Hamiltonian. Here, the pseudo interaction potential $U_{3\text{D}}(\mathbf{r}_1,\mathbf{r}_2)$ between the atoms is defined as

$$U_{3\text{D}}(\mathbf{r}_1,\mathbf{r}_2) = \frac{4\pi\hbar^2}{\mathfrak{m}} a\delta(\mathbf{r}_1-\mathbf{r}_2), \tag{5.4}$$

and a denotes the characteristic scattering length. In an experiment, a is tuned by changing the magnetic field, giving Feshbach resonances [303]. Since the optical potential of Eq. (5.1) separates into the three spatial components, one can independently solve them in the non-interacting case. Thus we can concentrate only on the x direction dependence of Eq. (5.2) and Eq. (5.3) for our calculations. For interacting particles, this argument holds approximately if one assumes that either the control pulses remain in the adiabatic regime (without excitations in the y and z directions) or the optical potential in the y and z directions is strong enough such that the interaction energy is low enough to not excite the atoms in those dimensions. A mixture of both assumptions is valid for our work. We write the single-atom Hamiltonian of

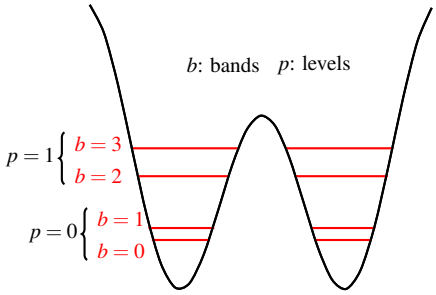

Figure 5.2: Level scheme of the multi-band Fermi-Hubbard model for one double well of the superlattice potential described by Eq. (5.1). The bands appear in pairs, with each pair corresponding to one level p of the model. For instance, four bands form two levels, where the zeroth ($b = 0$) and first ($b = 1$) bands form level $p = 0$, and the second ($b = 2$) and third ($b = 3$) bands form level $p = 1$.

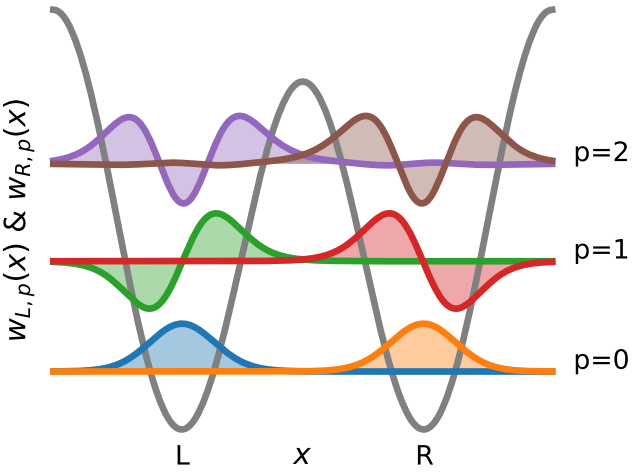

Figure 5.3: The Wannier states $w_{L,p}$ and $w_{R,p}$ in the left and the right bases of the first three levels $p = 0$, $p = 1$, and $p = 2$ for the corresponding optical potential in the x direction. Each level p is constructed by a linear combination of the two bands $b = 2p$ and $b = 2p + 1$ as shown also in Fig. 5.2.

Eq. (5.2) in Fourier space as

$$\tilde{H}_1(q) = \frac{\hbar^2}{2\mathfrak{m}} q^2 + \tilde{V}(q), \tag{5.5}$$

where $\tilde{V}(q)$ is the Fourier expansion of the lattice potential with quasi-momentum q. We assume a lattice with L sites and discretized values for the momenta $q = fk_s + k$ with $f \in \mathbb{Z}$, $k = k_s(2n+1-L)/2L$, and $n \in [0, L-1]$ in the first Brillouin zone.

From Bloch's theorem, the eigenfunctions of $\tilde{H}_1(q)$ can be written in the form

$$\Phi_{b,k}(x) = e^{ikx/\hbar}\, \phi_{b,k}(x)$$
$$\text{where } \phi_{b,k}(x) = \sum_m C_{m,b,k}\, e^{ifk_s x}.$$

Here, $C_{m,b,k}$ are coefficients obtained by solving for the eigenstates of Eq. (5.5), the index b denotes the band index, and $\phi_{b,k}(x)$ are periodic functions with periodicity $d = \lambda_\ell/2$, i.e., $\phi_{b,k}(x) = \phi_{b,k}(x+d)$. Bloch states $\Phi_{b,k}(x)$ are localized in momentum space, but completely delocalized in real space. Equivalently, we can define a set of basis states called Wannier states, which are localized in real space [169–171]. We choose the Wannier states as our basis in which the system is specified. This is motivated as we assume the wave function of the atoms to be localized on one side of the double well and close to the ground state of the optical lattice. Under these assumptions, the wave functions can be described with only a few Wannier states. We can calculate Wannier functions w_b based on the idea that these states are defined as the eigenstates of the position operator X such that

$$\mathrm{X}_b\, w_b(x-x_0) = x_0\, w_b(x-x_0).$$

For this, we write the position operator

$$\mathrm{X}_{b,k',k} = \int \Phi^*_{b,k'}(x)\, x\, \Phi_{b,k}(x)dx$$

in terms of the Bloch state basis $\Phi_{b,k}(x)$. The Wannier function $w_b(x-x_0)$ in band b at position $x - x_0$ in the x direction is defined as

$$w_b(x-x_0) = \frac{1}{\sqrt{L}} \sum_k e^{-i(kx_0+\chi_k)}\, \Phi_{b,k}(x)$$

with a momentum-dependent phase χ_k, which is given by the condition that the Wannier states are the eigenstates of the position operator X. Note that even if the Wannier states build an orthonormal basis, they are not the eigenstates of the Hamiltonian. Nevertheless, the stronger the optical potential gets, the flatter the bands become in k, and with that Wannier states match closer with the eigenstate of the Hamiltonian. For a double well system as shown in Fig. 5.2, one can always take a linear combination of two bands ($2p$ and $2p+1$) to construct the left w_L and right w_R basis states of the level p. For that, one only needs to apply the condition that the Wannier states w_L and w_R are still the eigenstates of the position operator X. Examples of Wannier states are shown in Fig. 5.3.

Instead of simulating the real-space Hamiltonian of Eq. (5.3), we can also describe fermionic atoms trapped in the optical lattices with the Fermi-Hubbard model [175, 176] as

$$\hat{H} = -J \sum_{i\neq j,\sigma} (c^\dagger_{i\sigma} c_{j\sigma} + h.c.) + U \sum_i \mathfrak{n}_{i\uparrow}\mathfrak{n}_{i\downarrow}, \tag{5.6}$$

Model	Gate	Fermi-Hubbard parameters	Experimental parameters
Two-band	SWAP	$J(t)$	$V_s(t)$, $V_\ell(t)$
	$\sqrt{\text{SWAP}}$	$J(t)$ U	$V_s(t)$, $V_\ell(t)$ a
Higher-band	SWAP	$J_p(t)$	$V_s(t)$, $V_\ell(t)$
	$\sqrt{\text{SWAP}}$	$J_p(t)$ $U^{\alpha\beta\gamma\delta}_{mnop}(t)$	$V_s(t)$, $V_\ell(t)$ a, $V_s(t)$, $V_\ell(t)$

Table 5.1: Different Fermi-Hubbard parameters and the corresponding tunable experimental parameters. There are two Fermi-Hubbard parameters: interaction strength U and hopping strength J. For the two-band Fermi-Hubbard model, J is time-dependently tuned using the lattice depths V_s and V_ℓ. Whereas, we assume that U is time-independent and tuned by the scattering length a. The conversion relations between the experimental parameters and the Fermi-Hubbard parameters are given by Eq. (5.8)-(5.9). For the higher-band model, we have multiple J_p for different p levels of the double well controlled by V_s and V_ℓ with Eq. (5.18). Similarly, we have multiple time-dependent $U^{\alpha\beta\gamma\delta}_{mnop}(t)$ tuned by a, V_s and V_ℓ with Eq. (5.19) as detailed in Sec. 5.4.1.

where the operator $c^\dagger_{i\sigma}$ (or $c_{i\sigma}$) creates (or annihilates) an atom in the spin state $\sigma \in \{\uparrow, \downarrow\}$ at the lattice site i. The operators $c^\dagger_{i\sigma}$ and $c_{j\sigma'}$ have anti-commutation relation as $\{c^\dagger_{i\sigma}, c_{j\sigma'}\} = \delta_{ij}\delta_{\sigma\sigma'}$, and $\mathfrak{n}_{i\sigma} = c^\dagger_{i\sigma}c_{i\sigma}$ is the number operator. The first term represents the hopping between site i and j of the lattice with amplitude J. The second term describes the interaction of strength U between two atoms of opposite spins, sitting on the same site i of the lattice. The model of Eq. (5.6) is sufficient to describe the atoms in the optical lattice with periodic single wells. However, for a superlattice with periodic double wells and relevant depth, the gap between the two lowest energy bands becomes very small inside each double well as shown in Figs. 5.1 and 5.2. Therefore, we extend the one-band Fermi-Hubbard model to a two-band model for describing the dynamics of the double well. We assume that all the higher bands ($b > 1$) as shown in Fig. 5.2 are still separated by a large energy gap and the two-band model sufficiently describes the system.

The two-band Fermi-Hubbard model for two atoms in a single double well [157, 178] is given by

$$\hat{H} = -J\sum_{\sigma}(c^\dagger_{L\sigma}c_{R\sigma} + h.c.) + U\sum_{\alpha=L,R}\mathfrak{n}_{\alpha\uparrow}\mathfrak{n}_{\alpha\downarrow}\,, \tag{5.7}$$

where $c^\dagger_{L\sigma}$ (or $c_{L\sigma}$) and $c^\dagger_{R\sigma}$ (or $c_{R\sigma}$) create (or annihilate) a fermion in spin state

$\sigma \in \{\uparrow, \downarrow\}$ on the left (L) or the right (R) side of the double well respectively. Equation (5.7) resembles Eq. (5.6) with the site index i replaced by the left (L) and right (R) side of the double well. The first term represents the hopping between the left and the right side of the double well with amplitude J. The second term describes the interaction of strength U between two atoms of opposite spins, sitting on the same side of the double well. Throughout the paper, we work with a symmetric double well, i.e. $\varphi(t)$=0 [see Eq. (5.1)]. Thus U is identical for the left and right wells. The gates are based on the hopping and the onsite interaction of the atoms in the double well, which are given by

$$J = -\int w_R(x) H_1(x) w_L(x) dx, \tag{5.8}$$

$$U = \iint U_{3D}(\mathbf{r}_1, \mathbf{r}_2)\, w_\alpha^2(\mathbf{r}_1)\, w_\alpha^2(\mathbf{r}_2)\, d\mathbf{r}_1\, d\mathbf{r}_2, \tag{5.9}$$

where U is assumed to be independent of $\alpha \in \{L, R\}$. The pseudo interaction potential $U_{3D}(\mathbf{r}_1, \mathbf{r}_2)$ is defined in Eq. (5.4) and $H_1(x)$ is the single-atom Hamiltonian from Eq. (5.2) in the x direction. The function $w_\alpha(\mathbf{r}) = w_\alpha(x)w_0(y)w_0(z)$ is the three-dimensional Wannier state, where $w_L(x)$ and $w_R(x)$ represent the states in the x direction on the left (L) and the right (R) side of the double well, respectively. The Wannier states of the lowest band in the y and the z direction are $w_0(y)$ and $w_0(z)$, respectively. As explained in Table 5.1, the hopping strength J is calculated from the time-dependent lattice depths $V_s(t)$ and $V_\ell(t)$. The onsite interaction U depends on the constant scattering length a, along with the lattice depths $V_s(t)$ and $V_\ell(t)$. In the two-band description, U is almost independent of the change in the long lattice depth V_ℓ and it increases with increasing short lattice depth V_s. However, U can be tuned over a much larger range by changing a, V_y, and V_z compared to changing V_s [167]. As a simplification, for the two-band model, we assume that the change in the onsite interaction depends only on the change in the s-wave scattering with tunable constant scattering length a. We can calculate $J(t)$ and U from the experimental parameters V_s, V_ℓ and a using Eqs. (5.8) and (5.9) respectively. However, the reverse calculation of the experimental parameters $V_s(t)$ and $V_\ell(t)$ from a given $J(t)$ is more problematic as explained in Sec. 5.3.2.

5.2.2 Objective

The two-qubit gates for the fermionic system in the superlattice can be represented using the spin non-conserving basis states $|\uparrow\uparrow\rangle$, $|\uparrow\downarrow\rangle$, $|\downarrow\uparrow\rangle$, and $|\downarrow\downarrow\rangle$, where each state represents atoms on the left (L) and the right (R) side of the double well [106, 177]. So, the state $|\uparrow\downarrow\rangle$ describes that the first atom in the left (L) well is in the spin-up

state and the second atom in the right (R) well observes a spin-down state. In this basis, the total spin of the system is not conserved. The SWAP and $\sqrt{\text{SWAP}}$ gates are represented in this basis as

$$\text{SWAP} = \begin{bmatrix} 1&0&0&0\\ 0&0&1&0\\ 0&1&0&0\\ 0&0&0&1 \end{bmatrix}, \quad \sqrt{\text{SWAP}} = \begin{bmatrix} 1&0&0&0\\ 0&(1+i)/2&(-1+i)/2&0\\ 0&(-1+i)/2&(1+i)/2&0\\ 0&0&0&1 \end{bmatrix}.$$

In the two-band Fermi-Hubbard model, two fermionic atoms with the spin up or down can only attain the state $|\uparrow\uparrow\rangle$ or $|\downarrow\downarrow\rangle$ respectively, and hence are fixed by Pauli's exclusion principle. Therefore, applying a SWAP or $\sqrt{\text{SWAP}}$ gate will not change their states. Therefore, we focus on the basis $|\uparrow\downarrow\rangle$ and $|\downarrow\uparrow\rangle$. From the symmetry of the Hamiltonian, SWAP or $\sqrt{\text{SWAP}}$ gate will perform the same operation on $|\uparrow\downarrow\rangle$ and $|\downarrow\uparrow\rangle$, which means any pulses transferring the state $|\uparrow\downarrow\rangle$ to $|\downarrow\uparrow\rangle$ will also transfer $|\downarrow\uparrow\rangle$ to $|\uparrow\downarrow\rangle$. Hence, it is sufficient to optimize the transfer of the state

$$\Psi_0 := |\uparrow\downarrow\rangle \quad \text{to} \quad \Psi_{\text{SWAP}} := |\downarrow\uparrow\rangle$$

using a time-dependent control $J(t)$ at $U = 0$ and later verify that this also transfers $|\downarrow\uparrow\rangle$ to $|\uparrow\downarrow\rangle$. Similarly, it is enough for the optimization of the $\sqrt{\text{SWAP}}$ gate to optimize the transfer of the state

$$\Psi_0 \quad \text{to} \quad \Psi_{\sqrt{\text{SWAP}}} := [(1+i)\,|\uparrow\downarrow\rangle - (1-i)\,|\downarrow\uparrow\rangle]/2$$

using $J(t)$ and the time-independent control U. Therefore, we only need to solve a state-to-state transfer problem for obtaining the SWAP and $\sqrt{\text{SWAP}}$ gates in the two-band Fermi-Hubbard model.

With one atom in the spin-up state and a second one in the spin-down state, we can have four possible states $|D0\rangle$, $|\uparrow\downarrow\rangle$, $|\downarrow\uparrow\rangle$, and $|0D\rangle$, where D denotes double occupancy on the left or the right side of the double well. The states $|D0\rangle$ and $|0D\rangle$ are out of our two-qubit computational basis. Hence, our goal is to minimize the probability that the states $|D0\rangle$ and $|0D\rangle$ are observed at the end of the SWAP or $\sqrt{\text{SWAP}}$ gates. Additionally, the double well can accommodate up to four fermionic atoms with two atoms in the spin-up state and two atoms in the spin-down state. One-atom states serve as single-qubit states. However, for two-qubit gates, states with three and four atoms are error states. Hence, we do not consider these error states in the optimization and only check the performance of our optimized pulses for these error states in Sec. 5.6.

5.3 Optimization with a two-band Fermi-Hubbard model

As explained in Sec. 5.2.2, we aim to optimize the transfer from Ψ_0 to Ψ_{SWAP} or $\Psi_{\sqrt{\text{SWAP}}}$ by minimizing the population of the state $|D0\rangle$ and $|0D\rangle$. First, we optimize the hopping parameter $J(t)$ for the SWAP gate using analytical methods. Later, we compare our results with the numerical optimization in Sec. 5.3.2.

5.3.1 Analytical optimization

In this section, we study the problem of finding the time-optimal pulse sequence to perform the SWAP gate. In particular, we find the minimum time for transferring the state $|\uparrow\downarrow\rangle$ to $|\downarrow\uparrow\rangle$ in the two-band Fermi-Hubbard model without any interaction, i.e., for $U = 0$. The interaction strength U can, in principle, be tuned to zero either by changing the internal atomic state to a non-interacting one or by tuning the magnetic field to set $a = 0$ [304, 305]. The time optimal pulse also transfers the state $|\downarrow\uparrow\rangle$ to $|\uparrow\downarrow\rangle$. Similar problems have been extensively studied in other systems [235, 236, 239, 241, 299]. The system Hamiltonian is given by

$$H'(t) = \begin{bmatrix} U & -J(t) & -J(t) & 0 \\ -J(t) & 0 & 0 & -J(t) \\ -J(t) & 0 & 0 & -J(t) \\ 0 & -J(t) & -J(t) & U \end{bmatrix} \tag{5.10}$$

in the basis corresponding to the basis states $|D0\rangle$, $|\uparrow\downarrow\rangle$, $|\downarrow\uparrow\rangle$, $|0D\rangle$. We switch to a new basis $(|D0\rangle + |0D\rangle)/\sqrt{2}$, $|\uparrow\downarrow\rangle$, $|\downarrow\uparrow\rangle$, $(|D0\rangle - |0D\rangle)/\sqrt{2}$ which allows us to neglect the state $(|D0\rangle - |0D\rangle)/\sqrt{2}$ (in our analytic optimization) as it does not couple with the other states. Therefore, the time-evolution with $\tilde{J}(t)=-\sqrt{2}J(t)$ and $U=0$ is

$$i \begin{pmatrix} \dot{x}_1 \\ \dot{x}_2 \\ \dot{x}_3 \end{pmatrix} = \begin{bmatrix} 0 & 0 & \tilde{J}(t) \\ 0 & 0 & \tilde{J}(t) \\ \tilde{J}(t) & \tilde{J}(t) & 0 \end{bmatrix} \begin{pmatrix} x_1 \\ x_2 \\ x_3 \end{pmatrix} \tag{5.11}$$

where x_1, x_2, and x_3 correspond to complex coefficients of the states $|\uparrow\downarrow\rangle$, $|\downarrow\uparrow\rangle$, and $(|D0\rangle + |0D\rangle)/\sqrt{2}$ respectively. Thus, optimizing the SWAP gate reduces to finding $\tilde{J}(t)$ for evolving the system from $(1,0,0)^T$ to $(0,1,0)^T$. In order to obtain the time-optimal solution, we follow the standard approach [235, 236, 239, 241, 299] which is based on solving suitable Euler-Lagrange equations. The calculation is detailed in Appendix 5.11.1 and shows that time-optimal $J(t)$ is a constant pulse. Other more

direct approaches might be applicable in this particular case, but the calculations in Appendix 5.11.1 also prepare the ground for future work to explore analytical solutions beyond the considered two-band Fermi-Hubbard model.

Result 1 *The time optimal SWAP gate in the two-band Fermi-Hubbard model without any interaction (i.e. $U = 0$) is given by a constant pulse $J(t) = J_{max}$, where J_{max} is the maximal experimentally possible hopping strength J. The minimum gate duration to transfer the state from $|\uparrow\downarrow\rangle$ to $-|\downarrow\uparrow\rangle$ or vice-versa is given by $T{=}\pi/(2J_{max})$. For $J_{max} = 34.03$ kHz, we get $T{=}\pi/(2J_{max}) = 0.046$ ms. The explicit form of the state evolution follows from Eq. (5.31).*

Remark 1 *The state $|\uparrow\downarrow\rangle$ can only be transformed into $-|\downarrow\uparrow\rangle$ using a real $J(t)$. The -1 phase of $|\downarrow\uparrow\rangle$ appears since the Hamiltonian is written using the spin-ordered convention where the creation operators are applied on the vacuum $|00\rangle$ in the order $c^\dagger_{R\downarrow}c^\dagger_{L\downarrow}c^\dagger_{R\uparrow}c^\dagger_{L\uparrow}$ and thus*

$$\text{SWAP}' = \begin{bmatrix} 1 & 0 & 0 & 0 \\ 0 & 0 & -1 & 0 \\ 0 & -1 & 0 & 0 \\ 0 & 0 & 0 & 1 \end{bmatrix}.$$

We can also write the Hamiltonian using the site-ordered convention where the creation operators are applied on the vacuum $|0\rangle$ in the order $c^\dagger_{R\downarrow}c^\dagger_{R\uparrow}c^\dagger_{L\downarrow}c^\dagger_{L\uparrow}$. The site-ordered convention gives the usual SWAP operation. One can apply the matrix $\text{diag}(1,-1,-1,1)$ *on* SWAP$'$ *to get* SWAP*, which requires a phase change conditional on the spin parity. Optimizations performed in this work uses the spin-ordered convention, but the results are easily adaptable to site-ordered convention. Therefore, we neglect the phase of the target states for our numerical optimizations.*

In the next section, we use a gradient-based numerical optimization to find the optimal $J(t)$ for the SWAP gate and compare it with the analytical result.

5.3.2 Numerical optimization

As explained in Sec. 5.2.1, the hopping parameter J is tuned by changing the lattice depths V_s and V_ℓ, while the interaction strength U is controlled by the constant scattering length a. The conversion relations between the experimental parameters and the Fermi-Hubbard parameters are given by Eqs. (5.8)-(5.9). To perform experiments with optimal control pulses, we need to convert the optimized J and U to the experimental parameters V_s, V_ℓ, and a. However, reconstructing V_s and V_ℓ from J is non-trivial and introduces noise. To test the reconstruction performance, we start with an initial set of V_s and V_ℓ [shown in Fig. 5.4(a)], expressed in units of their respective recoil energies $E_{rs}{=}\hbar^2k_s^2/(2\mathfrak{m})$ and $E_{r\ell}{=}\hbar^2k_\ell^2/(2\mathfrak{m})$. These lattice depths generate an exponentially changing J, as shown in Fig. 5.4(b). We then attempt to reconstruct the initial lattice

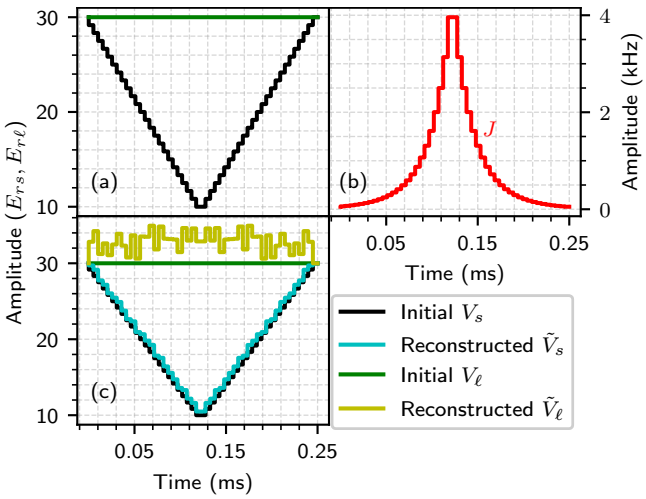

Figure 5.4: Relation between (a) lattice depths V_s and V_ℓ in their respective recoil energies $E_{rs(\ell)}{=}\hbar^2 k^2_{s(\ell)}/2m$ and (b) the corresponding hopping strength J via Eq. (5.8). (c) The non-recommended noisy reconstruction of V_s and V_ℓ from the hopping strength J in (b) significantly differs from their initial values in (a). This is avoided by directly optimizing V_s and V_ℓ as detailed in Sec. 5.3.2.

depths from J using a pre-stored data table of V_s, V_ℓ, and J. As shown in Fig. 5.4(c), the reconstructed long lattice depth $\tilde{V}_\ell$ does not match the initial V_ℓ, and the back conversion also introduces noise in the reconstructed short lattice depth $\tilde{V}_s$.

Remark 2 *Optimizing J and converting it back to lattice depths V_s and V_ℓ is not effective for obtaining smooth and realistic pulses. Therefore, for the remainder of this work, we directly optimize the experimental parameters V_s, V_ℓ, and a to achieve the optimized SWAP and $\sqrt{\text{SWAP}}$ gates.*

We can apply a gradient-based optimization technique known as GRAPE [37] which can also utilize Newton or quasi-Newton (BFGS) methods [41, 78, 268, 269, 306] and can include different transfer functions [307, 308] to optimize V_s and V_ℓ for the SWAP gate with $a = 0$. For the $\sqrt{\text{SWAP}}$ gate, we use the optimized V_s and V_ℓ from the SWAP gate and conduct a one-dimensional search with the target state $\Psi_{\sqrt{\text{SWAP}}}$ to identify the optimal scattering length a for the $\sqrt{\text{SWAP}}$ gate. Algorithm 1 briefly explains the optimization steps for the SWAP and $\sqrt{\text{SWAP}}$ gates for a two-band Fermi-Hubbard model.

We need to calculate gradients of the cost function with respect to V_s and V_ℓ for the gradient-based optimization of the SWAP gate. For this, we can express the Hamiltonian of Eq. (5.11) as a control Hamiltonian given by

$$H(t) = J(t)\, H_J, \tag{5.12}$$

where H_J is constant in time and $U = 0$ for the SWAP gate. Now, our goal is to

Algorithm 1: Optimization of the SWAP and $\sqrt{\text{SWAP}}$ gates using the two-band model

SWAP:
Input: $a = 0$
Optimization parameters: $V_s(t)$ and $V_\ell(t)$
Step 1: Define the SWAP-gate cost function $C_{\text{SWAP}} = 1 - |\langle\Psi_{\text{SWAP}}|\Psi(T)\rangle|^2$
Step 2: Minimize C_{SWAP} to find optimal V_s and V_ℓ using gradient-based optimization with the spline-fit method
Output: Optimized $V_s(t)$ and $V_\ell(t)$ for the SWAP gate

$\sqrt{\textbf{SWAP}}$:
Input: $V_s(t)$ and $V_\ell(t)$ from the SWAP gate
Optimization parameters: a
Step 1: Define the $\sqrt{\text{SWAP}}$-gate cost function $C_{\sqrt{\text{SWAP}}} = 1 - |\langle\Psi_{\sqrt{\text{SWAP}}}|\Psi(T)\rangle|^2$
Step 2: Perform a one-dimensional search to minimize $C_{\sqrt{\text{SWAP}}}$ and optimize a
Output: Optimized a for the $\sqrt{\text{SWAP}}$ gate

transfer a quantum system from the given initial pure state $\Psi_{\text{ini}} = \Psi_0$ to the target pure state $\Psi_{\text{tar}} = \Psi_{\text{SWAP}}$ in time T by varying the control pulse $J(t)$ while minimizing the cost function

$$C = 1 - |\langle\Psi_{\text{tar}}|\Psi(T)\rangle|^2. \tag{5.13}$$

We divide the total control duration T into N_T equal steps of duration $\Delta t = T/N_T$, which results in a piecewise constant $J(t)$. The time evolution of the quantum system during the jth time step is given by

$$\mathcal{U}_j = \exp[-i\Delta t J(j) H_J]. \tag{5.14}$$

The cost function (5.13) can be written as

$$C = 1 - |\langle\Psi_{\text{tar}}|\mathcal{U}_{N_T}\cdots\mathcal{U}_1|\Psi_{\text{ini}}\rangle|^2 \tag{5.15}$$

To minimize C, at every iteration of the algorithm, we update the controls by

$$J(j) \to J(j) - \mathfrak{e}\frac{\delta C}{\delta J(j)},$$

where $\mathfrak{e}$ is a small unitless step matrix.

Now, in our case, we perform a change of controls from the experimental parameters $V_k \in \{V_s, V_\ell\}$ to the Fermi-Hubbard parameter J, where V_k and J are piecewise constant with N_T time steps. Hence, we follow the derivation in [78], where the product rule is

applied to the gradient calculation and one obtains

$$\frac{\delta C}{\delta V_k(j)} = \sum_{s=1}^{N_T} \frac{\delta J(s)}{\delta V_k(j)} \frac{\delta C}{\delta J(s)}.$$

The derivative $\delta C/\delta J(s)$ is here calculated with the help of the Fréchet-derivative method [270] using the Python package SciPy [271]. We use a spline-fit method for calculating the Fermi-Hubbard parameter J and its gradient with respect to the lattice depths at each time step and every optimization iteration, i.e., $\delta J(s)/\delta V_k(j)$. For this, we create a grid of 100×100 pairs (V_s, V_ℓ), where V_s ranges from $2E_{rs}$ to $30E_{rs}$ and V_ℓ ranges from $30E_{r\ell}$ to $50E_{r\ell}$. We calculate and store the value of J for each point on the grid. Using the pre-stored data set of triples (V_s, V_ℓ, J), we fit a bivariate spline function of degree three using Scipy [271] and calculate the fit coefficients. Finally, we can calculate with these coefficients the values of J and $\delta J/\delta V_k$ at new values of $V_k \in \{V_s, V_\ell\}$ during the optimization. To obtain a good fit, we should have enough pre-stored data set of triples (V_s, V_ℓ, J), and we see that a grid of 100×100 is sufficient. As explained in Appendix 5.11.3, the spline-fit method is computationally efficient and enables faster optimization compared to calculating J and $\delta J/\delta V_k$ analytically or with the finite-difference method using Eq. (5.8).

We begin by optimizing the SWAP gate across multiple gate durations, ranging from 0.03 ms to 0.09 ms and each time step $\Delta t = 0.005$ ms. For a simple optimization example, we use a linearly decreasing V_s as an initial guess for the pulse sequence while keeping $V_\ell = 30E_{r\ell}$ constant. The bounds for V_s are fixed between $2E_{rs}$ and $30E_{rs}$. The scattering length a is set to zero for the SWAP gate. The numerical optimization imposes constraints on the start and the end of the pulses to ensure that it is experimentally feasible. These constraints, in turn, force the resulting hopping parameter $J_{\text{numerical}}$ to start and end at zero. Figure 5.5(a) illustrates the optimized SWAP gate error as a function of the gate duration. The infidelity decreases rapidly, becoming less than 10^{-8} for durations longer than 0.06 ms, which is close to the analytical quantum speed limit of 0.046 ms, calculated in the Appendix. 5.11.1. However, these additional constraints prevent the optimization from fully achieving the analytical quantum speed limit. Now, as explained in Sec. 5.2.2, for the two-band Fermi-Hubbard model, basis states $|\uparrow\uparrow\rangle$ and $|\downarrow\downarrow\rangle$ do not change under SWAP, and from the symmetry of the Hamiltonian in Eq. (5.11), we must reach the state $|\uparrow\downarrow\rangle$ from the initial state $|\downarrow\uparrow\rangle$. We verify this explicitly by calculating the full SWAP gate error as

$$C^F_{SWAP} = 1 - \frac{1}{N_i} \sum_{(\Psi_{\text{ini}}, \Psi_{\text{tar}})} |\langle \Psi_{\text{tar}} | \mathcal{U}_{N_T} \cdots \mathcal{U}_1 | \Psi_{\text{ini}} \rangle|^2, \tag{5.16}$$

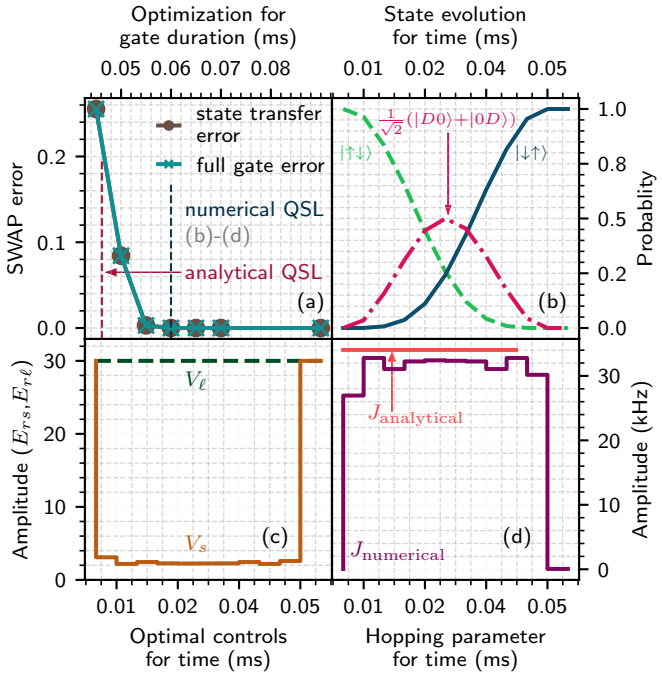

Figure 5.5: (a) The error of the SWAP gate is numerically minimized for different gate durations based on a Fermi-Hubbard model; the numerical quantum speed limit (QSL) of 0.06 ms is close to the analytical one from Sec. 5.3.1 with 0.046 ms. The full gate error defined by Eq. (5.16) matches the state transfer error defined by Eq. (5.13). (b) Corresponding state evolution of duration 0.06 ms from $|\uparrow\downarrow\rangle$ to $|\downarrow\uparrow\rangle$ with an intermediate state $(|D0\rangle + |0D\rangle)/\sqrt{2}$. The symmetry in the Hamiltonian of Eq. (5.11) also suggests that the same pulse will transfer the state $|\downarrow\uparrow\rangle$ to $|\uparrow\downarrow\rangle$. (c)-(d) Time dependence of the optimized lattice parameters V_s and V_ℓ and hopping parameter $J_{\text{numerical}}$; a minimum V_s results in a maximal $J_{\text{numerical}}$ having a similar form as $J_{\text{analytical}}$. The discrepancy between $J_{\text{numerical}}$ and $J_{\text{analytical}}$ results from the constraints included in the optimization.

where $(\Psi_{\text{ini}}, \Psi_{\text{tar}})$ denotes the N_i different possible tuples of initial and target states. For the SWAP gate with the two-band Fermi Hubbard model, we take two sets $\{|\uparrow\downarrow\rangle, |\downarrow\uparrow\rangle\}$ and $\{|\downarrow\uparrow\rangle, |\uparrow\downarrow\rangle\}$, an calculate the full SWAP gate error. We show that the full SWAP gate error matches exactly with the error of transferring the state from $|\uparrow\downarrow\rangle$ to $|\downarrow\uparrow\rangle$. The evolution of the three basis states is depicted in Figure 5.5(b). Starting from $|\uparrow\downarrow\rangle$, the system evolves into $|\downarrow\uparrow\rangle$, while the probability of the third state $(|D0\rangle + |0D\rangle)/\sqrt{2}$ peaks at half of the gate duration. The symmetry in the time evolution also suggests that the same pulse will transfer the state $|\downarrow\uparrow\rangle$ to $|\uparrow\downarrow\rangle$. The optimized pulses V_s and V_ℓ for the 0.06 ms gate duration are shown in Figure 5.5(c) where V_s approaches the minimum bound of $2E_{rs}$. Aside from the additional imposed bounds, $J_{\text{numerical}}$ attempts to reach the maximum $J = 34.03$ kHz and closely resembles $J_{\text{analytical}}$ as shown in Figure 5.5(d).

Result 2 *The shortest, numerically optimized SWAP gate has a duration of* 0.06 *ms with an upper bound of* $J_{max} = 34.03$ *kHz. The corresponding pulse resembles the analytical time-optimal pulse except for the additional constraints imposed in the numerical calculations, which forces* $J_{\text{numerical}}$ *to start and end at zero.*

5.4 Effect of higher bands and offsite terms

5.4.1 Hamiltonian description

As discussed in the previous section, atoms in the double well are described by the two-band Fermi-Hubbard model and characterized by the nearest-neighbor hopping J and the onsite interaction U. However, if the pulses are changed non-adiabatically, the atoms may be excited within the lattice, causing the two-band Fermi-Hubbard model to fail in accurately describing the system. In such cases, it is necessary to account for the higher bands of the Fermi-Hubbard model and the offsite interactions between atoms located on different sites in the double well. To incorporate these higher bands and offsite interactions, we generalize the two-band Hamiltonian as shown in Fig. 5.2. The bands appear in pairs, with each pair corresponding to one level p of the Fermi-Hubbard model so we have $M{=}b/2$ levels for b bands. For instance, four bands form two levels with $p \in \{0, 1\}$, where the zeroth $(b = 0)$ band and the first $(b = 1)$ band form the level $p = 0$, and the second $(b = 2)$ and the third $(b = 3)$ band form the level $p = 1$.

The extended higher-band Fermi-Hubbard Hamiltonian for a double well is given

by

$$\hat{H} = -\sum_{p}\sum_{\sigma} J_p(c^{\dagger}_{pL\sigma}c_{pR\sigma}+h.c.) \tag{5.17a}$$

$$+\sum_{m,n,o,p}\sum_{\alpha,\beta,\gamma,\delta} U^{\alpha\beta\gamma\delta}_{mnop}c^{\dagger}_{m\alpha\uparrow}c^{\dagger}_{n\beta\downarrow}c_{o\gamma\downarrow}c_{p\delta\uparrow} \tag{5.17b}$$

$$+\sum_{p}\sum_{\alpha}\sum_{\sigma}\epsilon_{p\alpha}\mathfrak{n}_{p\alpha\sigma}, \tag{5.17c}$$

where $\alpha,\beta,\gamma,\delta \in \{L,R\}$, $m,n,o,p \in \{1,\ldots,M\}$ and $\sigma \in \{\uparrow,\downarrow\}$. The term in Eq. (5.17a) describes hopping with amplitudes J_p for different levels p of the well, as illustrated in Fig. 5.6(a). Specifically, J_0 corresponds to the hopping term J in the two-band model. The hopping amplitude J_p is given by

$$J_p = -\int w_{pL}(x)\left[-\frac{\hbar^2}{2\mathfrak{m}}\partial_x^2 + V(x)\right] w_{pR}(x)\,dx. \tag{5.18}$$

The interaction strength $U^{\alpha\beta\gamma\delta}_{mnop}$ is calculated using the Wannier functions as follows:

$$U^{\alpha\beta\gamma\delta}_{mnop} = \iint U_{3\mathrm{D}} w^{\dagger}_{m\alpha}(\mathbf{r}_1) w^{\dagger}_{n\beta}(\mathbf{r}_2) w_{o\gamma}(\mathbf{r}_2) w_{p\delta}(\mathbf{r}_1) d\mathbf{r}_1 d\mathbf{r}_2, \tag{5.19}$$

where $U_{3\mathrm{D}} := U_{3\mathrm{D}}(\mathbf{r}_1,\mathbf{r}_2)$. Finally, the Hamiltonian includes an onsite energy term corresponding to the energies ϵ_{pj} in Eq. (5.17c), which are calculated from

$$\epsilon_{p\alpha} = \int w_{p\alpha}(x)\left[-\frac{\hbar^2}{2\mathfrak{m}}\partial_x^2 + V(x,t)\right] w_{p\alpha}(x)\,dx. \tag{5.20}$$

While the Wannier functions associated with different bands are orthonormal, resulting in zero overlap, the integral over four different Wannier functions used in Eq. (5.19) is not necessarily zero. However, the interaction strength $U^{\alpha\beta\gamma\delta}_{mnop}$, which is determined by the Wannier functions, is typically negligible when $m \neq n \neq o \neq p$. Thus we consider

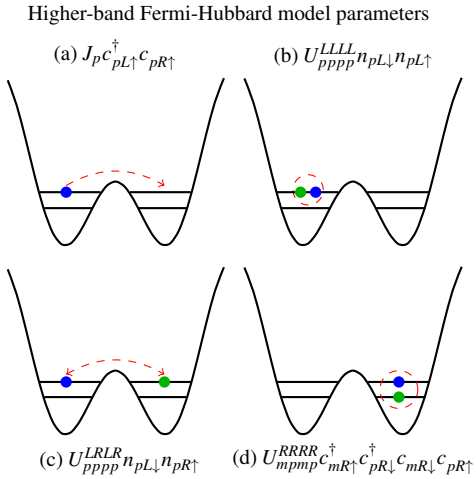

Figure 5.6: Different hopping and interaction processes in a symmetric double well for a Fermi-Hubbard model with higher bands. Each level p in the double well is made from two energy bands as shown in Fig. 5.2. (a) Single-atom hopping term [see Eq. (5.17a)] between wells for level p with hopping strength J_p calculated from Eq. (5.18). (b)-(d) Two atoms of opposite spin interact with strength $U^{\alpha\beta\gamma\delta}_{mnop}$ calculated from Eq. (5.19), where $\alpha, \beta, \gamma, \delta$ refer to the left (L) or the right (R) well and m, n, o, p denote different levels: (b) U^{LLLL}_{pppp} has two atoms on level p in the left (L) well [see Eq. (5.21a)] ; (c) U^{LRLR}_{pppp} has two atoms on level p in different wells [see Eq. (5.21b)]; (d) U^{RRRR}_{mpmp} has two atoms on different levels p, m but in the right (R) well [see Eq. (5.21c)].

just the following interaction terms from Eq. (5.17b) with significant contributions:

$$\hat{H}_{\text{int}} = \sum_p \sum_\alpha U^{\alpha\alpha\alpha\alpha}_{pppp} \mathfrak{n}_{p\alpha\downarrow} \mathfrak{n}_{p\alpha\uparrow} \tag{5.21a}$$

$$+ \sum_{p,m} \sum_{\alpha,\beta} \sum_\sigma U^{\beta\alpha\alpha\beta}_{mppm} \mathfrak{n}_{p\alpha\sigma} \mathfrak{n}_{m\beta(-\sigma)} \tag{5.21b}$$

$$+ \sum_{p,m} \sum_{\alpha,\beta} U^{\beta\alpha\alpha\beta}_{mpmp} c^\dagger_{m\beta\uparrow} c^\dagger_{p\alpha\downarrow} c_{m\beta\downarrow} c_{p\alpha\uparrow} \tag{5.21c}$$

$$+ \sum_{p,m} \sum_{\alpha,\beta} U^{\alpha\alpha\beta\beta}_{ppmm} c^\dagger_{p\alpha\uparrow} c^\dagger_{p\alpha\downarrow} c_{m\beta\downarrow} c_{m\beta\uparrow} \tag{5.21d}$$

$$+ \sum_p \sum_\alpha \sum_\sigma U^{\alpha\alpha LR}_{pppp} \mathfrak{n}_{p\alpha,-\sigma} \left(c^\dagger_{pL\sigma} c_{pR\sigma} + h.c.\right). \tag{5.21e}$$

Remark 3 *For the Eqs. (5.21b)-(5.21d), we only consider interaction terms such that the two atoms either have the same energy levels p and m or they sit on the same side α and β of the double well, i.e.,*

$$p = m \;\; \textit{if} \;\; \alpha \neq \beta \;\; \textit{and} \;\; \alpha = \beta \;\; \textit{if} \;\; p \neq m.$$

The interaction term in Eq. (5.21a) involves onsite interactions with strengths $U^{\alpha\alpha\alpha\alpha}_{pppp}$, corresponding to interactions at level p and side α, as shown in Fig. 5.6(b).

Additionally, during gate operations, the short lattice depth V_s decreases significantly, as depicted in Fig. 5.5(c). Consequently, the barrier between the double well becomes sufficiently small that atoms on either side or at different levels start to interact. This is represented by the offsite interaction term $\mathfrak{n}_{p\alpha\sigma}\mathfrak{n}_{m\beta(-\sigma)}$, proportional to $U^{\beta\alpha\alpha\beta}_{mppm}$, as described in Eq. (5.21b) and illustrated in Fig. 5.6(c). The term $c^\dagger_{m\beta\uparrow}c^\dagger_{p\alpha\downarrow}c_{m\beta\downarrow}c_{p\alpha\uparrow}$ in Eq. (5.21c) and Fig. 5.6(d) describes the spin exchange process with strength $U^{\beta\alpha\beta\alpha}_{mpmp}$ between two atoms at levels p and m and sides α and β. The term $c^\dagger_{p\alpha\uparrow}c^\dagger_{p\alpha\downarrow}c_{m\beta\downarrow}c_{m\beta\uparrow}$ in Eq. (5.21d) represents the correlated pair tunneling of two atoms within the double well.

Lastly, we have a correction term proportional to $\Delta J_{p\alpha} = U^{\alpha\alpha LR}_{pppp}$ in Eq. (5.21e) yields

$$\Delta J_{p\alpha} = \iint U_{3\mathrm{D}}\,|w_{p\alpha}(\mathbf{r}_1)|^2 w_{pL}(\mathbf{r}_2) w_{pR}(\mathbf{r}_1) d\mathbf{r}_1 d\mathbf{r}_2. \tag{5.22}$$

This term accounts for density-assisted hopping, which corrects the hopping parameter J_p when another atom of opposite spin is in the double well on side α.

5.4.2 Simulations

To study the effects of these new terms, we perform a time evolution of the system using the Hamiltonian in Eq. (5.17) with a non-adiabatic approach. Because the x direction terms of the potential in Eq. (5.1) change non-adiabatically while keeping the y and z direction terms constant, the Wannier functions in the x direction vary at each time step during the evolution. Consequently, after each unitary evolution at time step t, we compute the updated Wannier functions w_t, and transform the evolved state onto these new Wannier states. The non-adiabatic time evolution is described by

$$\Psi(t{+}1) = P(w_{t+1}, w_t)\, e^{-iH_t\delta t}\Psi(t). \tag{5.23}$$

Here, $P(w_{t+1}, w_t)$ denotes the basis transformation operator, which describes the non-adiabaticity of the time evolution by changing the basis of the state into the new Wannier basis states at every time step. Since calculating the Wannier functions as described in Sec. 5.2 is necessary to construct $P(w_{t+1}, w_t)$ for each time step, we cannot utilize the spline method employed in Sec. 5.3.2, and instead, we must directly compute the parameters J, U, ΔJ, and ϵ from Eqs. (5.18)-(5.20) for each time step.

We use this new simulation method to assess the validity of the two-band model. We simulate the four-band and six-band Fermi-Hubbard model using the pulses optimized from the two-band model. We optimize the SWAP gate for various durations ranging from 0.05 ms to 0.35 ms within the two-band Fermi-Hubbard model [see Sec. 5.3.2]. Figure 5.7(a) presents the infidelities for the two-band model at different

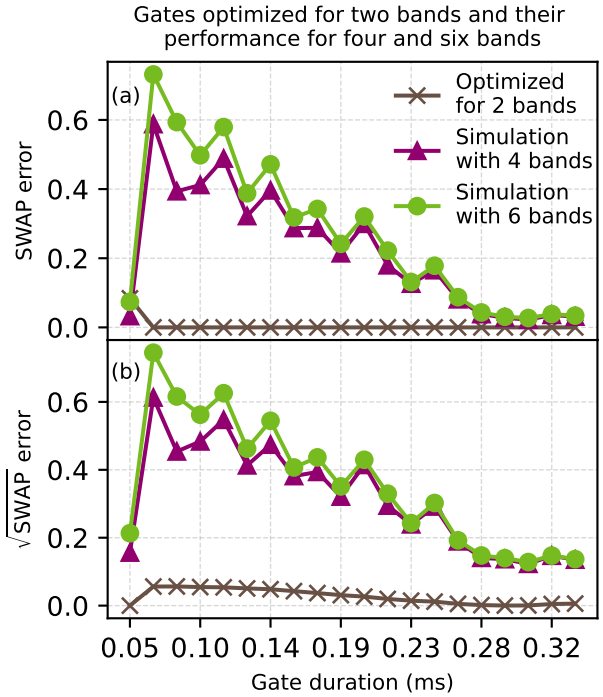

Figure 5.7: The SWAP and $\sqrt{\text{SWAP}}$ gates have been numerically optimized using a two-band Fermi-Hubbard model for different gate durations as in Fig. 5.5(a). Their performance is compared to Fermi-Hubbard simulations with four and six bands. (a) For SWAP, we see much higher gate errors for four and six bands as compared to two bands for gate durations of less than 0.28 ms while (b) high gate errors are observed for $\sqrt{\text{SWAP}}$ with four and six bands and all gate durations.

gate durations. It is evident that high-fidelity gates can be achieved for very short gate durations using the two-band model. We then apply these optimized control pulses to simulate the four-band and six-band models. As shown in Fig. 5.7(a), the simulations with higher bands exhibit significant deviations from the two-band results, with the discrepancies increasing for shorter gate durations.

We conduct a similar analysis for the $\sqrt{\text{SWAP}}$ gate, as shown in Fig. 5.7(b). Here, we use the optimized time-dependent lattice depths V_s and V_ℓ from the SWAP gate optimizations and optimize only the time-independent scattering length a using the two-band model. The interaction strength U is calculated from a using Eq. (5.9). Figure 5.7(b) shows that, similar to the SWAP gate, very low infidelities for the $\sqrt{\text{SWAP}}$ gate can be achieved using the two-band Fermi-Hubbard model. Next, we simulate the four-band and six-band models using the optimal controls from the two-band model. For short gate durations, we again observe significant divergence of the higher-band simulations from the two-band model results [see Fig. 5.7(b)]. However, unlike the SWAP gate, the higher-band simulations fail to match the two-band results even for longer gate durations in the case of the $\sqrt{\text{SWAP}}$ gate. This discrepancy is likely due to the additional off-site interactions present in the higher-band model [see Eq. (5.17)],

Algorithm 2: Optimization of the SWAP and $\sqrt{\text{SWAP}}$ gates with higher-band models

SWAP: Same as in the SWAP optimization in Algorithm 1. Instead of the spline-fit method,
a combination of approximate analytical and finite-difference gradients is used.

$\sqrt{\text{SWAP}}$:
Optimization parameters: $V_s(t), V_\ell(t)$, and a
Step 1: Define the $\sqrt{\text{SWAP}}$-gate cost function $C_{\sqrt{\text{SWAP}}} = 1 - |\langle \Psi_{\sqrt{\text{SWAP}}} | \Psi(T) \rangle|^2$
Step 2: Minimize $C_{\sqrt{\text{SWAP}}}$ and optimize $V_s(t)$ and $V_\ell(t)$ using a gradient-based optimization
Step 3: Perform a one-dimensional search to find the optimized a for $C_{\sqrt{\text{SWAP}}}$
Output: Optimized $V_s(t), V_\ell(t)$, and a for $\sqrt{\text{SWAP}}$

whereas the two-band model includes only onsite interactions. Furthermore, in the two-band model, the Wannier states used in Eq. (5.9) are computed at the start of the time evolution and are assumed to remain constant throughout. This assumption holds for an adiabatic time evolution, where the initially calculated Wannier states are eigenstates of the Hamiltonian at all times. However, for fast gates with non-adiabatic changes in lattice depths, the Wannier states $w_{pL}(t)$ and $w_{pR}(t)$ vary during the evolution. This variation introduces additional errors in the gate fidelity, which are accounted for in the higher-band simulations through the basis transformation operators in Eq. (5.23).

Result 3 *Simulations in higher-band Fermi-Hubbard models of pulses optimize using a two-band model show significantly higher errors for the SWAP and $\sqrt{\text{SWAP}}$ gates. This suggests that for non-adiabatic gate operations, the two-band model is not sufficient and optimizations using higher-band Fermi-Hubbard models are essential.*

5.5 Optimization with higher-band Fermi-Hubbard model

We showed in Sec. 5.4 that the optimization with a two-band Fermi-Hubbard model is insufficient in describing the fast SWAP and $\sqrt{\text{SWAP}}$ gates. To better capture the behavior of the system and generate efficient gates, we must include higher bands of the model into our optimization. In analogy to the two-band model, we optimize the SWAP and $\sqrt{\text{SWAP}}$ gates using gradient-based methods with a higher-band Fermi-Hubbard model. We use our non-adiabatic simulation method described in Sec. 5.4.2. We optimize V_s and V_ℓ for the SWAP gate with the scattering length $a = 0$. In contrast to the two-band model, where the $\sqrt{\text{SWAP}}$ gate is controlled by the lattice

depths V_s and V_ℓ from the SWAP gate optimization, we independently optimize V_s and V_ℓ for the target state $\Psi_{\sqrt{\text{SWAP}}}$ and then perform a one-dimensional search to find the optimal a. This is described in the Algorithm 2. For the two-band model in Sec. 5.3.2, we calculate the gradient of the cost function C with respect to V_s and V_ℓ using spline-fit method whereas the gradient for the one-dimensional search is trivial and easily computed using finite-differences. However for the higher-band model, in the absence of a spline-fitting approach, the gradients dC/dV_s and dC/dV_ℓ can be computed either analytically or through finite-differences. In Appendix 5.11.2, we derive an approximate analytical expression for the gradient that is considerably faster than the finite-difference method as shown in Appendix 5.11.3. This approximation allows for an accelerated optimization process. Subsequently, we can employ the finite-difference method to refine the optimization, enabling convergence to the minimum of the cost function.

5.5.1 State-to-state transfer optimization

First, we optimize the transfer from the initial state Ψ_0 to the target state Ψ_{SWAP}, for different gate durations using the four-band Fermi-Hubbard model. We try to find the optimal V_s and V_ℓ for variable gate durations from 0.06 ms to 0.20 ms. We constrain the optimization with bounds on V_s and V_ℓ given by the pairs (0.1 E_{rs}, 45 E_{rs}) and (7 $E_{r\ell}$, 35 $E_{r\ell}$) respectively. The optimized SWAP infidelities are presented in Fig. 5.8(a) where the error is less than 0.001 for gate durations larger than 0.08 ms. We emphasize that compared to the four-band simulation in Fig. 5.7(a), we achieve a significantly lower infidelity after optimizing for the four-band model with similar gate durations. The improvement in fidelity comes from the enhanced controllability by including the higher bands with multiple hopping parameters. To validate the four-band model, we simulate the system with six bands using the optimized controls from the four-band optimization. The gate error in the six-band model shows negligible deviation from the error in the four-band model [see Fig. 5.8(a)]. Specifically, the error in the six-band simulation is less than 0.001 for gate durations greater than 0.1 ms. This result suggests that excitations beyond four bands are negligible, indicating that the four-band Fermi-Hubbard model is sufficient to capture most the dynamics of the double-well system under the SWAP gate. We also examine the effect of the upper bound of the long lattice depth V_ℓ on the gate fidelity. The SWAP gate is optimized for upper bounds given by 30, 40, and 50 times the value of $E_{r\ell}$, and the resulting infidelities are shown in Fig. 5.8(b) on a logarithmic scale. We observe that gate fidelity improves with a higher upper bound on V_ℓ, as increased V_ℓ leads to more localized Wannier states and enhances the hopping strength J.

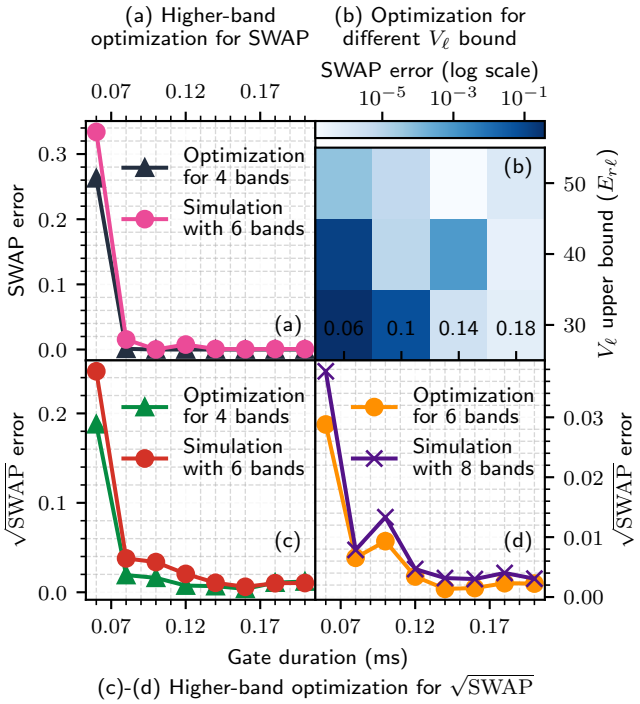

Figure 5.8: Higher-band Fermi-Hubbard optimizations for SWAP and $\sqrt{\text{SWAP}}$. (a) SWAP gate optimizations for four bands have an error of less than 0.001 for gate durations of more than 0.08 ms. These optimized pulses for four bands are used in six-band simulations which match closely with errors of less than 0.001 for gate durations larger than 0.1 ms. This suggests that four-band optimizations are sufficient for the high-fidelity SWAP gate. (b) SWAP gate optimization errors for upper bounds given by 30, 40, and $50E_{r\ell}$ for V_ℓ and the four-band model; For each upper bound, the error is shown with gate durations of 0.06, 0.1, 0.14, and 0.18 ms. Larger upper bounds result in smaller gate errors, especially for shorter gate durations. (c) Similar optimizations and simulations for $\sqrt{\text{SWAP}}$. The four-band optimizations have errors of less than 0.007 for gate durations larger than 0.12 ms. The corresponding six-band simulations slightly differ with errors of less than 0.007 for gate durations larger than 0.16 ms. (d) Improved $\sqrt{\text{SWAP}}$ optimizations with errors of less than 0.005 for gate durations larger than 0.12 ms by increasing the upper bound for V_ℓ to 45 $E_{r\ell}$ and optimizing for six bands. The corresponding eight-band simulations have errors of less than 0.005 for gate durations larger than 0.12 ms and show negligible excitation beyond six bands.

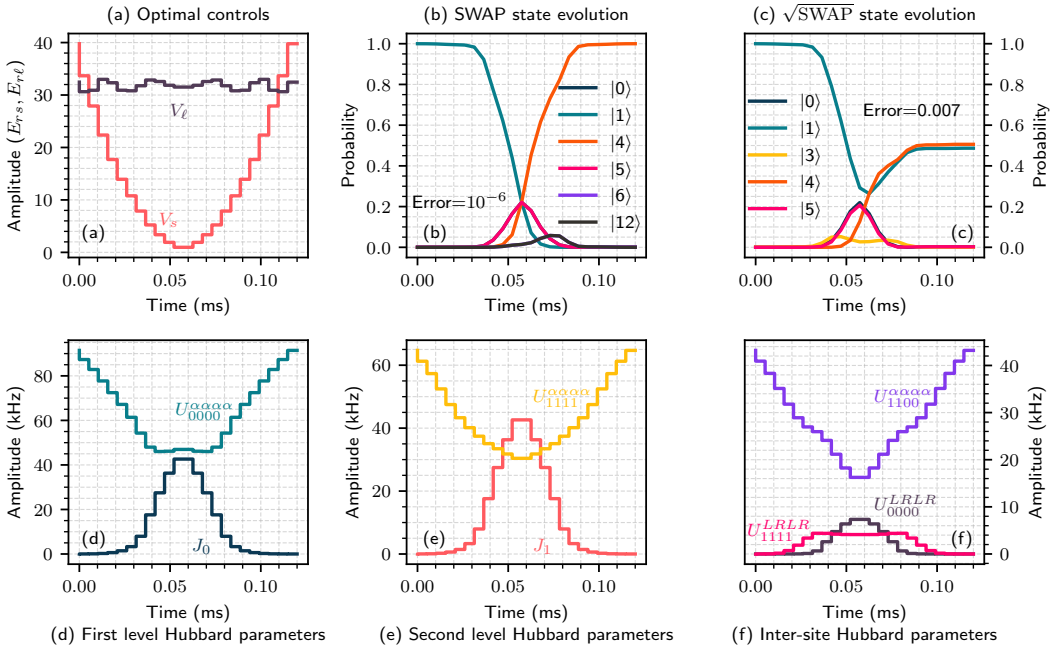

Figure 5.9: Four-band Fermi-Hubbard model optimizations for a short gate duration of 0.12 ms relying on excitations to higher bands and multiple hopping and interaction strengths. (a) Optimal controls V_s and V_ℓ in their respective recoil energies $E_{rs(\ell)} = \hbar^2 k^2_{s(\ell)}/(2m)$. (b) State evolution under SWAP from $|1\rangle = |\uparrow\downarrow\rangle$ to $|4\rangle = |\downarrow\uparrow\rangle$ for 0.12 ms with optimal controls from (a) and state labeling scheme as in Sec. 5.6 and Table. 5.2. (c) State evolution under $\sqrt{\text{SWAP}}$ from $|1\rangle = |\uparrow\downarrow\rangle$ to $[(1+i)\,|1\rangle - (1-i)\,|4\rangle]/2 = [(1+i)\,|\uparrow\downarrow\rangle - (1-i)\,|\downarrow\uparrow\rangle]/2$ with optimal controls from (a) and optimized scattering length $a = 1995.22 \times a_0$ where $a_0 = 5.29 \times 10^{-11}$ m is the Bohr radius. (d)-(f) The corresponding Fermi-Hubbard parameters: Each level p in the double well consists of two energy bands $2p$ and $2p{+}1$, resulting in two levels for the four-band Fermi-Hubbard model. (d) The hopping parameter J_0 on the first level and between the left and the right side of the double well increases with decreasing V_s and increasing V_ℓ. The onsite interaction $U^{\alpha\alpha\alpha\alpha}_{0000}$ on the first level is directly proportional to V_s and V_ℓ. (e) The second-level hopping parameter J_1 and the onsite interaction $U^{\alpha\alpha\alpha\alpha}_{1111}$ behave similar as in (d). (f) The offsite interaction U^{LRLR}_{0000} and U^{LRLR}_{1111} between the left and right sides on the first and the second level have a small magnitude and become significant for small V_s. Here, $U^{\alpha\alpha\alpha\alpha}_{1100}$ represents the interaction between the first and the second level on the same side of the double well and behaves similar as $U^{\alpha\alpha\alpha\alpha}_{pppp}$.

Next, we optimize the lattice depths V_s and V_ℓ and the scattering length a for the $\sqrt{\text{SWAP}}$ gate i.e., for transferring the state Ψ_0 to the state $\Psi_{\sqrt{\text{SWAP}}}$, using the same initial conditions and bounds as in the SWAP-gate optimization. As shown in Fig. 5.8(c), the infidelity increases for shorter pulse durations. The four-band optimizations yield errors of less than 0.007 for gate durations longer than 0.12 ms. Similar to the SWAP gate, we compare our results with six-band simulations, as illustrated in Fig. 5.8(c). The six-band simulations differ slightly from the four-band results, showing errors of less than 0.007 for gate durations longer than 0.16 ms, indicating the presence of higher-band excitations in the system. This can be mitigated by increasing the upper bound on V_ℓ to 45 $E_{r\ell}$ and optimizing within the six-band model, as shown in Fig. 5.8(d). We further compare the optimization in the six-band model with simulations in the eight-band model and observe negligible excitations beyond six bands. Both the six-band optimization and the eight-band simulation result in gate errors smaller than 0.005 for gate durations longer than 0.12 ms. This suggests that for the $\sqrt{\text{SWAP}}$ gate, good pulses can be identified through four-band or six-band optimizations where the six-band model gives lower higher-band excitation compared to the four-band model.

5.5.2 Dynamics with optimzed controls

We focus on one set of optimal lattice depths V_s and V_ℓ for a duration of 0.12 ms as shown in Fig. 5.9(a), which have been optimized for the $\sqrt{\text{SWAP}}$ gate. The optimal scattering length is $a = 1995.22\ a_0$, where $a_0 = 5.29 \times 10^{-11}$ m is the Bohr radius. The controls are simple and realistic, adhering to experimental constraints. The corresponding time evolution for the SWAP and $\sqrt{\text{SWAP}}$ gates is illustrated in Fig. 5.9(b)-(c). The system begins in the state Ψ_0 and evolves to the target states Ψ_{SWAP} and $\Psi_{\sqrt{\text{SWAP}}}$ for the SWAP and $\sqrt{\text{SWAP}}$ gates, respectively. The symmetry in the system suggests that the same pulse will transfer the state Ψ_{SWAP} to Ψ_0 for SWAP gate. Notably, there is excitation and de-excitation from higher-band states during the time evolution, resulting in faster gate operations. The combined probabilities for all the states involving the second level are less than 10^{-7} and 10^{-4} at the end of the SWAP and $\sqrt{\text{SWAP}}$ gates, respectively. This suggests that the optimized controls effectively minimize excitations to higher levels at the end of the gates, which is crucial for any quantum operation. The remaining error arises from probabilities on the order of 10^{-3} for the first-level states $|D0\rangle$ and $|0D\rangle$ in the case of the $\sqrt{\text{SWAP}}$ gate.

We also examine the impact of the optimal V_s, V_ℓ, and a on the higher-band Fermi-Hubbard parameters of Eq. (5.17). Each level p in the double well is composed of two energy bands, $2p$ and $2p + 1$, yielding two levels in the four-band Fermi-Hubbard

model. The hopping parameter J_0 represents the hopping between the left (L) and right (R) sides of the well on the first level (or equivalently the hopping J of the two-band Fermi-Hubbard model) and $U_{0000}^{\alpha\alpha\alpha\alpha}$ corresponds to the interaction U of the two-band Fermi-Hubbard model as shown in Fig. 5.9(d). The value of J_0 increases with decreasing V_s and increasing V_ℓ, as these conditions lead to a higher overlap between the Wannier functions w_{0L} and w_{0R}. Conversely, the onsite interaction $U_{0000}^{\alpha\alpha\alpha\alpha}$ decreases with decreasing V_s as shown in Fig. 5.9(d).

For the two-band Fermi-Hubbard model optimization in Sec. 5.3.2, we assume that the interaction strength is independent of changes in the Wannier functions and remains constant and proportional to a. However, we observe that this assumption breaks down with our optimal lattice depths for the four-band Fermi-Hubbard model, as V_s becomes shallow for fast gates. In the four-band Fermi-Hubbard model, an additional hopping parameter J_1 and onsite interaction strength $U_{1111}^{\alpha\alpha\alpha\alpha}$ arise, as shown in Fig. 5.9(e). The parameter J_1 has a larger magnitude compared to J_0 because the overlap between the Wannier functions w_{1L} and w_{1R} for the second level is greater than that for the first level. Conversely, $U_{1111}^{\alpha\alpha\alpha\alpha}$ has a smaller magnitude compared to $U_{0000}^{\alpha\alpha\alpha\alpha}$ due to the reduced overlap of the Wannier functions on the same site at the second level. Additionally, there are significant contributions from offsite interactions $U_{mnop}^{\alpha\beta\gamma\delta}$ when the lattice depths are shallow.

Figure 5.9(f) illustrates the variation of three different offsite interactions with time-dependent lattice depths. The terms U_{0000}^{LRLR} and U_{1111}^{LRLR} represent the offsite interactions between the left (L) and right (R) sides of the double well for the first and second levels, respectively. Similar to J_p, the offsite interaction U_{pppp}^{LRLR} is proportional to the overlap between the wave functions on the left and right sides, thus it increases as V_s decreases. The term $U_{1100}^{\alpha\alpha\alpha\alpha}$ represents the interaction between atoms occupying different levels but residing on the same side α. For $U_{pppp}^{\alpha\alpha\alpha\alpha}$, the interaction $U_{1100}^{\alpha\alpha\alpha\alpha}$ decreases as the Wannier functions spread out with a shallower short lattice.

Note that the optimized gates are distinct from superexchange processes where $U \gg J$, which avoid the $|D0\rangle$ and $|0D\rangle$ states, but result in long gate times [159]. For the optimized pulses shown in Fig. 5.9(a), we obtain $U_{0000}^{\alpha\alpha\alpha\alpha}/J_0 = 5.34$ and $U_{1111}^{\alpha\alpha\alpha\alpha}/J_1 = 3.64$, where these ratios are calculated by integrating the time-dependent curves in Fig. 5.9(d)-(e). This ratio is close to the exchange ratio $U/J = 4/\sqrt{3}$, which permits population in the $|D0\rangle$ and $|0D\rangle$ states. Our optimized control operates near this exchange ratio, but is further refined to minimize population in the $|D0\rangle$ and $|0D\rangle$ states while achieving faster gates. Similar parameter regimes could be accessed through adiabatic control, but this would result in slower gates. The speedup in our case arises from non-adiabatically modulating V_s and V_l to dynamically enhance J from an initially negligible value. This results in pulses that are experimentally feasible and

helps manage excitations to higher energy levels efficiently.

Result 4 *Efficient SWAP and* $\sqrt{\text{SWAP}}$ *gates are found using higher-band Fermi-Hubbard models. The control duration can be as short as* 0.08 *ms for transferring the state* Ψ_0 *to* Ψ_{SWAP} *and* 0.12 *ms for transferring* Ψ_0 *to* $\Psi_{\sqrt{\text{SWAP}}}$ *which is five times shorter than typical experimental state transfer durations [157, 178]. The results for* $\sqrt{\text{SWAP}}$ *are improved by optimizing with the six-band model and increasing the upper bound on* V_ℓ.

In the following Sections 5.6 and 5.7, we discuss how the obtained gates perform when they are applied to error states with three and four atoms in a double well as well as their robustness under multiple error sources. Afterwards, we consider the full gate optimization using higher bands in the Fermi-Hubbard model (see Sec. 5.8).

5.6 Multi-atom dynamics

We have demonstrated performance enhancements for SWAP and $\sqrt{\text{SWAP}}$ for two atoms of opposite spins in a double well. However, in a real experimental setup, multiple double wells are controlled by global lasers V_s and V_ℓ, and some double wells may contain more or fewer than two atoms after state preparation. To fully characterize the system, it is essential to consider all possible atomic configurations within a double well and analyze the impact of our optimized pulses on these configurations. For fermionic atoms, 16 different states can exist within a double well with up to four atoms:

- 0 atoms: $|00\rangle$
- 1 atom: $|{\uparrow}0\rangle$, $|0{\uparrow}\rangle$, $|{\downarrow}0\rangle$, $|0{\downarrow}\rangle$
- 2 atoms: $|{\uparrow\downarrow}\rangle$, $|{\downarrow\uparrow}\rangle$, $|{\uparrow\uparrow}\rangle$, $|{\downarrow\downarrow}\rangle$, $|D0\rangle$, $|0D\rangle$
- 3 atoms: $|D{\uparrow}\rangle$, $|{\uparrow}D\rangle$, $|D{\downarrow}\rangle$, $|{\downarrow}D\rangle$
- 4 atoms: $|DD\rangle$,

where $D = {\uparrow\downarrow}$ represents a double occupancy on one side of the double well. One-atom states serve as single-qubit states, and for two-qubit gates, states with three and four atoms are error states. For adiabatic gates, the three-atom states behave similar to the one-atom states, and the four-atom state $|DD\rangle$ remains unchanged, as both sites are already fully occupied. However, for fast gate operations, these doubly occupied atoms can be individually excited to higher energy levels within the double well.

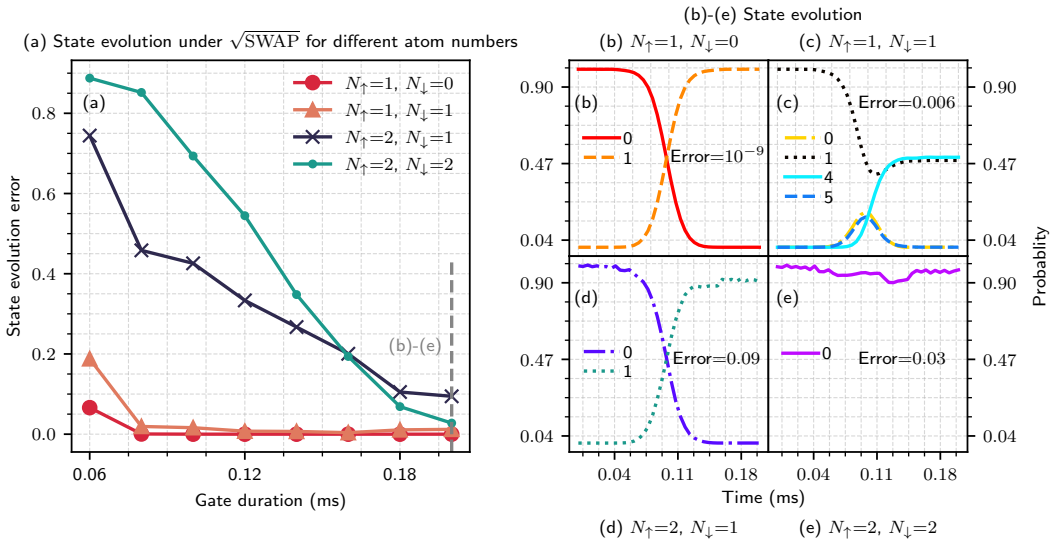

Figure 5.10: State evolution errors under $\sqrt{\text{SWAP}}$ for different atom numbers using the optimized control pulses from Fig. 5.8(c) as compared to the usual case of two atoms with $N_\uparrow$=1 and $N_\downarrow$=1 in a double well and measured with a four-band Fermi-Hubbard simulation. (a) Single atoms with $N_\uparrow$=1 and $N_\downarrow$=0 have an infidelity of less than 0.0005 for gate durations larger than 0.08 ms. Two atoms with $N_\uparrow$=1 and $N_\downarrow$=1 agree with the optimized infidelities from Fig. 5.8(c). The error states with three and four atoms with either $N_\uparrow$=2 and $N_\downarrow$=1 or $N_\uparrow$=2 and $N_\downarrow$=2 result in higher infidelities of around 10^{-2} for a duration of 0.20 ms. (b)-(e) Corresponding state evolutions for a duration of 0.20 ms. Further optimizations are possible for error states with three or four atoms if required.

We investigate the dynamics of various atomic configurations in a double well by using the method described in Appendix 5.11.4 for calculating and assigning the computational states with a given number of atoms. For this comparison, we employ the optimized controls V_s, V_ℓ, and a derived for the two-atom $\sqrt{\text{SWAP}}$ gate from Sec. 5.5.1. The optimized gate errors for the two-atom case are repeated in Fig. 5.10(a) for reference. In the ideal scenario, the single-atom states undergo a SWAP operation from the left to the right side of the double well, or vice versa. This implies that our initial state for the one-atom case is $I = 0$ and the target state is $I = 1$. As illustrated in Fig. 5.10(a), the state evolution error of the one-atom dynamics corresponding to a state with $N_\uparrow$=1 and $N_\downarrow$=0 is negligible, as the single atom is unaffected by the atom-atom interaction induced by a. Similarly, in an ideal situation, the three-atom states should also perform a SWAP operation. For example, if the initial state is $|D\uparrow\rangle$, the target state should be $|\uparrow D\rangle$. However, as shown in Fig. 5.10(a), the error for the three-atom configurations with $N_\uparrow$=2 and $N_\downarrow$=1 increase with shorter pulses due to the atom-atom interactions and excitations to higher energy levels. A similar analysis was conducted for the four-atom state with $N_\uparrow$=2 and $N_\downarrow$=2, where both the initial and target states are the same, i.e., $|DD\rangle$. This state exhibits higher state evolution error compared to the three-atom states, as more atoms are excited to higher levels and undergo multiple atom-atom interactions. The three- and four-atom configurations converge to infidelities below 0.1 for a gate duration of 0.20 ms.

The time evolution for one-, two-, three-, and four-atom cases under and a gate duration of 0.20 ms is presented in Fig. 5.10(b)-(e). In the one-atom case, the system evolves from the state $|\uparrow 0\rangle$ to $|0\uparrow\rangle$, demonstrating the desired dynamics, as shown in Fig. 5.10(b). For the two-atom case, the system performs the $\sqrt{\text{SWAP}}$ gate with high fidelity, transitioning from Ψ_0 to $\Psi_{\sqrt{\text{SWAP}}}$ as depicted in Fig. 5.10(c). In the three-atom case, starting from $|D\uparrow\rangle$, the system evolves to $|\uparrow D\rangle$ with an infidelity of 0.09 [see Fig. 5.10(d)]. Finally, the four-atom state $|DD\rangle$ is shown to excite to higher bands, resulting in an error of 0.027 in maintaining the $|DD\rangle$ state [see Fig. 5.10(e)]. It is important to note that in Fig. 5.10(b)-(e), we only display the states that exhibit probabilities greater than 0.05 at any time step during the evolution.

Remark 4 *The optimized pulses for the $\sqrt{\text{SWAP}}$ gate from Fig. 5.8(c) result in a high state-evolution infidelity for error states with three and four atoms compared to states with one and two atoms. In particular, for shorter pulse durations, the atoms interact with each other and excite to the higher bands. However these error states can be suppressed with good initial state preparation, rendering them less significant for gate operations.*

If necessary, the optimization protocols can be extended to include infidelities from

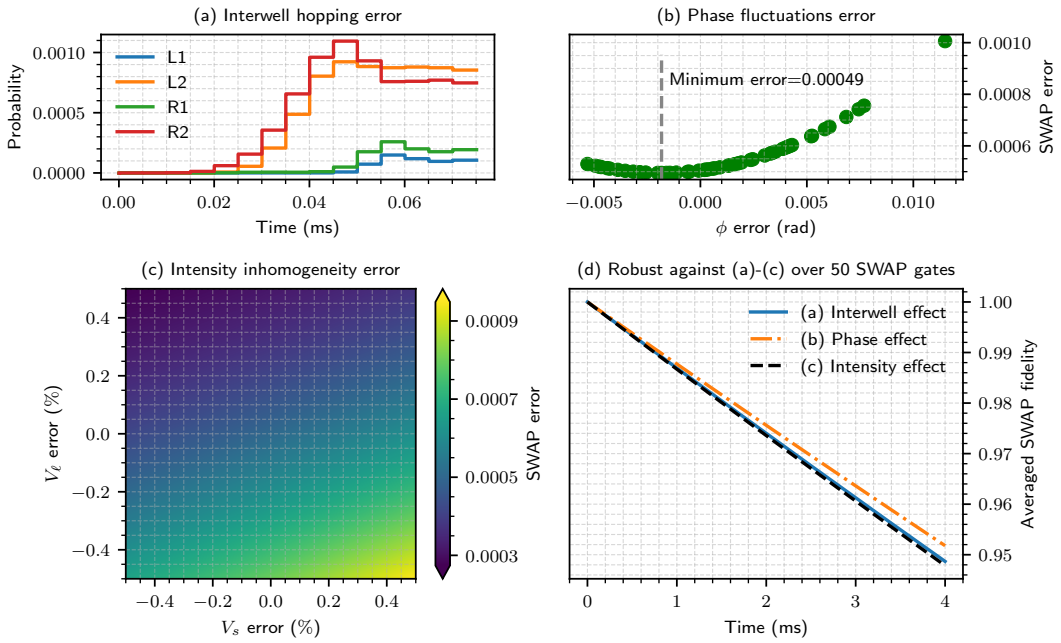

Figure 5.11: Robustness of a SWAP gate against inter-well hopping, phase fluctuations, and intensity inhomogeneity for an optimized control with a duration of 0.08 ms: (a) Inter-well hopping for three double wells where $L1, L2, R1$ and $R2$ denote the probability of the atom being in the first and the second levels of the adjoining left and right double wells, respectively. (b) Phase fluctuations error by numerically introduced errors in the relative phase chosen from a Gaussian distribution with a standard deviation of 4.5 mrad [157]. (c) Intensity inhomogeneity errors by numerically introduced errors in the laser depths V_s and V_ℓ chosen uniformly within $\pm 0.5\%$ [157]. (d) Exponential fit for the SWAP fidelity for each error source from (a)-(c) using 50 SWAP gates. The intensity inhomogeneity is the most dominant source of error whereas phase fluctuations are the smallest. For all errors, the exponential decay time of $\tau_d > 74$ ms (or 460 gates) predicts a very long coherence time for the chosen error strengths [157, 178].

different atomic configurations in the cost function defined in Eq. (5.16), optimizing the full dynamics for more comprehensive experimental scenarios.

5.7 Robustness of the optimized control pulses

In this section, we assess the robustness of the optimal control pulses in the presence of different types of error sources [157, 178]. The first error source involves potential tunneling from the target double well to neighboring wells. This means that during the gate operation, the atom has a finite probability of moving to the neighboring wells which reduces the gate fidelity. To test the robustness of the optimal control pulses against inter-well tunneling, we use a set of optimized V_s and V_ℓ obtained from the SWAP optimization [see Sec. 5.5.1] of 0.08 ms duration and 0.999 fidelity as shown in Fig. 5.8(a). We simulate a system with three double wells where the middle double

well is our target well and the left and right double wells act as the neighboring wells. We take only half of the adjacent left and right double wells resulting in eight possible states with two on the left double well, four on the middle double well, and two on the right double well for a single atom within the four-band model. In Fig. 5.11(a), we present the time evolution of the states in the neighboring wells during the gate operation. Here, $L1$ and $L2$ represent the first and second levels of the left neighbor where $R1$ and $R2$ are the first and second levels of the right neighbor. When the atoms are in the first level, the overlap of the Wannier functions of different double wells is low, resulting in small hopping probabilities $L1$ and $R1$. The hopping probabilities $L2$ and $R2$ increase slightly when the atoms are in the second level due to the higher overlap of the Wannier functions, as shown in Fig. 5.11(a). The maximum probability of the atom tunneling to states outside the target double well at any time is negligible ($\approx 10^{-3}$) and the atom also tunnels back to the target double well since the probabilities in the neighboring wells decrease. This analysis considers the case where the neighboring double wells are initially empty. When the neighboring wells are occupied by atoms, the hopping probabilities change accordingly. For example, if there is an atom in the neighboring well with the same spin as the hopping atom, the hopping will be suppressed due to Pauli exclusion principle. However, if the atoms have opposite spins and the scattering length a is non-zero, the hopping will slightly increase due to a correction from the density-assisted hopping term, similar to Eq. (5.22).

The second error comes from the phase instability of the lattice potential. In our simulations, we consider a symmetric double well with a relative phase of ϕ=0, but in a real experiment, the relative phase fluctuations can lead to dephasing. Phase errors can generally be categorized into two types. The first type consists of time-independent or static phase fluctuations, which introduce a constant energy offset in the system. The second type consists of time-dependent phase fluctuations or drifts, which, if sufficiently strong, can lead to dephasing effects. In our work, we incorporate the static phase error into Eq. (5.2), resulting in an energy offset between the left and right sites of the double well, thereby modifying the effective hopping amplitude. This alteration contributes to an increase in the gate error. When the gate is applied repeatedly over multiple cycles, this accumulated error leads to the damping of the Rabi oscillations, manifesting as a loss of coherence in the system's dynamics. To understand the impact of these fluctuations, we sample 50 phase errors from a Gaussian distribution with a 4.5 mrad standard deviation [157]. We simulate our four-band model using these 50 phase errors with the same controls of 0.08 ms duration. As shown in Fig. 5.11(b), the infidelity increases negligibly as ϕ changes, demonstrating the robustness of the controls against phase fluctuations.

Lastly, we study the effect of the inhomogeneity in the laser intensities. These

inhomogeneities lead to different coupling strengths across the lattice resulting in different gate errors. We test the robustness of the controls V_s and V_ℓ against these fluctuations by uniformly selecting 400 pulses on a 20×20 grid with extremal values given by the pairs ($V_s \pm e$, $V_\ell \pm e$) and an error of $e \leq 0.5\%$ [157]. Figure 5.11(c) shows that the infidelity increases with increasing V_s error as a result of decreasing tunneling strength J. For increasing V_ℓ, J increases and results in a decreasing infidelity.

To identify the dominant error sources among the three errors discussed, we run the simulations with each error source over 50 gate durations. This results in the damping of the Rabi oscillations and exponential decay of the SWAP fidelity over duration of 4 ms as shown in Fig. 5.11(d). For phase and intensity errors, each data point is an average of the fidelity over 20 and 25 error pulses respectively. In agreement with the experimental observations in [157], we see that inter-well hopping is one of the dominant sources of error whereas phase fluctuations cause the least damping. The larger effect of the intensity error can be explained by the fact that V_s and V_ℓ are the controls for the optimization, so any variation in them has a significant effect on the fidelity. Note that while the damping of the Rabi oscillations appears similar to the effects caused by decoherence mechanisms such as dephasing and relaxation, our system remains closed even in the presence of additional noise sources. Therefore, in our case, what we refer to as dephasing corresponds to an accumulated coherent gate error rather than interaction with an external environment. The fidelity after one gate duration is greater than 0.998 for all of the error sources. The exponential decay time τ_d is greater than 74 ms or 460 Rabi oscillations for all errors. This is a predicted improvement of one order of magnitude compared to the experimental decay time τ_d=27 ms or 33 oscillations [157]. This extended coherence time is primarily due to the faster gate duration of 0.08 ms compared to the experimental gate duration of 0.4 ms [157].

Result 5 *The optimal control pulses are extremely robust against intensity inhomogeneity, phase fluctuations and inter-well hopping usually appearing in experiments. The inter-well hopping is one of the dominant sources of error whereas phase fluctuations cause the least damping which agrees with the experimental results [157]. The exponential decay time τ_d is greater than* 460 *Rabi oscillations with gate duration of* 0.08 *ms, which is almost an order of magnitude improvement compared to the experimental τ_d [157].*

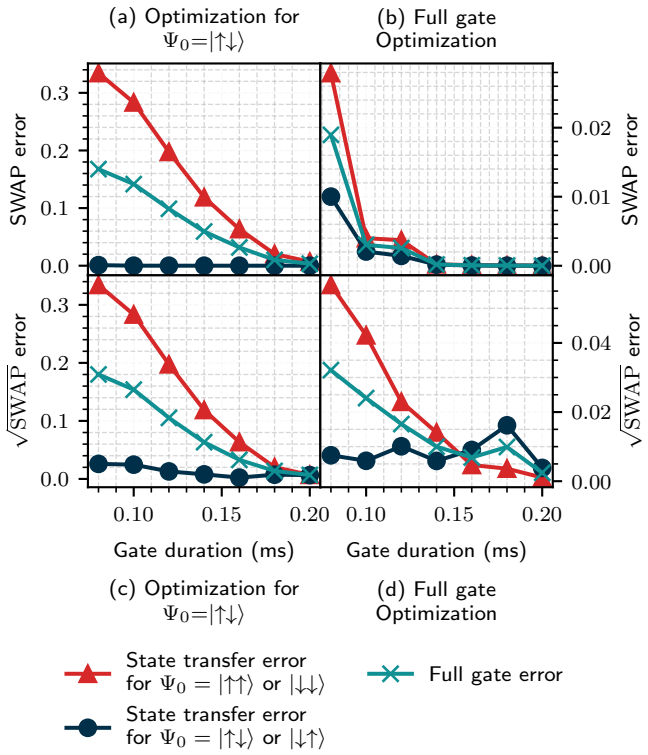

Figure 5.12: Comparison of the optimization for one initial state Ψ_0 with the full gate optimization for different gate durations. (a) State evolution errors for SWAP and different initial states using optimized controls from Fig. 5.8(a). The initial states $\Psi_{\text{ini}} = |\uparrow\downarrow\rangle$ and $|\downarrow\uparrow\rangle$ have the same error due to the symmetry of the Hamiltonian and they have an error of less than 0.001 for gate durations larger than 0.08 ms [same as Fig. 5.8(a)]. The initial states $\Psi_{\text{ini}} = |\uparrow\uparrow\rangle$ and $|\downarrow\downarrow\rangle$ also follow the same dynamics but they have significantly higher errors for gate durations shorter than 0.20 ms. We show the full gate infidelity calculated with Eq. (5.16), which is larger than 0.01 for gate durations shorter than 0.20 ms. (b) State evolution for SWAP and different initial states after the full gate optimization with the cost function of Eq. (5.16). Optimized controls from Fig. 5.8(a) are used as the initial guess for the full gate optimization. The state evolution error for $\Psi_{\text{ini}} = |\uparrow\uparrow\rangle$ and $|\downarrow\downarrow\rangle$ is significantly reduced compared to (a), and we have a full gate error of less than 0.005 for gate durations larger than 0.1 ms. (c) Similar analysis is done for $\sqrt{\text{SWAP}}$ and different gate durations and controls from Fig. 5.8(c). (d) The full gate error after further optimization is in the range of 0.009−0.001 for gate durations larger than 0.16 ms.

5.8 Full gate optimization with higher-band Fermi-Hubbard model

Recall for the two-band Fermi-Hubbard model from Sec. 5.3.2 that the states $|\uparrow\uparrow\rangle$ and $|\downarrow\downarrow\rangle$ do not change under SWAP and the states $|\uparrow\downarrow\rangle$ and $|\downarrow\uparrow\rangle$ follow similar dynamics since the Hamiltonian is symmetric. Hence, the optimization for reaching the target state $\Psi_{\text{tar}} = |\downarrow\uparrow\rangle$ also optimizes the full gate as shown in Fig. 5.5(a).

However, for the higher-band Fermi-Hubbard model, the states $|\uparrow\uparrow\rangle$ and $|\downarrow\downarrow\rangle$ can evolve to other states involving higher levels, e.g., for the four-band Hubbard model, $|\uparrow\uparrow\rangle$ or $|\downarrow\downarrow\rangle$ can have six possible states. An efficient SWAP or $\sqrt{\text{SWAP}}$ should maximize the probability of the states $|\uparrow\uparrow\rangle$ and $|\downarrow\downarrow\rangle$ to stay in the lowest level at the end of the gate. To check the performance of our optimized controls from Fig. 5.8, we simulate the system with different initial states and calculate the infidelity of reaching the respective target states using Eq. (5.13) and the full gate error using Eq. (5.16) with $N_i = 4$. Figure 5.12(a) shows the state evolution errors for different initial states $|\uparrow\uparrow\rangle$, $|\downarrow\downarrow\rangle$, $|\uparrow\downarrow\rangle$, and $|\downarrow\uparrow\rangle$. The states $|\uparrow\downarrow\rangle$ and $|\downarrow\uparrow\rangle$ have the same errors as in Fig. 5.8(a) under SWAP gate. However, the states $|\uparrow\uparrow\rangle$ and $|\downarrow\downarrow\rangle$ have significantly higher errors for gate durations shorter than 0.20 ms since the atoms excite to the second level. This results in a full gate error larger than 0.01 for gate durations shorter than 0.20 ms. We thus minimize the full gate error by minimizing the cost function defined in Eq. (5.16) and using the controls from Fig. 5.8(a) as the initial guess. In Fig. 5.12(b), we show the state evolution errors after the full gate optimization. The errors with initial states $|\uparrow\uparrow\rangle$ and $|\downarrow\downarrow\rangle$ are significantly reduced, and we get a full gate error of less than 0.005 for gate durations larger than 0.10 ms.

We perform the same analysis for $\sqrt{\text{SWAP}}$ and calculate the state evolution error for different initial states as shown in Fig. 5.12(c), using the optimized controls from Fig. 5.8(c). Similar to the SWAP gate, we see that the states $|\uparrow\uparrow\rangle$ and $|\downarrow\downarrow\rangle$ are exciting to higher levels, resulting in significant full gate error for gate durations less than 0.20 ms. After optimizing for all four initial states, we can decrease the state evolution errors and achieve a full gate error of less than 0.009 for gate durations larger than 0.16 ms [see Fig. 5.12(c)].

Result 6 *With the full gate optimization, excitation to the higher bands is minimized for initial states* $|\uparrow\uparrow\rangle$ *and* $|\downarrow\downarrow\rangle$*, and the gate duration is found to be* 0.10 *ms for SWAP with fidelity of* 0.997 *and* 0.16 *ms for* $\sqrt{\text{SWAP}}$ *gate with fidelity of* 0.993.

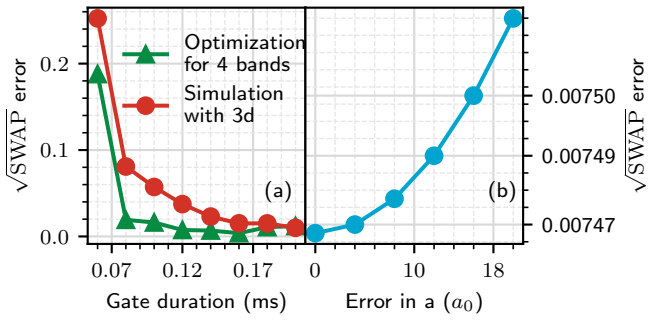

Figure 5.13: (a) Comparison of the $\sqrt{\text{SWAP}}$ gate error between the one-dimensional four-band model and the full three-dimensional simulation for various gate durations. The increase in gate error for the three-dimensional case highlights the effect of excitations in the y and z directions. (b) Robustness analysis of the $\sqrt{\text{SWAP}}$ gate error against deviations in the scattering length. The gate error remains close to the ideal case for deviations Δa ranging from $4a_0$ to $20a_0$, demonstrating negligible sensitivity of the optimized control pulses (0.12 ms gate duration) to scattering length deviations.

5.9 Effect of high interaction strength

So far, we assume that there are no excitations in the y and z directions of the optical lattice. However, increasing the scattering length a to high values can generate interactions in the y and z directions, resulting in excitations to higher levels. These excitations, if not suppressed, will result in a decrease of gate fidelities. The Hamiltonian for the three-dimensional system is written as

$$\begin{aligned} H_{3d} = H_J^x \otimes I^y \otimes I^z + I^x \otimes H_E^y \otimes I^z \\ + I^x \otimes I^y \otimes H_E^z + U^x \otimes U^y \otimes U^z, \end{aligned} \tag{5.24}$$

where H_J^x is the hopping plus the onsite energy in the x direction, given by Eqs. (5.17a) and (5.17c), H_E^y and H_E^z are onsite energy terms in the y and z directions respectively, and I is the identity matrix in different directions. Note that there is no hopping in the y and z directions. The interaction term U^x is calculated from the one-dimensional form of Eq. (5.19), whereas U^y and U^z are calculated from an updated formula given by ($l \in \{y, z\}$)

$$U^l = \iint w_m^\dagger(l)\, w_n^\dagger(l)\, w_o(l)\, w_p(l)\, \mathrm{d}l. \tag{5.25}$$

We consider two energy levels, i.e., $m, n, o, p \in \{0, 1\}$, resulting in four states for each of the y and z directions with two atoms. Combined with the four-band model in the x direction, we have a total of 256 basis states for the three-dimensional simulation using H_{3d}. We simulate the three-dimensional model with optimized controls for different gate durations from Fig. 5.8(c) and calculate the $\sqrt{\text{SWAP}}$ gate error. We compare the gate error from the three-dimensional simulation to the four-band one-dimensional

model in Fig. 5.13(a). For the gate duration of 0.12 ms, the infidelity of the $\sqrt{\text{SWAP}}$ gate with the four-band model is 0.007, as shown in Fig. 5.8(c) and Fig. 5.9(c). The infidelity with the three-dimensional model increases to 0.037 due to small excitations in the y and z directions. In principle, one can make a deeper lattice in the y and z directions compared to $45E_{ry}$ and $45E_{rz}$ used in our simulations to tightly squeeze the atoms. Additionally, we can also perform optimizations to suppress the excitations in these directions.

We optimize the time-independent scattering length a to arbitrary values with respect to an upper bound. However, tuning the magnetic field to achieve the exact a value is difficult. Therefore, we analyze the robustness of the $\sqrt{\text{SWAP}}$ gate against deviations in the scattering length. For this, we simulate the system with the four-band Fermi-Hubbard model using the optimized controls from Fig. 5.9(a) 0.12 ms gate duration, and $a = 1995.22 \times a_0$. We take different deviation Δa values from $4a_0$ to $20a_0$, resulting in an effective scattering length of $a+\Delta a$. As shown in Fig. 5.13(b), the increase in gate error is negligible for this range of deviation, showing the robustness of our optimized pulses.

5.10 Conclusion

Using open-loop quantum optimal control, we design pulses for the SWAP and $\sqrt{\text{SWAP}}$ gates for fermionic atoms trapped in a superlattice reaching fidelities in the range of 10^{-3} for realistic experimental parameters. We use Fermi-Hubbard models for the optimization, which widely describe fermionic atoms trapped in optical lattices or superlattices. In this work, we treat the gate optimization as a state-to-state transfer for the SWAP and $\sqrt{\text{SWAP}}$ gates using the two-band Fermi-Hubbard model. So, optimizing a SWAP gate corresponds to optimizing the transfer of the state $|\uparrow\downarrow\rangle$ to $|\downarrow\uparrow\rangle$. A $\sqrt{\text{SWAP}}$ gate optimization corresponds to optimization of transfer of the state $|\uparrow\downarrow\rangle$ to $[(1+i)\,|\uparrow\downarrow\rangle - (1-i)\,|\downarrow\uparrow\rangle]/2$. First, using the two-band Fermi-Hubbard model, we find the time-optimal control for the SWAP gate analytically and calculate the quantum speed limit in the presence of bounds on the control. We match the analytical study with the numerical optimization of the SWAP gate and show a numerical quantum speed limit closely matching with the analytical one with feasibility constraints. We also calculate the full gate fidelities, which is the summation of state transfer fidelities for all computational states, and show that gate fidelities are equivalent to the optimized state transfer fidelities.

Next, we show the limitations of the two-band Fermi-Hubbard model in the case of fast gates, where it is not sufficient to provide the full dynamics of the double well system. We describe higher-band Fermi-Hubbard models and update our time-evolution

method to account for the non-adiabatic change of the Hamiltonian. We detail a formula to calculate the approximate analytical gradient of the cost function and use a combination of this and the finite-difference method in the optimization. We find that optimization with four bands is sufficient for the SWAP gate, whereas the performance of the $\sqrt{\text{SWAP}}$ gate is further improved by a six-band optimization. Our numerical simulations demonstrate that high-fidelity SWAP and $\sqrt{\text{SWAP}}$ gates can be realized with significantly reduced control durations using realistic experimental parameters. We achieve a SWAP between the states $|\uparrow\downarrow\rangle$ and $|\downarrow\uparrow\rangle$ in 0.08 ms with fidelity of 0.999 and a $\sqrt{\text{SWAP}}$ pulse preparing the entangled state $[(1+i)\,|\uparrow\downarrow\rangle - (1-i)\,|\downarrow\uparrow\rangle]/2$ in 0.12 ms with fidelity of 0.995, representing a five-fold improvement over experimental state transfer times [157, 178]. These findings emphasize the potential of higher-band Fermi-Hubbard models for accelerating and optimizing quantum gates.

We test our optimal control pulses for $\sqrt{\text{SWAP}}$ gate on the different atom configurations in the double well. The three-atom and four-atom error states observe significant errors, especially for short gate durations, while these errors can be optimized if necessary. We check the robustness of the optimal control pulses against inter-well hopping, phase fluctuations, and intensity inhomogeneity. We show that the optimal pulses are extremely robust against all errors with inhomogeneous intensity and inter-well hopping being the dominant ones. Furthermore, by employing the full gate optimization, we minimize excitations to higher bands for initial states $|\uparrow\uparrow\rangle$ and $|\downarrow\downarrow\rangle$, achieving a SWAP gate fidelity of 0.997 in 0.10 ms and a $\sqrt{\text{SWAP}}$ gate fidelity of 0.993 in 0.16 ms. We also explain the different gradient methods used in the paper and compare their performance based on the number of function evaluations and the optimization duration. Our work therefore performs a detailed study of fermionic atoms trapped in a superlattice system and designs faster and more efficient gates. One can readily adapt the modeling and optimization scheme of this work for bosons as well by employing the Bose-Hubbard model. Unlike fermions, bosons differ in their interaction energy, which permits double occupancy by atoms with the same spin states. Furthermore, the creation and annihilation operators for bosons obey the standard commutation relations, in contrast to the fermionic anti-commutation relations.

Our optimization model is inspired by experiments and incorporates realistic parameters [157]. The experiments performed in [157] use phase modulation to perform the SWAP operation, whereas our optimization uses the lattice depths V_s and V_l as the control [178]. This gives the advantage of minimizing the effect of phase noise, which is critical in optical lattice experiments. The pulses generated from optimizing the SWAP and $\sqrt{\text{SWAP}}$ gates are both reasonably smooth and experimentally implementable. Thus applying these optimized controls into real experiments will enable higher gate fidelities. For more realistic pulses, we can include the transfer function

information in the optimization [307]. The optimized pulses must work with minimal excitation in the y and z directions, which can be achieved with deeper y and z lattice depths. Experiments utilizing optimal control will not only enhance gate performance, but they will enable us to assess and refine our existing models, such as by accounting for heating effects. Moreover, pulses optimized by open-loop approaches are a good starting point for further feedback-based optimizations directly applied in experiments. This iterative approach will pave the way for robust and efficient quantum gates, which are crucial for quantum simulation and computation.

5.11 Appendix

5.11.1 Analytical SWAP optimization

In this appendix, we find the time-optimal control $J(t)$ and the analytical quantum speed limit for SWAP gate. We solve the Euler-Lagrange equations for the two-band Fermi-Hubbard model described in Sec. 5.3.1. We show in Sec. 5.2.2 that for the two-band Fermi-Hubbard model, optimizing the transfer from state $|\uparrow\downarrow\rangle$ to $|\downarrow\uparrow\rangle$ is sufficient to optimize the SWAP gate. As described in Sec. 5.3.1, the time-evolution with $\tilde{J}(t)=-\sqrt{2}J(t)$ and $U=0$ is

$$i\begin{pmatrix}\dot{x}_1\\ \dot{x}_2\\ \dot{x}_3\end{pmatrix} = \begin{bmatrix}0 & 0 & \tilde{J}(t)\\ 0 & 0 & \tilde{J}(t)\\ \tilde{J}(t) & \tilde{J}(t) & 0\end{bmatrix}\begin{pmatrix}x_1\\ x_2\\ x_3\end{pmatrix} \tag{5.26}$$

where x_1, x_2, and x_3 correspond to complex coefficients of the states $|\uparrow\downarrow\rangle$, $|\downarrow\uparrow\rangle$, and $(|D0\rangle + |0D\rangle)/\sqrt{2}$ respectively. Thus, optimizing the SWAP gate reduces to finding $\tilde{J}(t)$ for evolving the system from $(1,0,0)^T$ to $(0,1,0)^T$, or at least up to a phase factor as we see below.

With $x_1 = r_1 + ir_4, x_2 = r_2 + ir_5$, $x_3 = r_6 + ir_3$, and real $r_j = r_j(t)$ and $\tilde{J}(t)$, we obtain

$$\dot{r}_1 = \tilde{J}(t)r_3,\ \dot{r}_2 = \tilde{J}(t)r_3,\ \dot{r}_3 = -\tilde{J}(t)r_1 - \tilde{J}(t)r_2 \ \text{ and}$$
$$\dot{r}_4 = -\tilde{J}(t)r_6,\ \dot{r}_5 = -\tilde{J}(t)r_6,\ \dot{r}_6 = \tilde{J}(t)r_4 + \tilde{J}(t)r_5.$$

So the variables r_1, r_2, and r_3 are decoupled from r_4, r_5, and r_6. We obtain two independent three-dimensional subsystems and we work with the first subsystem of

them [299]. The ordinary differential equations are given by

$$\begin{pmatrix} \dot{r}_1 \\ \dot{r}_2 \\ \dot{r}_3 \end{pmatrix} = \begin{bmatrix} 0 & 0 & \tilde{J}(t) \\ 0 & 0 & \tilde{J}(t) \\ -\tilde{J}(t) & -\tilde{J}(t) & 0 \end{bmatrix} \begin{pmatrix} r_1 \\ r_2 \\ r_3 \end{pmatrix}. \tag{5.27}$$

Clearly, $r_1^2 + r_2^2 + r_3^2 = 1$, provided we start in the subspace r_1, r_2, and r_3. From Eq. (5.27),

$$\dot{r}_1 = \dot{r}_2 \text{ implies } r_1 = r_2 + C \tag{5.28}$$

for a suitable real constant C. Minimizing the transfer time T is equivalent [299] to minimizing the functional

$$\mathcal{E} = \int_0^T \tilde{J}^2(t)\, dt = \int_0^T \mathcal{L}\, dt,$$

and $\tilde{J}(t) = -\sqrt{2}J(t)$ needs to be bounded for the optimal solution to be well defined. Applying Eq. (5.27), the Lagrangian of the system is given by

$$\mathcal{L} = \tilde{J}^2(t) = \frac{\dot{r}_1^2}{r_3^2} = \frac{\dot{r}_1^2}{1-r_1^2-r_2^2} = \frac{\dot{r}_1^2}{1-r_1^2-(r_1-C)^2}.$$

The upper bound on the control can be re-normalized by the maximum amplitude that is possible in an experiment. We use the Euler-Lagrange equations

$$\frac{d}{dt}\left[\frac{\partial \mathcal{L}}{\partial \dot{r}_1}\right] = \frac{\partial \mathcal{L}}{\partial r_1} \tag{5.29}$$

to find the optimal solution. Computing the left hand side of Eq. (5.29), we have

$$\frac{\partial \mathcal{L}}{\partial \dot{r}_1} = \frac{2\dot{r}_1}{r_3^2} \text{ which implies } \frac{d}{dt}\left[\frac{\partial \mathcal{L}}{\partial \dot{r}_1}\right] = 2\frac{d}{dt}\left[\frac{\dot{r}_1}{r_3^2}\right]$$

and the corresponding right hand side is given by

$$\begin{aligned} \frac{\partial \mathcal{L}}{\partial r_1} &= \frac{\partial}{\partial r_1}\left[\frac{\dot{r}_1^2}{1-r_1^2-r_2^2}\right] \\ &= -\frac{\dot{r}_1^2}{(1-r_1^2-r_2^2)^2}\frac{\partial}{\partial r_1}[1-r_1^2-(r_1-C)^2] = \frac{\dot{r}_1^2}{r_3^4}(4r_1-2C). \end{aligned}$$

Therefore, Eq. (5.29) simplifies to

$$\frac{d}{dt}\left[\frac{\dot{r}_1}{r_3^2}\right] = \frac{\dot{r}_1^2}{r_3^4}(2r_1-C). \tag{5.30}$$

We separately compute

$$\begin{aligned}\frac{d}{dt}\left[\frac{\dot{r}_1}{r_3^2}\right] &= \frac{1}{r_3}\frac{d}{dt}\left[\frac{\dot{r}_1}{r_3}\right] + \frac{\dot{r}_1}{r_3}\frac{d}{dt}\left[\frac{1}{r_3}\right] \\ &= \frac{1}{r_3}\frac{d}{dt}\left[\frac{\dot{r}_1}{r_3}\right] - \frac{\dot{r}_1}{r_3^3}\left[-\tilde{J}(t)r_1 - \tilde{J}(t)r_2\right] \\ &= \frac{1}{r_3}\frac{d}{dt}\left[\frac{\dot{r}_1}{r_3}\right] - \frac{\dot{r}_1}{r_3^3}\left[-\frac{\dot{r}_1}{r_3}r_1 - \frac{\dot{r}_1}{r_3}(r_1 - C)\right] \\ &= \frac{1}{r_3}\frac{d}{dt}\left[\frac{\dot{r}_1}{r_3}\right] + \frac{\dot{r}_1^2}{r_3^4}(2r_1 - C)\end{aligned}$$

and we substitute this back into Eq. (5.30) and obtain

$$\frac{d}{dt}\left[\frac{\dot{r}_1}{r_3}\right] = 0 = \frac{d\tilde{J}(t)}{dt}.$$

This finally implies that $\tilde{J}(t)$ and $J(t)$ are constant. We substitute $\tilde{J}(t) = -\sqrt{2}A$ in Eq. (5.26) where A is a suitable constant. We now consider the initial conditions $x_1(0) = 1$, $x_2(0) = 0$, and $x_3(0) = 0$. Note that this implies $C = 1$ in Eq. (5.28). For these initial conditions, we directly solve Eq. (5.26) (which has now only constant coefficients) and obtain

$$x_1 = \cos^2(At),\ x_2 = -\sin^2(At),\ x_3 = i\sin(2At)/\sqrt{2}. \tag{5.31}$$

For the target state $(0, -1, 0)^T$, we get $AT = \pi/2 + n\pi$. Hence, the fastest transfer from $(1, 0, 0)^T$ to $(0, -1, 0)^T$ can be attained in a time of $T = \pi/(2A)$. This defines our quantum speed limit for the SWAP gate and is given by the constant hopping parameter $J(t) = A$. Clearly, $J(t) = A$ needs to be bounded by a maximal allowed $J_{\max}$, i.e. $J(t) \leq J_{\max}$. The value of $J_{\max}$ depends on the experimental setup and we set $J_{\max} = 34.03$ kHz for the two-band numerical simulations in Sec. 5.3.2. That means the quantum speed limit for the two-band SWAP gate is $T = \pi/(2J_{\max})$. We obtain the control $J(t) = A = 34.03$ kHz and the corresponding quantum speed limit is $T = 0.046$ ms.

5.11.2 Approximate analytical gradient

As explained in Sec. 5.5, we can not use the fast spline-fit method (described in Sec. 5.3.2 and Appendix 5.11.3) for calculating the gradients of the cost function C for optimizations using higher-band models. In this appendix, we derive an approximate analytical formula for the gradients and use it in the optimizations performed in Sec. 5.5.1. Our primary focus is to find an analytical formula for calculating dC/dV_k

where $V_k \in \{V_s, V_\ell\}$. The cost function C for the target state Ψ_{tar} and the modified time evolution of Eq. (5.23) is

$$C=1-|\langle\Psi_{\text{tar}}|\,\mathcal{U}_{N_T}\cdot\cdot P(w_{t+1},w_t)\mathcal{U}_t P(w_t,w_{t-1})\cdot\cdot\mathcal{U}_1|\Psi_{\text{ini}}\rangle|^2.$$

Using the product rule, one infers that dC/dV_k has three terms proportional to $\partial P(w_{t+1}, w_t)/\partial V_k$, $\partial\mathcal{U}_t/\partial V_k$, and $\partial P(w_t, w_{t-1})/\partial V_k$. We approximate the gradient of the unitary evolution operator $\mathcal{U}_t$ as

$$\frac{\partial e^{-iH_t\partial t}}{\partial V_k} = -iH_t'\partial t e^{-iH_t\partial t}, \tag{5.32}$$

where H_t is the higher-band Fermi-Hubbard Hamiltonian (5.17) at time step t. To calculate H_t' from (5.17), we need to calculate $\partial J_p/\partial V_k$ and $\partial\epsilon_{pm}/\partial V_k$; all other terms proportional to a are zero. The hopping parameter J_p and the onsite energy ϵ_p is calculated from Eqs. (5.18) and (5.20) which can also be written as

$$J_p = \frac{E_{2p+1} - E_{2p}}{2}\ ;\ \epsilon_p = \frac{E_{2p+1} + E_{2p}}{2},$$

where E_j is the energy of the jth band of the double well. Therefore we can calculate $\partial J_p/\partial V_k$ and $\partial\epsilon_{pm}/\partial V_k$ as

$$\frac{\partial J_p}{\partial V_k} = \frac{1}{2}\Big(\frac{\partial E_{2p+1}}{\partial V_k} - \frac{\partial E_{2p}}{\partial V_k}\Big),\ \frac{\partial \epsilon_p}{\partial V_k} = \frac{1}{2}\Big(\frac{\partial E_{2p+1}}{\partial V_k} + \frac{\partial E_{2p}}{\partial V_k}\Big). \tag{5.33}$$

Moreover, $\partial E_i/\partial V_k$ can be calculated from

$$\frac{\partial E_i}{\partial V_k} = \sum_j v_{ij}^\dagger \frac{\partial \tilde{H}_1(q)}{\partial V_k} v_{ij}, \tag{5.34}$$

where $\tilde{H}_1(q)v_{ij} = E_{ij}v_{ij}$ and $v_{ij}^\dagger v_{ij} = 1$ [309]. Here, $\tilde{H}_1(q)$ denotes the Fourier transform of the Hamiltonian in Eq. (5.1) and v_{ij} are the eigenstates of $\tilde{H}_1(q)$ [see Sec. 5.2 and Eq. (5.5)]. Thus we can calculate $\partial\mathcal{U}_t/\partial V_k$ using Eq. (5.32)-(5.34) and eventually the final gradient dC/dV_k. Next, the basis transformation operator $P(w_{t+1}, w_t)$ depends on the Wannier function w_t so that

$$\frac{\partial P(w_{t+1}, w_t)}{\partial V_k} = P(w_{t+1}, \frac{\partial w_t}{\partial V_k}).$$

The gradient of the Wannier functions is calculated via [309]

$$\frac{\partial w_i}{\partial V_k} = -\sum_j [\tilde{H}_1(q) - E_{ij}\mathcal{I}]^+ \left[\frac{\partial \tilde{H}_1(q)}{\partial V_k} - \frac{\partial E_{ij}}{\partial V_k}\right] v_{ij},$$

where $\mathcal{I}$ is the identity operator and $[\tilde{H}_1(q)-E_{ij}\mathcal{I}]^+$ is the Moore-Penrose inverse of $[\tilde{H}_1(q)-E_{ij}\mathcal{I}]$. The contribution of $\partial P(w_{t+1}, w_t)/\partial V_k$ is negligible in the final gradient dC/dV_k. So, we set this term to zero, speeding up the calculations by avoiding several matrix multiplications. Similarly, we ignore the term $\partial P(w_t, w_{t-1})/\partial V_k$. This approximate analytical gradient computation is significantly faster than the finite-difference method, as shown in Appendix 5.11.3. However, it becomes difficult to optimize pulses further when we are getting close to the minimum since the approximate analytical method does not provide an exact gradient. Therefore, we reach the minimum SWAP- and $\sqrt{\text{SWAP}}$-gate error by combining the approximate analytical and finite-difference methods.

5.11.3 Comparison of different methods to compute gradients

Throughout the paper, we have used gradient-based methods for optimizing the lattice depths V_s and V_ℓ and the scattering length a. We optimize V_s and V_ℓ for the SWAP gate, and V_s, V_ℓ, and a for the $\sqrt{\text{SWAP}}$ gate using GRAPE-like algorithms. The gradient calculation for the optimization of a is trivial and finite differences work efficiently since we need to optimize only one parameter. However, V_s and V_ℓ are time-dependent and piecewise-constant controls, so we need more sophisticated and faster ways of calculating the gradient. One straightforward way for calculating gradients is to use the finite-difference method to calculate dC/dV_k for $k \in \{s, \ell\}$ at every time step. We use the efficient built-in finite-difference implementation from Scipy [271] for the comparison in this section. We can also calculate the gradient analytically using the approximation discussed in Sec. 5.11.2. For the two-band optimization performed in Sec. 5.3.2, we use the spline-fit method to calculate the gradients. For the spline-fit method, we first store a data set of triples (V_s, V_ℓ, J). From the stored data set, we fit a spline function $J{=}S(V_s, V_\ell)$ over the grid of pairs (V_s, V_ℓ). We use the SciPy package [271] for the spline-fit and this function also provides us with the gradient of the estimated J at any pair (V_s, V_ℓ). We use these gradients in the GRAPE algorithm to run the full optimization (refer to Sec. 5.3.2 for details). One can also use automatic differentiation for gradient calculation [310], but it can be slow in the presence of multiple matrix diagonalizations for calculating the Wannier states. Hence, we do not analyze the performance of automatic differentiation here. Two parameters are used to test the efficiency of different gradient methods. First, we check the number of cost function evaluations in the optimization for a particular gradient method. Secondly, the total optimization run times are compared for different gradients.

We compare the gradient methods for the two-band model at varying gate durations. Figure 5.14(a) shows that the finite-difference method results in the highest

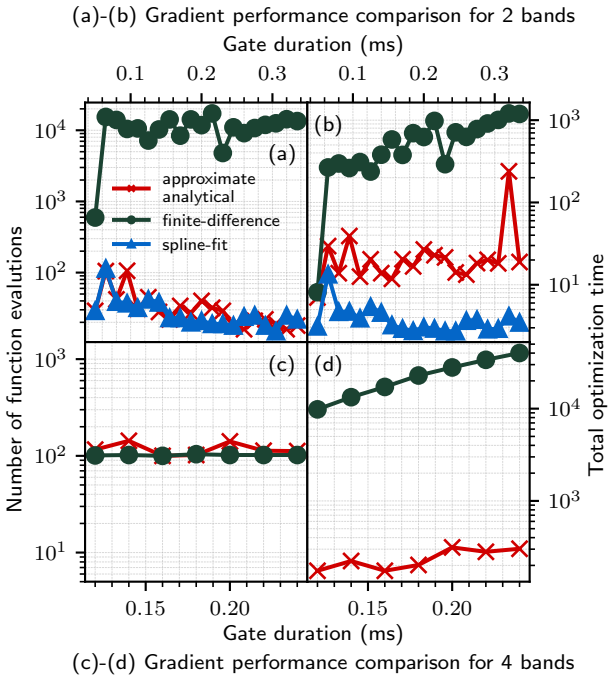

Figure 5.14: Performance of the approximate analytical, the finite-difference, and the spline method for computing the gradient for two-band (a)-(b) and four-band (c)-(d) Fermi-Hubbard optimizations: (a)-(b) Overall spline method performs best both in the number of evaluations and the total optimization time and remains mostly constant regardless of the gate duration, while the finite-difference method preforms worst and its total optimization time increases with the gate duration. (c)-(d) The number of function evaluations for the approximate analytical gradient computation is comparable with the finite-difference method, which however performs much worse for the total optimization time. The spline method is not available for four bands.

number of function evaluations for every gate duration, whereas the approximate analytical and spline-fit methods are comparable. Function evaluations decrease for longer gate durations due to lower initial gate error and easier optimization tasks for longer durations. Figure 5.14(b) provides insights into the performance of different gradient methods. The finite difference method is the slowest to reach the minima and optimization times increase linearly with the gate duration. The approximate analytical and spline-fit method result in run times that are relatively independent of the gate duration. But the approximate analytical gradient needs a longer time compared to the spline fit. As the spline fit calculates J and dC/dV_k from existing fitted functions, it avoids several matrix diagonalizations and multiplications needed for calculating the Wannier states, which render the approximate analytical gradient computationally more expensive.

A similar comparison is done for the four-band model where we compare the performance of the approximate analytical gradient with the finite-difference gradient. Note, that since we have to calculate basis transformation operators at every time

$\uparrow$	$\downarrow$	$I_\uparrow$	$I_\downarrow$	$I = I_\uparrow\binom{S}{N_\downarrow} + I_\downarrow$
0001	0001	0	0	0
0001	0010	0	1	1
:	:	:	:	:
0010	0001	1	0	4
:	:	:	:	:
1000	1000	3	3	15

Table 5.2: A scheme explaining the calculation and labeling of the computational states for $N_\uparrow = 1$ and $N_\downarrow = 1$. In the first column, the total number of bits is the number of sites and the number of ones in each bit configuration represents the number of spins up. The same applies to the second column, where the spins up are replaced with the spins down. The states are ordered first with spin-up (first and third column) and then with spin-down (second and fourth column). The final label (fifth column) is computed from Eq. (5.35).

step, we cannot use the spline-fit method for higher-band optimization. We set an upper bound on the number of function evaluations for both the finite-difference and the approximate analytical method. As we can see in Fig. 5.14(c) both methods have maximal function evaluations for all gate durations. However, finite differences lead to longer optimization times when compared to the approximate analytic method as shown in Fig. 5.14(d). This suggests that the spline-fit method performs significantly better than the approximate analytical and finite-difference methods, but for higher bands we cannot use the spline-fit method. In that case, the use of approximate analytical gradients is computationally effective. However, since the approximate analytical method does not give an exact gradient, we use a combination of the approximate analytical and finite-difference methods to minimize the cost function in Sec. 5.5.1. Hence, we use multiple methods for gradient calculation depending on the complexity of the system. Different methods have different trade-offs and combining them enables fast and efficient optimizations.

5.11.4 Assignment of computational basis

In this appendix, we describe the method used for finding computational basis states and labeling them for different number of atoms in a double well. We use this labeling method in Sec. 5.6 to simulate the dynamics of different atom configurations. Suppose we have M levels and N atoms in the double well. Now since each level consists of the left and right sides of the double well, we have a total of $S{=}2{\times}M$ sites. Now suppose, we have $N_\uparrow$ atoms with spin up and $N_\downarrow$ with spin down, i.e. $N{=}N_\uparrow{+}N_\downarrow$. We can arrange $N_\uparrow$ spin-up identical fermionic atoms in $\binom{S}{N_\uparrow}{=}S!/N_\uparrow!(S{-}N_\uparrow)!$ ways in

S sites. For each configuration of the spin-up atoms, we can arrange the spin-down atoms in $\binom{S}{N_\downarrow}=S!/N_\downarrow!(S-N_\downarrow)!$ ways. The total number of possibilities we can arrange $N=N_\uparrow+N_\downarrow$ atoms in a double well is the number of computational states and is given by $N_B = \binom{S}{N_\uparrow} \times \binom{S}{N_\downarrow}$. As an example, Table 5.2 shows the possible computational basis states for two atoms with one spin-up and one spin-down used in the four-band Fermi-Hubbard model in Sec. 5.5. Here $M=2, S=4, N=2, N_\uparrow=1$, and $N_\downarrow=1$. So the total number of computational states is 16. We represent the spin-up and spin-down state by S bits and label our computational state using the following formula

$$I = I_\uparrow \binom{S}{N_\downarrow} + I_\downarrow, \tag{5.35}$$

where these values observe $I_\uparrow \in \{0, \ldots, \binom{S}{N_\uparrow}-1\}$, $I_\downarrow \in \{0, \ldots, \binom{S}{N_\downarrow}-1\}$, and $I \in \{0, \ldots, N_B-1\}$.

6

Symmetry analysis for VQE on Rydberg atom simulators

As quantum computing progresses, variational quantum eigensolvers (VQE) for ground-state preparation have become an attractive option in leveraging current quantum hardware. However, a major challenge in implementing VQE is understanding whether a given quantum system can even reach the target ground state. In this work, we study reachability conditions for VQE by analyzing their inherent symmetries. We consider a Rydberg-atom quantum simulator with global controls and evaluate its ability to reach ground states for Ising and Heisenberg target Hamiltonians. Symmetry-based conclusions for a smaller number of qubits are corroborated by VQE simulations, demonstrating the reliability of our approach in predicting whether a given quantum architecture could successfully reach the ground state. Our framework also suggests approaches to overcome symmetry restrictions by adding additional quantum resources or choosing different initial states, offering practical guidance for implementing VQE in quantum simulation architectures. Finally, we illustrate connections to adiabatic state preparation.

This chapter has been published as preprint, with minor changes, as Juhi Singh, Andreas Kruckenhauser, Rick van Bijnen, and Robert Zeier, *Ground-state reachability for variational quantum eigensolvers: a Rydberg-atom case study*, arXiv.2506.22387. The thesis author conducted most of the analysis (based on the variational quantum eigensolver codes written by Andreas Kruckenhauser, major part of Magma code written by Robert Zeier), composed all the figures (with the exception of Fig. 6.8) and wrote most of the manuscript with input from the co-authors.

6.1 Introduction

One promising solution to address limitations of classical computing is to apply quantum co-processors, which process information at the quantum level using qubits instead of digital bits [4, 311, 312]. This enables us to leverage superposition and entanglement to eventually outperform classical algorithms [313]. Although ideal quantum processors are still developing, imperfect devices from fifty to thousand qubits have demonstrated intriguing performance for certain tasks, marking the start of the noisy intermediate scale quantum (NISQ) era [2, 31, 312, 314–321].

On the software front, various research groups have been developing effective algorithms applicable to quantum computing and simulation. Among these are variational quantum algorithms, which enable the use of current quantum hardware by integrating with classical optimization techniques [30, 198–200, 322]. These algorithms leverage a parameterized quantum circuit to prepare trial wavefunctions, which are iteratively adjusted in a feedback loop with a classical computer minimizing a cost function reflecting the quality of a prepared quantum state. Variational quantum eigensolvers (VQE) [200–203] aim at preparing a good approximation of the ground state of an Hamiltonian, while using the energy of the state as a cost function. VQE optimizes variational parameters of a quantum circuit based on a sequence of quantum logic gates for digital quantum simulators [323, 324]. Different ansätze have been proposed and analyzed for variational optimization tasks [204–207, 325]. Moreover, for analog quantum simulators, multiple unitary blocks are driven using the parameterized controls [192, 326, 327] which are variationally adjusted. These algorithms are particularly intriguing within the framework of quantum phase transitions [327–330]. After reaching the ground state, one can experimentally analyze its characteristics, such as correlation functions, and investigate how the system responds to externally applied perturbations.

Variational algorithms have been successfully implemented on various platforms, including photonic processors [200, 331], superconducting qubits [326, 332, 333], and trapped ion systems [325, 327, 328, 334, 335]. Alongside these platforms, neutral atoms excited to Rydberg states gained attention as a promising quantum processing platform, offering coherent control [14, 15, 284, 336, 337] over hundreds of atoms [16, 338–342] trapped in reconfigurable optical arrays [343–345]. In particular, these systems can be controlled via global and/or local external fields, enabling the execution of parameterized quantum circuits suitable for VQE applications [17, 346]. However, it is generally difficult to predict whether a given set of control parameters is sufficient to prepare the ground state of a particular target Hamiltonian [347].

Control theory has been extensively applied both experimentally and theoretically

to address such challenges [348–350]. By using Lie-algebraic principles, control theory offers a robust framework for characterizing operations that a quantum device can perform [224, 351, 352]. The Lie algebra is used to study controllability, simulability, and reachability conditions for different quantum devices [195–197, 207, 352–362]. However, calculating the Lie algebra becomes difficult for increasing system sizes. For larger number of qubits, we can still determine and study the symmetries of a quantum system, i.e., the matrices that commute with the considered Hamiltonians [195, 197].

In this work, we apply and extend the Lie-algebra and symmetry tools developed in [195–197, 207, 327, 352, 361, 362] to match available quantum resources with the desired target ground states, assessing whether a given variational circuit can, in principle, prepare the ground state of a given target Hamiltonian. We focus on the ground state preparation for an Rydberg-atom analog simulator with global controls. We first consider the Lie-algebra and simulability structure of the resource Hamiltonians without and with the target Hamiltonian, which reveals that the ability to simulate a target Hamiltonian does not imply that one can reach its ground state(s). For a complete analysis, we determine the invariant subspaces of the resource Hamiltonians highlighting that the success of VQE depends critically on the position of the initial state and the target ground state in the invariant subspaces. We relate our symmetry analysis for testing the ground state reachability to adiabatic state preparation [363] and the adiabatic theorem [364–369]. Lastly, we illustrate how symmetries can guide us in preparing a suitable initial state to reach the ground state of the target Hamiltonian. This study provides tools aimed at analyzing and improving the execution of variational quantum algorithms.

The work is structured as follows: In Sec. 6.2, we describe the considered Rydberg-atom quantum simulator and its resource Hamiltonians and we detail the VQE approach based on the example of Ising and Heisenberg target Hamiltonians. In Section 6.3, we introduce tools for the analysis of the reachability for VQE. In particular, Sec. 6.3.3 contains our symmetry analysis based on invariant subspaces. Section 6.4 extends our symmetry analysis to up to ten qubits. Different initial states and their VQE performance are considered in Sec. 6.5. Section 6.6 discusses connections to adiabatic state preparation. Finally, we present our conclusions in Sec. 6.7. Certain aspects are deferred to appendices.

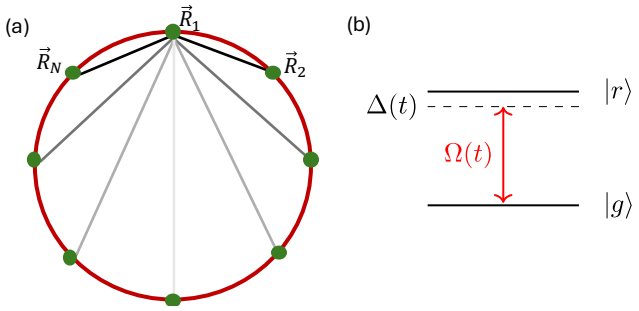

Figure 6.1: (a) Circular geometry: Illustration of the spatial positioning of laser trapped neutral atoms (green dots). Atoms excited to Rydberg states experience long-range van der Waals interactions which are visualized by the black lines (shown only for the atom at the position $\vec{R}_1$). The opacity of the lines reflects the interaction strength between a pair of atoms. (b) Level scheme of a single Rydberg atom: The ground state $|g\rangle$ is coupled with the Rydberg state $|r\rangle$ with a coupling $\Omega(t)$ and detuning $\Delta(t)$.

6.2 Variational quantum eigensolver (VQE)

6.2.1 Resource Hamiltonians

Neutral atoms excited to Rydberg states can act as an analog quantum simulator, capable of executing parameterized quantum circuits. In particular, we consider a setup where external control fields act globally on all atoms, thus a parametrized quantum circuit can be implemented by modulating control field parameters over time. Furthermore, the setup consists of N neutral atoms trapped in an optical lattice or tweezer array, with the qubit being encoded in a ground and Rydberg state of each atom [370–373]. For such an encoding the interactions between a pair of atoms in the Rydberg state are typically of van der Waals type (long-range) and always present.

The associated time-dependent system Hamiltonian reads in natural units ($\hbar = 1$)

$$H(t) = \Omega(t)\, H_\Omega - \Delta(t)\, H_\Delta + H_d, \tag{6.1}$$

where $\Omega(t)$ and $\Delta(t)$ denotes the time-dependent Rabi frequency and detuning of a globally acting laser field, respectively. The associated coupling Hamiltonians are defined as $H_\Omega := \sum_{n=1}^{N} \sigma_x^{(n)}$ and $H_\Delta := \sum_{n=1}^{N} \sigma_z^{(n)}$, where $\sigma_j^{(n)}$ is a Pauli matrix σ_j with $j \in \{x, y, z\}$ acting on the n^{th} atom. We are using the notation

$$\sigma_x := \left(\begin{smallmatrix} 0 & 1 \\ 1 & 0 \end{smallmatrix}\right),\ \sigma_y := \left(\begin{smallmatrix} 0 & -i \\ i & 0 \end{smallmatrix}\right),\ \sigma_z := \left(\begin{smallmatrix} 1 & 0 \\ 0 & -1 \end{smallmatrix}\right),\ \mathbb{1} = \left(\begin{smallmatrix} 1 & 0 \\ 0 & 1 \end{smallmatrix}\right).$$

The term H_d, called drift Hamiltonian, describes the interaction between atoms in the

Rydberg state and is in general given by

$$H_d := \sum_{1\leq n<m\leq N} \frac{C_6}{|\vec{R}_n - \vec{R}_m|^6}(\mathbb{1}-\sigma_z^{(n)})(\mathbb{1}-\sigma_z^{(m)}). \tag{6.2}$$

The strength of interaction is determined by the C_6-coefficient of the considered Rydberg state and the distance between the pair of atoms at positions $\vec{R}_n$ and $\vec{R}_m$.

For the remainder of this manuscript, we consider the N atoms to be arranged equidistantly on a ring as shown in Fig. 6.1. Due to the rotational symmetry of the atom arrangement the single particle terms of H_d from Eq. (6.2) can be absorbed in the global detuning $\Delta(t)$ and H_d can be written as

$$H_d := \sum_{1\leq n<m\leq N} \frac{C_6}{|\vec{R}_n - \vec{R}_m|^6}\sigma_z^{(n)}\sigma_z^{(m)}, \tag{6.3}$$

up to a global shift. In the ring geometry neighboring atoms experience the strongest interaction strength ($C_6/|\vec{R}_n - \vec{R}_{n\pm1}|^6$) and atoms sitting on opposite sides of the ring are interacting weakest.

6.2.2 VQE and the target Hamiltonian

The hybrid quantum-classical VQE algorithm prepares trial states $\Psi(\tau)$ that aim to approximate the ground state of a given target Hamiltonian $\mathcal{H}$. The VQE circuit is composed out of M layers of unitaries U_j, with $j \in \{1, \ldots, M\}$. Each unitary U_j is generated by time evolution of a set of resource Hamiltonians with associated external control knobs that act as variational parameters. The set of resource Hamiltonians considered throughout this work is constructed from the different drift and driving Hamiltonians following the hardware constraints detailed in Sec. 6.2.1 and is given by $\mathcal{G}_R := \{H_d, H_\Omega, H_\Delta\}$. The external control (variational) parameters are the Rabi frequency Ω_j, the detuning Δ_j, and the evolution duration δt_j of each layer j. Note, the parameters Ω_j and Δ_j are considered to be constant over the time interval δt_j. The trial state $\Psi(\tau)$ is prepared by evolving an initial state $\Psi(0)$ with the VQE circuit

$$\Psi(\tau) = U_M(\Omega_M, \Delta_M, \delta t_M)\cdots U_1(\Omega_1, \Delta_1, \delta t_1)\Psi(0),$$

see Fig. 6.2. Here $\tau = \sum_{j=1}^{M} \delta t_j$ is the total evolution time.

The trial state is used to measure the energy expectation value of the target Hamiltonian $\mathcal{H}$

$$E(\tau) = \Psi^\dagger(\tau)\,\mathcal{H}\,\Psi(\tau).$$

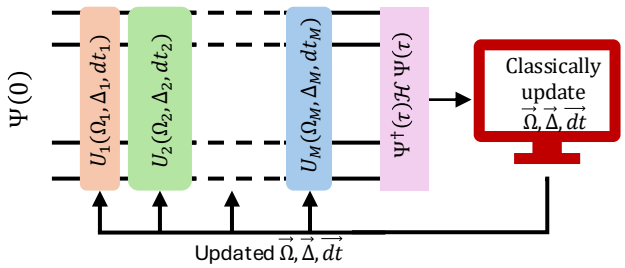

Figure 6.2: VQE circuit executed on the analog Rydberg-atom device by applying parametrized unitaries U_j for durations δt_j. The unitaries U_j are generated by globally acting controls Ω_j and Δ_j [see Eq. (6.1)]. The expectation value of the target Hamiltonian $\mathcal{H}$ with final state state $\Psi(\tau)$ is minimized by classically updating the VQE parameters $\vec{\Omega}$, $\vec{\Delta}$ and $\vec{\delta t}$.

This energy $E(\tau)$ defines the cost function and is minimized by a classical optimizer. The classical optimization iteratively updates the variational parameters of the VQE circuit: $\vec{\Omega} = (\Omega_1, \cdots, \Omega_M)$, $\vec{\Delta} = (\Delta_1, \cdots, \Delta_M)$, and $\vec{\delta t} = (\delta t_1, \cdots, \delta t_M)$. After several iterations, the VQE circuit prepares a state with an energy close to the ground state of the target Hamiltonian $\mathcal{H}$.

The success of VQE optimization relies heavily on the chosen ansatz and the initial state. It is generally difficult to predict whether a certain set of quantum resources is able to prepare the ground state of a particular target Hamiltonian $\mathcal{H}$. We examine this question in the succeeding sections for the groundstate of the Ising and the Heisenberg Hamiltonian on the ring illustrated in Fig. 6.1.

The Ising model's Hamiltonian is in the presence of a longitudinal and transverse field given by

$$\mathcal{H}_I = \Omega \sum_{n=1}^{N} \sigma_x^{(n)} - \Delta \sum_{n=1}^{N} \sigma_z^{(n)} + J \sum_{n=1}^{N} \sigma_z^{(n)} \sigma_z^{(n+1)}. \tag{6.4}$$

This model resembles the Hamiltonian of the Rydberg-atom simulator in Eq. (6.1) except for the drift term, which is truncated to nearest neighbor. The target Hamiltonian of the Heisenberg model is given by

$$\mathcal{H}_H = h \sum_{n=1}^{N} \sigma_z^{(n)} + J \sum_{n=1}^{N} \sum_{j \in \{x,y,z\}} \sigma_j^{(n)} \sigma_j^{(n+1)}. \tag{6.5}$$

Here, J denotes the isotropic interaction strength between neighboring spins, and h denotes the strength of an effective magnetic field in $z-$direction. Preparing the groundstate of these Hamiltonians presents a promising avenue for research. For example, the Ising model on a 2D triangular lattice with $J < 0$ exhibits frustration [374],

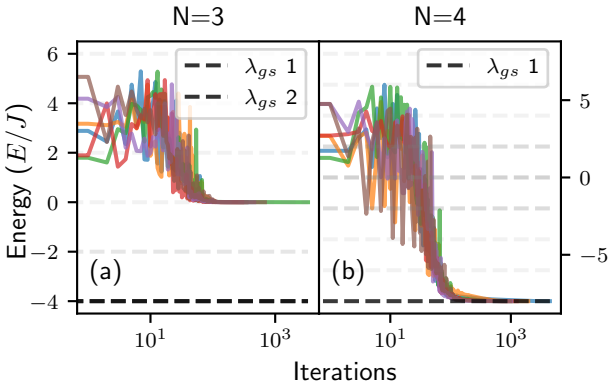

Figure 6.3: VQE for the Heisenberg model: (a)-(b) Variational energy with 10 random circuit initializations as a function of the optimization iterations (5000 iterations per initialization) for three and four sites. The energy of the variational states is compared to the eigenenergies λ of the target Hamiltonian $\mathcal{H}_H$ (grey dashed lines) and the ground state energy λ_{gs} (black dashed line) for $J = h$. (a) The three-site system has two degenerate ground states. VQE does not reach the ground state and gets stuck in the second excited state. (b) VQE reaches the ground state of $\mathcal{H}_H$ for four sites in all ten runs.

while the Heisenberg model on a 2D triangular lattice has been studied in the context of high-temperature superconductivity and the quantum Hall effect [375].

In our reachability analysis, we consider for the Ising Hamiltonian $\mathcal{H}_I$ of Eq. (6.4) the parameter choice $\Omega = \Delta = J$. Similarly, for the Heisenberg Hamiltonian from Eq. (6.5), we set $h = J$. As a starting point, we discuss here VQE of the Heisenberg target Hamiltonian $\mathcal{H}_H$ for three and four sites. Figure 6.3 presents optimization trajectories, i.e. trial state energy as a function of optimization steps. Each curve represents one of ten optimization runs, all starting from the same inital state but using different random starting points in the parameter space. Figure 6.3(a) illustrates that the VQE is unable to reach the ground state of $\mathcal{H}_H$ for three sites and gets stuck in one of the excited states. But, for four sites, the VQE reaches the ground state of $\mathcal{H}_H$ in all ten runs [see Fig. 6.3(b)]. The difference between the three and four-qubit case suggests a symmetry obstruction for reaching the ground state.

6.3 Tools for analyzing reachability

We aim at developing criteria to decide if the ground state(s) of a target Hamiltonian $\mathcal{H}$ are reachable from the initial state by following dynamics facilitated by the resource Hamiltonians $\mathcal{G}_R := \{H_d, H_\Omega, H_\Delta\}$. In order to understand the restrictions for VQE with a Rydberg-atom simulator, we consider multiple tools, some of which will be more useful and effective than others.

In Sec. 6.3.1, we recall the notion of a Lie algebra and its reductive decomposition (vide infra). Determining the Lie algebra $\mathfrak{g}_R := \langle \mathcal{G}_R \rangle_{\text{Lie}}$ generated by the resource Hamiltonians $\mathcal{G}_R$ and the reductive decomposition of $\mathfrak{g}_R$ can provide valuable information about the reachability and will help us to understand the structure of few-qubit examples. Indeed, combining the knowledge of the Lie algebra and its reductive decomposition with the structure of the invariant subspaces (see Sec. 6.3.3) provides a complete picture to decide reachability. However, computing the Lie algebra will be in larger cases quite challenging, and even more so for the reductive decomposition. Therefore, we would like to avoid the computation of the Lie algebra in larger examples.

Much more computationally feasible is the symmetry analysis in Sec. 6.3.3 based on the invariant subspaces, especially if we restrict us to the coarse-grained structure determined by the isotypic subspaces (vide infra). Thus one proposed approach to the reachability relies on the invariant subspaces, which leads to necessary conditions depending on whether the initial and target ground states lie in the same isotypic (or irreducible) subspace. Even beyond direct computations, partial knowledge of the inherent symmetries of the resource Hamiltonians $\mathcal{G}_R$ based on physical considerations can already yield obstructions to the reachability of the ground state(s) of the target Hamiltonian $\mathcal{H}$. Moreover, we can potentially extrapolate from smaller examples to provide information on the reachability of larger examples. In the later Sec. 6.6, we propose a complementary approach to reachability based on adiabatic state preparation and we connect this approach to the structure of the invariant subspaces.

Before the symmetry analysis in Sec. 6.3.3, we study in Sec. 6.3.2 to what degree the simulability (vide infra) of the target Hamiltonian $\mathcal{H}$ relates to the reachability of its ground states. This does neither lead to necessary nor sufficient conditions, but we consider it important to clarify and emphasize the distinction between simulability and reachability.

6.3.1 Lie algebras

We start by recalling Lie algebras and their reductive decompositions [376–378] generated by the resource Hamiltonians $\mathcal{G}_R$ and similarly when extending the generators with either the target Hamiltonian $\mathcal{H}_I$ or $\mathcal{H}_H$ [see Eqs. (6.4) and (6.5)]. Recall that the (real) Lie algebra $\mathfrak{g} := \langle \mathcal{G} \rangle_{\text{Lie}}$ generated by a set of hermitian Hamiltonians $\mathcal{G} = \{H_1, ..., H_p\}$ (such as $\mathcal{G}_R$) contains all (real) linear combinations $r_j h_j + r_k h_k$ with $r_j \in \mathbb{R}$ and all commutators $[h_j, h_k] := h_j h_k - h_k h_j$ for each $h_j, h_k \in \mathfrak{g}$, while starting from the skew-hermitian elements $h_j := iH_j$. The dimension of $\mathfrak{g}$ is given by its maximal number of linearly independent elements.

The reductive decomposition $\mathfrak{g} = \mathfrak{g}_1 \oplus \cdots \oplus \mathfrak{g}_k$ decomposes $\mathfrak{g}$ into its simple or abelian components $\mathfrak{g}_j$ with $[\mathfrak{g}_j, \mathfrak{g}_k] = 0$. In this work, the symbol $\oplus$ refers to direct sums of simple or abelian components of a Lie algebra. In particular, the center $Z(\mathfrak{g})$ of a Lie algebra $\mathfrak{g}$ consists of all its elements $z \in \mathfrak{g}$ such that $[z, h_j] = 0$ for all $h_j \in \mathfrak{g}$. An m-dimensional center $Z(\mathfrak{g})$ will be represented by a direct sum $\mathfrak{u}(1) \oplus \cdots \oplus \mathfrak{u}(1)$ of m one-dimensional abelian components. The corresponding computational techniques are detailed in Appendix 6.8.1.

6.3.2 Simulability analysis

As a first attempt to study the reachability, we analyze the simulability of the target Hamiltonian $\mathcal{H}$ by applying the resource Hamiltonians based on computing the relevant Lie algebras (see Sec. 6.3.1). We discuss whether this will resolve the reachability question. But, below, we will conclude that this is not the case!

The set of resource Hamiltonians $\mathcal{G}_R$ can simulate the dynamics of the target Hamiltonian $\mathcal{H}$ if and only if the Lie algebra $\mathfrak{h} := \langle \mathcal{G}_R \cup \{\mathcal{H}\} \rangle_{\text{Lie}}$ is contained in the Lie algebra $\mathfrak{g}_R := \langle \mathcal{G}_R \rangle_{\text{Lie}}$, or equivalently, iff $\mathfrak{g}_R = \mathfrak{h}$ [195, 351]. Note that $\mathfrak{h}$ is generated by $\mathcal{H}$ and the resource Hamiltonians $\mathcal{G}_R$, while $\mathfrak{g}_R$ is generated only by the resource Hamiltonians $\mathcal{G}_R$.

We consider the Heisenberg target Hamiltonian and determine the Lie algebras $\mathfrak{g}_R$ and $\mathfrak{h}_H := \langle \mathcal{G}_R \cup \{\mathcal{H}_H\} \rangle_{\text{Lie}}$ for three and four qubits. The corresponding Lie algebras are shown in Table 6.1 by detailing their reductive decompositions and centers. We observe that the Lie algebras $\mathfrak{g}_R$ and $\mathfrak{h}_H$ agree for three qubits but differ by an element of the center in $\mathfrak{h}_H$ for four qubits. The corresponding dimensions of the center of $\mathfrak{g}_R$ and $\mathfrak{h}_H$ are one and two for four qubits, whereas they are the same for the three-qubit system. The simulability condition of $\mathfrak{h}_H = \mathfrak{g}_R$ suggests that the VQE, in principle, can simulate the Heisenberg Hamiltonian for a system of three qubits. However, simulating the dynamics of $\mathcal{H}_H$ by resource Hamiltonians is not completely feasible for a system of four qubits (due to the additional center element).

How does this compare with the VQE results presented in Fig. 6.3? Contrary to the suggestions from the simulability analysis, the VQE was unable to reach the ground state energy for the three-qubit system and successfully converged to the ground state for the four-qubit system. These observations imply that the simulability analysis alone is not enough to capture the symmetry constraints governing VQE optimization. Consequently, we need to provide an alternative approach that could (partially) predict the reachability of the ground state of the target Hamiltonian.

Number of qubits	Resource Lie algebra $\mathfrak{g}_R$	Extension by adding the Heisenberg target $\mathcal{H}_H$
3	$\mathfrak{su}(4)\oplus\mathfrak{su}(2)\oplus\mathfrak{u}(1)$	–
4	$\mathfrak{su}(6)\oplus\mathfrak{su}(3)\oplus\mathfrak{su}(3)\oplus\mathfrak{u}(1)$	$\oplus\mathfrak{u}(1)$

Table 6.1: Lie algebras and simulability analysis without and with the Heisenberg target Hamiltonian. We compare the Lie algebra $\mathfrak{g}_R$ of the infinitesimal resource Hamiltonians $\mathcal{G}_R$ with the Lie algebra $\mathfrak{h}_H$ of the resource Hamiltonians combined with the Heisenberg target Hamiltonian, i.e. $\mathcal{G}_R \cup \{\mathcal{H}_H\}$, for three and four qubits. We describe the Lie algebras by their reductive decompositions. The dimension of the center $Z(\mathfrak{g})$ is equal to the number of one-dimensional abelian components $\mathfrak{u}(1)$. For the three-qubit case, the Lie algebras $\mathfrak{g}_R$ and $\mathfrak{h}_H$ agree (and their centers also agree). For four qubits, the dimension of $\mathfrak{h}_H$ is by one larger than $\mathfrak{g}_R$ due to an additional center element. The additional center element in the extended Lie algebra for four qubits is acting on all $\mathbb{C}^3$ blocks in Fig. 6.4.

6.3.3 Symmetry analysis and invariant subspaces

We study the symmetries and invariant subspaces to assess the reachability the target ground state(s) for the given resource Hamiltonians $\mathcal{G}_R$. An *invariant* subspace of $\mathcal{G}_R$ (and of its generated Lie algebra $\mathfrak{g}_R$) is a subspace that its mapped to itself by the infinitesimal action of the resource Hamiltonians $\mathcal{G}_R$. We refer to [379–384] for more general context and results on invariant subspaces and representation theory.

To determine the decomposition into invariant subspaces, we first compute the commutant of the resource Hamiltonians $\mathcal{G}_R$ [195, 197]. The *symmetries* of the resource Hamiltonians (and the generated Lie algebra) are formally described by the commutant. The *commutant* is the matrix subspace of all complex matrices simultaneously commuting with the Hamiltonians $\mathcal{G}_R$ (i.e. $[S, iH_v] = 0$ for $S \in \mathbb{C}^{d\times d}$, $d = 2^N$, and $H_v \in \mathcal{G}_R$). It can be calculated as the simultaneous null space of the matrices $\mathbb{1}_d \otimes H_v - H_v \otimes \mathbb{1}_d$ for all $H_v \in \mathcal{G}_R$. This enables us to also calculate the center $\mathcal{Z}(\mathfrak{g}_R)$ of the generated Lie algebra from the commutant (see Appendix 6.8.2) without determining the Lie algebra $\mathfrak{g}_R$ and its reductive decomposition as in Sec. 6.3.1.

As our action via $\mathcal{G}_R$ corresponds to a subgroup of the unitary group (i.e. a compact Lie group), we know that all representations are completely reducible (i.e. semisimple) and thus decompose into irreducible (i.e. simple) representations [376] (and the same applies to invariant subspaces). Recall that an invariant subspace is *irreducible* if it cannot be further decomposed into smaller invariant subspaces. We denote an invariant subspace as *isotypic* (or primary) if it contains all and only the irreducible subspaces from the decomposition of the whole space that are isomorphic to each other (see, e.g., [385, p. 156] and [386, p. VIII.61]). We can construct projection matrices to the

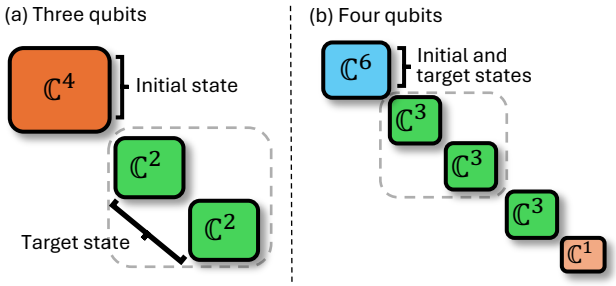

Figure 6.4: Block structure and invariant subspaces: Symmetry analysis of the VQE for the Heisenberg Hamiltonian with three and four qubits showing the invariant subspaces and the support of the initial state and the Heisenberg target ground state. Irreducible subspaces inside a gray dashed box are constructed from the same isotypic subspace. (a) For three qubits, the two isotypic subspces are $\mathbb{C}^4$ and $\mathbb{C}^2 \boxplus \mathbb{C}^2$ where the first one $\mathbb{C}^4$ is irreducible and the second one splits into two irreducible subspaces $\mathbb{C}^2 \boxplus \mathbb{C}^2$. Here, $\boxplus$ represents a direct sum of subspaces. The initial state has only support in $\mathbb{C}^4$ and the target ground state has only support in $\mathbb{C}^2 \boxplus \mathbb{C}^2$. Clearly, the target ground state can never be reached. (b) For four qubits, both the initial and the target state lie in the same irreducible component $\mathbb{C}^6$.

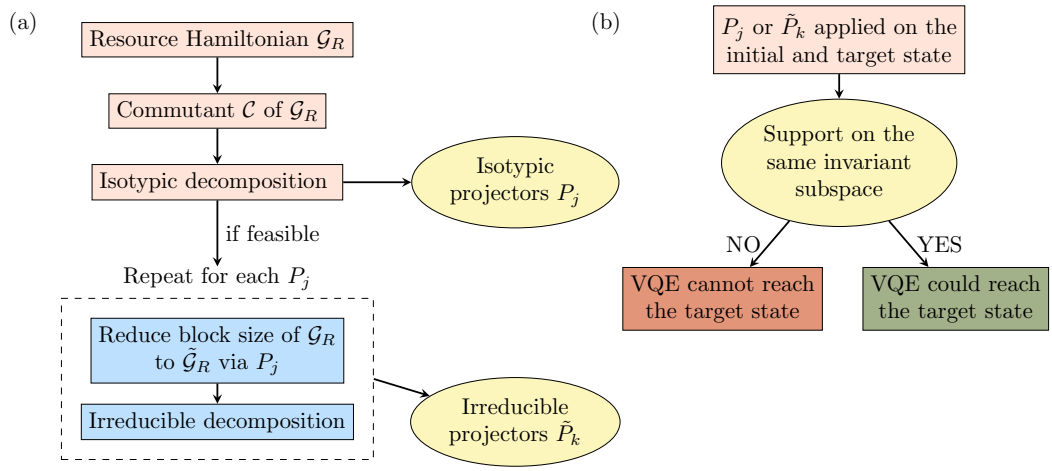

Figure 6.5: Flowchart for the symmetry analysis. (a) First, the commutant $\mathcal{C}$ is calculated from the resource Hamiltonians $\mathcal{G}_R$, followed by the computation of the isotypic projectors P_j. For smaller number of qubits, we can further break up the isotypic subspace, leading to the irreducible projectors $\tilde{P}_k$. They are obtained by reducing the resource Hamiltonians to a block size corresponding to the isotypic subspace of P_j. (b) The isotypic or irreducible projectors P_j or $\tilde{P}_k$ are applied to the initial and target states. If the initial and target states belong to the same invariant subspace(s), then the target state could be reached.

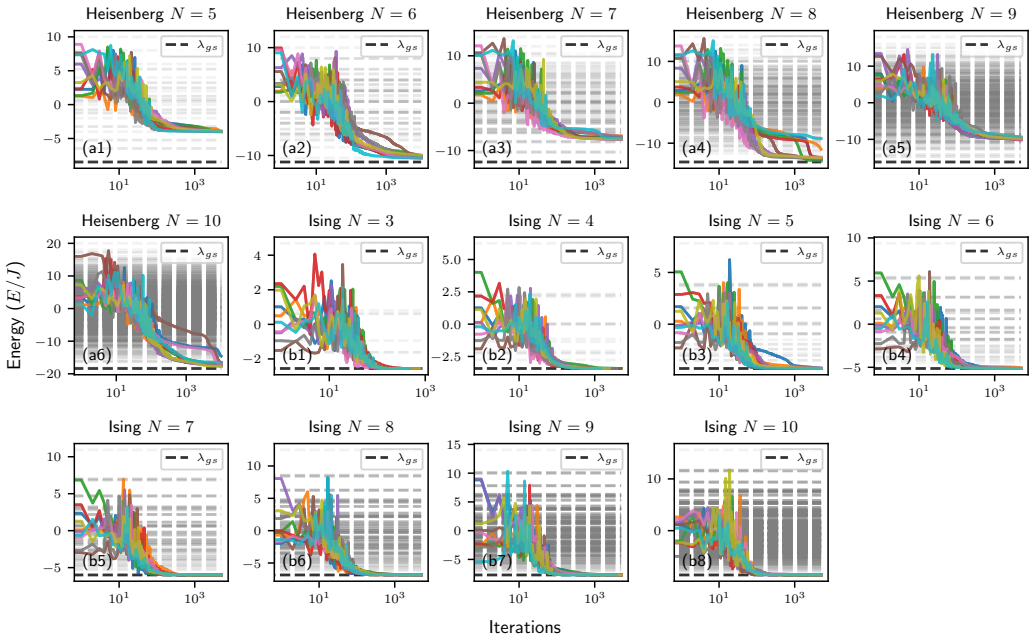

Figure 6.6: VQE for the Heisenberg and Ising ground state showing the expectation value of the energy compared to the eigenenergies λ (grey horizontal lines) and the ground state energy λ_{gs} (black horizontal line) of the target Hamiltonian as a function of the optimization steps for different number of qubits N and ten random circuit initializations. (a1)-(a6) For the Heisenberg target Hamiltonian $\mathcal{H}_H$ of Eq. (6.5) with $J = h = 1$, the optimization fails to reach the ground state while reaching only an excited state for all qubit numbers, except for $N \in \{4, 8, 10\}$. (b1)-(b8) For the Ising Hamiltonian $\mathcal{H}_I$ of Eq. (6.4) with $J = \Omega = \Delta = 1$ at least one instance of the optimization runs reaches the ground state energy for all considered qubit numbers, indicating that the resource Hamiltonians are in principle capable of preparing the ground state.

isotypic subspaces using effective algorithms based on first computing the center of the commutant [387]. If computationally feasible, this is combined with the so-called meataxe algorithm [382] to determine the irreducible subspaces in each isotypic one. But we first reduce the block size of the resource Hamiltonians by projecting them to a block size corresponding to the isotypic components with the help of the isotypic projectors (see App. 6.8.2). Figure 6.5(a) provides an overview and App. 6.8.2 details the computation of the isotypic and irreducible projectors.

We now discuss how the structure of the invariant subspaces affects the reachability of the ground state(s) from the initial state during the execution of VQE by providing necessary conditions. For this discussion, we assume that we know the ground state(s) by explicitly calculating them for the target Hamiltonian. This will not be possible for high qubit numbers but allows to get some insight into this structure starting from a small number of qubits. We project the computed ground state(s) with the isotypic (or the irreducible) projectors. Similarly, the conventional initial state $(1, 0, \ldots, 0)^T \in \mathbb{C}^d$

for $d = 2^N$ is projected. We record the supports in the various invariant subspaces, i.e., whether the projection is not zero. Clearly, any infinitesimal action of the resource Hamiltonians $\mathcal{G}_R$ on the initial state with support in one or more multiple invariant subspace(s) will preserve these invariant subspace(s). Thus the VQE can only reach the ground state(s) from a particular initial state if they lie in the same invariant subspace(s).

However, the condition that the initial and the target state lie in the same (irreducible) invariant subspace is not sufficient for the target state to be reachable from the initial state. This can even seen in a simple two-qubit example [195, 197]: both local unitary operations $\mathrm{SU}(2) \otimes \mathrm{SU}(2)$ and the full special unitary group $\mathrm{SU}(4)$ act irreducibly on the four-dimensional Hilbert space, while local unitary operations *cannot* reach entangled states from non-entangled ones. Thus our analysis based on containment in the same invariant subspace(s) will provide only a necessary condition for reachability.

We will now illustrate this analysis with the Heisenberg example for three and four qubits. Figure 6.4 shows the support for the initial and the target state on the occurring invariant subspaces. For three qubits, one observes the three irreducible, invariant subspaces $\mathbb{C}^4 \boxplus \mathbb{C}^2 \boxplus \mathbb{C}^2$, where both $\mathbb{C}^4$ and $\mathbb{C}^2 \boxplus \mathbb{C}^2$ are isotypic subspaces. Here, $\boxplus$ represents a direct sum of subspaces. The initial state has only support in the first isotypic subspace and the target state has only support in the second isotypic subspace. This implies that the VQE can never reach the Heisenberg target ground state for three qubits while starting from our choice of initial state. For four qubits, one obtains the invariant subspaces $\mathbb{C}^6 \boxplus \mathbb{C}^3 \boxplus \mathbb{C}^3 \boxplus \mathbb{C}^3 \boxplus \mathbb{C}^1$ with the four isotypic subspaces $\mathbb{C}^6$, $\mathbb{C}^3$, $\mathbb{C}^3 \boxplus \mathbb{C}^3$, and $\mathbb{C}^1$. Both the initial and the target state have a nonzero support only in the first isotypic (and irreducible) subspace $\mathbb{C}^6$. Thus the necessary condition for reachability is fulfilled and the symmetries of the resource Hamiltonians $\mathcal{G}_R = \{H_d, H_\Delta, H_\Omega\}$ do not prevent us from reaching the Heisenberg target ground state. This analysis is consistent with the VQE simulations in Fig. 6.3.

We emphasize that adding the Hamiltonian $\mathcal{H}_H$ to the resources would not help in reaching the target state. For the discussed three-qubit case, the generated Lie algebra $\mathfrak{g}_R$ is unchanged (see Table 6.1). Although the Lie algebra $\mathfrak{g}_R$ is extended by an additional center element for four qubits, the support of this element is restricted to outside of the subspace $\mathbb{C}^6$ which contains both the initial and the target state [as visualized in Fig. 6.4(b)]. Consequently, this additional center element cannot affect the reachability of the Heisenberg target ground state.

Number of qubits	Support		
	Initial state	Heisenberg target state(s)	Ising target state(s)
3	$\mathbb{C}^4$	$(\mathbb{C}^2 \boxplus \mathbb{C}^2)$	$\mathbb{C}^4$
4	$\mathbb{C}^6$	$\mathbb{C}^6$	$\mathbb{C}^6$
5	$\mathbb{C}^8$	$(\mathbb{C}^6 \boxplus \mathbb{C}^6)$	$\mathbb{C}^8$
6	$\mathbb{C}^{13}$	$\mathbb{C}^7$	$\mathbb{C}^{13}$
7	$\mathbb{C}^{18}$	$(\mathbb{C}^{18} \boxplus \mathbb{C}^{18})$	$\mathbb{C}^{18}$
8	$\mathbb{C}^{30}$	$\mathbb{C}^{30}$	$\mathbb{C}^{30}$
9	$\mathbb{C}^{46}$	$(\mathbb{C}^{56} \boxplus \mathbb{C}^{56})$	$\mathbb{C}^{46}$
10	$\mathbb{C}^{30}$	$\mathbb{C}^{30}$	$\mathbb{C}^{30}$

Table 6.2: Reachability of the Heisenberg and Ising target states for the VQE with the Rydberg-atom platform of Sec. 6.2. The invariant subspaces are determined together with the support of the initial state and the Heisenberg target state for three to ten qubits. The full decomposition of the invariant subspaces for the Heisenberg and Ising model is shown in Table 6.4 in Appendix 6.8.2. Two or more (isomorphic) irreducible subspaces inside two parentheses belong to one isotypic subspace. An isotypic subspace decomposes into irreducible subspaces which are represented with different colors if we have computationally determined the respective irreducible projectors (which applies only for up to eight qubits). The initial states for the VQE are same for both Heisenberg and Ising case. For the Heisenberg model, the initial and the target states are shown to be in different isotypic subspaces, except for four, eight, and ten qubits. This implies that the Heisenberg target state can never be reached for three, five, six, seven, and nine qubits using the chosen initial state. For the Ising case, the initial and the target states are always in the same irreducible subspace for three to ten qubits.

6.4 Larger system sizes

The VQE optimizations shown in Fig. 6.3 aim at finding the ground state of the Heisenberg Hamiltonian of Eq. (6.5), they are now extended for up to ten qubits in Fig. 6.6(a1)-(a6). The VQE only succeed for four, eight, and ten qubits. Whereas, Fig. 6.6(b1)-(b8) reveals that the VQE optimizations are successful for the Ising Hamiltonian of Eq. (6.4) with three to ten qubits.

This is now compared with the corresponding results from the symmetry analysis as summarized in Table 6.2. Following the analysis in Sec. 6.3.3, Table 6.2 lists the non-zero support of the initial state as well as the target ground state(s). We observe for five-qubit Heisenberg case that the initial state lies in the invariant subspace $\mathbb{C}^8$, while the ground state of the Heisenberg Hamiltonian lies in one of the isotypic subspaces of the form $\mathbb{C}^6 \boxplus \mathbb{C}^6$. Thus the ground state cannot be reach by the VQE. A similar

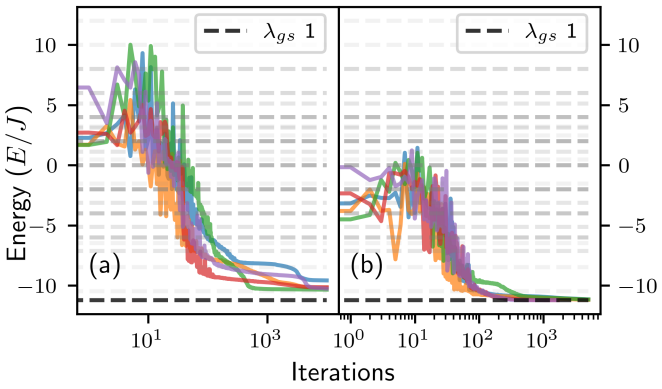

Figure 6.7: Comparison of VQE performance with different initial states for the six-qubit Heisenberg target ground state. (a) The VQE fails to converge to the target ground state when initialized from the trivial initial state introduced in Sec. 6.5 using six layers and 10000 iterations, indicating confinement within the $\mathbb{C}^{13}$ subspace. (b) By initializing VQE with an eigenvector ν_i from the projection operator related to the $\mathbb{C}^7$ subspace, the ground state is reached in all ten optimization runs in 5000 iterations.

analysis rules out the reachability for six, seven, and nine qubits in agreement with the VQE results from Fig. 6.6(a1)-(a6). For four, eight, and ten qubits, the initial and the target ground state are contained in the same irreducible subspace which corresponds to the successful VQE runs in Fig. 6.3(b) and Fig. 6.6(a1)-(a6). On the other hand, the symmetries of the resource Hamiltonians do not prevent us from reaching the Ising target ground state during the VQE as they both only have a nonzero support in a same irreducible subspace for up to ten qubits. This agrees with the corresponding VQE optimizations in Fig. 6.6(b1)-(b8).

Similar to the discussion in Sec. 6.3.3, we check whether adding the target Hamiltonian would affect and change the result of the reachability analysis in Appendix 6.8.3.

6.5 Initial state selection

One straightforward approach to resolve the symmetry restrictions resulting from the resource Hamiltonians is to choose a different initial state. The trivial initial state considered in the manuscript so far is the unique groundstate of $-\sum_{n=1}^{N}\sigma_z^{(n)}$, i.e. the state vector $(1,0,\ldots,0)^T \in \mathbb{C}^d$ for $d = 2^N$ in the conventional computational basis ordering. As clarified by the symmetry analysis, VQE can successfully prepare the ground state only if the initial state and the target ground state are situated within the same invariant subspace (which can be either an isotypic or irreducible subspace). Thus, any state residing in a suitable invariant subspace containing the target state can serve as an effective initial state for VQE.

We consider the six-qubit Heisenberg case and compute the eigenvectors of the

projector for the invariant subspace associated with the target ground state. All these eigenvectors, along with their linear combinations, could be suitable initial states for the VQE process. As illustrated in Fig. 6.7(a), the VQE fails to converge to the target ground state when initialized from the initial state introduced earlier, even with six layers and after 10^4 iterations. The VQE is confined to the subspace $\mathbb{C}^{13}$ and cannot access the ground state (see Table 6.2). To resolve this, we compute the projection operator associated with the subspace $\mathbb{C}^7$ connected to the target state and determine its eigenvectors ν_j. We run the VQE while using one of the eigenvectors ν_j as initial state. The results of this approach are presented in Fig. 6.7(b) and one observes a fast convergence to the ground state.

6.6 Connections to adiabatic state preparation

An interesting parallel can be drawn between variational state preparation and adiabatic state preparation or quantum annealing [363]. Indeed, original proposals for variational state preparation were inspired by trotterizing adiabatic paths [322], and later works found for instance that variational parameter initializations mimicking an adiabatic path provided good initial guesses for the parameter optimization process [388]. In this context, we now relate our symmetry analysis to adiabatic state preparation and find that some conclusions can be carried over between the two protocols. Moreover, insights from adiabatic state preparation enable us to establish an adiabatic path from the initial state $|\psi_0\rangle$ to a ground state of the target Hamiltonian $\mathcal{H}_T$ assuming a spectral gap is separating the ground states from the rest of the spectrum during the adiabatic evolution (and additional assumptions). This perspective is connected to the structure of the invariant subspaces with the help of three illustrative examples.

We start by relating the initial state $|\psi_0\rangle$ to a specific initial parent Hamiltonian $\mathcal{H}_0$ that has $|\psi_0\rangle$ as one of its ground states. Our goal is to reach a ground state of a given target Hamiltonian $\mathcal{H}_T$ by slowly varying the time-dependent Hamiltonian

$$H(\tau) = (1-\tau)\mathcal{H}_0 + \tau\mathcal{H}_T. \tag{6.6}$$

Here, the parameter τ changes from 0 to 1 while $H(0) = \mathcal{H}_0$ and $H(1) = \mathcal{H}_T$. In the adiabatic theorem [364–369], one usually assumes a nonzero gap between the ground-state energy of $H(\tau)$ and its second lowest energy for $0 \leq \tau \leq 1$ (among more technically assumptions). If the the system starts at $\tau = 0$ in the ground state of $\mathcal{H}_0$ and the time evolution of the Hamiltonian is sufficiently slow, the evolved state will then approximately remain in a ground state throughout the evolution, thus approximately

resulting in the ground state of $\mathcal{H}_T$.

To verify that the ground state maintains a nonzero energy gap from the first excited state throughout the evolution, one can determine the energy spectrum of $H(\tau)$ for τ ranging from 0 to 1 (see Fig. 6.8). In particular, crossings in the spectrum involving the ground state imply a zero gap. The adiabatic theorem has been extended to cases without a gap [389], which highlights that having a nonzero gap is in general not a necessary condition.

The Hamiltonians $\mathcal{H}_0$ and $\mathcal{H}_T$ can be used perform the described adiabatic evolution by applying the unitary

$$U = \mathcal{T} \exp\left(-i \int_0^1 H(t)\, dt\right), \tag{6.7}$$

where $\mathcal{T}$ denotes the time-ordering operator. Thus the Lie algebra $\langle\{\mathcal{H}_0,\mathcal{H}_T\}\rangle_{\text{Lie}}$ generated by $\mathcal{H}_0$ and $\mathcal{H}_T$ is able to infinitesimally implement U. In this section, we will now make the simplifying assumption that the resource Lie algebra $\mathfrak{g}'_R$ generated by a given set of resource Hamiltonians can always generated the dynamics of both $\mathcal{H}_0$ and $\mathcal{H}_T$, i.e., $\mathfrak{g}'_R$ always contains both $i\mathcal{H}_0$ and $i\mathcal{H}_T$. Note that this assumption is not statisfied in all possible cases (see Tables 6.1 and 6.3). If our assumption is met, the adiabatic evolution between ground states will be reflected by the fact they have support within the same invariant subspace of $\{\mathcal{H}_0, \mathcal{H}_T\}$ such that the Lie algebra $\mathfrak{g}'_R$ can infinitesimally connect them.

To clarify this idea, we study the case of one initial parent Hamiltonian

$$\mathcal{H}_0 = \frac{1}{2}\sum_{n=1}^{3} \sigma_z^{(n)}, \tag{6.8}$$

and three example target Hamiltonians $\mathcal{H}_T$, under the assumption that the resource Lie algebra $\mathfrak{g}'_R$ contains both $\mathcal{H}_0$ and $\mathcal{H}_T$. In the first example, $\mathcal{H}_T$ is given by

$$\mathcal{H}_1 = \frac{1}{2}\sum_{n=1}^{3} \sigma_z^{(n)} + \frac{1}{4}\sum_{n=1}^{3}\sum_{j\in\{x,y,z\}} \sigma_j^{(n)}\sigma_j^{(n+1)}. \tag{6.9}$$

Figure 6.8(a) highlights a crossing in the eigenspectrum of $H(\tau)$ related to the ground-state energy. This results in a zero gap and cannot confirm an adiabatic path to reach the target ground state. We can also validate this using our symmetry analysis: The Lie algebra generated by $\mathcal{H}_0$ and $\mathcal{H}_1$ is two-dimensional and abelian as $[\mathcal{H}_0, \mathcal{H}_1] = 0$. The corresponding invariant subspaces of $\mathcal{H}_0 \cup \mathcal{H}_1$ are

$$\mathbb{C}^1 \boxplus \mathbb{C}^1 \boxplus (\mathbb{C}^1 \boxplus \mathbb{C}^1) \boxplus \mathbb{C}^1 \boxplus \mathbb{C}^1 \boxplus (\mathbb{C}^1 \boxplus \mathbb{C}^1).$$

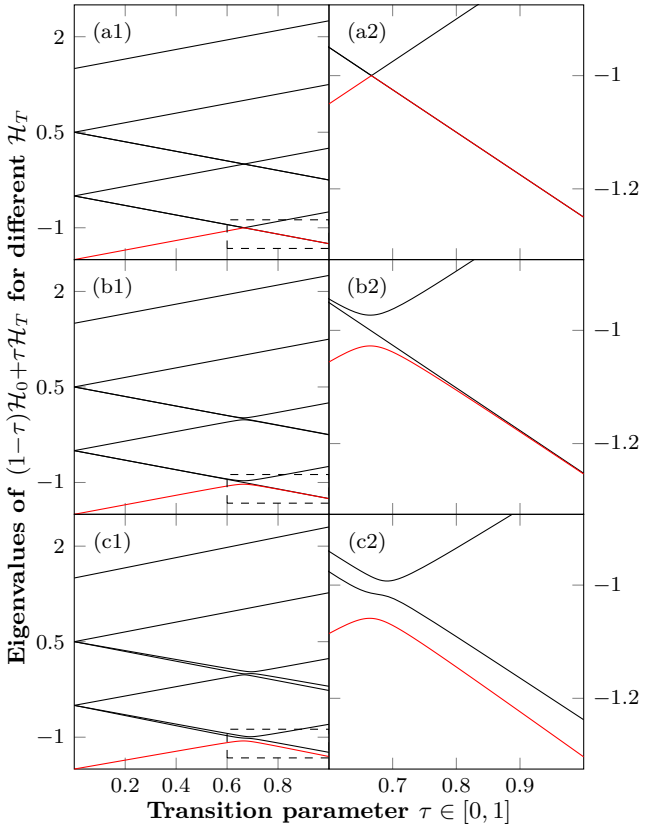

Figure 6.8: Energy spectrum of $H(\tau)$ [see Eq. (6.6)] with τ ranging from 0 to 1 for the initial parent Hamiltonian $\mathcal{H}_0$ [see Eq. (6.8)] and different target Hamiltonians $\mathcal{H}_T \in \{\mathcal{H}_1, \mathcal{H}_2, \mathcal{H}_3\}$ [see Eqs. (6.9)-(6.11)]. The energy spectrum of $H(\tau)$ with $\mathcal{H}_1$ is illustrated in (a1), where (a2) contains a magnified version of the dashed rectangular part in (a1). The ground state energy is represented using the red solid line. Similarly (b1)-(b2) and (c1)-(c2) correspond to $\mathcal{H}_2$ and $\mathcal{H}_3$ respectively.

We calculate the ground states of $\mathcal{H}_0$ and $\mathcal{H}_1$ and project them onto the different invariant subspaces. We observe that the initial ground state has only support on one of the subspaces $\mathbb{C}^1$, while the two degenerate ground states of $\mathcal{H}_1$ have only support on one of the subspaces $(\mathbb{C}^1 \boxplus \mathbb{C}^1)$. This clearly rules out any path to the target ground state. But with more resources and a larger resource Lie algebra $\mathfrak{g}'_R$, the invariant subspaces will combine and one can eventually reach the target ground state.

In the second example, we add a local σ_x term to $\mathcal{H}_1$ so that the new target Hamiltonian is given by

$$\mathcal{H}_2 = \mathcal{H}_1 + \frac{1}{20}\sigma_x^{(1)}. \tag{6.10}$$

By inspecting the eigenspectrum of $H(\tau)$ in Fig. 6.8(b), the gap between the ground state and the first excited state is quite small but remains finite, thereby allowing for an adiabatic path between the ground states of $\mathcal{H}_0$ and $\mathcal{H}_2$. This agrees with our symmetry analysis. The dimension of the Lie algebra $\mathfrak{su}(6) \oplus \mathfrak{su}(2) \oplus \mathfrak{u}(1)$ generated by $\mathcal{H}_0$ and $\mathcal{H}_2$ is 39. The Hilbert space decomposes into the invariant subspaces $\mathbb{C}^2 \boxplus \mathbb{C}^6$, where both the initial and target ground states have only support on the subspace $\mathbb{C}^6$ on which the Lie algebra acts transitively.

Finally, in the third example, we add an extra σ_z term to $\mathcal{H}_2$ so that the new target Hamiltonian is given by

$$\mathcal{H}_3 = \mathcal{H}_2 + \frac{1}{20}\sigma_z^{(2)} = \mathcal{H}_1 + \frac{1}{20}\sigma_x^{(1)} + \frac{1}{20}\sigma_z^{(2)}. \tag{6.11}$$

The gap in the eigenspectrum of $H(\tau)$ in Fig. 6.8(c) is clearly visible which again implies an adiabatic path. The Lie algebra generated by $\mathcal{H}_0$ and $\mathcal{H}_3$ is $\mathfrak{su}(8)$ and therefore has a dimension of 63, which yields a single invariant subspace $\mathbb{C}^8$, in which both the initial and target ground states lie. Thus one can reach the ground state of $\mathcal{H}_3$ starting from the ground state of $\mathcal{H}_0$.

These examples highlight a connection between our symmetry results and adiabatic state preparation. Assuming that the resource Lie algebra $\mathfrak{g}'_R$ contains both $i\mathcal{H}_0$ and $i\mathcal{H}_T$ and that there is a nonzero spectral gap (and further technical assumptions), one can establish an adiabatic path between the ground states of $\mathcal{H}_0$ and $\mathcal{H}_T$. This complements our reachability analysis based on symmetries. But even without an adiabatic path, one reach the target ground state if one increases the available resources to enlarge the generated Lie algebra and enable transitions that would otherwise be forbidden.

6.7 Conclusion

We have developed symmetry tools to analyze the ground-state reachability for VQE. These methods have been illustrated and applied to a Rydberg-atom platform with restricted global control Hamiltonians. For a small number of qubits, this enabled us to a priori predict whether the VQE could be successful in reaching the target state from the chosen initial state. For this, we have analyzed the generated Lie algebras as well as the invariant subspaces resulting from the restricted control. We have then determined whether the initial and target states are contained in different invariant subspaces which would rule out the reachability of the target state. Even beyond a small number of qubits, the developed symmetry tools provide guidance on how inherent symmetries in controlled quantum systems might limit the applicability of VQE, which could then be translated into insights into engineering suitable additional interactions in quantum simulation platforms. Finally, we have connected our symmetry analysis to adiabatic state preparation, which can be used to establish an adiabatic path to the target ground state. This provides a complementary tool to analyze reachability.

In all our analysis, we have assumed that we have access to the target ground state (which VQE is supposed to find) or even more precise spectral information. In a practical, large-scale VQE scenario with restricted controls, this information will be usually not available. So an open question remains whether suitable accessible properties of the target Hamiltonian and, possibly, an initial parent Hamiltonian can be used to confirm reachability. In absence of such a criteria, more control capabilities to break inherent symmetries are certainly advantageous.

6.8 Appendix

6.8.1 Lie-algebra computations

We provide further details for the Lie-algebra computations following the description in Sec. 6.3.1. All computations are implemented using the computer algebra system Magma [390] which enables computations with exact fields such as the rational field or number fields (including cyclotomic fields) [391]. Recall that number fields are field extensions of finite degree of the rational field. Computations with exact fields are complemented with numerical computations based on inexact fields such as (approximated) real or complex fields. Often computations over the (not approximated) real field can be substituted with exact computations over the rational field or a suitable number field. The employed computational techniques in this work (and particularly in the Appendices 6.8.1 and 6.8.2) build on and partially extend computational tools

Number of qubits	Resource Lie algebra $\mathfrak{g}_R$	Extension by adding $\mathcal{H}_H$	$\mathcal{H}_I$
3	$\mathfrak{su}(4)\oplus\mathfrak{su}(2)\oplus\mathfrak{u}(1)$	–	–
4	$\mathfrak{su}(6)\oplus\mathfrak{su}(3)\oplus\mathfrak{su}(3)\oplus\mathfrak{u}(1)$	$\oplus\mathfrak{u}(1)$	$\oplus\mathfrak{u}(1)$
5	$\mathfrak{su}(8)\oplus\mathfrak{su}(6)\oplus\mathfrak{su}(6)\oplus\mathfrak{u}(1)$	–	–
6	$\mathfrak{su}(13)\oplus\mathfrak{su}(11)\oplus\mathfrak{su}(9)$ $\oplus\mathfrak{su}(7)\oplus\mathfrak{su}(3)\oplus\mathfrak{u}(1)$	$\oplus\mathfrak{u}(1)$	$\oplus\mathfrak{u}(1)$
7	$\mathfrak{su}(18)\oplus\mathfrak{su}(18)\oplus\mathfrak{su}(18)$ $\oplus\mathfrak{su}(18)\oplus\mathfrak{su}(2)\oplus\mathfrak{u}(1)$	–	–

Table 6.3: Lie algebras specified by their reductive decompositions for three to seven qubits: we compare the Lie algebra $\mathfrak{g}_R$ of the infinitesimal resources Hamiltonians $\mathcal{G}_R$ with the Lie algebras $\mathfrak{h}_H$ or $\mathfrak{h}_I$ generated by the resources Hamiltonians combined with the Heisenberg or the Ising target Hamiltonian, i.e. $\mathcal{G}_R \cup \{\mathcal{H}_H\}$ and $\mathcal{G}_R \cup \{\mathcal{H}_I\}$. For the case of four and six qubits, we observe that $\mathfrak{h}_H$ and $\mathfrak{h}_I$ have one extra abelian component $\mathfrak{u}(1)$ compared to $\mathfrak{g}_R$ and the dimension of the center of the Lie algebra is increased from 1 to 2.

applied in [195–197, 352, 361, 362] and, most recently, in [207].

Starting from a set of (hermitian) generators $\mathcal{G}$ (such as the resource Hamiltonians $\mathcal{G}_R = \{H_d, H_\Delta, H_\Omega\}$), we can compute the Lie-algebra closure $\mathfrak{g} := \langle\mathcal{G}\rangle_{\text{Lie}}$ by repeatedly computing commutators (starting from the elements iH_j for H_j in $\mathcal{G}$) and determining the (linear-algebra) rank of a set of Lie-algebra elements. For the Lie-algebra closure, $\mathfrak{g}$ is considered as a Lie subalgebra of $\mathfrak{su}(2^n)$ [or $\mathfrak{u}(2^n)$] which is specified by its structure constants [378] over a Pauli-string basis, where Pauli strings are given by n-fold tensor products of Pauli operators σ_j with $j \in \{x, y, z\}$ and the 2×2 identity matrix $\mathbb{1}_2$. If the generators can be determined as linear combinations over the rational field (or a suitable number field contained in the real field), the generated Lie algebra can be exactly calculated as all rank computations can be exactly performed.

Based on a basis for $\mathfrak{g}$ (as detailed above), we can determine its reductive decomposition $\mathfrak{g} = \mathfrak{g}_1 \oplus \cdots \oplus \mathfrak{g}_k$ into simple or abelian components $\mathfrak{g}_j$ using MAGMA [378, 390] by first computing the components $\mathfrak{g}_j$ and then identifying the simple components as one of the classical simple Lie algebras $\mathfrak{su}(p)$ with $p \geq 2$, $\mathfrak{so}(2p+1)$, $\mathfrak{sp}(p)$, and $\mathfrak{so}(2p)$ for suitable integers $p \geq 1$ or one of the five exceptional ones [376, 378]. But we are referring only to the corresponding compact real forms as all considered Lie algebras are compact [376], i.e., they are contained in $\mathfrak{u}(2^n)$.

Table 6.3 details the reductive decompositions for the Lie algebra $\mathfrak{g}_R$ generated by the resource Hamiltonians $\mathcal{G}_R = \{H_d, H_\Delta, H_\Omega\}$ for three to seven qubits. Similarly, Table 6.3 also specifies the Lie algebras $\mathfrak{h}_H$ and $\mathfrak{h}_I$ obtained when the generating set $\mathcal{G}_R$

Number of qubits	Invariant subspaces	Support: Initial state	Support: Heisenberg target state(s)	Support: Ising target state(s)
3	$\mathbb{C}^4 \boxplus (\mathbb{C}^2 \boxplus \mathbb{C}^2)$	$\mathbb{C}^4$	$(\mathbb{C}^2 \boxplus \mathbb{C}^2)$	$\mathbb{C}^4$
4	$\mathbb{C}^6 \boxplus (\mathbb{C}^3 \boxplus \mathbb{C}^3) \boxplus \mathbb{C}^3 \boxplus \mathbb{C}^1$	$\mathbb{C}^6$	$\mathbb{C}^6$	$\mathbb{C}^6$
5	$\mathbb{C}^8 \boxplus (\mathbb{C}^6 \boxplus \mathbb{C}^6) \boxplus (\mathbb{C}^6 \boxplus \mathbb{C}^6)$	$\mathbb{C}^8$	$(\mathbb{C}^6 \boxplus \mathbb{C}^6)$	$\mathbb{C}^8$
6	$\mathbb{C}^{13} \boxplus (\mathbb{C}^{11} \boxplus \mathbb{C}^{11}) \boxplus (\mathbb{C}^9 \boxplus \mathbb{C}^9) \boxplus \mathbb{C}^7 \boxplus \mathbb{C}^3 \boxplus \mathbb{C}^1$	$\mathbb{C}^{13}$	$\mathbb{C}^7$	$\mathbb{C}^{13}$
7	$(\mathbb{C}^{18} \boxplus \mathbb{C}^{18}) \boxplus (\mathbb{C}^{18} \boxplus \mathbb{C}^{18}) \boxplus (\mathbb{C}^{18} \boxplus \mathbb{C}^{18}) \boxplus \mathbb{C}^{18} \boxplus \mathbb{C}^2$	$\mathbb{C}^{18}$	$(\mathbb{C}^{18} \boxplus \mathbb{C}^{18})$	$\mathbb{C}^{18}$
8	$(\mathbb{C}^{33} \boxplus \mathbb{C}^{33}) \boxplus (\mathbb{C}^{30} \boxplus \mathbb{C}^{30}) \boxplus (\mathbb{C}^{30} \boxplus \mathbb{C}^{30}) \boxplus \mathbb{C}^{30} \boxplus \mathbb{C}^{21} \boxplus \mathbb{C}^{13} \boxplus \mathbb{C}^6$	$\mathbb{C}^{30}$	$\mathbb{C}^{30}$	$\mathbb{C}^{30}$
9	$(\mathbb{C}^{58} \boxplus \mathbb{C}^{58}) \boxplus (\mathbb{C}^{56} \boxplus \mathbb{C}^{56}) \boxplus (\mathbb{C}^{56} \boxplus \mathbb{C}^{56}) \boxplus (\mathbb{C}^{56} \boxplus \mathbb{C}^{56}) \boxplus \mathbb{C}^{46} \boxplus \mathbb{C}^{14}$	$\mathbb{C}^{46}$	$(\mathbb{C}^{56} \boxplus \mathbb{C}^{56})$	$\mathbb{C}^{46}$
10	$(\mathbb{C}^{105} \boxplus \mathbb{C}^{105}) \boxplus (\mathbb{C}^{105} \boxplus \mathbb{C}^{105}) \boxplus (\mathbb{C}^{99} \boxplus \mathbb{C}^{99}) \boxplus (\mathbb{C}^{99} \boxplus \mathbb{C}^{99}) \boxplus \mathbb{C}^{78} \boxplus \mathbb{C}^{58} \boxplus \mathbb{C}^{42} \boxplus \mathbb{C}^{30}$	$\mathbb{C}^{30}$	$\mathbb{C}^{30}$	$\mathbb{C}^{30}$

Table 6.4: Reachability of the Heisenberg and Ising target state for the Rydberg atom platform of Sec. 6.2. The invariant subspaces are determined together with the support of the initial state and the Heisenberg and Ising target ground state(s) for three to ten qubits. We use the color scheme from Table 6.2. For the Heisenberg case, the initial and the target states are in different symmetry sectors, except for four, eight, and ten qubits. This implies that the Heisenberg target state can never be reached for three, five, six, seven, and nine qubits using VQE starting from the chosen initial state. For example, for five qubits, one observes the three invariant subspaces $\mathbb{C}^8 \boxplus \mathbb{C}^6 \boxplus \mathbb{C}^6 \boxplus \mathbb{C}^6 \boxplus \mathbb{C}^6$. The initial state has only support in the first one $\mathbb{C}^8$ and the target state has only support in the second and third one $\mathbb{C}^6$ and $\mathbb{C}^6$.

is extended by the Heisenberg and the Ising Hamiltonians $\mathcal{H}_H$ and $\mathcal{H}_I$ [see Eqs. (6.5) and (6.4)]. We observe in Table 6.3 that the Lie algebras $\mathfrak{h}_H$ and $\mathfrak{h}_I$ are isomorphic. In particular, the Lie algebras $\mathfrak{g}_R$, $\mathfrak{h}_H$, $\mathfrak{h}_I$ are isomorphic for three, five, and seven qubits. But, for four and six qubits, $\mathfrak{g}_R$ differs from $\mathfrak{h}_H$ and $\mathfrak{h}_I$ by an element of the Lie center in $\mathfrak{h}_H$ and $\mathfrak{h}_I$, where the dimension of the Lie centers of $\mathfrak{g}_R$ and respectively $\mathfrak{h}_H$ and $\mathfrak{h}_I$ are one and two.

6.8.2 Symmetry computations

In this appendix, we provide further details relevant to the symmetry analysis discussed in Sec. 6.3.3 while highlighting computational aspects as in Appendix 6.8.1. In a first step, we compute the commutant of the resource Hamiltonians $\mathcal{G}_R = \{H_d, H_\Delta, H_\Omega\}$ (see Sec. 6.3.3) and the commutant will now be denoted by $\mathcal{C}$.

Based on the commutant $\mathcal{C}$, we can determine the Lie-algebra center $\mathcal{Z}(\mathfrak{g}_R) = \mathcal{C} \cap \mathfrak{g}_R$ of $\mathfrak{g}_R$ without computing $\mathfrak{g}_R$. Consider a skew-hermitian basis of the commutant with basis elements b_k and $k \in \{1, \ldots, \dim(\mathcal{C})\}$. We project the resource Hamiltonians H_j onto this basis using the formula $i\mathrm{Tr}(H_j b_k)/\mathrm{Tr}(b_k b_k)$, where $\mathrm{Tr}(M)$ denotes the trace of a matrix M. A basis of the projected operators, which are expanded as a linear combination of the elements b_k, then forms a basis of the Lie center $\mathcal{Z}(\mathfrak{g}_R)$. If one is only interested in the dimension of $\mathcal{Z}(\mathfrak{g}_R)$, one can compute the rank of the matrix R with entries $R_{ij} = \mathrm{Trace}(C_i^\dagger H_j)$, where the C_j describe any basis of $\mathcal{C}$ and the matrix R has $|\mathcal{G}_R|$ columns and $\dim(\mathcal{C})$ rows (see [195]).

We can compute the isotypic and irreducible projectors as outlined in Sec. 6.3.3. We detail now one particular optimization for determining the irreducible projectors by first reducing the block size of the resource Hamiltonians with respect to a considered isotypic projector P_j [see Fig. 6.5(a)]. Following some idea in [207], we can construct rectangular matrices Q_j and $Q_j^\dagger$, where the columns of $Q_j^\dagger$ are given by an orthonormal eigenbasis of P_j. We use the Gram-Schmidt process for the orthogonalization and then normalize each eigenvector ν_j by $\nu_j' = \nu_j/|\nu_j|$, where $|\nu_j| = \sqrt{\langle \nu_j | \nu_j \rangle}$ and field extensions are required for the square roots. Hence, we can write the matrix Q_j as $Q_j = D_{\mathrm{sqrt}} Q_j'$, where Q_i' contains the orthogonal eigenbasis of P_j and D_{sqrt} is a diagonal matrix containing all the normalization factors $|\nu_j|$. Similarly, we can write $Q_j^\dagger = Q_j'^\dagger D_{\mathrm{sqrt}}$. We then apply the formula $\tilde{H}_v = Q_j H_v Q_j^\dagger$ for $H_v \in \mathcal{G}_R$. Consequently, the meataxe algorithm [382] mentioned in Sec. 6.3.3 can be applied to smaller matrices.

This then enables us to compute the projections of state vectors s via sP_j for an isoyptic subspace or $sQ_j^\dagger \tilde{P}_j$ for an irreducible subspace. For Hamiltonians W or Lie algebra elements iW, we similarly have the formulas $P_j W P_j$ and $\tilde{P}_j Q_j W Q_j^\dagger \tilde{P}_j$. Thus we can determine the non-zero support. In summary, Table 6.4 details the invariant

Number of qubits	Lie center dimension for $\mathfrak{g}_R$	$\mathfrak{h}_H$ and $\mathfrak{h}_I$	Impact from the extended center for $\mathfrak{h}_H$	$\mathfrak{h}_I$
3	1	1	N/A	N/A
4	1	2	None	None
5	1	1	N/A	N/A
6	1	2	Possible	None
7	1	1	N/A	N/A
8	1	2	None	None
9	1	2	Possible	None
10	1	2	None	None

Table 6.5: The impact of additional Lie center element(s) on the reachability of the target ground state(s) when extending the resource Hamiltonians with the respective Heisenberg or Ising target Hamiltonians $\mathcal{H}_H$ or $\mathcal{H}_I$. This then results in the extended Lie algebras $\mathfrak{h}_H$ or $\mathfrak{h}_I$. A potential impact on the VQE is shown by "Possible" and no effect by "None"; "N/A" indicates the non-existence of additional center elements. Refer to the text of Appendix 6.8.3 for further details.

subspaces and the non-zero support of the initial and the target state(s) for three to ten qubits.

6.8.3 Lie centers when adding the target Hamiltonian to the resource Hamiltonians

In this Appendix, we discuss whether adding the target Hamiltonian to the resource Hamiltonians would affect the result of the reachability analysis. The Lie algebras $\mathfrak{g}_R$, $\mathfrak{h}_H$, and $\mathfrak{h}_I$ without and with the target Hamiltonians and their reductive decompositions have been computed for up to seven qubits. The results are detailed in Table 6.3 of Appendix 6.8.1 and they suggest that the extended Lie algebras $\mathfrak{h}_H$ and $\mathfrak{h}_I$ differ from the resource Lie algebra $\mathfrak{g}_R$ by at most one additional center element. So, our analysis beyond seven qubits is predicated by general correctness of this observation. The Lie-algebra center dimension is calculated without and with the Heisenberg and the Ising target Hamiltonian. We observe in certain cases an extended Lie center which is reflected in a larger Lie-center dimension as recorded in column three of Table 6.3. These additional center elements could potentially lead to an extended reachability.

We can effectively compute the Lie centers via the commutant beyond seven qubits and analyze the support of the corresponding center elements. Table 6.5 summarizes the results by detailing the Lie-center dimensions as well as the potential impact on

the isotypic subspaces with non-zero support for the initial and the target states. An additional center element is observed for four, six, eight, nine, and ten qubits. They have no impact on the initial and the target state in the invariant subspace $\mathbb{C}^6$, $\mathbb{C}^{30}$, and $\mathbb{C}^{30}$ for four, eight, and ten qubits respectively. This means that time evolutions enabled by the additional center element do not affect the invariant subspace containing the initial and the target state.

However, the initial and the target states are located in the different invariant subspaces $\mathbb{C}^{13}$ and $\mathbb{C}^7$ for six qubits as shown in Table 6.2. The additional center element does not act on the initial state, but it does act on the target state. These observations do not change our assessment of the reachability of the Heisenberg target ground state. A similar argument applies to the case of nine qubits. For the Ising model, the additional center element has zero support in the isotypic subspaces that have nonzero support for the initial state and the target state. We conclude from Table 6.5 that the additional center elements cannot affect the VQE for the Ising model with all considered qubits. Thus adding the target Hamiltonian to the resource Hamiltonians appears to not help to reach the target ground state for up to ten qubits.

7 Summary and outlook

7.1 Summary and conclusions

In this thesis, we have developed and implemented analytical and numerical methods from control theory for modeling, simulating, and optimizing quantum systems. This thesis has addressed several goals associated with neutral atom devices, starting from elementary gate operations and reaching quantum simulation tasks. We developed and integrated new theoretical and numerical tools into the existing quantum control stack. While most of these developments are general in application, they have been designed with a prior focus on neutral atoms. Rather than working abstractly, pursuing experimentally oriented goals makes these new tools more practical and applicable — likely with only slight modifications needed for other systems as well.

For this purpose, we first provided a review of the existing control methods used as the starting point of the work done in this thesis. We described the principal ideas of any quantum control problem and gave a description of both analytical and numerical methods required to tackle different tasks. We also discussed ways to make these optimization algorithms more practical by taking into account experimental imperfections. With these control methods in the background, we next explained our target system for this thesis: neutral atoms. In this regard, we focused only on the physical principles, control mechanisms, and operational challenges, without going into experimental setup details or extensive application reviews. Neutral atoms or ultracold atoms are a prominent platform for performing quantum computation and simulation tasks. Over the last decade, extensive research has been conducted to further improve this system, and now it has reached a stage where control methods can be implemented to achieve high levels of precision. In order to achieve this, both quantum and classical noise sources must be characterized and included in the optimization routines.

With this goal, our original research contributions address several pressing control problems within neutral atom systems. First, we demonstrated how including technical

imperfections — such as pulse distortions from experimental devices like acousto-optic modulators — directly into control optimization can significantly improve the fidelity of quantum operations. For this, we developed a theoretical tool for estimating especially the nonlinear distortions, with a key feature of this tool being platform independence. By extending numerical techniques like GRAPE to account for these non-linearities, we showed a practical pathway toward enhancing the reliability of quantum operations, e.g., quantum gates.

Next, we moved to a slightly more complex quantum system where fermionic atoms are trapped in a superlattice: a special form of optical lattice. In this setup, using modified and efficient numerical control techniques, we tackled the challenge of implementing high-fidelity, fast, and robust quantum gates. These systems have the potential for performing efficient quantum simulation tasks, e.g., simulating Fermi-Hubbard dynamics. In our work, we showed how dynamically tuning the system parameters allows us to engineer interactions on different bands of the Fermi-Hubbard model. This is then used to design fast gates through tailored numerical optimization while suppressing unwanted population leakage. This study is also very insightful for practical quantum simulation tasks using these systems as it provides an understanding of the non-trivial changes occurring in the dynamics.

Finally, moving further toward quantum simulation applications of ultracold atoms, we investigated the potential of Rydberg atom-based analog quantum simulators for performing the variational quantum eigensolver (VQE). Rydberg systems naturally generate Ising-like interactions and hence represent an ideal platform for performing these types of variational algorithms. However, in the presence of only global control — which is the state of the art currently — the simulator faces some limitations in terms of convergence. Using Lie-algebra-based control theory tools, we examined these symmetry-induced limitations and provided reachability criteria. This analysis was performed for specific examples such as Ising and Heisenberg models and for small system sizes. However, the results can be projected to understand larger system sizes and pave the way for further development of tools in this regard. This analysis not only highlights the importance of system symmetries in analog simulators but also informs the selection and design of initial states best suited to a given hardware platform.

7.2 Outlook

Looking ahead, the development of new gate schemes, algorithms, and improvements in experimental components holds great promise for new use cases of quantum control methods in practical quantum technologies. With increasing demands for precision, longer coherence times, and larger system sizes, the role of advanced control tech-

niques is becoming more critical. In this regard, the work presented in this thesis has the potential to be further developed and applied to various other areas in quantum technologies.

The estimation method for nonlinear systems presented in Chapter 4 is general in the sense that it can be easily adapted to other quantum platforms. The only requirement for this generalization is the availability of a measurement device such as a photodiode or an oscilloscope. Recently, our method has been implemented experimentally with some modifications to estimate and correct for distortions in a neutral atom device [392].

We engineered control pulses that are highly tailored and depend on the system Hamiltonian. However, noise in real experiments results in deviations in the dynamics, which decreases the fidelities of these controls. In Chapter 5, we explored some of the major sources of noise and errors in the fermionic system and showed that our pulses are quite robust against them. This lays the groundwork for further improving these controls by including more sources of errors and performing robust optimization. This would require not only improvements in optimization routines but also the design of new experiments to better characterize known error sources. Furthermore, some analytical schemes such as DRAG or shortcut to adiabaticity can be used to design fast gates in this setup.

Finally, control theory can provide significant insight into quantum simulation tasks in the presence of noise sources. Specifically, the work done in Chapter 6 can be further extended to understand how noise affects these variational algorithms. For example, noise channels, which can be modeled as Pauli operations, can be included in the dynamics to examine whether they affect the reachability of the desired quantum state. The tools presented in Chapter 6 have the potential to be further extended and applied to different system topologies, which will reveal the dependence of symmetries on different configurations. With more data in hand, we can potentially find some physical reasoning for these symmetry limitations and anticipate results for larger system sizes.

In summary, this thesis demonstrates how control theory is well-positioned to act as both a diagnostic and design tool for neutral atom quantum systems, enabling improved quantum operations and studying the potential of these devices. Through the joint efforts of theoretical, computational, and experimental advancements, we can move toward the realization of scalable and high-performance quantum technologies.

References

[1] J. P. Dowling and G. J. Milburn, *Quantum technology: the second quantum revolution*, Philosophical Transactions of the Royal Society A **361**, 1655–1674 (2003).

[2] J. Preskill, *Quantum Computing in the NISQ era and beyond*, Quantum **2**, 79 (2018).

[3] M. A. Nielsen and I. L. Chuang, *Quantum Computation and Quantum Information*, 2nd ed. (Cambridge University Press, Cambridge, 2023).

[4] R. P. Feynman, *Simulating physics with computers*, Int. J. Theor. Phys. **21**, 467–488 (1982).

[5] A. Montanaro, *Quantum algorithms: an overview*, npj Quantum Information **2**, 15023 (2016).

[6] T. D. Ladd, F. Jelezko, R. Laflamme, Y. Nakamura, C. Monroe, and J. L. O'Brien, *Quantum computing*, Nature **464**, 45–53 (2010).

[7] J. Clarke and F. K. Wilhelm, *Superconducting quantum bits*, Nature **453**, 1031–1042 (2008).

[8] H. Häffner, C. Roos, and R. Blatt, *Quantum computing with trapped ions*, Phys. Rep. **469**, 155-203 (2008).

[9] M. Greiner, O. Mandel, T. Esslinger, T. W. Hänsch, and I. Bloch, *Quantum phase transition from a superfluid to a Mott insulator in a gas of ultracold atoms*, Nature **415**, 39–44 (2002).

[10] M. H. Devoret and R. J. Schoelkopf, *Superconducting circuits for quantum information: An outlook*, Science **339**, 1169-1174 (2013).

[11] M. Gong, M.-C. Chen, Y. Zheng, S. Wang, C. Zha, *et al.*, *Genuine 12-qubit entanglement on a superconducting quantum processor*, Phys. Rev. Lett. **122**, 110501 (2019).

[12] J. I. Cirac and P. Zoller, *Quantum computations with cold trapped ions*, Phys. Rev. Lett. **74**, 4091–4094 (1995).

[13] D. Leibfried, R. Blatt, C. Monroe, and D. Wineland, *Quantum dynamics of single trapped ions*, Rev. Mod. Phys. **75**, 281–324 (2003).

[14] D. Bluvstein, S. J. Evered, A. A. Geim, S. H. Li, H. Zhou, *et al.*, *Logical quantum processor based on reconfigurable atom arrays*, Nature **626**, 58-65 (2024).

[15] S. J. Evered, D. Bluvstein, M. Kalinowski, S. Ebadi, T. Manovitz, *et al.*, *High-fidelity parallel entangling gates on a neutral-atom quantum computer*, Nature **622**, 268-272 (2023).

[16] F. Gyger, M. Ammenwerth, R. Tao, H. Timme, S. Snigirev, *et al.*, *Continuous operation of large-scale atom arrays in optical lattices*, Phys. Rev. Res. **6**, 033104 (2024).

[17] A. L. Shaw, Z. Chen, J. Choi, D. K. Mark, P. Scholl, *et al.*, *Benchmarking highly entangled states on a 60-atom analogue quantum simulator*, Nature **628**, 71-77 (2024).

[18] S. Jandura and G. Pupillo, *Time-Optimal Two- and Three-Qubit Gates for Rydberg Atoms*, Quantum **6**, 712 (2022).

[19] M. Mohan, R. de Keijzer, and S. Kokkelmans, *Robust control and optimal rydberg states for neutral atom two-qubit gates*, Phys. Rev. Res. **5**, 033052 (2023).

[20] D. Jaksch, H.-J. Briegel, J. I. Cirac, C. W. Gardiner, and P. Zoller, *Entanglement of atoms via cold controlled collisions*, Phys. Rev. Lett. **82**, 1975–1978 (1999).

[21] G. K. Brennen, C. M. Caves, P. S. Jessen, and I. H. Deutsch, *Quantum logic gates in optical lattices*, Phys. Rev. Lett. **82**, 1060–1063 (1999).

[22] L. Henriet, L. Beguin, A. Signoles, T. Lahaye, A. Browaeys, *et al.*, *Quantum computing with neutral atoms*, Quantum **4**, 327 (2020).

[23] S. J. Glaser, U. Boscain, T. Calarco, C. P. Koch, W. Köckenberger, *et al.*, *Training schrödinger's cat: quantum optimal control*, Eur. Phys. J. D. **69**, 279 (2015).

[24] C. P. Koch, U. Boscain, T. Calarco, G. Dirr, S. Filipp, *et al.*, *Quantum optimal control in quantum technologies. Strategic report on current status, visions and goals for research in Europe*, EPJ Quantum Technol. **9**, 19 (2022).

[25] T. Pichler, T. Caneva, S. Montangero, M. D. Lukin, and T. Calarco, *Noise-resistant optimal spin squeezing via quantum control*, Phys. Rev. A **93**, 013851 (2016).

[26] G. De Chiara, T. Calarco, M. Anderlini, S. Montangero, P. J. Lee, *et al.*, *Optimal control of atom transport for quantum gates in optical lattices*, Phys. Rev. A **77**, 052333 (2008).

[27] A. Omran, H. Levine, A. Keesling, G. Semeghini, T. T. Wang, *et al.*, *Generation and manipulation of schrödinger cat states in rydberg atom arrays*, Science **365**, 570-574 (2019).

[28] N. Khaneja, *Time optimal control of coupled spin dynamics: A global analysis*, Automatica **111**, 108639 (2020).

[29] T. Caneva, T. Calarco, and S. Montangero, *Chopped random-basis quantum optimization*, Phys. Rev. A **84**, 022326 (2011).

[30] M. Cerezo, A. Arrasmith, R. Babbush, S. C. Benjamin, S. Endo, *et al.*, *Variational quantum algorithms*, Nat. Rev. Phys. **3**, 625–644 (2021).

[31] K. Bharti, A. Cervera-Lierta, T. H. Kyaw, T. Haug, S. Alperin-Lea, *et al.*, *Noisy intermediate-scale quantum algorithms*, Rev. Mod. Phys. **94**, 015004 (2022).

[32] U. Hohenester, *Optimal quantum gates for semiconductor qubits*, Phys. Rev. B **74**, 161307 (2006).

[33] B. Khani, J. M. Gambetta, F. Motzoi, and F. K. Wilhelm, *Optimal generation of fock states in a weakly nonlinear oscillator*, Phys. Scr. **2009**, 014021 (2009).

[34] M. H. Goerz, E. J. Halperin, J. M. Aytac, C. P. Koch, and K. B. Whaley, *Robustness of high-fidelity Rydberg gates with single-site addressability*, Phys. Rev. A **90**, 032329 (2014).

[35] S. Conolly, D. Nishimura, and A. Macovski, *Optimal Control Solutions to the Magnetic Resonance Selective Excitation Problem*, IEEE Trans. Med. Imaging **5**, 106-115 (1986).

[36] A. P. Peirce, M. A. Dahleh, and H. Rabitz, *Optimal control of quantum-mechanical systems: Existence, numerical approximation, and applications*, Phys. Rev. A **37**, 4950–4964 (1988).

[37] N. Khaneja, T. Reiss, C. Kehlet, T. Schulte-Herbrüggen, and S. J. Glaser, *Optimal control of coupled spin dynamics: design of nmr pulse sequences by gradient ascent algorithms*, J. Magn. Reson. **172**, 296-305 (2005).

[38] N. Rach, M. M. Müller, T. Calarco, and S. Montangero, *Dressing the chopped-random-basis optimization: A bandwidth-limited access to the trap-free landscape*, Phys. Rev. A **92**, 062343 (2015).

[39] R. Heck, O. Vuculescu, J. J. Sørensen, J. Zoller, M. G. Andreasen, *et al.*, *Remote optimization of an ultracold atoms experiment by experts and citizen scientists*, PNAS **115**, E11231-E11237 (2018).

[40] R. Nigmatullin and S. G. Schirmer, *Implementation of fault-tolerant quantum logic gates via optimal control*, New J. Phys. **11**, 105032 (2009).

[41] P. de Fouquieres, S. Schirmer, S. Glaser, and I. Kuprov, *Second order gradient ascent pulse engineering*, J. Magn. Reson. **212**, 412-417 (2011).

[42] S. van Frank, A. Negretti, T. Berrada, R. Bücker, S. Montangero, *et al.*, *Interferometry with non-classical motional states of a bose–einstein condensate*, Nat. Commun. **5**, 4009 (2014).

[43] T. Caneva, T. Calarco, R. Fazio, G. E. Santoro, and S. Montangero, *Speeding up critical system dynamics through optimized evolution*, Phys. Rev. A **84**, 012312 (2011).

[44] F. Motzoi, J. M. Gambetta, P. Rebentrost, and F. K. Wilhelm, *Simple pulses for elimination of leakage in weakly nonlinear qubits*, Phys. Rev. Lett. **103**, 110501 (2009).

[45] D. Petrosyan, F. Motzoi, M. Saffman, and K. Mølmer, *High-fidelity rydberg quantum gate via a two-atom dark state*, Phys. Rev. A **96**, 042306 (2017).

[46] D. Bouwmeester, A. Ekert, and A. Zeilinger, eds., *The Physics of Quantum Information* (Springer, Berlin, 2001).

[47] N. Zettili, *Quantum Mechanics: Concepts and Applications* (Wiley, New York, 2001).

[48] E. Schrödinger, *Quantisierung als eigenwertproblem*, Annalen der Physik **384**, 361–376 (1926).

[49] G. Auletta, M. Fortunato, and G. Parisi, *Quantum Mechanics* (Cambridge University Press, 2009) p. 513–543.

[50] G. Gour, *Quantum Resource Theories* (Cambridge University Press, 2025) p. 23–74.

[51] J. J. Sakurai and J. Napolitano, *Modern Quantum Mechanics*, 2nd ed. (Cambridge University Press, 2017) graduate-level quantum mechanics textbook.

[52] A. Rivas and S. F. Huelga, *Open Quantum Systems* (Springer, 2011) pp. 15–17.

[53] G. E. Bowman, in *Essential Quantum Mechanics* (Oxford University Press, 2007).

[54] A. Bohm, P. Kielanowski, and G. B. Mainland, *Quantum Physics: States, Observables and Their Time Evolution* (Springer, Cham, 2019).

[55] A. Rivas and S. F. Huelga, *Open Quantum Systems: An Introduction* (Springer, 2012).

[56] H.-P. Breuer and F. Petruccione, *The Theory of Open Quantum Systems* (Oxford University Press, Oxford, 2007).

[57] S. Attal, A. Joye, and C.-A. Pillet, *Open Quantum Systems II: The Markovian Approach*, Lecture Notes in Mathematics, Vol. 1881 (Springer, Berlin, Heidelberg, 2006).

[58] A. Barchielli, Markovian dynamics for a quantum/classical system and quantum trajectories (2024), arXiv:2403.16065 [quant-ph] .

[59] H.-P. Breuer, E.-M. Laine, and J. Piilo, *Measure for the degree of non-markovian behavior of quantum processes in open systems*, Phys. Rev. Lett. **103**, 210401 (2009).

[60] V. Gorini, A. Kossakowski, and E. Sudarshan, *Completely positive dynamical semigroups of n-level systems*, Journal of Mathematical Physics **17**, 821–825 (1976).

[61] G. Lindblad, *On the generators of quantum dynamical semigroups*, Commun. Math. Phys. **48**, 119—130 (1976).

[62] D. Manzano, *A short introduction to the lindblad master equation*, AIP Advances **10**, 025106 (2020), arXiv:1906.04478 [quant-ph] .

[63] J. Berberich, R. L. Kosut, and T. Schulte-Herbrüggen, Bringing quantum systems under control: A tutorial invitation to quantum computing and its relation to bilinear control systems (2024), arXiv:2412.00736 [eess.SY] .

[64] W. S. Levine, ed., *The Control Handbook* (CRC Press, Boca Raton, 1996).

[65] G. Dirr and U. Helmke, *Lie theory for quantum control*, GAMM-Mitteilungen **31**, 59–93 (2008).

[66] I. I. Rabi, J. R. Zacharias, S. Millman, and P. Kusch, *A new method of measuring nuclear magnetic moment*, Phys. Rev. **53**, 318–318 (1938).

[67] I. I. Rabi, *Space quantization in a gyrating magnetic field*, Phys. Rev. **51**, 652–654 (1937).

[68] S. Machnes, U. Sander, S. J. Glaser, P. de Fouquières, A. Gruslys, *et al.*, *Comparing, optimizing, and benchmarking quantum-control algorithms in a unifying programming framework*, Phys. Rev. A **84**, 022305 (2011).

[69] F. Frank, T. Unden, J. Zoller, R. S. Said, T. Calarco, *et al.*, *Autonomous calibration of single spin qubit operations*, npj Quantum Information **3**, 48 (2017).

[70] K. Tsurumoto, R. Kuroiwa, H. Kano, Y. Sekiguchi, and H. Kosaka, *Quantum teleportation-based state transfer of photon polarization into a carbon spin in diamond*, Communications Physics **2**, 1–6 (2019).

[71] L. H. Pedersen, N. M. Møller, and K. Mølmer, *Fidelity of quantum operations*, Journal of Physics A: Mathematical and Theoretical **55**, 085301 (2022).

[72] J. M. Gambetta, F. Motzoi, S. T. Merkel, and F. K. Wilhelm, *Analytic control methods for high-fidelity unitary operations in a weakly nonlinear oscillator*, Physical Review A **83**, 012308 (2011).

[73] L. S. Theis, F. Motzoi, S. Machnes, and F. K. Wilhelm, *Counteracting systems of diabaticities using drag controls: The status after 10 years*, EPL (Europhysics Letters) **123**, 60001 (2018).

[74] A. De, Fast quantum control for weakly nonlinear qubits: On two-quadrature adiabatic gates (2015), arXiv:1509.07905.

[75] Q. Guo *et al.*, *Reducing leakage of single-qubit gates for superconducting quantum processors*, PRX Quantum **5**, 030353 (2024).

[76] E. Lucero *et al.*, Reduced phase error through optimized control of a superconducting qubit (2010), arXiv:1007.1690.

[77] B. Li, *Practical Methods for Efficient Analytical Control in Superconducting Qubits*, Ph.D. thesis, Universität zu Köln (2025), phD thesis.

[78] F. Motzoi, J. M. Gambetta, S. T. Merkel, and F. K. Wilhelm, *Optimal control methods for rapidly time-varying Hamiltonians*, Phys. Rev. A **84**, 022307 (2011).

[79] V. Bergholm, W. Wieczorek, T. Schulte-Herbrüggen, and M. Keyl, *Optimal control of hybrid optomechanical systems for generating non-classical states of mechanical motion*, Quantum Sci. Technol. **4**, 190501 (2019).

[80] J. P. Palao and R. Kosloff, *Optimal control theory for unitary transformations*, Phys. Rev. A **68**, 062308 (2003).

[81] J. P. Palao and R. Kosloff, *Quantum Computing by an Optimal Control Algorithm for Unitary Transformations*, Phys. Rev. Lett. **89**, 188301 (2002).

[82] M. H. Goerz, D. Basilewitsch, F. Gago-Encinas, M. G. Krauss, K. P. Horn, *et al.*, *Krotov: A Python implementation of Krotov's method for quantum optimal control*, SciPost Phys. **7**, 80 (2019).

[83] P. Cerfontaine, T. Botzem, J. Ritzmann, and et al., *Closed-loop control of a gaas-based singlet-triplet spin qubit with 99.5% gate fidelity and low leakage*, Nature Communications **11**, 4144 (2020).

[84] S. Rosi, A. Bernard, N. Fabbri, L. Fallani, C. Fort, *et al.*, *Fast closed-loop optimal control of ultracold atoms in an optical lattice*, Phys. Rev. A **88**, 021601 (2013).

[85] J. D. Sterk, H. Coakley, J. Goldberg, V. Hietala, J. Lechtenberg, *et al.*, *Closed-loop optimization of fast trapped-ion shuttling with sub-quanta excitation*, npj Quantum Information **8**, 65 (2022).

[86] X.-d. Yang, C. Arenz, I. Pelczer, Q.-M. Chen, R.-B. Wu, *et al.*, *Assessing three closed-loop learning algorithms by searching for high-quality quantum control pulses*, Phys. Rev. A **102**, 062605 (2020).

[87] Z. Tošner, T. Vosegaard, C. Kehlet, N. Khaneja, S. J. Glaser, and N. C. Nielsen, *Optimal control in NMR spectroscopy: Numerical implementation in SIMPSON*, J. Magn. Reson. **197**, 120-134 (2009).

[88] P. de Fouquieres, S. G. Schirmer, S. J. Glaser, and I. Kuprov, *Second order gradient ascent pulse engineering*, J. Magn. Reson. **212**, 412–417 (2011).

[89] F. Preti, T. Calarco, and F. Motzoi, *Continuous quantum gate sets and pulse-class meta-optimization*, PRX Quantum **3**, 040311 (2022).

[90] P. Doria, T. Calarco, and S. Montangero, *Optimal control technique for many-body quantum dynamics*, Phys. Rev. Lett. **106**, 190501 (2011).

[91] M. M. Müller, R. S. Said, F. Jelezko, T. Calarco, and S. Montangero, *One decade of quantum optimal control in the chopped random basis*, Rep. Prog. Phys. **85**, 076001 (2022).

[92] L. Rossignolo, F. Roy, C. Ferrie, and S. Montangero, *Quocs: An open-source python package for optimal quantum control simulations*, arXiv preprint arXiv:2212.11144 (2022).

[93] J. R. Johansson, P. D. Nation, and F. Nori, *Qutip 2: A python framework for the dynamics of open quantum systems*, Computer Physics Communications **184**, 1234–1240 (2013).

[94] S. Machnes, E. Assémat, D. Tannor, and F. K. Wilhelm, *Tunable, flexible, and efficient optimization of control pulses for practical qubits*, Phys. Rev. Lett. **120**, 150401 (2018).

[95] W. Sun and Y.-X. Yuan, *Optimization Theory and Methods: Nonlinear Programming* (Springer, New York, 2010) p. 541.

[96] D. P. Bertsekas, *Nonlinear Programming*, 2nd ed. (Athena Scientific, Belmont, MA, 1999).

[97] N. Khaneja, R. Brockett, and S. J. Glaser, *Time optimal control in spin systems*, Phys. Rev. A **63**, 032308 (2001).

[98] U. Rasulov and I. Kuprov, *Instrumental distortions in quantum optimal control*, The Journal of Chemical Physics **162**, 10.1063/5.0264092 (2025).

[99] P. M. Poggi, G. De Chiara, S. Campbell, and A. Kiely, *Universally robust quantum control*, Phys. Rev. Lett. **132**, 193801 (2024).

[100] Y. Zhang, H. Wu, X. Yang, T. Xie, Y.-X. Wang, *et al.*, *Robust quantum control for the manipulation of solid-state spins*, Phys. Rev. Appl. **19**, 034068 (2023).

[101] F. Gelin *et al.*, *Interacting circular rydberg atoms trapped in optical tweezers*, PRX Quantum **6**, 010353 (2025), measurement and characterization of dipole-dipole interactions between circular Rydberg atoms.

[102] D. Barredo *et al.*, *A dual-species rydberg array*, Nature Physics 10.1038/s41567-024-02638-2 (2024), demonstration of interspecies Rydberg blockade and quantum state transfer.

[103] H. Menke *et al.*, *Tutorial: Calculation of rydberg interaction potentials*, arXiv preprint arXiv:1612.08053 (2017), detailed tutorial on calculating Rydberg interaction potentials.

[104] M. Saffman, T. G. Walker, and K. Mølmer, *Quantum information with rydberg atoms*, Reviews of Modern Physics **82**, 2313–2363 (2010), comprehensive review of Rydberg-mediated quantum information processing.

[105] J. Pritchard *et al.*, *Rydberg atom quantum technologies*, arXiv preprint arXiv:1907.09231 (2019), topical review on Rydberg atoms for quantum technologies.

[106] J. Nemirovsky and Y. Sagi, *Fast universal two-qubit gate for neutral fermionic atoms in optical tweezers*, Phys. Rev. Res. **3**, 013113 (2021).

[107] D. González-Cuadra *et al.*, *Fermionic quantum processing with programmable neutral atom arrays*, Proceedings of the National Academy of Sciences **120**, e2304294120 (2023).

[108] P. Atkins, J. de Paula, and J. Keeler, *Atkins' Physical Chemistry*, 12th ed. (Oxford University Press, 2022) see chapters on atomic spectra and quantum theory for detailed discussions of the Balmer and Rydberg series.

[109] N. Bohr, *On the constitution of atoms and molecules, part i*, Philosophical Magazine **26**, 1–25 (1913), bohr's quantum theory of the hydrogen atom, explaining the Balmer and Rydberg series.

[110] N. Šibalić and C. S. Adams, *Rydberg Physics*, 2399-2891 (IOP Publishing, 2018).

[111] C. S. Adams, J. D. Pritchard, and J. P. Shaffer, *Rydberg atom quantum technologies*, Journal of Physics B: Atomic, Molecular and Optical Physics **53**, 012002 (2019), free article.

[112] X. Wu, X. Liang, Y. Tian, F. Yang, C. Chen, *et al.*, *A concise review of rydberg atom based quantum computation and quantum simulation**, Chinese Physics B **30**, 020305 (2021).

[113] T. L. Nguyen, J. M. Raimond, C. Sayrin, R. Cortiñas, T. Cantat-Moltrecht, *et al.*, *Towards quantum simulation with circular rydberg atoms*, Phys. Rev. X **8**, 011032 (2018).

[114] R. G. Cortiñas, M. Favier, B. Ravon, P. Méhaignerie, Y. Machu, *et al.*, *Laser trapping of circular rydberg atoms*, Phys. Rev. Lett. **124**, 123201 (2020).

[115] A. Signoles, E. K. Dietsche, A. Facon, D. Grosso, S. Haroche, *et al.*, *Coherent transfer between low-angular-momentum and circular rydberg states*, Phys. Rev. Lett. **118**, 253603 (2017).

[116] I. I. Beterov, E. A. Yakshina, D. B. Tretyakov, V. M. Entin, N. V. Al'yanova, *et al.*, *Implementation of single-qubit quantum gates based on a microwave transition in a single rubidium atom in an optical dipole trap*, Journal of Experimental and Theoretical Physics **132**, 341–353 (2021).

[117] C. Sheng, X. He, P. Xu, R. Guo, K. Wang, *et al.*, *High-fidelity single-qubit gates on neutral atoms in a two-dimensional magic-intensity optical dipole trap array*, Phys. Rev. Lett. **121**, 240501 (2018).

[118] B. Nikolov, E. Diamond-Hitchcock, J. Bass, N. L. R. Spong, and J. D. Pritchard, *Randomized benchmarking using nondestructive readout in a two-dimensional atom array*, Phys. Rev. Lett. **131**, 030602 (2023).

[119] Y.-Y. Jau, A. M. Hankin, T. Keating, I. H. Deutsch, and G. W. Biedermann, *Entangling atomic spins with a rydberg-dressed spin-flip blockade*, Nature Physics **12**, 71–74 (2016).

[120] A. Browaeys and T. Lahaye, *Many-body physics with individually controlled rydberg atoms*, Nature Physics **16**, 132–142 (2020).

[121] I. S. Madjarov, J. P. Covey, A. L. Shaw, J. Choi, A. Kale, *et al.*, *High-fidelity entanglement and detection of alkaline-earth rydberg atoms*, Nature Physics **16**, 857–861 (2020).

[122] N. Schine, A. W. Young, W. J. Eckner, M. J. Martin, and A. M. Kaufman, *Long-lived bell states in an array of optical clock qubits*, Nature Physics **18**, 1067–1073 (2022).

[123] G. Unnikrishnan, P. Ilzhöfer, A. Scholz, C. Hölzl, A. Götzelmann, *et al.*, *Coherent control of the fine-structure qubit in a single alkaline-earth atom*, Physical Review Letters **132**, 10.1103/physrevlett.132.150606 (2024).

[124] K. R. Brown, A. C. Wilson, Y. Colombe, C. Ospelkaus, A. M. Meier, *et al.*, *Single-qubit-gate error below* $\mathbf{10^{-4}}$ *in a trapped ion*, Phys. Rev. A **84**, 030303 (2011).

[125] D. D. Yavuz, P. B. Kulatunga, E. Urban, T. A. Johnson, N. Proite, *et al.*, *Fast ground state manipulation of neutral atoms in microscopic optical traps*, Phys. Rev. Lett. **96**, 063001 (2006).

[126] M. P. A. Jones, J. Beugnon, A. Gaëtan, J. Zhang, G. Messin, *et al.*, *Fast quantum state control of a single trapped neutral atom*, Phys. Rev. A **75**, 040301 (2007).

[127] E. Charron, M. A. Cirone, A. Negretti, J. Schmiedmayer, and T. Calarco, *Theoretical analysis of a realistic atom-chip quantum gate*, Phys. Rev. A **74**, 012308 (2006).

[128] J. B. Naber, L. Torralbo-Campo, T. Hubert, and R. J. C. Spreeuw, *Raman transitions between hyperfine clock states in a magnetic trap*, Physical Review A **94**, 10.1103/physreva.94.013427 (2016).

[129] J. Kim, Lecture notes 10: Two-photon transitions, `https://people.ee.duke.edu/~jungsang/ECE590_01/LectureNotes10.pdf`, accessed: 2025-06-01.

[130] D. A. Steck, Quantum and atom optics, Available online at `http://steck.us/teaching` (2025), revision 0.16.4, 7 May 2025.

[131] D. Jaksch, J. I. Cirac, P. Zoller, S. L. Rolston, R. Côté, and M. D. Lukin, *Fast quantum gates for neutral atoms*, Phys. Rev. Lett. **85**, 2208–2211 (2000).

[132] S. Jandura, J. D. Thompson, and G. Pupillo, *Optimizing rydberg gates for logical-qubit performance*, PRX Quantum **4**, 020336 (2023).

[133] H. Levine, A. Keesling, G. Semeghini, A. Omran, T. T. Wang, *et al.*, *Parallel implementation of high-fidelity multiqubit gates with neutral atoms*, Phys. Rev. Lett. **123**, 170503 (2019).

[134] Z. Fu, P. Xu, Y. Sun, Y.-Y. Liu, X.-D. He, *et al.*, *High-fidelity entanglement of neutral atoms via a Rydberg-mediated single-modulated-pulse controlled-phase gate*, Phys. Rev. A **105**, 042430 (2022).

[135] G. Giudici, S. Veroni, G. Giudice, H. Pichler, and J. Zeiher, Fast entangling gates for rydberg atoms via resonant dipole-dipole interaction (2024), arXiv:2411.05073 [quant-ph] .

[136] X.-F. Shi, *Quantum logic and entanglement by neutral rydberg atoms: methods and fidelity*, Quantum Science and Technology **7**, 023002 (2022).

[137] S. de Léséleuc, *Quantum simulation of spin models with assembled arrays of Rydberg atoms*, Ph.D. thesis, Université Paris-Saclay, Institut d'Optique Graduate School, Palaiseau, France (2018), thèse présentée et soutenue à Palaiseau, le 10 décembre 2018.

[138] H. Levine, A. Keesling, A. Omran, H. Bernien, S. Schwartz, *et al.*, *High-fidelity control and entanglement of rydberg-atom qubits*, Phys. Rev. Lett. **121**, 123603 (2018).

[139] N. V. Vitanov, A. A. Rangelov, B. W. Shore, and K. Bergmann, *Stimulated raman adiabatic passage in physics, chemistry, and beyond*, Reviews of Modern Physics **89**, 10.1103/revmodphys.89.015006 (2017).

[140] B. M. Sparkes, D. Murphy, R. J. Taylor, R. W. Speirs, A. J. McCulloch, and R. E. Scholten, *Stimulated raman adiabatic passage for improved performance of a cold-atom electron and ion source*, Phys. Rev. A **94**, 023404 (2016).

[141] Y.-X. Du, Z.-T. Liang, Y.-C. Li, X.-X. Yue, Q.-X. Lv, *et al.*, *Experimental realization of stimulated raman shortcut-to-adiabatic passage with cold atoms*, Nature Communications **7**, 12479 (2016), arXiv:1601.06058.

[142] J. T. Wilson, S. Saskin, Y. Meng, S. Ma, R. Dilip, *et al.*, *Trapping alkaline earth rydberg atoms optical tweezer arrays*, Phys. Rev. Lett. **128**, 033201 (2022).

[143] A. Cooper, J. P. Covey, I. S. Madjarov, S. G. Porsev, M. S. Safronova, and M. Endres, *Alkaline-earth atoms in optical tweezers*, Phys. Rev. X **8**, 041055 (2018).

[144] M. A. Norcia, A. W. Young, and A. M. Kaufman, *Microscopic control and detection of ultracold strontium in optical-tweezer arrays*, Phys. Rev. X **8**, 041054 (2018).

[145] W. Gunton, The loading and storage of li and rb in an optical dipole trap (2009).

[146] A. M. Kaufman and K.-K. Ni, *Quantum science with optical tweezer arrays of ultracold atoms and molecules*, Nature Physics **17**, 1324–1333 (2021).

[147] M. Takamoto and H. Katori, *Spectroscopy of the* $^1s_0$–$^3p_0$ *clock transition of* ^{87}Sr *in an optical lattice*, Phys. Rev. Lett. **91**, 223001 (2003).

[148] J. Tallant, D. Booth, and J. P. Shaffer, *Photoionization rates of cs rydberg atoms in a 1064-nm far-off-resonance trap*, Phys. Rev. A **82**, 063406 (2010).

[149] M. Saffman and T. G. Walker, *Analysis of a quantum logic device based on dipole-dipole interactions of optically trapped rydberg atoms*, Phys. Rev. A **72**, 022347 (2005).

[150] F. Schäfer, T. Fukuhara, S. Sugawa, Y. Takasu, and Y. Takahashi, *Tools for quantum simulation with ultracold atoms in optical lattices*, Nature Reviews Physics **2**, 411–425 (2020).

[151] A. Derevianko and H. Katori, *Colloquium: Physics of optical lattice clocks*, Rev. Mod. Phys. **83**, 331–347 (2011).

[152] F. Gkritsis, D. Dux, J. Zhang, N. Jain, C. Gogolin, and P. M. Preiss, *Simulating chemistry with fermionic optical superlattices*, PRX Quantum **6**, 010318 (2025).

[153] A. Pagano, S. Weber, D. Jaschke, T. Pfau, F. Meinert, *et al.*, *Error budgeting for a controlled-phase gate with strontium-88 rydberg atoms*, Phys. Rev. Res. **4**, 033019 (2022).

[154] E. Urban, T. A. Johnson, T. Henage, L. Isenhower, D. D. Yavuz, *et al.*, *Observation of rydberg blockade between two atoms*, Nature Physics **5**, 110–114 (2009).

[155] M. D. Lukin, M. Fleischhauer, R. Cote, L. M. Duan, D. Jaksch, *et al.*, *Dipole blockade and quantum information processing in mesoscopic atomic ensembles*, Phys. Rev. Lett. **87**, 037901 (2001).

[156] M. Hirose and P. Cappellaro, *Time-optimal control with finite bandwidth*, Quantum Information Processing **17**, 88 (2018).

[157] T. Chalopin, P. Bojović, D. Bourgund, S. Wang, T. Franz, *et al.*, (2024), arXiv:2405.19322 .

[158] S. Dörscher, A. Al-Masoudi, M. Bober, V. Schkolnik, C. Grebing, *et al.*, *Dynamical decoupling of laser phase noise in compound atomic clocks*, Communications Physics **3**, 185 (2020).

[159] S. Trotzky, P. Cheinet, S. Fölling, M. Feld, U. Schnorrberger, *et al.*, *Time-resolved observation and control of superexchange interactions with ultracold atoms in optical lattices*, Science **319**, 295-299 (2008).

[160] B. Yang, H. Sun, C.-J. Huang, H.-Y. Wang, Y. Deng, *et al.*, *Cooling and entangling ultracold atoms in optical lattices*, Science **369**, 550-553 (2020), https://www.science.org/doi/pdf/10.1126/science.aaz6801 .

[161] M. Anderlini, P. J. Lee, B. L. Brown, J. Sebby-Strabley, W. D. Phillips, and J. V. Porto, *Controlled exchange interaction between pairs of neutral atoms in an optical lattice*, Nature **448**, 452-456 (2007).

[162] T. Calarco, U. Dorner, P. S. Julienne, C. J. Williams, and P. Zoller, *Quantum computations with atoms in optical lattices: Marker qubits and molecular interactions*, Phys. Rev. A **70**, 012306 (2004).

[163] Z. Idziaszek and T. Calarco, *Two atoms in an anisotropic harmonic trap*, Phys. Rev. A **71**, 050701 (2005).

[164] T. Calarco, E. A. Hinds, D. Jaksch, J. Schmiedmayer, J. I. Cirac, and P. Zoller, *Quantum gates with neutral atoms: Controlling collisional interactions in time-dependent traps*, Phys. Rev. A **61**, 022304 (2000).

[165] N. B. Jørgensen, M. G. Bason, and J. F. Sherson, *One- and two-qubit quantum gates using superimposed optical-lattice potentials*, Phys. Rev. A **89**, 032306 (2014).

[166] C. Kittel, *Introduction to Solid State Physics*, 7th ed. (Wiley, New York, 1996).

[167] F. Görg, Ultracold fermionic atoms in optical superlattices (2014).

[168] U. Bissbort, *Dynamical effects and disorder in ultracold bosonic matter*, doctoralthesis, Universitätsbibliothek Johann Christian Senckenberg (2013).

[169] G. H. Wannier, *The structure of electronic excitation levels in insulating crystals*, Phys. Rev. **52**, 191–197 (1937).

[170] W. Kohn, *Analytic properties of bloch waves and wannier functions*, Phys. Rev. **115**, 809–821 (1959).

[171] W. Kohn, *Construction of wannier functions and applications to energy bands*, Phys. Rev. B **7**, 4388–4398 (1973).

[172] T. Uehlinger, G. Jotzu, M. Messer, D. Greif, W. Hofstetter, *et al.*, *Artificial graphene with tunable interactions*, Phys. Rev. Lett. **111**, 185307 (2013).

[173] I. Bloch, *Ultracold quantum gases in optical lattices*, Nature Physics **1**, 23–30 (2005).

[174] I. Bloch, J. Dalibard, and W. Zwerger, *Many-body physics with ultracold gases*, Rev. Mod. Phys. **80**, 885–964 (2008).

[175] T. Esslinger, *Fermi-hubbard physics with atoms in an optical lattice*, Annu. Rev. Condens. Matter Phys. **1**, 129-152 (2010).

[176] W. Hofstetter, J. I. Cirac, P. Zoller, E. Demler, and M. D. Lukin, *High-temperature superfluidity of fermionic atoms in optical lattices*, Phys. Rev. Lett. **89**, 220407 (2002).

[177] D. Hayes, P. S. Julienne, and I. H. Deutsch, *Quantum logic via the exchange blockade in ultracold collisions*, Phys. Rev. Lett. **98**, 070501 (2007).

[178] A. Impertro, S. Karch, J. F. Wienand, S. Huh, C. Schweizer, *et al.*, *Local readout and control of current and kinetic energy operators in optical lattices*, Phys. Rev. Lett. **133**, 10.1103/PhysRevLett.133.063401 (2024).

[179] Y. Wang, X. Dai, X. Zhao, G. Sun, K. Gao, and W. Zhang, A stable phase-locking-free single beam optical lattice with multiple configurations (2025), arXiv:2501.01843 [quant-ph] .

[180] Q. Beaufils, G. Tackmann, X. Wang, B. Pelle, S. Pelisson, *et al.*, *Laser controlled tunneling in a vertical optical lattice*, Phys. Rev. Lett. **106**, 213002 (2011).

[181] S. Pucher, V. Klüsener, F. Spriestersbach, J. Geiger, A. Schindewolf, *et al.*, *Fine-structure qubit encoded in metastable strontium trapped in an optical lattice*, Phys. Rev. Lett. **132**, 150605 (2024).

[182] I. H. Deutsch, G. K. Brennen, and P. S. Jessen, *Quantum computing with neutral atoms in an optical lattice*, Fortschritte der Physik **48**, 925-943.

[183] I. H. Deutsch and P. S. Jessen, *Quantum-state control in optical lattices*, Phys. Rev. A **57**, 1972–1986 (1998).

[184] O. Morsch, G. M. Palma, and D. Rossini, *Quantum simulations of complex systems*, Rivista del Nuovo Cimento , 43 (2025), arXiv:2505.20442 [quant-ph] .

[185] M. Foss-Feig, G. Pagano, A. C. Potter, and N. Y. Yao, Progress in trapped-ion quantum simulation (2024), arXiv:2409.02990 [quant-ph] .

[186] I. Buluta and F. Nori, *Quantum simulators*, Science **326**, 108-111 (2009), https://www.science.org/doi/pdf/10.1126/science.1177838 .

[187] K. Wintersperger, F. Dommert, T. Ehmer, *et al.*, *Neutral atom quantum computing hardware: performance and end-user perspective*, EPJ Quantum Technology **10**, 32 (2023).

[188] A. M. Childs, D. Maslov, Y. Nam, N. J. Ross, and Y. Su, *Toward the first quantum simulation with quantum speedup*, Proceedings of the National Academy of Sciences **115**, 9456-9461 (2018), https://www.pnas.org/doi/pdf/10.1073/pnas.1801723115 .

[189] M. Müller, S. Diehl, G. Pupillo, and P. Zoller, Engineered open systems and quantum simulations with atoms and ions (2012), arXiv:1203.6595 [quant-ph] .

[190] S. Lloyd, *Universal quantum simulators*, Science **273**, 1073–1078 (1996).

[191] S. Flannigan, N. Pearson, G. H. Low, A. Buyskikh, I. Bloch, *et al.*, *Propagation of errors and quantitative quantum simulation with quantum advantage*, Quantum Science and Technology **7**, 045025 (2022).

[192] M. D'Arcangelo, L.-P. Henry, L. Henriet, D. Loco, N. Gouraud, *et al.*, *Leveraging analog quantum computing with neutral atoms for solvent configuration prediction in drug discovery*, Phys. Rev. Res. **6**, 043020 (2024).

[193] J. yoon Choi, S. Hild, J. Zeiher, P. Schauß, A. Rubio-Abadal, *et al.*, *Exploring the many-body localization transition in two dimensions*, Science **352**, 1547-1552 (2016), https://www.science.org/doi/pdf/10.1126/science.aaf8834 .

[194] I. Bloch, J. Dalibard, and S. Nascimbène, *Quantum simulations with ultracold quantum gases*, Nat. Phys. **8**, 267–276 (2012).

[195] Z. Zimborás, R. Zeier, T. Schulte-Herbrüggen, and D. Burgarth, *Symmetry criteria for quantum simulability of effective interactions*, Phys. Rev. A **92**, 042309 (2015).

[196] T. Schulte-Herbrüggen, R. Zeier, M. Keyl, and G. Dirr, in *Quantum Information: From Foundations to Quantum Technology Applications*, Vol. 2, edited by D. Bruss and G. Leuchs (Wiley, Weinheim, 2019) 2nd ed., pp. 607–641.

[197] R. Zeier and T. Schulte-Herbrüggen, *Symmetry principles in quantum systems theory*, J. Math. Phys. **52**, 113510 (2011).

[198] S. Endo, Z. Cai, S. C. Benjamin, and X. Yuan, *Hybrid Quantum-Classical Algorithms and Quantum Error Mitigation*, J. Phys. Soc. Jpn. **90**, 032001 (2021).

[199] Y. Cao, J. Romero, J. P. Olson, M. Degroote, P. D. Johnson, *et al.*, *Quantum Chemistry in the Age of Quantum Computing*, Chem. Rev. **119**, 10856–10915 (2019).

[200] A. Peruzzo, J. McClean, P. Shadbolt, M.-H. Yung, X.-Q. Zhou, *et al.*, *A variational eigenvalue solver on a photonic quantum processor*, Nat. Commun. **5**, 4213 (2014).

[201] J. R. McClean, J. Romero, R. Babbush, and A. Aspuru-Guzik, *The theory of variational hybrid quantum-classical algorithms*, New J. Phys. **18**, 023023 (2016).

[202] D. Wecker, M. B. Hastings, and M. Troyer, *Progress towards practical quantum variational algorithms*, Phys. Rev. A **92**, 042303 (2015).

[203] J. Tilly, H. Chen, S. Cao, D. Picozzi, K. Setia, *et al.*, *The Variational Quantum Eigensolver: A review of methods and best practices*, Phys. Rep. **986**, 1–128 (2022).

[204] J. R. McClean, S. Boixo, V. N. Smelyanskiy, R. Babbush, and H. Neven, *Barren plateaus in quantum neural network training landscapes*, Nat. Commun. **9**, 4812 (2018).

[205] M. Cerezo, G. Verdon, H.-Y. Huang, L. Cincio, and P. J. Coles, *Challenges and opportunities in quantum machine learning*, Nat. Comput. Sci. **2**, 567–576 (2022).

[206] M. Cerezo, A. Sone, T. Volkoff, L. Cincio, and P. J. Coles, *Cost function dependent barren plateaus in shallow parametrized quantum circuits*, Nat. Commun. **12**, 1791 (2021).

[207] S. Kazi, M. Larocca, M. Farinati, P. J. Coles, M. Cerezo, and R. Zeier, Analyzing the quantum approximate optimization algorithm: ansatze, symmetries, and Lie algebras (2024), arXiv:2410.05187 .

[208] S. Szalay, Z. Zimborás, M. Máté, G. Barcza, C. Schilling, and Ö. Legeza, *Fermionic systems for quantum information people*, Journal of Physics A: Mathematical and Theoretical **54**, 393001 (2021).

[209] A. Szabo and N. S. Ostlund, *Modern Quantum Chemistry: Introduction to Advanced Electronic Structure Theory* (Dover Publications, Mineola, New York, 1996).

[210] P. W. Atkins and R. S. Friedman, *Molecular Quantum Mechanics*, 4th ed. (Oxford University Press, Oxford, 2005).

[211] P. Coleman, Simple examples of second quantization, in *Introduction to Many-Body Physics* (Cambridge University Press, 2015) p. 71–94.

[212] J. Eisert, Advanced quantum mechanics (20104301) – chapter 3: Elements of second quantization, https://www.physik.fu-berlin.de/en/einrichtungen/ag/ag-eisert/teaching/ws19-20/AdvancedQuantumMechanicsChapter0.pdf (2020), lecture notes, Freie Universität Berlin.

[213] C. Gross, T. Zibold, E. Nicklas, J. Estève, and M. K. Oberthaler, *Nonlinear atom interferometer surpasses classical precision limit*, Nature **464**, 1165–1169 (2010).

[214] D. Kielpinski, C. Monroe, and D. J. Wineland, *Architecture for a large-scale ion-trap quantum computer*, Nature **417**, 709–711 (2002).

[215] G. Feng, J. J. Wallman, B. Buonacorsi, F. H. Cho, D. K. Park, *et al.*, *Estimating the coherence of noise in quantum control of a solid-state qubit*, Phys. Rev. Lett. **117**, 260501 (2016).

[216] T. E. Skinner and N. I. Gershenzon, *Optimal control design of pulse shapes as analytic functions*, J. Magn. Reson. **204**, 248-255 (2010).

[217] S. Gustavsson, O. Zwier, J. Bylander, F. Yan, F. Yoshihara, *et al.*, *Improving Quantum Gate Fidelities by Using a Qubit to Measure Microwave Pulse Distortions*, Phys. Rev. Lett. **110**, 040502 (2013).

[218] P. E. Spindler, Y. Zhang, B. Endeward, N. Gershernzon, T. E. Skinner, *et al.*, *Shaped optimal control pulses for increased excitation bandwidth in EPR*, J. Magn. Reson. **218**, 49-58 (2012).

[219] T. Kaufmann, T. J. Keller, J. M. Franck, R. P. Barnes, S. J. Glaser, *et al.*, *DAC-board based X-band EPR spectrometer with arbitrary waveform control*, J. Magn. Reson. **235**, 95-108 (2013).

[220] P. E. Spindler, P. Schöps, W. Kallies, S. J. Glaser, and T. F. Prisner, *Perspectives of shaped pulses for EPR spectroscopy*, J. Magn. Reson. **280**, 30-45 (2017).

[221] D. D. Rife and J. Vanderkooy, *Transfer-function measurement with maximum-length sequences*, AES: J. Audio Eng. Soc. **37**, 419 – 444 (1989).

[222] I. N. M. Le, J. D. Teske, T. Hangleiter, P. Cerfontaine, and H. Bluhm, *Analytic filter-function derivatives for quantum optimal control*, Phys. Rev. Applied **17**, 024006 (2022).

[223] C. Brif, R. Chakrabarti, and H. Rabitz, *Control of quantum phenomena: past, present and future*, New J. Phys. **12**, 075008 (2010).

[224] D. D'Alessandro, *Introduction to Quantum Control and Dynamics*, 2nd ed. (CRC Press, Boca Raton, 2022).

[225] I. Hincks, C. Granade, T. W. Borneman, and D. G. Cory, *Controlling quantum devices with nonlinear hardware*, Phys. Rev. Applied **4**, 024012 (2015).

[226] G. Jäger and U. Hohenester, *Optimal quantum control of Bose-Einstein condensates in magnetic microtraps: Consideration of filter effects*, Phys. Rev. A **88**, 035601 (2013).

[227] N. Wittler, F. Roy, K. Pack, M. Werninghaus, A. S. Roy, *et al.*, *Integrated tool set for control, calibration, and characterization of quantum devices applied to superconducting qubits*, Phys. Rev. Applied **15**, 034080 (2021).

[228] J. J. Sørensen, J. S. Nyemann, F. Motzoi, J. Sherson, and T. Vosegaard, *Optimization of pulses with low bandwidth for improved excitation of multiple-quantum coherences in NMR of quadrupolar nuclei*, J. Chem. Phys. **152**, 054104 (2020).

[229] J. J. W. H. Sørensen, M. O. Aranburu, T. Heinzel, and J. F. Sherson, *Quantum optimal control in a chopped basis: Applications in control of Bose-Einstein condensates*, Phys. Rev. A **98**, 022119 (2018).

[230] N. Khaneja, S. J. Glaser, and R. Brockett, *Sub-riemannian geometry and time optimal control of three spin systems: Quantum gates and coherence transfer*, Phys. Rev. A **65**, 032301 (2002).

[231] C. H. Bennett, J. I. Cirac, M. S. Leifer, D. W. Leung, N. Linden, *et al.*, *Optimal simulation of two-qubit hamiltonians using general local operations*, Phys. Rev. A **66**, 012305 (2002).

[232] G. Vidal, K. Hammerer, and J. I. Cirac, *Interaction Cost of Nonlocal Gates*, Phys. Rev. Lett. **88**, 237902 (2002).

[233] R. Zeier, M. Grassl, and T. Beth, *Gate Simulation and Lower Bounds on the Simulation Time*, Phys. Rev. A **70**, 032319 (2004).

[234] A. Carlini, A. Hosoya, T. Koike, and Y. Okudaira, *Time-optimal quantum evolution*, Phys. Rev. Lett. **96**, 060503 (2006).

[235] N. Khaneja, B. Heitmann, A. Spörl, H. Yuan, T. Schulte-Herbrüggen, and S. J. Glaser, *Shortest paths for efficient control of indirectly coupled qubits*, Phys. Rev. A **75**, 012322 (2007).

[236] H. Yuan, R. Zeier, and N. Khaneja, *Elliptic functions and efficient control of ising spin chains with unequal couplings*, Phys. Rev. A **77**, 032340 (2008).

[237] R. Zeier, H. Yuan, and N. Khaneja, *Time-optimal synthesis of unitary transformations in a coupled fast and slow qubit system*, Phys. Rev. A **77**, 032332 (2008).

[238] A. Carlini, A. Hosoya, T. Koike, and Y. Okudaira, *Time-optimal CNOT between indirectly coupled qubits in a linear Ising chain*, J. Phys. A **44**, 145302 (2011).

[239] M. Nimbalkar, R. Zeier, J. L. Neves, S. B. Elavarasi, H. Yuan, *et al.*, *Multiple-spin coherence transfer in linear ising spin chains and beyond: Numerically optimized pulses and experiments*, Phys. Rev. A **85**, 012325 (2012).

[240] A. Carlini and T. Koike, *Time-optimal transfer of coherence*, Phys. Rev. A **86**, 054302 (2012).

[241] L. Van Damme, R. Zeier, S. J. Glaser, and D. Sugny, *Application of the pontryagin maximum principle to the time-optimal control in a chain of three spins with unequal couplings*, Phys. Rev. A **90**, 013409 (2014).

[242] H. Yuan, R. Zeier, N. Pomplun, S. J. Glaser, and N. Khaneja, *Time-optimal polarization transfer from an electron spin to a nuclear spin*, Phys. Rev. A **92**, 053414 (2015).

[243] R. Freeman, *Spin choreography* (Oxford University Press Oxford, 1998).

[244] D. Guéry-Odelin, A. Ruschhaupt, A. Kiely, E. Torrontegui, S. Martínez-Garaot, and J. G. Muga, *Shortcuts to adiabaticity: Concepts, methods, and applications*, Rev. Mod. Phys. **91**, 045001 (2019).

[245] H. Liu, S. J. Glaser, and G. P. Drobny, *Development and optimization of multipulse propagators: Applications to homonuclear spin decoupling in solids*, J. Chem. Phys. **93**, 7543-7560 (1990).

[246] D. L. Goodwin, W. K. Myers, C. R. Timmel, and I. Kuprov, *Feedback control optimisation of ESR experiments*, J. Magn. Reson. **297**, 9-16 (2018).

[247] C. J. Bardeen, V. V. Yakovlev, K. R. Wilson, S. D. Carpenter, P. M. Weber, and W. S. Warren, *Feedback quantum control of molecular electronic population transfer*, Chem. Phys. Lett. **280**, 151-158 (1997).

[248] A. I. Solomon and S. G. Schirmer, *Quantum control of two-qubit entanglement dissipation*, J. Russ. Laser Res. **32**, 502–510 (2011).

[249] F. Motzoi, E. Halperin, X. Wang, K. B. Whaley, and S. Schirmer, *Backaction-driven, robust, steady-state long-distance qubit entanglement over lossy channels*, Phys. Rev. A **94**, 032313 (2016).

[250] J. Singh, R. Zeier, T. Calarco, and F. Motzoi, Raw data files (2023).

[251] V. Mathews and G. L. Sicuranza, *Polynomial signal processing* (Wiley, New York, 2000).

[252] C. Cheng, Z. Peng, W. Zhang, and G. Meng, *Volterra-series-based nonlinear system modeling and its engineering applications: A state-of-the-art review*, Mech. Syst. Signal Process. **87**, 340–364 (2017).

[253] Y. W. Lee and M. Schetzen, *Measurement of the Wiener Kernels of a Non-linear System by Cross-correlation*, Int. J. Control **2**, 237–254 (1965).

[254] M. J. Korenberg, S. B. Bruder, and P. J. McLlroy, *Exact orthogonal kernel estimation from finite data records: Extending Wiener's identification of nonlinear systems*, Ann. Biomed. Eng. **16**, 201–214 (1988).

[255] R. A. Horn and C. R. Johnson, *Matrix analysis* (Cambridge University Press, Cambridge, 1985).

[256] G. H. Golub and C. F. Van Loan, *Matrix computations*, 3rd ed. (The John Hopkins University Press, Baltimore, 1996).

[257] H. Weimer, M. Müller, I. Lesanovsky, P. Zoller, and H. P. Büchler, *A Rydberg quantum simulator*, Nat. Phys. **6**, 382–388 (2010).

[258] A. Browaeys, D. Barredo, and T. Lahaye, *Experimental investigations of dipole-dipole interactions between a few Rydberg atoms*, J. Phys. B **49**, 152001 (2016).

[259] S. de Léséleuc, D. Barredo, V. Lienhard, A. Browaeys, and T. Lahaye, *Analysis of imperfections in the coherent optical excitation of single atoms to Rydberg states*, Phys. Rev. A **97**, 053803 (2018).

[260] S. Zeng, K. Bi, S. Xue, Y. Liu, X. Lv, and Q. Luo, *Acousto-optic modulator system for femtosecond laser pulses*, Rev. Sci. Instrum. **78**, 015103 (2007).

[261] O. Tzang, D. Hershkovitz, A. Nagler, and O. Cheshnovsky, *Pure sinusoidal photo-modulation using an acousto-optic modulator*, Rev. Sci. Instrum. **89**, 123102 (2018).

[262] A. Castro, J. Werschnik, and E. K. U. Gross, *Controlling the dynamics of many-electron systems from first principles: A combination of optimal control and time-dependent density-functional theory*, Phys. Rev. Lett. **109**, 153603 (2012).

[263] J. Li, X. Yang, X. Peng, and C.-P. Sun, *Hybrid quantum-classical approach to quantum optimal control*, Phys. Rev. Lett. **118**, 150503 (2017).

[264] J. Kelly, R. Barends, B. Campbell, Y. Chen, Z. Chen, *et al.*, *Optimal quantum control using randomized benchmarking*, Phys. Rev. Lett. **112**, 240504 (2014).

[265] M. A. Rol, C. C. Bultink, T. E. O'Brien, S. R. de Jong, L. S. Theis, *et al.*, *Restless tuneup of high-fidelity qubit gates*, Phys. Rev. Applied **7**, 041001 (2017).

[266] D. J. Egger and F. K. Wilhelm, *Adaptive hybrid optimal quantum control for imprecisely characterized systems*, Phys. Rev. Lett. **112**, 240503 (2014).

[267] A. R. Conn, N. I. M. Gould, and P. L. Toint, *Trust Region Methods* (SIAM: Society for Industrial and Applied Mathematics, 2000).

[268] R. H. Byrd, P. Lu, J. Nocedal, and C. Zhu, *A limited memory algorithm for bound constrained optimization*, SIAM Journal on Scientific Computing **16**, 1190-1208 (1995).

[269] M. Dalgaard, F. Motzoi, J. H. M. Jensen, and J. Sherson, *Hessian-based optimization of constrained quantum control*, Phys. Rev. A **102**, 042612 (2020).

[270] A. H. Al-Mohy and N. J. Higham, *Computing the Fréchet Derivative of the Matrix Exponential, with an Application to Condition Number Estimation*, SIAM J. Matrix Anal. Appl. **30**, 1639-1657 (2009).

[271] P. Virtanen, R. Gommers, T. E. Oliphant, M. Haberland, T. Reddy, *et al.*, *SciPy 1.0: Fundamental Algorithms for Scientific Computing in Python*, Nat. Methods **17**, 261–272 (2020).

[272] C. Monroe and J. Kim, *Scaling the ion trap quantum processor*, Science **339**, 1164-1169 (2013).

[273] M. Saffman, *Quantum computing with atomic qubits and rydberg interactions: progress and challenges*, J. Phys. B. **49**, 202001 (2016).

[274] C. Gross and I. Bloch, *Quantum simulations with ultracold atoms in optical lattices*, Science **357**, 995-1001 (2017).

[275] E. Knill, R. Laflamme, and G. J. Milburn, *A scheme for efficient quantum computation with linear optics*, Nature **409**, 46-52 (2001).

[276] R. Prevedel, P. Walther, F. Tiefenbacher, P. Böhi, R. Kaltenbaek, *et al.*, *High-speed linear optics quantum computing using active feed-forward*, Nature **445**, 65-69 (2007).

[277] F. Flamini, N. Spagnolo, and F. Sciarrino, *Photonic quantum information processing: a review*, Rep. Prog. Phys. **82**, 016001 (2018).

[278] P. Kok, W. J. Munro, K. Nemoto, T. C. Ralph, J. P. Dowling, and G. J. Milburn, *Linear optical quantum computing with photonic qubits*, Rev. Mod. Phys. **79**, 135–174 (2007).

[279] M. V. G. Dutt, L. Childress, L. Jiang, E. Togan, J. Maze, *et al.*, *Quantum register based on individual electronic and nuclear spin qubits in diamond*, Science **316**, 1312-1316 (2007).

[280] J. R. Weber, W. F. Koehl, J. B. Varley, A. Janotti, B. B. Buckley, *et al.*, *Quantum computing with defects*, PNAS **107**, 8513-8518 (2010).

[281] A. Imamoglu, D. D. Awschalom, G. Burkard, D. P. DiVincenzo, D. Loss, *et al.*, *Quantum information processing using quantum dot spins and cavity qed*, Phys. Rev. Lett. **83**, 4204–4207 (1999).

[282] J. R. Petta, A. C. Johnson, J. M. Taylor, E. A. Laird, A. Yacoby, *et al.*, *Coherent manipulation of coupled electron spins in semiconductor quantum dots*, Science **309**, 2180-2184 (2005).

[283] R. Hanson, L. P. Kouwenhoven, J. R. Petta, S. Tarucha, and L. M. K. Vandersypen, *Spins in few-electron quantum dots*, Rev. Mod. Phys. **79**, 1217–1265 (2007).

[284] H. Levine, A. Keesling, G. Semeghini, A. Omran, T. T. Wang, *et al.*, *Parallel Implementation of High-Fidelity Multiqubit Gates with Neutral Atoms*, Phys. Rev. Lett. **123**, 170503 (2019).

[285] M. H. Goerz, T. Calarco, and C. P. Koch, *The quantum speed limit of optimal controlled phasegates for trapped neutral atoms*, Journal of Physics B: Atomic, Molecular and Optical Physics **44**, 154011 (2011).

[286] D. Tong, S. M. Farooqi, J. Stanojevic, S. Krishnan, Y. P. Zhang, *et al.*, *Local blockade of rydberg excitation in an ultracold gas*, Phys. Rev. Lett. **93**, 063001 (2004).

[287] T. Vogt, M. Viteau, A. Chotia, J. Zhao, D. Comparat, and P. Pillet, *Electric-field induced dipole blockade with rydberg atoms*, Phys. Rev. Lett. **99**, 073002 (2007).

[288] L. S. Theis, F. Motzoi, F. K. Wilhelm, and M. Saffman, *High-fidelity rydberg-blockade entangling gate using shaped, analytic pulses*, Phys. Rev. A **94**, 032306 (2016).

[289] M. M. Müller, M. Murphy, S. Montangero, T. Calarco, P. Grangier, and A. Browaeys, *Implementation of an experimentally feasible controlled-phase gate on two blockaded rydberg atoms*, Phys. Rev. A **89**, 032334 (2014).

[290] Z. Zhu, Y. Kiefer, S. Jele, M. Gächter, G. Bisson, *et al.*, Splitting and connecting singlets in atomic quantum circuits (2025), arXiv:2409.02984 [quant-ph] .

[291] M. Lubasch, V. Murg, U. Schneider, J. I. Cirac, and M.-C. Bañuls, *Adiabatic preparation of a heisenberg antiferromagnet using an optical superlattice*, Phys. Rev. Lett. **107**, 165301 (2011).

[292] L. Tarruell and L. Sanchez-Palencia, *Quantum simulation of the hubbard model with ultracold fermions in optical lattices*, C. R. Phys. **19**, 365-393 (2018).

[293] M. R. Lam, N. Peter, T. Groh, W. Alt, C. Robens, *et al.*, *Demonstration of quantum brachistochrones between distant states of an atom*, Phys. Rev. X **11**, 011035 (2021).

[294] A. Pagano, D. Jaschke, W. Weiss, and S. Montangero, *Optimal control transport of neutral atoms in optical tweezers at finite temperature*, Phys. Rev. Res. **6**, 033282 (2024).

[295] C. Cicali, M. Calzavara, E. Cuestas, T. Calarco, R. Zeier, and F. Motzoi, Neutral atom transport and transfer between optical tweezers (2024), arXiv:2412.15173 [quant-ph] .

[296] M. Hughes, A. U. J. Lode, D. Jaksch, and P. Molignini, *Accuracy of quantum simulators with ultracold dipolar molecules: A quantitative comparison between continuum and lattice descriptions*, Phys. Rev. A **107**, 033323 (2023).

[297] Y. Bilinskaya, M. Hughes, and P. Molignini, *Realizing multiband states with ultracold dipolar quantum simulators*, Phys. Rev. Res. **6**, L042024 (2024).

[298] H. Yuan and N. Khaneja, *Efficient synthesis of quantum gates on a three-spin system with triangle topology*, Phys. Rev. A **84**, 062301 (2011).

[299] U. Boscain, G. Charlot, J.-P. Gauthier, S. Guérin, and H.-R. Jauslin, *Optimal control in laser-induced population transfer for two- and three-level quantum systems*, J. Math. Phys. **43**, 2107-2132 (2002).

[300] M. Rossignolo, T. Reisser, A. Marshall, P. Rembold, A. Pagano, *et al.*, *Quocs: The quantum optimal control suite*, Comput. Phys. Commun. **291**, 108782 (2023).

[301] P. Rembold, N. Oshnik, M. M. Müller, S. Montangero, T. Calarco, and E. Neu, *Introduction to quantum optimal control for quantum sensing with nitrogen-vacancy centers in diamond*, AVS Quantum Sci. **2**, 024701 (2020).

[302] J. Singh, J. A. P. Reuter, T. Calarco, F. Motzoi, and R. Zeier, Raw data files (2025).

[303] C. Chin, R. Grimm, P. Julienne, and E. Tiesinga, *Feshbach resonances in ultracold gases*, Rev. Mod. Phys. **82**, 1225–1286 (2010).

[304] A. Omran, *A microscope for Fermi gases*, Ph.D. thesis (2016).

[305] M. Boll, *Spin and density resolved microscopy of Hubbard chains*, Ph.D. thesis (2016).

[306] R. H. Byrd, J. Nocedal, and R. B. Schnabel, *Representations of quasi-newton matrices and their use in limited memory methods*, Mathematical Programming **63**, 129-156 (1994).

[307] J. Singh, R. Zeier, T. Calarco, and F. Motzoi, *Compensating for nonlinear distortions in controlled quantum systems*, Phys. Rev. Appl. **19**, 064067 (2023).

[308] U. Rasulov and I. Kuprov, Instrumental distortions in quantum optimal control (2025), arXiv:2502.02198 .

[309] J. H. Wilkinson, *The Algebraic Eigenvalue Problem* (Clarendon Press, Oxford, 1965).

[310] A. G. Baydin, B. A. Pearlmutter, A. A. Radul, and J. M. Siskind, *Automatic differentiation in machine learning: a survey*, J. Mach. Learn. Res. **18**, 5595–5637 (2017).

[311] D. S. Abrams and S. Lloyd, *Simulation of Many-Body Fermi Systems on a Universal Quantum Computer*, Phys. Rev. Lett. **79**, 2586–2589 (1997).

[312] F. Arute, K. Arya, R. Babbush, D. Bacon, J. C. Bardin, *et al.*, *Quantum supremacy using a programmable superconducting processor*, Nature **574**, 505–510 (2019).

[313] P. W. Shor, *Polynomial-time algorithms for prime factorization and discrete logarithms on a quantum computer*, SIAM J. Comput. **26**, 1484–1509 (1997).

[314] S. McArdle, S. Endo, A. Aspuru-Guzik, S. C. Benjamin, and X. Yuan, *Quantum computational chemistry*, Rev. Mod. Phys. **92**, 015003 (2020).

[315] H.-S. Zhong, H. Wang, Y.-H. Deng, M.-C. Chen, L.-C. Peng, *et al.*, *Quantum computational advantage using photons*, Science **370**, 1460–1463 (2020).

[316] Q. Zhu, S. Cao, F. Chen, M.-C. Chen, X. Chen, *et al.*, *Quantum computational advantage via 60-qubit 24-cycle random circuit sampling*, Sci. Bull. **67**, 240–245 (2022).

[317] L. S. Madsen, F. Laudenbach, M. Falamarzi Askarani, T. Vincent, J. F. F. Bulmer, *et al.*, *Quantum computational advantage with a programmable photonic processor*, Nature **606**, 75–81 (2022).

[318] Y. Kim, A. Eddins, S. Anand, K. X. Wei, E. van den Berg, *et al.*, *Evidence for the utility of quantum computing before fault tolerance*, Nature **618**, 500–505 (2023).

[319] A. Miessen, D. J. Egger, I. Tavernelli, and G. Mazzola, *Benchmarking digital quantum simulations above hundreds of qubits using quantum critical dynamics*, PRX Quantum **5**, 040320 (2024).

[320] M. Liu, R. Shaydulin, P. Niroula, M. DeCross, S.-H. Hung, *et al.*, *Certified randomness using a trapped-ion quantum processor*, Nature **640**, 343–348 (2025).

[321] A. D. King, A. Nocera, M. M. Rams, J. Dziarmaga, R. Wiersema, *et al.*, *Beyond-classical computation in quantum simulation*, Science **388**, 199-204 (2025).

[322] E. Farhi, J. Goldstone, and S. Gutmann, A quantum approximate optimization algorithm (2014), arXiv:1411.4028 .

[323] N. Moll, P. Barkoutsos, L. S. Bishop, J. M. Chow, A. Cross, *et al.*, *Quantum optimization using variational algorithms on near-term quantum devices*, Quantum Sci. Technol. **3**, 030503 (2018).

[324] C. Hempel, C. Maier, J. Romero, J. McClean, T. Monz, *et al.*, *Quantum Chemistry Calculations on a Trapped-Ion Quantum Simulator*, Phys. Rev. X **8**, 031022 (2018).

[325] C. D. Marciniak, T. Feldker, I. Pogorelov, R. Kaubruegger, D. V. Vasilyev, *et al.*, *Optimal metrology with programmable quantum sensors*, Nature **603**, 604–609 (2022).

[326] A. Kandala, A. Mezzacapo, K. Temme, M. Takita, M. Brink, *et al.*, *Hardware-efficient variational quantum eigensolver for small molecules and quantum magnets*, Nature **549**, 242–246 (2017).

[327] C. Kokail, C. Maier, R. van Bijnen, T. Brydges, M. K. Joshi, *et al.*, *Self-verifying variational quantum simulation of lattice models*, Nature **569**, 355–360 (2019).

[328] M. Meth, V. Kuzmin, R. van Bijnen, L. Postler, R. Stricker, *et al.*, *Probing phases of quantum matter with an ion-trap tensor-network quantum eigensolver*, Phys. Rev. X **12**, 041035 (2022).

[329] J. Kattemölle and J. van Wezel, *Variational quantum eigensolver for the Heisenberg antiferromagnet on the kagome lattice*, Phys. Rev. B **106**, 214429 (2022).

[330] K. N. Okada, K. Osaki, K. Mitarai, and K. Fujii, *Classically optimized variational quantum eigensolver with applications to topological phases*, Phys. Rev. Res. **5**, 043217 (2023).

[331] V. Cimini, M. Valeri, S. Piacentini, F. Ceccarelli, G. Corrielli, *et al.*, *Variational quantum algorithm for experimental photonic multiparameter estimation*, npj Quantum. Inf. **10**, 1–9 (2024).

[332] F. Arute, K. Arya, R. Babbush, D. Bacon, J. C. Bardin, *et al.*, *Hartree-Fock on a superconducting qubit quantum computer*, Science **369**, 1084–1089 (2020).

[333] A. Kandala, K. Temme, A. D. Córcoles, A. Mezzacapo, J. M. Chow, and J. M. Gambetta, *Error mitigation extends the computational reach of a noisy quantum processor*, Nature **567**, 491–495 (2019).

[334] G. Pagano, A. Bapat, P. Becker, K. S. Collins, A. De, *et al.*, *Quantum approximate optimization of the long-range ising model with a trapped-ion quantum simulator*, Proc. Natl. Acad. Sci. U.S.A. **117**, 25396-25401 (2020).

[335] Y. Nam, J.-S. Chen, N. C. Pisenti, K. Wright, C. Delaney, *et al.*, *Ground-state energy estimation of the water molecule on a trapped-ion quantum computer*, npj Quantum. Inf. **6**, 1–6 (2020).

[336] M. Peper, Y. Li, D. Y. Knapp, M. Bileska, S. Ma, *et al.*, *Spectroscopy and modeling of yb 171 rydberg states for high-fidelity two-qubit gates*, Phys. Rev. X **15**, 011009 (2025).

[337] A. Senoo, A. Baumgärtner, J. W. Lis, G. M. Vaidya, Z. Zeng, *et al.*, High-fidelity entanglement and coherent multi-qubit mapping in an atom array (2025), arXiv:2506.13632 .

[338] P. Scholl, M. Schuler, H. J. Williams, A. A. Eberharter, D. Barredo, *et al.*, *Quantum simulation of 2d antiferromagnets with hundreds of rydberg atoms*, Nature **595**, 233–238 (2021).

[339] S. Ebadi, T. T. Wang, H. Levine, A. Keesling, G. Semeghini, *et al.*, *Quantum phases of matter on a 256-atom programmable quantum simulator*, Nature **595**, 227–232 (2021).

[340] H. J. Manetsch, G. Nomura, E. Bataille, K. H. Leung, X. Lv, and M. Endres, A tweezer array with 6100 highly coherent atomic qubits (2024), arXiv:2403.12021 .

[341] R. Tao, M. Ammenwerth, F. Gyger, I. Bloch, and J. Zeiher, *High-fidelity detection of large-scale atom arrays in an optical lattice*, Phys. Rev. Lett. **133**, 013401 (2024).

[342] A. J. Park, J. Trautmann, N. Šantić, V. Klüsener, A. Heinz, *et al.*, *Cavity-enhanced optical lattices for scaling neutral atom quantum technologies to higher qubit numbers*, PRX Quantum **3**, 030314 (2022).

[343] D. Barredo, V. Lienhard, S. De Leseleuc, T. Lahaye, and A. Browaeys, *Synthetic three-dimensional atomic structures assembled atom by atom*, Nature **561**, 79–82 (2018).

[344] G. Semeghini, H. Levine, A. Keesling, S. Ebadi, T. T. Wang, *et al.*, *Probing topological spin liquids on a programmable quantum simulator*, Science **374**, 1242–1247 (2021).

[345] D. Bluvstein, H. Levine, G. Semeghini, T. T. Wang, S. Ebadi, *et al.*, *A quantum processor based on coherent transport of entangled atom arrays*, Nature **604**, 451–456 (2022).

[346] A. Michel, S. Grijalva, L. Henriet, C. Domain, and A. Browaeys, *Blueprint for a digital-analog variational quantum eigensolver using Rydberg atom arrays*, Phys. Rev. A **107**, 042602 (2023).

[347] M. Larocca, S. Thanasilp, S. Wang, K. Sharma, J. Biamonte, *et al.*, *Barren plateaus in variational quantum computing*, Nat. Rev. Phys. **7**, 174–189 (2025).

[348] R. d. Keijzer, O. Tse, and S. Kokkelmans, *Pulse based Variational Quantum Optimal Control for hybrid quantum computing*, Quantum **7**, 908 (2023).

[349] A. B. Magann, C. Arenz, M. D. Grace, T.-S. Ho, R. L. Kosut, *et al.*, *From pulses to circuits and back again: A quantum optimal control perspective on variational quantum algorithms*, PRX Quantum **2**, 010101 (2021).

[350] I. Kurniawan, G. Dirr, and U. Helmke, *Controllability Aspects of Quantum Dynamics:A Unified Approach for Closed and Open Systems*, IEEE Trans. Autom. Control **57**, 1984–1996 (2012).

[351] V. Jurdjevic and H. J. Sussmann, *Control systems on Lie groups*, J. Differ. Equ. **12**, 313–329 (1972).

[352] Z. Zimborás, R. Zeier, M. Keyl, and T. Schulte-Herbrüggen, *A dynamic systems approach to fermions and their relation to spins*, EPJ Quantum Technol. **1**, 1–53 (2014).

[353] V. Ramakrishna, M. V. Salapaka, M. Dahleh, H. Rabitz, and A. Peirce, *Controllability of molecular systems*, Phys. Rev. A **51**, 960–966 (1995).

[354] S. G. Schirmer, H. Fu, and A. I. Solomon, *Complete controllability of quantum systems*, Phys. Rev. A **63**, 063410 (2001).

[355] C. Altafini, *Controllability of quantum mechanical systems by root space decomposition of su(N)*, J. Math. Phys. **43**, 2051–2062 (2002).

[356] S. G. Schirmer, I. C. H. Pullen, and A. I. Solomon, *Identification of dynamical Lie algebras for finite-level quantum control systems*, J. Phys. A **35**, 2327 (2002).

[357] T. Polack, H. Suchowski, and D. J. Tannor, *Uncontrollable quantum systems: A classification scheme based on Lie subalgebras*, Phys. Rev. A **79**, 053403 (2009).

[358] S. G. Schirmer, A. I. Solomon, and J. V. Leahy, *Degrees of controllability for quantum systems and application to atomic systems*, J. Phys. A **35**, 4125 (2002).

[359] F. Albertini and D. D'Alessandro, *Controllability of symmetric spin networks*, J. Math. Phys. **59**, 052102 (2018).

[360] S. G. Schirmer, A. I. Solomon, and J. V. Leahy, *Criteria for reachability of quantum states*, J. Phys. A **35**, 8551 (2002).

[361] R. Zeier and Z. Zimborás, *On squares of representations of compact lie algebras*, J. Math. Phys. **56**, 081702 (2015).

[362] T. Schulte-Herbrüggen, G. Dirr, and R. Zeier, *Quantum systems theory viewed from kossakowski-lindblad lie semigroups — and* vice versa, Open Sys. Information Dyn. **24**, 1740019 (2017).

[363] E. Farhi, J. Goldstone, S. Gutmann, and M. Sipser, Quantum Computation by Adiabatic Evolution (2000), arXiv:quant-ph/0001106 .

[364] M. Born and V. Fock, *Beweis des Adiabatensatzes*, Z. Physik **51**, 165-180 (1928).

[365] T. Kato, *On the Adiabatic Theorem of Quantum Mechanics*, J. Phys. Soc. Jpn. **5**, 435-439 (1950).

[366] A. Messiah, *Quantum Mechanics*, Vol. 2 (North-Holland, Amsterdam, 1962).

[367] S. Teufel, *Adiabatic Perturbation Theory in Quantum Dynamics* (Springer, Berlin, 2003).

[368] S. Teufel, Quantum Adiabatic Theorem, in *Perturbation Theory: Mathematics, Methods and Applications*, edited by G. Gaeta (Springer, New York, 2022) pp. 419–431.

[369] B. Simon, *Tosio Kato's work on non-relativistic quantum mechanics, Part 2*, Bull. Math. Sci. **9**, 1950005 (2019).

[370] F. Robicheaux and J. Hernández, *Many-body wave function in a dipole blockade configuration*, Phys. Rev. A **72**, 063403 (2005).

[371] H. Weimer, R. Löw, T. Pfau, and H. P. Büchler, *Quantum critical behavior in strongly interacting rydberg gases*, Phys. Rev. Lett. **101**, 250601 (2008).

[372] H. Bernien, S. Schwartz, A. Keesling, H. Levine, A. Omran, *et al.*, *Probing many-body dynamics on a 51-atom quantum simulator*, Nature **551**, 579–584 (2017).

[373] J. Choi, A. L. Shaw, I. S. Madjarov, X. Xie, R. Finkelstein, *et al.*, *Preparing random states and benchmarking with many-body quantum chaos*, Nature **613**, 468–473 (2023).

[374] G. André, R. Bidaux, J. Carton, R. Conte, and L. de Seze, *Frustration effects in 2D regular Ising models*, J. Appl. Phys. **50**, 7345–7347 (1979).

[375] L. S. Lima, E. B. Cantuária, and G. M. Diniz, *Magnon Hall conductivity and thermal transport in frustrated antiferromagnets*, Physica C: Superconductivity and its Applications **559**, 50–54 (2019).

[376] B. C. Hall, *Lie Groups, Lie Algebras, and Representations*, 2nd ed. (Springer, New York, 2015).

[377] N. Jacobson, *Lie Algebras* (Dover Publications, New York, 1979).

[378] W. A. de Graaf, *Lie Algebras: Theory and Algorithms* (Elsevier, Amsterdam, 2000).

[379] F. Lorenz, *Algebra, Volume II* (Springer, New York, 2008).

[380] N. Jacobson, *Basic Algebra I*, 2nd ed. (Freeman, San Francisco, 1985).

[381] N. Jacobson, *Basic Algebra II*, 2nd ed. (Freeman, San Francisco, 1989).

[382] K. Lux and H. Pahlings, *Representations of Groups: A Computational Approach* (Cambridge University Press, Cambridge, 2010).

[383] C. W. Curtis and I. Reiner, *Representation Theory of Finite Groups and Associative Algebras* (Wiley, New York, 1962).

[384] C. W. Curtis and I. Reiner, *Methods of Representation Theory, Volume I* (Wiley, New York, 1981).

[385] C. Proccesi, *Lie Groups* (Springer, New York, 2007).

[386] N. Bourbaki, *Algebra, Chapter 8* (Springer, Cham, 2022).

[387] W. Eberly and M. Giesbrecht, in *Proceedings of the 1996 international symposium on Symbolic and algebraic computation*, ISSAC '96 (New York, NY, USA, 1996) pp. 170–178.

[388] S. H. Sack and M. Serbyn, *Quantum annealing initialization of the quantum approximate optimization algorithm*, Quantum **5**, 491 (2021).

[389] J. E. Avron and A. Elgart, *Adiabatic Theorem without a Gap Condition*, Comm. Math. Phys. **203**, 445-463 (1999).

[390] W. Bosma, J. Cannon, and C. Playoust, *The* MAGMA *Algebra System I: The User Language*, J. Symb. Comput. **24**, 235–265 (1997).

[391] H. Cohen, *A Course in Computational Algebraic Number Theory* (Springer, Berlin, 1993).

[392] S. Yang, G. Masella, V. Moeini, A. Bellahsene, C. Li, *et al.*, *Compact arbitrary optical waveform modulator with digital feedback*, Phys. Rev. Appl. **23**, 054009 (2025).

Acknowledgement

I would like to sincerely thank my Ph.D. supervisors — Robert Zeier, Felix Motzoi, and Tommaso Calarco — for giving me the opportunity to work in a renowned research group and for guiding me through such interesting and meaningful projects. I deeply appreciate Felix for being not only an incredible mentor but also a wonderful friend. A very special thank you goes to Robert for teaching me nearly all the research skills I possess today, for trusting me with a challenging and exciting series of projects, and for giving me the responsibility to represent our group at several important occasions. These experiences collectively shaped my understanding of what it takes to become an independent researcher. My sincere gratitude also extends to my co-authors and collaborators for their constant efforts in making our projects successful. I am grateful to Joachim Hemberger and Christian Gross for joining my thesis committee — your time, feedback, and expertise are truly appreciated.

A heartfelt thank you to everyone at PGI-8, Forschungszentrum Jülich, for all the scientific and non-scientific conversations. The last few years of my journey wouldn't have been nearly as exciting without all of you. I would like to thank Boxi, Shahrukh and Jesus for helping me throughout the thesis process.

A very special set of thanks goes to my friends Ashutosh, Priyanka, Kunal, and Aditi, who patiently handled my countless mental breakdowns. We all became a second family in this small town, making life here not just livable but genuinely enjoyable. I want to thank Ashutosh and Kunal also for all the quantum physics discussions and for answering my endless stream of "stupid" questions. My heartfelt gratitude also extends to Waseem, Tripathi, Preeti, and Kaustubh, who — despite being 6000 kilometers away — have remained constant pillars of strength in my life. Your unwavering support means the world to me.

A very loving thank you to Prasad, for your constant support throughout this journey, for making sure I didn't turn into a complete workaholic, and for reminding me to live a life beyond work. Your presence made this process a little lighter and a lot more meaningful.

Last but certainly not least, I want to thank my family for your selfless love and unwavering support in every phase of my life. A special thanks to my siblings for handling so many responsibilities back home while their little sister was off learning the ways of physics.

List of publications

3. **Juhi Singh**, Andreas Kruckenhauser, Rick van Bijnen, and Robert Zeier, *Ground-state reachability for variational quantum eigensolvers: a Rydberg-atom case study*, arXiv.2506.22387 (2025).

2. **Juhi Singh**, Jan Reuter, Tommaso Calarco, Felix Motzoi, and Robert Zeier, *Optimizing two-qubit gates for ultracold atoms using Fermi-Hubbard models*, arXiv:2503.06768 (2025).

1. **Juhi Singh**, Robert Zeier, Tommaso Calarco, and Felix Motzoi, *Compensating for Nonlinear Distortions in Controlled Quantum Systems*, Physical Review Applied 19, 064067 (2023).

Curriculum vitae

01.2021 - present	Research Center Jülich and University of Cologne
	Ph.D. candidate
	Supervisor: Prof. Dr. Tommaso Calarco
	and Prof. Dr. Felix Motzoi
07.2018 - 06.2020	Savitribai Phule Pune University
	Master of Science in Physics
	Supervisor: Dr. Ankita Katre
06.2014 - 07.2017	Patna University
	Bachelor of Science in Physics
	Supervisor: Prof. Dr. Aprajita Krishna